DESIGN, ANALYSIS AND CONTROL OF A 5-PHASE FRACTIONAL SLOT SURFACE MOUNTED PM MACHINE FOR APPLICATIONS WITH A WIDE SPEED RANGE

Thesis submitted for the degree of

Doctor of Philosophy

at the University of Leicester

By

WALEED JEBIR HASSAN

Supervisor

Paul W. Lefley

DEPARTMENT OF ENGINEERING
UNIVERSITY OF LEICESTER
UNITED KINGDOM

September 2018

ABSTRACT

DESIGN, ANALYSIS AND CONTROL OF A FIVE-PHASE FRACTIONAL SLOT SURFACE MOUNTED PM MACHINE FOR APPLICATIONS WITH A WIDE SPEED RANGE

By

WALEED JEBIR HASSAN

Reliability problems associated with a three-phase electrical machine lead the researcher to investigate multi-phase machines, where the number of phases is greater than three, and which are starting to attract a growing interest. A five-phase surface mounted permanent magnet synchronous motor (SPM) can be considered as a candidate for fault-tolerant critical applications such as electrical actuators in aircraft and aerospace applications, in addition to other characteristics like high torque-to-mass ratio and high efficiency. This thesis is concerned with the design, analysis and control of a five-phase SPM machine equipped with a fractional slot winding. In particular, it examines the possibility of using five-phase SPM machines for fault tolerant, wide speed range applications.

The thesis covers three sub-areas. The first describes the design, analysis and test of a five-phase SPM motor with improved capability in fault event and flux-weakening operation. A five-phase SPM motor has been designed by deriving all necessary equations required for optimising the machine to produce an acceptable torque at high operating speeds above the corner speed.

The second aims to explore the effect of varying the motor drive parameters on the optimum flux-weakening performance of the Multi-Frequency (MF) five-phase SPM drive. It is shown that the fundamental magnet flux linkage determines the maximum reachable speed in the flux-weakening mode of operation. The back-emf ratio increases the normalised electromagnetic torque for speeds below the base speed, while it decreases the normalised electromagnetic torque for speeds higher than the base speed.

The third deals with the modelling and control of five-phase PM synchronous machines with a non-sinusoidal shape of the rotor flux. A discrete PI controllers for currents and speed were designed based on the two virtual machines analysis. The simulation and practical results showed a good dynamic response.

Dedicated to the memory of my father, the memory of my mother, my children, my brothers and my sisters. I would like to give my heartfelt appreciation to my wife, who has accompanied me with her love, unlimited patience, understanding and encouragement. Without her support, I would never be able to accomplish this work.

ACKNOWLEDGMENT

First of all, I would like to thank my supervisor Dr. Paul Lefley for his appreciated effort and support over all these years.

I would like to thank Mr. Mohan Kansara. My conversations and discussions with Dr. Kansara both at the professional and personal level have always been very enjoyable.

Special thanks are given to Mr Luigi Alessandro for his technical help and support.

I would like to thank my thesis examiners Dr. Stephen Dodd and Prof. Emil Levi for their suggestions, which helped me to improve the final version of my thesis.

I would like to thank the Ministry of Higher Education and Scientific Research-Republic of Iraq for granting a Ph.D. scholarship.

Also, I would like to thank all my friends who helped me and wished me good luck in my life.

TABLE OF CONTENTS

List of Tables . . . . . **viii**

List of Figures . . . . . **x**

Key to Symbols . . . . . **xvi**

Key to Abbreviations . . . . . **xx**

1 Introduction **1**
1.1 Research Description 1
1.2 Research Aims 2
1.3 Major Research Contributions 3
1.4 Thesis Organisation 4

2 FSCWs for Fault-Tolerance and Wide Speed Range Five-Phase PM Synchronous Machines **6**
2.1 Review of the Literature 6
2.2 FSCWs for Fault-Tolerant Machines 8
2.2.1 Advantages of FSCW 9
2.2.2 Difficulties Linked to FSCW 10
2.2.3 Comparison Between SL and DL Windings 11
2.3 Star of Slots Theory 12
2.3.1 Winding Factor 14
2.3.2 Choosing the Slot-Pole Combination 15

3 Designing an Extended Flux Weakening Capability of a Five-Phase SPM Machine **19**
3.1 Introduction 19
3.2 MMF and Inductances of FSCWs 21
3.2.1 MMF 21
3.3 Inductances 22
3.3.1 Calculation of the Slot Leakage Inductance 31
3.3.2 Inductances in the Rotating Reference Frame 33
3.4 Magnet Flux Linkage Calculation 34
3.5 Resistance Calculation 38
3.6 Calculation of the Number of Turns N_{coil} and the Magnet Remanence B_r 39
3.7 Finite Element Approach For Optimal Flux Weakening 40
3.7.1 Inductance Calculations 40
3.7.2 Magnet Flux Linkage Calculation 43
3.7.3 Calculating N_{coil} and B_r 44

4 Design of Five-Phase FSCW PM Synchronous Machine 45
4.1 Design Methodology . . . 45
4.2 Initial Sizing of the Prototype Machine . . . 52
4.3 Machine Design Optimization . . . 56
4.4 Results for Optimal Flux-Weakening Design . . . 58
4.4.1 Resistance . . . 60
4.4.2 Inductances . . . 60
4.5 Back-emf and Magnet Flux Linkage . . . 62
4.6 Cogging Torque . . . 64
4.7 Characteristic Current . . . 65

5 Modelling and Control of the MF Five-Phase PM Synchronous Motor Based Drive 67
5.1 Modelling of the Two- Level Five-Phase Voltage Source Inverter . . . 67
5.1.1 Phase Voltage Space Vectors of the Five-Phase VSI . . . 69
5.2 Modelling of the MF Five-Phase PM Synchronous Motor . . . 73
5.2.1 Phase Domain Model of the MF Five-Phase PM Synchronous Motor . . . 73
5.2.2 Machine Model in the Stator Reference Frame . . . 75
5.3 Machine Model in the Rotor Reference Frame . . . 76
5.3.1 Voltage Transformation . . . 77
5.3.2 Flux Transformation . . . 79
5.3.3 Electromagnetic Torque Transformation . . . 80
5.3.4 Mechanical System . . . 80
5.4 Field Orientation Control of the Drive System . . . 81
5.4.1 The Control Structure of the Five-Phase PM Synchronous Motor Drive System . . . 81
5.4.2 Current Controller . . . 82
5.4.3 Speed Controller . . . 88
5.4.4 Symmetric Sampling SPWM . . . 92
5.5 The Dynamic Performance of the Drive System . . . 95
5.5.1 Simulation . . . 95
5.5.2 Dynamic Test of the Prototype Motor . . . 96

6 Flux Weakening Theoretical Limitation for Five-Phase SPM Drive 103
6.1 Introduction . . . 104
6.2 Voltage and Current Constraints of MF-SPM . . . 107
6.3 Machine Model and Hypothesis . . . 110
6.4 Per Unit Model . . . 111
6.5 Results . . . 117
6.5.1 Characteristics of the SF Five-Phase SPM Machine . . . 117
6.5.2 Drive System Characteristics for Different Back-emf Ratios . 117
6.5.3 Drive System Characteristics for Different Inductance Ratios 120
6.6 Discussion . . . 120

7 Flux Weakening Control for Five-Phase SPM Permanent Magnet Synchronous Machines 125
7.1 Introduction . . . 125
7.2 MTPA and Flux-Weakening Circle Diagram . . . 126
7.3 Operating Region Under Current and Voltage Constraints . . . 128
7.3.1 Finite-Speed Drive System . . . 129
7.3.2 Infinite-Speed Drive System . . . 130
7.4 Rated speed, Maximum Speed and i_{ds1}^{r*} Current . . . 131
7.5 Flux Weakening Control with Feed-Forward Compensation . . . 133

8 Conclusions and Future Work 138
8.1 Conclusions and Contributions . . . 138
8.2 Future Work . . . 140

REFERENCES . . . 143

Appendices 155

A Machine Fabrication and Test Bench Description 155
A.1 Machine Fabrication . . . 155
A.2 Test Bench Description . . . 155
A.2.1 The dSPACE DS1103 Workstation . . . 158

B Voltage Source Inverter 161

C Flux Weakening Control 164

D The Star of Slots 166

LIST OF TABLES

2.1 Synchronous winding factors for five-phase FSCWs [52]. 16

2.2 Cogging torque indicator for five-phase FSCWs. 16

2.3 Net radial force indicator for five-phase FSCWs. 17

3.1 The dimensions summary of the prototype five-phase SPM machine. . 25

4.1 Standard values for torque per-unit motor volume (TRV). 46

4.2 The rotor to stator diameter ratio as a function of pole number. . . . 46

4.3 Practical ranges for the air-gap thickness. 47

4.4 Typical phase conductor current densities. 50

4.5 The design specifications. 52

4.6 Parameters with assigned constant values. 57

4.7 Summary of the dimensions, specifications and the numerically calculated parameters of the designed SPM machine. 58

4.8 The measured and calculated per phase resistance of the prototype five-phase machine at 25 °C. 60

4.9 Lab prototype five-phase machine stator inductance components, analytical calculation and numerical simulation in dq coordinates. 62

4.10 Prototype five-phase machine stator back-emf and magnet flux linkage: lab measurement, analytical calculation and numerical simulation. 64

4.11 The numerically calculated value, the analytically calculated value of the characteristic current, and the rated current of the prototype machine. All variables are rms quantities. 66

5.1 Distribution of the harmonic families for Y-connected, five-phase machine. 71

5.2 Practical measurements of the machine parameters. 86

5.3 Proportional and integral gains of the machine electrical dynamics controllers. 89

B.1 Phase-to-neutral voltages of a star connected load supplied from a five-phase VSI. 162

B.2 Space vector table of the phase voltages for a five-phase VSI. 163

LIST OF FIGURES

2.1 Winding layouts for FSCWs 6 slot/ 4 pole three-phase SPM machine. (a) double-layer windings. (b) single-layer windings. 10

2.2 Star of slots of 10 slot/ 8 pole fractional slot winding. 13

2.3 Geometrical design and winding layout of DL 10 slot/ 8 pole five-phase PM synchronous machine. 14

3.1 Phase winding function harmonic content of 10 slot/ 8 pole DL FSCW SPM machine. N_a : Winding function of phase a. 21

3.2 Resultant rotating MMF wave of 10-slot 8-pole DL FSCW SPM machine. 22

3.3 Plots of the turns function, average and winding function of phase a. 24

3.4 Geometrical design and winding layout of the prototype DL FSCW 10 slot/ 8 pole five-phase SPM machine. 25

3.5 Plots of the turns function, average value and the resulting winding function of all five phases and phase a-b combined. 26

3.6 Plots of the winding function of phases a, b and the resulting product. 27

3.7 Winding function of phase a 29

3.8 Graphical depiction of the phase a winding function for few terms of the Fourier expansion. (a): Adding up 20 terms (red waveforms). (b): Adding up 100 terms. (c): Harmonics content. 31

3.9 Simplified slot geometry. 33

3.10 Relationship between the air-gap flux density and its fundamental. . . 35

3.11 Simple layout of a 2-pole PM motor with surface magnets. 37

3.12 References for the rotor reference frame. (a) Fundamental harmonic component with a positive sequence (+). (b) Third harmonic component with a negative sequence (-). 42

4.1 Stator slot form and dimensions. 50

4.2 Initial sizing flowchart for the designed machine. 51

4.3 Flux-line pattern of the designed machine at the rated load. 59

4.4 Airgap flux density of DL 10 slot/ 8 pole five-phase SPM machine. . . 59

4.5 The back-emf waveform of the lab prototype five-phase machine. . . . 63

4.6 The harmonic content of the lab prototype five-phase machine. 64

4.7 The numerical simulation waveform of the back-emf of the lab prototype machine. 65

4.8 Cogging torque of DL 10 slot/ 8 pole five-phase SPM. Optimum magnet angle is 37.46°. 65

4.9 The torque-speed characteristic of the designed machine. 66

5.1 Five-leg VSI supplying a five-phase PM synchronous motor. 68

5.2 Power converter 69

5.3 Five-phase VSI phase voltage space vectors in the: a. $\alpha_1 - \beta_1$ plane, and b. $\alpha_2 - \beta_2$ plane [77]. 72

5.4 Two 2D and mutually decoupled planes of a five-phase motor. (a) $\alpha_1 - \beta_1$ plane. (b) $\alpha_2 - \beta_2$ plane. 76

5.5 References for the rotor reference frame. (a) Fundamental harmonic component with a positive sequence (+). (b) Third harmonic component with a negative sequence (-). 77

5.6 Field orientation control diagram of the five-phase PM synchronous motor. 82

5.7 Electrical part of the machine dynamics and current controllers. . . . 83

5.8 The discrete models for designing the $D_x(z)$ controllers for $i^r_{ds1}, i^r_{qs1}, i^r_{ds2}$ and i^r_{qs2}. 84

5.9 Backward difference approximation discrete PI controller. 85

5.10 The discrete root locus of the negative feedback loop of the rotor i^r_{ds1} and i^r_{qs1} axes currents. 87

5.11 The discrete root locus of the negative feedback loop of the rotor i^r_{ds2} and i^r_{qs2} axes currents. 88

5.12 Feedback control system for the speed controller design. 90

5.13 The discrete root locus and the selected closed-loop poles for the speed controller. 93

5.14 Symmetric sampling SPWM at carrier frequency. 94

5.15 SIMULINK Model of the symmetric sampling SPWM. 94

5.16 Comparison of the digitised sample reference signal with the carrier PWM signal. 95

5.17 Motor speed response for a step change in the speed set-point speed at $t = 0, 0.3$ and 0.7 sec. 96

5.18 Motor speed response for a step change and acceleration/deceleration ramp in the speed set-point at $t = 0, 0.3$ and 0.7 sec. 97

5.19 The response of the electromagnetic torque at the rated speed (2000 rpm) for a step change in the load torque of 2 N.m. at t =0.3 sec. . . 97

5.20 The response of the q_1-axis current at the rated speed (2000 rpm) for a step change in the load torque of 2 N.m. at t =0.3 sec. 97

5.21 The response of the q_2-axis current at the rated speed (2000 rpm) for a step change in load torque of 2 N.m. at t =0.3 sec. 98

5.22 The response of the α_1-axis, β_1-axis, α_2-axis, and β_2-axis currents at the rated speed (2000 rpm) for a step change in load torque of 2 N.m. at t =0.3 sec. 98

5.23 The response of the i_a, i_b, i_c, i_d and i_e phase currents at the rated speed of 2000 rpm for a step load torque of 2 N.m. at t =0.3 sec. . . . 98

5.24 The speed response of the prototype motor for a step change in the speed set-point speed at $t = 1.15$ sec. 99

5.25 The q_1-axis current response of the prototype motor. 100

5.26 The d_1-axis current response of the prototype motor. 100

5.27 The q_2-axis current response of the prototype motor. 100

5.28 The d_2-axis current response of the prototype motor. 101

5.29 The α_1-axis and β_1-axis currents response of the prototype motor. . . 101

5.30 The response of the i_a, i_b, i_c, i_d and i_e phase currents of the prototype motor. 101

5.31 Steady state phase currents of the prototype motor when the third harmonic is not injected. 102

6.1 Mode of operations of PM synchronous motors. 105

6.2 linear modulation region. 109

6.3 Phasor diagram of the MF five-phase permanent magnet synchronous motor. 112

6.4 Characteristics of the SF five-phase SPM machine based drive with λ_{m1n} as a parameter. 118

6.5 Calculated characteristics of an MF five-phase SPM machine based drive for unity inductance ratio ($L_{21} = 1$). 121

6.6 Calculated characteristics of an MF five-phase SPM machine based drive for inductance ratio $L_{21} = 0.5$. 122

6.7 Calculated characteristics of an MF five-phase SPM machine based drive for inductance ratio $L_{21} = 1.5$. 123

6.8 Calculated characteristics of an MF five-phase SPM machine based drive for $\lambda_{m1n} = 0.71$ and 0.85, $E_{b21} = 0.5$ and different inductance ratios. 124

7.1 Voltage and current constraints of surface-mounted permanent magnet synchronous machine depicted in $d_1 - q_1$ plane [109]. 128

7.2 Voltage constraint, current constraint and current trajectory in a finite-speed SPM drive depicted in $d_1 - q_1$ plane. 129

7.3 Voltage constraint, current constraint and current trajectory in an infinite-speed SPM machine drive in which $I_{s\max} > \frac{\lambda_{m1}}{L_{s1}}$ depicted in $d_1 - q_1$ plane. 130

7.4 Voltage constraint, current constraint and current trajectory of the MM in infinite-speed SPM machine drive in which $I_{s\max} = \frac{\lambda_{m1}}{L_{s1}}$ depicted in $d_1 - q_1$ plane. 131

7.5 Motor speed response for commanded speeds 2000 rpm at t =0 sec and 4000 rpm at t =0.5 sec for a step load torque of 1.1 N.m at t =0.2 sec. 135

7.6 The response of the electromagnetic torque for speed demands of 2000 rpm at t =0 sec, 4000 rpm at t =0.5 sec and a step load torque of 1.1 N.m at t = 0.2 sec. 135

7.7 The response of the q_1-axis current for speed demands of 2000 rpm at t =0 sec, 4000 rpm at t =0.5 sec and a step load torque of 1.1 N.m at t = 0.2 sec. 136

7.8 The response of the d_1-axis current for speed demands of 2000 rpm at t =0 sec, 4000 rpm at t =0.5 sec and a step load torque of 1.1 N.m at t = 0.2 sec. 136

7.9 The response of the phase currents for speed demands of 2000 rpm at t =0 sec, 4000 rpm at t =0.5 sec and a step load torque of 1.1 N.m at t = 0.2 sec. 137

A.1 Stator, rotor, covers and bearings of the prototype motor. 156

A.2 Prototype machine stator core. 156

A.3 The frame of the prototype motor. 157

A.4 The cylindrical shaped rotor, including bearings. 157

A.5 General view of the test bench. 159

A.6 The CLP1103 Connector Panel. 159

A.7 The test instrumentation panel of the host PC. 160

B.1 Prototype five phase two-level VSI. 161

C.1 The currents demand control. 164

C.2 Flux-Weakening control Block. 164

C.3 Constant torque control block. 165

KEY TO SYMBOLS

A_c	Cross section area of one conductor [m^2]
A_g	Air-gap area [m^2]
A_m	Magnet area [m^2]
A_P	Area of one pole measured along the rotor surface [m^2]
A_{slot}	Slot area [m^2]
B	Friction coefficient of the load and the machine [$N\,m\,rad\,s^{-1}$]
B_{g1}	Peak fundamental of the magnet air-gap flux density [T]
B_{gm}	Air-gap magnetic flux density [T]
B_m	Magnetic flux density in the magnet [T]
B_r	Remanent flux density [T]
b_{ss1}	Slot bottom width [m]
b_{ss2}	Slot top width [m]
$b_{s\circ}$	Slot opening width [m]
$D_{r\circ}$	Rotor outer diameter [m]
$D_{s\circ}$	Stator outer diameter [m]
D_{si}	Stator inner diameter [m]
E_{b21}	Ratio of the back-emf of the SM to the back-emf of the MM
$F_{m/g}$	Magnet to the air-gap thickness ratio
$F_{r/s}$	Rotor to stator diameter ratio
f_{LKG}	Flux leakage factor
F_{α_m/α_P}	Magnet angle divided by the pole pitch ratio
g	Air-gap length [m]
g_e	Effective air-gap length [m]
GCD	Greatest common divisor
H_{gm}	Magnetic field intensity in the air-gap [A-turn/m]
H_m	Magnetic field intensity in the magnet [A-turn/m]
h_m	Radial thickness of the magnets [m]
h_{ss}	Slot depth [m]
$h_{s\circ}$	Slot opening height [m]
I_b	Phase base current [A]
I_{ch}	Characteristic current of the machine [A]

I_{max}	Maximum available current per phase [A]
I_R	Rated armature current per phase [A]
J	Moment of inertia of the load and machine rotor combined in [kg m^2]
J_c	Current density in a slot conductor [A/m^2]
k_c	Carter's coefficient for correcting the air-gap
k_{sf}	Slot fill factor
k_{st}	Lamination stacking factor
k_{dv}	The v^{th} harmonic distribution factor
k_{pv}	The v^{th} harmonic pitch factor
k_{wv}	The v^{th} harmonic winding factor
k_{w1}	Synchronous component winding factor
l_{av}	Average length of a coil turn of a slot winding [m]
L_b	Machine base inductance [H]
LCM	Lowest common multiple
L_d	The d-axis inductance of three-phase PM synchronous machine [H]
L_{d1}	d-axis inductance of the first plane [H]
L_{d2}	d-axis inductance of the second plane [H]
l_{eff}	Effective axial length of the machine [m]
L_{ls}	Stator leakage inductance [H]
L_{nn}	For $n = a, b, c, d$ and e is the stator phase magnetising inductance [H]
L_{nm}	For $n, m = a, b, c, d$ and e is the stator phase mutual inductance [H]
L_{q1}	q-axis inductance of the first plane [H]
L_{q2}	q-axis inductance of the second plane [H]
L_s	Synchronous inductance [H]
L_{st}	Axial stack length [m]
L_{21}	Ratio of the inductance of the SM to the inductance of the MM
M_{max}	Maximum modulation index
M_1	Modulation index of the first plane
M_2	Modulation index of the second plane
m	Machine phase number
N_{cog}	Number of cogging torque periods during a rotation of a slot pitch

N_{coil}	Number of turns per coil
n_c	Number of coils per phase
$n_m(\theta)$	Turns function of phase m
N_n	Winding function of phases n
n_p	Number of parallel paths of the stator phase winding
N_{sr}	Number of turns per phase connected in series
P	Number of machine poles
$P_\circ$	Required rated power during the design stage [W]
P_b	Machine base power [W]
p	Number of machine pole pairs
Q	Number of the stator slots
q	Number of slots per pole and phase
q_{ph}	Number of spokes per phase
$R_{r\circ}$	Rotor outside radius
r_s	Phase winding resistance [Ω]
$T_\circ$	Required rated torque during the design stage [N m]
T_b	Machine base torque [N m]
T_l	Load torque [N m]
t	Machine periodicity
V_b	Machine base voltage [V]
V_K	Inverter pole voltage, ($K \in \{A, B, C, D, E\}$) [V]
V_{max}	Maximum available voltage per phase [V]
V_R	Rated fundamental phase voltage [V]
$V_{r\circ}$	Rotor volume [m^3]
ω_m	Rotor mechanical speed [rads^{-1}]
w_{ry}	Rotor core thickness [m]
w_{sy}	Stator back iron depth [m]
w_{tb}	Tooth width [m]
y_q	Slot pitch measured in the number of slots
α_m	Magnet arc angle [mechanical radians]
α_s^m	Slot angle [mechanical rad]
α_s^e	Slot angle [electrical rad]

ϕ_1	Input power factor angle of the first plane
ϕ_2	Input power factor angle of the second plane
λ_{m1}	Amplitudes of the fundamental harmonic flux linkage established by the permanent-magnets [Wb]
λ_{m2}	Amplitudes of the third harmonic flux linkage established by permanent-magnets [Wb]
γ_1	Current-angle by which the currents I_{1s} leads the back-emf phasor
γ_2	Current-angle by which the currents I_{2s} leads the back-emf phasor
λ_b	Machine base flux linkage [H]
$\mu_\circ$	Permeability of air [H/m]
μ_{rm}	Relative permeability of the magnets
ω_b	Machine base speed [rad/sec]
ρ	Copper resistivity [Ω m]
θ_e	Rotor angle [electrical rad]
θ	Rotor angle [mechanical rad]
τ_s	Slot pitch [m];

KEY TO ABBREVIATIONS

2-D	Two dimensional
FOC	Field orientation control method
DTC	Direct torque control method
DL	Double-layer
FEA	Finite element analysis
FS	Fractional-slot
FSCW	Fractional-slot concentrated winding
IM	Induction motor
IPM	Interior permanent magnet synchronous motor
MF	Multi-frequency
MM	Main virtual machine
MMF	Magnetomotive force
PM	Permanent magnet
SM	Secondary virtual machine
SL	Single-layer
SPM	Surface mounted permanent magnet synchronous motor
TRV	Torque per-unit motor volume
SPWM	Sinusoidal pulse with modulation
VSI	Voltage source inverter
WFM	Winding function method

Chapter 1

Introduction

1.1 Research Description

Fixed speed motors are not fitting for all applications in all conditions; consequently, the demand for adjusting the speed according to an application is required. Variable speed AC drives are used to control the speed of an AC motor, either an induction motor (IM) or a synchronous motor. AC drives are used in a wide variety of industrial applications. For example, AC drives are often used with fans to provide adjustable airflow in heating and air conditioning systems. The flow of water and chemicals in industrial processes is usually controlled by adjusting the speed of pumps. Water and wastewater processing, paper mills, tunnel boring, oil drilling platforms or mining are commonly controlled by variable speed AC drives. For a wide speed range-variable speed drive, especially in traction applications, permanent magnet (PM) synchronous motors are the candidate. Although AC induction motors can operate at high speed, their dynamic performance, efficiency and power density are moderate compared to PM synchronous motors.

There are two main classes of PM synchronous motors. The first is surface mounted PM synchronous motors (SPM) where the magnets are located on the rotor outer surface. The second is interior PM synchronous motors (IPM) where the magnets are buried in the rotor. Variable-speed IPM motor drives offer a wide field-weakening range with good torque versus speed characteristic as a result of the additional reluctance torque component to the magnet torque component. Usually, IPM motors are designed with thin bridges and centre posts in the rotor to minimise

the flux shunting between the magnets. Those bridges and centre posts are counted as the most crucial mechanical limiting design factor where the rotor structural integrity significantly degrades due to centrifugal forces in high-speed operation.

Thus far, the conventional SPM motor drives are extensively used for industrial servo drives. Their flux weakening speed range is generally limited to below 2:1. In this motor drive, SPM motors are equipped with distributed windings designed to have a sinusoidal back-emf and operated with sinusoidal currents. Since the inductance of the distributed winding is generally low, it is difficult to achieve a wide speed range out of satisfying the optimum flux weakening condition by reducing the magnet flux linkage as this is the only torque producing component.

The fault-tolerant capability is another crucial feature of AC motor drive in applications such as traction, aerospace, ship propulsion and safety-critical applications such as the more-electric aircraft. Furthermore, reliability and fault-tolerant aspects of motor drives are favourable in the industrial environment, due to the related productivity enhancement. A three-phase induction motor drive with connected neutral and divided dc bus may be used for fault-tolerant applications, where it continues to operate under the loss of one phase but, the bearing maintenance cost of the motor will increase due to the zero sequence component of the current. Three-phase PM synchronous machine drives have been traditionally thought of as having poor fault-tolerant capability compared to other drive types. Nevertheless, the distinct advantages they offer such as high power density and high efficiency lead to the need to improve the fault-tolerant capability of these drive systems by utilising fractional-slot concentrated windings (FSCWs) and a multi-phase drive system.

The research results presented in this thesis are focused on the analysis, design, control, implementation and experimental evaluation of a fault-tolerant SPM machine drive system with extended high-speed operation by using high inductance five-phase fractional-slot concentrated windings.

1.2 Research Aims

The research aims of the work were to :

1. *Develop a discrete-time domain current regulator based on the developed discrete-*

time domain model of the Multi-Frequency (MF) five-phase surface mounted permanent magnet synchronous motor (MF five-phase SPM) drive which can be implemented to control the prototype five-phase motor drive system.

2. *Investigate the effect of varying the motor drive parameters on the optimum flux-weakening performance of the MF five-phase SPM.*
3. *Analyse the harmonic contents of Fractional Slot (FS) windings for a given slot-pole configuration based on the Winding Function Method (WFM), and characterise its suitability for low cogging torque, low harmonic losses and flux weakening capability.*
4. *Design and build a prototype five-phase SPM synchronous motor for experimental validation of the results reached by analytical and simulation investigations.*
5. *Design and build a five-phase motor drive system including a two-level VSI and its gate drive boards, current sensors, voltage transducer, speed encoder with accompanying DSP control system to be used for investigating the performance of the prototype machine under different operating conditions.*

1.3 Major Research Contributions

1. This research has provided, for the first time, a clear explanation of the effect of varying the motor drive parameters on the optimum flux-weakening performance of a MF five-phase SPM motor for achieving the necessary conditions for optimal flux weakening. Part of the research results are presented in [1].
2. This investigation has presented, for the first time (based on the author's knowledge) an optimised design for a 10 slot/ 8 pole five-phase SPM motor equipped with FSCWs for flux-weakening capability.
3. This is one of very few works in which a digital controller has been designed and simulated for a FSCW five-phase SPM machine, which has opened the door for the use in industrial applications.
4. For classical-sinusoidal distributed windings, in most cases, there are many ready to use mathematical equations and design software. However, for FSCW multi-phase PM machines, the design software needs to be modi-

fied, and the analytical equations needs to be derived. All harmonic and Fourier analyses which are presented in this thesis were calculated by hand or through numerical calculation.

5. Design and build a prototype FSCW five-phase SPM motor.

1.4 Thesis Organisation

This thesis is organised in 8 chapters, followed by 4 appendices.

Chapter 2 presents the literature review of fault-tolerance PM machines. FSCW is selected for further investigations due to its high fault-tolerant capability and high-speed operation. The discussion is concluded with the selection of the slot-pole combination.

In chapter 3 analytical expressions for magnet flux linkage, inductances and resistance of 10 slots-8 poles, five-phase SPM motor necessary for calculating the optimum flux weakening condition during the machine design stage are presented. Numerical calculation of the same parameters is another option which is also studied in this chapter. The star of slots theory is used to determine the winding layout of the above slot-pole combination, concentrated FSCWs, while the winding function theory (WFT) is used to calculate the magnetising inductance of the armature winding.

Chapter 4 deals with the design of a prototype five-phase fractional-slot SPM motor with non-overlapped coils, to be used in fault tolerant- extended speed range applications.

The modelling and control of MF five-phase SPM motor with a non-sinusoidal shape of the rotor flux are addressed in chapter 5. The control scheme was suggested to be a variable speed drive system with flux weakening capability for speeds higher than the rated speed. A decoupling transformation was applied to the two-level five-phase Voltage Source Inverter (VSI) to obtain the voltage space vectors, represented in two two-dimensional (2-D) planes. The mathematical model of the MF five-phase SPM motor in terms of the physical (natural phase) variables is considered first. The voltage, current and flux space vectors, represented in (2-D) planes, are obtained with the use of a decoupling transformation. The mapping of harmonics of different

order after transformation is explained. A rotor transformation is applied, and the dynamic model of the MF five-phase SPM motor is obtained using a two-phase fictitious equivalent to the five-phase machine approach. A discrete-time domain current regulator is developed based on the developed discrete-time domain model of the MF five-phase SPM motor.

Chapter 6 deals with the effect of varying the motor drive parameters on the flux-weakening performance of the five-phase SPM motor drive equipped with both sinusoidally distributed windings and fractional slot windings. A lossless, steady-state, DQ model of an MF five-phase SPM motor under the voltage constraint of the two-level VSI in the linear modulation region of the SPWM approach is utilised for further normalisation. Only the fundamental and the third harmonics are assumed to be in the spectrum of the back-emf waveform. A new DQ normalisation for an MF five-phase SPM drive, based on the rated quantities of the first DQ plane, is developed and used in the optimisation process. Non-linear optimisation problem that aims to maximise the electromagnetic torque of an MF five-phase SPM machine under the voltage and current constraints, for operation in the linear modulation region, is formulated.

In chapter 7 a flux-weakening control for a five-phase SPM motor is presented. The prototype drive system was simulated under feed-forward flux-weakening technique.

Chapter 8 provides conclusions and a summary of the thesis, highlighting the most critical findings from each chapter. Guidelines for future research are also given.

Chapter 2

FSCWs for Fault-Tolerance and Wide Speed Range Five-Phase PM Synchronous Machines

In this chapter, a literature review of the fault-tolerant requirements for PM machines is presented first. Then, based on the fault-tolerance requirements, stator winding layouts are investigated for a five-phase drive system. The discussion is concluded for the selection of slot-pole combination.

2.1 Review of the Literature

The research of fault-tolerant PM machine drive systems can be categorised into two subcategories. The first is how to design an electric machine to be a fault-tolerant. The second is how to configure and control a PM motor drive system in both healthy and faulty operating conditions. According to a definition provided by Bianchi [2], the fault tolerance of an electrical machine is the ability of the machine to operate during a temporary fault such as phase-to-phase or a three-phase short circuit, without being damaged beside its ability to run under continuous faulty operating conditions, such as, an open or a short-circuited phase.

In 1980 Thomas Jahns published new ideas for using three-phase induction machines as fault-tolerant machines [3]. A three-phase induction motor with a neutral connection and divided dc bus can be used for fault-tolerant applications, where

it will continue to work under loss of one phase. But, the maintenance cost of the bearing of the motor will increase due to the zero sequence component of the current [4].

A systematic literature review was presented by A.M. El-Refaie [5] about different topologies of fault-tolerant PM machines and drives. Together, these reviews outline that a fault-tolerant PM machine requires a relatively acceptable performance under faulty conditions compared with the performance in fault-free conditions. Furthermore and ultimately, it will fail safely without leading to destruction of the various components of the motor drive system.

In 1996, Mecrow et al. published a paper in which they reported the requirements for a fault-tolerant PM machine drive [6]. Those requirements include electrical, magnetic, thermal and physical separation of all phases including the power converter. What's more, the authors have pointed out some of the ways in which it is feasible to realise those requirements. They have suggested locating each phase in separate slots such that there is no overlap between the end-turn windings of various phases. This design aspect can be realised by using single-layer (SL) FSCW beside each phase is independently supplied by a single-phase H-bridge power converter. Based on those requirements, a significant and growing body of literature has studied the design optimisation of fault-tolerant machines [7–24].

The study of the feasible slot-pole combination for fault-tolerant PM machines was first carried out by A. J. Mitcham et al. [9]. The authors have developed a new approach for selecting pole and slot numbers with insignificant magnetic coupling between phases regardless of magnet depth and other details of the design.

In [25], remarkable design thoughts of fault-tolerant FSCW PM motors were presented. A method to design FSCW PM motors was demonstrated for both double-layer (DL) and single-layer (SL) winding layouts. The analytical computation is extended to determine the harmonics of the magnetomotive force (MMF) distribution. The findings show that the SL windings configurations present the poorest performance compared to DL configurations by reason of the high harmonic content of the MMF that may cause an unbalanced saturation and a torque ripple.

For dealing with distinctive types of faults for example, the loss of two phases, multi-phase motors are potential fault-tolerant machines. A five-phase PM motor

has been chosen for its inherently high fault-tolerant capability [4], [26]. It can continue to operate safely under closed-loop control after losing up to two phases [2]. It can be designed to overcome the fault occurrence [4, 27]. Among its principal advantages are high controllability, reliability and smooth torque production in the presence of a fault. [26]. Reference [11] presents an analysis for both the open circuit of one and two phases and the short circuit at the machine terminals of one phase and the postfault current control strategies. The authors concluded that appropriate current control strategies enable the drive to operate in the presence of the fault while producing a smooth torque. Several papers addressed the various design aspects of five-phase fault tolerant PM machines, power converter topologies as well as post-fault current control strategies for different types of faults [10–12, 27–34]

For a fault-tolerant PM motor drive to be capable of sustaining winding short-circuit faults, the phase windings have to be designed with high enough phase inductance to limit the short-circuit currents to a given value [6]. Examples of PM motor designs with high phase inductance can be found in [35–38].

2.2 FSCWs for Fault-Tolerant Machines

This section presents an extensive investigation of the fractional-slot concentrated winding and the reasons behind the use of this kind of windings for fault−tolerant electrical machines. The advantages and difficulties involved in using concentrated windings are discussed. The star of slots method, which is used to calculate their winding layout, is briefly presented. Further, the MMF harmonic contents, as well as the fundamental winding factor, are explained. Finally, an analysis that shows how to choose the slot-pole combination is presented.

The configuration of stator windings in an AC machine has a substantial influence on its performance characteristics. The AC windings can be classified into two types, distributed windings and concentrated windings. A distributed winding generally produces a more sinusoidal MMF distribution, which makes it very popular in servo PM motor drive applications. However, because of the manufacturing limitation, the slot fill factor is generally low, around 35%-45% [7]. This low slot fill factor has a significant effect on limiting the maximum torque and power density. Furthermore,

the long end-winding connection may cause substantial copper losses. However, since the inductance of the distributed winding is generally low, it is not suitable for wide speed range applications.

The concentrated windings can be classified into integral slot winding and fractional slot winding based on whether the value of q, the number of slots per pole and phase, is an integer or a decimal [39]. The configurations of the FSCWs could be single−layer (SL) or double−layer (DL) or more. In this research, the focus will be on the main two types of FSCWs, namely DL and SL windings. The layout of single−layer FSCW is such that each slot is equipped by a coil side of only one phase. The layout of DL FSCW is such that two coil sides of the same phase or two different phases equip each slot [7]. An example of two FSCWs arrangements for 4 pole/ 6 slot three-phase SPM machine is shown in Figure 2.1.

Several important design rules for fault-tolerant PM machines were presented by Mecrow et al. [6]. The requirements for fault tolerant electrical machines can be summarised as follows:

- d-axis inductance is equal to 1pu [6]. This allows operating the machine with shorted windings without excessive heating.
- Each phase is physically separated from the others [6], [28]. Such a physical separation is necessary to prevent a phase-to-phase fault. It can be achieved by locating each phase in separate slots such that there is no overlap of the end-turn windings. This design aspect can be realised with SL FSCWs and DL FSCWs.
- The mutual inductances between the phases are as low as possible to prevent the flux produced by the healthy phases to be linked with the faulty phase, and produce short-circuit currents, and therefore high joule losses [6], [28].
- The number of rotor poles must be close to the number of stator slots [6], [9].
- An electrical separation among the phases. Supplying each phase by a separate full-bridge converter could be a practical application of this requirement [3,28].

2.2.1 Advantages of FSCW

Based on the fault-tolerance requirements of PM machines, FSCWs are more popular in machine design for fault-tolerant applications. The SL FSCW configuration

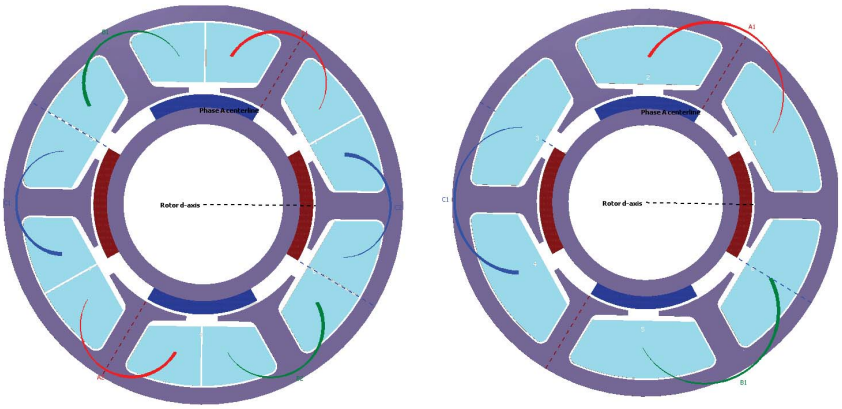

(a) (b)

Figure 2.1: Winding layouts for FSCWs 6 slot/ 4 pole three-phase SPM machine. (a) double-layer windings. (b) single-layer windings.

constitutes such an excellent fault-tolerant design. In general, FSCWs have reduced copper volume end winding, which leads to a substantial reduction in the copper losses. This type of winding is more straightforward to fabricate compared to the distributed lap winding so that the production cost would be less [7]. For this type of concentrated winding, the slot fill factor can be increased to 70% if coupled with segmented stator structures [7], which can increase power density and torque density. Furthermore, the overlap between coils in the end winding region is eliminated, which can reduce the chance for short circuit faults between different phases.

In addition to physical separation FSCWs can be used in designing multi-phase electrical machines for fault tolerant applications [40]. FSCW SPM motors have high values of stator leakage inductance, which permits the increase in the flux-weakening operational range [41]. Thus, PM machines with FSCWs were investigated in this thesis.

Despite the large number of advantages of this type of windings, there are some difficulties that make electric machine designers tend to use other type of winding. The most important difficulties are listed in the next subsection.

2.2.2 Difficulties Linked to FSCW

The most obvious difficulties linked with the use of FSCW can be identified as follows:

- Performance, design steps, and detailed analytical solutions of PM synchronous

machine equipped with FSCWs are not well established in the literature [7].

- Significant rotor losses and parasitic effects such as noise, vibration, unbalanced magnetic forces, and torque ripple due to the various harmonic contents of MMF that are not in synchronism with the rotor [42].

For some applications, SL FSCWs are more favourable while for some applications DL FSCWs are fitting. The next subsection presents the critical aspects of both windings.

2.2.3 Comparison Between SL and DL Windings

This section covers the key points of comparison between the two main types of FSCWs, namely SL and DL windings. The study of two prototype PM synchronous machine equipped with SL and DL FSCW in [43, 44], showed that SL windings exhibit higher self-inductance and lower mutual inductance compared to DL windings, making it suitable for fault tolerant applications and constant power operation range. Furthermore, it was demonstrated that both winding layouts associate with similar cogging torque when they have the same slot-pole configuration.

In [45] it was shown that when a stator with unequal tooth width, and equipped with an SL winding provides a higher torque capability and a lower torque ripple as compared to a standard equal tooth stator fitted with the same winding.

The investigation of El-Refaie and Jahns in [46] shows that machines with DL stator windings have lower spatial subharmonic components in MMF distributions, resulting in lower torque ripple and magnet eddy-current losses. A comparison of the design aspects between SL and DL windings configurations as provided by El-Refaie et al. in [7] shows that DL windings compared with SL windings exhibit significant phase to phase coupling through mutual slot leakage inductance, shorter end windings, lower phase inductance due to lower phase leakage inductance, lower rotor losses mainly due to lower MMF space harmonic content, support many slot/pole combinations, more difficult to manufacture, a lower synchronous winding factor, and a more sinusoidal back-emf.

2.3 Star of Slots Theory

Star of slots is a graphical method used many years ago for designing large synchronous generators [40]. It can be considered as an excellent tool for designing FSCWs [2]. Using the star of slot theory for designing FSCWs is a recent area of research which is developed by Nicola Bianchi [2, 28]. The primary use of this method is to determine the winding arrangement of the FSCWs. Furthermore, the star of slots method can be used for analysing the harmonic content of the back-emf and air-gap MMF distribution.

The use of star of slots for designing FSCWs is entirely covered in [40]. Due to the importance as well as the use of this method in determining the winding layout of the prototype motor, the author decided to summarise the critical steps in this method. In this method the winding layout of double-layer FSCW, as a general case, is designed for an m-phase machine such that each phase is displaced in space by $2\pi/m$ mechanical radians from other phases so that the EMFs in the phases are equal and have the maximum main harmonic waveform.

The star of slots is shaped by phasors. The number of phasors is equal to the number of slots, and each phasor is numbered according to the number of the corresponding slot. For example, phasor number 1 corresponds to slot number 1 etc. A given winding layout for m-phase machine is feasible when the following condition is satisfied:

$$\frac{Q}{mt} \qquad \text{is integer} \tag{2.1}$$

where Q is the slot number, and t is the machine periodicity. The machine periodicity is given by the greatest common divisor (GCD) between Q and pole pairs (p):

$$t = GCD\left\{Q, p\right\} \tag{2.2}$$

The star of slots is formed by Q/t spokes, and each spoke contains t phasors. The electrical angle between the phasors of two adjacent slots is $\alpha_s^e = p\alpha_s^m$ where, α_s^m is the slot angle in mechanical radians, i.e. $\alpha_s^m = 2\pi/Q$. The angle between two spokes results in:

$$\alpha_{ph} = \frac{2\pi}{(Q/t)} = \frac{\alpha_s^e}{p}t \tag{2.3}$$

The phasors that belong to the first phase are determined by drawing two opposite sectors, each of them covering π/m radians. Hence, the phasors that are within the two sectors belong to the first phase. The coil sides within one sector are connected with positive polarity, while the coil sides within the other sector are connected with negative polarity. For the other phases, it is enough to rotate the two sectors by an angle $2k\pi/m$ radians, where $k = 1, 2, \cdots\cdots, (m-1)$ and to repeat the selection.

Producing a winding layout by using the star of slots method requires developing a software program capable of producing the star of slots plot for a given Q, p and m. Luigi Alberti developed a program which is capable of generating the winding layout of integral- and fractional- slot windings a three-phase machine called KOIL, based on the star of slots plots method [47]. For generating the winding layout of FSCW five-phase machine, a program was developed using MATLAB software, which is capable of generating the star of slots plot for any m-phase machine. The star of slots of 10 slots/8 poles FSCW five-phase machine is shown in Figure 2.2, while the corresponding winding layout is shown in Figure 2.3.

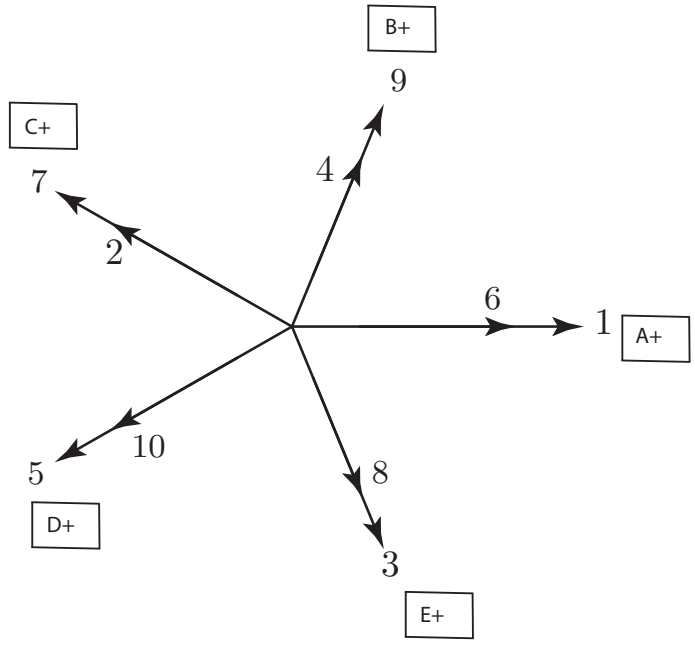

Figure 2.2: Star of slots of 10 slot/ 8 pole fractional slot winding.

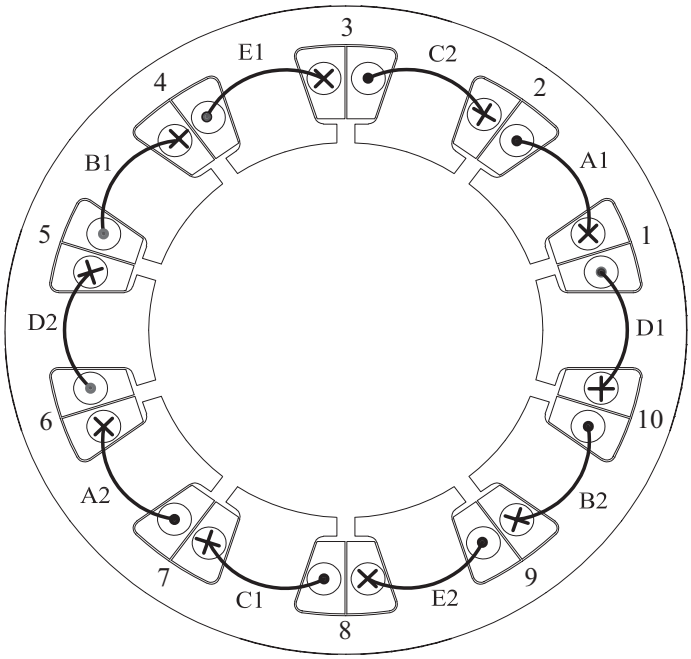

Figure 2.3: Geometrical design and winding layout of DL 10 slot/ 8 pole five-phase PM synchronous machine.

2.3.1 Winding Factor

To realise the torque density improvement by harmonic current injection, the winding factor of useful harmonics of multi-phase windings should be high enough. Accordingly, it is required to obtain the proper slot/pole combinations with relatively high synchronous and harmonic winding factors for the FSCWs multi-phase motor design. There are several methods for the winding factor calculation [2, 48–51]. The star of slots theory is adopted in this thesis. The winding factors are calculated for FSCWs. The harmonic winding factor is defined as [2, 40]:

$$k_{wv} = k_{dv} k_{pv} \tag{2.4}$$

k_{wv} is the v^{th} harmonic winding factor, k_{dv} is the v^{th} harmonic distribution factor, and k_{pv} is the v^{th} harmonic pitch factor. The harmonic pitch factors can be calculated as [2]:

$$k_{pv} = \sin\left(\frac{\sigma_{wv}}{2}\right) \tag{2.5}$$

where σ_{wv} is the coil span angle given by $\sigma_{wv} = (2\pi v y_q)/Q$, y_q is the slot pitch measured in the number of slots, approximated by $y_q = round\{Q/(2p)\}$. The

harmonic distribution factors can be calculated as:

$$k_{dv} = \frac{\sin\left(\frac{q_{ph}}{2}\frac{\alpha_{phv}}{2}\right)}{\frac{q_{ph}}{2}\sin\left(\frac{\alpha_{ph}}{2}\right)} \qquad \text{If } Q/mt \text{ even}$$
$$k_{dv} = \frac{\sin\left(\frac{q_{ph}}{2}\frac{\alpha_{phv}}{2}\right)}{q_{ph}\sin\left(\frac{\alpha_{ph}}{4}\right)} \qquad \text{If } Q/mt \text{ odd} \tag{2.6}$$

where $q_{ph} = Q/mt$ is the number of spokes per phase, α_{phv} is the angle between two v^{th} spokes. The main harmonic winding factor is calculated by using the same harmonic factor equations with $v = p$.

2.3.2 Choosing the Slot-Pole Combination

1. Winding factor: The winding factor of the synchronous frequency (MMF harmonic which is equal to the machine pole-pairs) should be as high as possible. This leads to a higher effective number of turns, and hence, a lower current for the same torque [42]. For five-phase machines, the third harmonic ($v = 3p$) may be utilised to provide extra constant torque. Accordingly, the winding factor of the third harmonic has also been presented. Table 2.1 represents the winding factor(s) of many combinations for FSCWs five-phase machines. Three groups have been identified by colours, depending on the value of the winding factor [52]. In Table 2.1, it appears that there are only two slot-pole combinations which supports SL FSCW, 20 slot/14 pole and 20 slot/18 pole. Both of those slot-pole combinations are suitable for low-speed as well as high torque applications. In other words, choosing FSCW five-phase PM machines for fault-tolerant as well as wide speed applications can be realised by adopting DL windings configurations. However, if the fully physical separation is not a critical requirement, the DL solution is favoured due to its advantages in rotor losses and mechanical balancing [28, 53–55]. Based on the calculated values of the winding factors, the combinations ($2p = Q \pm 2$) and ($2p = Q \pm 1$) are the candidates.

2. Cogging torque: Cogging is the ripple torque which occurs in the absence of currents in PM synchronous machines when the rotor tries to align with the stator to maximise the permanence of the magnetic circuit regarding the PMs. One method of decreasing this source of torque ripple is by selecting an appropriate combination of the number of poles and slots, which can increase the cogging torque frequency

Table 2.1: Synchronous winding factors for five-phase FSCWs [52].

Poles / Slots	2	4	6	8	12	14	16	18
5	0.588 0.951	0.951 0.588	0.951 0.588	0.588 0.951	0.588 0.951	0.951 0.588	0.951 0.588	0.588 0.951
10		0.588 0.951	0.809 0.309	0.951 0.588	0.951 0.588	0.809 0.309	0.588 0.951	
15	***harm1*** ***harm3***		0.588 0.951	0.7 0.318	0.951 0.588	0.980 0.830	0.980 0.830	0.951 0.588
20				0.588 0.951	0.809 0.309	0.891 0.156	0.951 0.588	0.988 0.891
Five-Phase Combinations								
High winding factor (first harmonic)		**Not bad winding factor (first harmonic)**		**High winding factor (third harmonic)**		**Single layer winding**		

$1/N_{cog}$ and, as a result, its amplitude is decreased. N_{cog} represents the number of cogging torque periods during a rotation of a slot pitch, and its value is given by equation (2.7). N_{cog} should be as high as possible [42, 47].

$$N_{cog} = \frac{2p}{GCD\{Q, 2p\}} = \frac{LCM\{Q, 2p\}}{Q} \tag{2.7}$$

The lowest common multiple (LCM) of the number of stator slots (Q) and the number of rotor poles ($2p$) is used as an indicator for choosing a suitable ($Q - 2p$) combinations. Table 2.2 presents the practical list of the $LCMs$ which support the five-phase configurations equipped with fractional-slot concentrated windings.

Table 2.2: Cogging torque indicator for five-phase FSCWs.

	$LCM\{Q, 2p\}$ indicator for five-phase FSCW											
$Q/2p$	2	4	6	8	10	12	14	16	18	20	22	24
5	10	20	30	40	-	60	70	80	90	-	110	120
10	-	20	30	40	-	60	70	80	90	-	110	120
15	30	60	30	120	-	60	210	240	90	-	330	120
20	-	-	60	40	-	60	140	80	180	-	220	120
25	50	100	150	200	50	300	350	400	450	100	550	600
30	-	60	-	120	-	60	210	240	90	-	330	120
35	70	140	210	280	-	420	70	560	630	-	770	840
40	-	-	120	-	-	120	280	80	360	-	440	120
45	90	180	90	360	-	180	630	720	90	-	990	360
50	-	100	150	200	-	300	350	400	450	100	550	600
55	110	220	330	440	-	660	770	880	990	-	110	1320
60	-	-	-	120	-	-	420	240	180	-	660	120

3. Net radial force on the machine: The net radial force between the stator and rotor is resulting from the attraction between the stator iron core and the rotor magnet beside the interaction between the armature and magnet fields [42]. The main radial force in FSCW PM synchronous machines is mainly produced by the interaction between the harmonic contents in the magnet field and the spatial harmonic contents in armature MMF [55]. The following is utilised as an indicator for choosing the slot-pole combination for an application [42, 55].

- Choosing $GCD\{Q, 2p\}$ to be an even number and high causes the net radial force on the machine to be very low.
- In DL FSCW machines with $2p = Q \pm 2$, the lowest order of radial force is 2.
- In SL FSCW machines with $2p = Q \pm 2$, the lowest order of radial force is 2 when Q/t is even, and is 1 when Q/t is odd.
- In FSCW machines with $2p = Q \pm 1$, the lowest order of radial force is 1. The amplitude of the first radial force harmonic is higher in machines with $2p = Q \pm 1$. Table 2.3 presents the $GCD(Q, 2p)$ for five-phase slot/pole combinations that support FSCW.

Table 2.3: Net radial force indicator for five-phase FSCWs.

Q/2p	Net radial Force Indicator (k=GCD{Q,2p}) for 5-phase FSCW											
	2	4	6	8	10	12	14	16	18	20	22	24
5	1	1	1	1	-	1	1	1	1	-	1	1
10	-	2	2	2	-	2	2	2	2	-	2	2
15	1	1	3	1	-	3	1	1	3	-	1	3
20	-	-	2	4	-	4	2	4	2	-	2	4
25	1	1	1	1	5	1	1	1	1	5	1	1
30	-	2	-	2	-	6	2	2	6	-	2	6
35	1	1	1	1	-	1	7	1	1	-	1	1
40	-	-	2	-	-	4	2	8	2	-	2	8
45	1	1	3	1	-	3	1	1	9	-	1	3
50	-	2	2	2	-	2	2	2	2	10	2	2
55	1	1	1	1	-	1	1	1	1	-	11	1
60	-	-	-	4	-	-	2	4	6	-	2	12

4. Fault tolerant applications: The subject of choosing a slot-pole configuration for a particular fault-tolerant aspect is well addressed in [2]. The research results which were presented in [2] are utilised for choosing a slot-pole combination:

- Machines with even Q/t ratio exhibit zero mutual inductance with DL wind-

ings as in 20/18 and 20/22 slot/pole combinations.

- High efficiency machines require low rotor loss. Slot/pole combination with low MMF harmonics are preferred.
- Limiting short circuit current requires high magnetizing inductance. Solutions with $2p = Q - 2$ are preferred.
- Because of geometrical constraints only the combinations with even slot number can be transformed to a single-layer layout.

The choice of slot/pole combination is effected by an additional constrains such as the switching frequency of the voltage source inverter (VSI) and the requred efficiency for machine. In order to avoid excessive iron losses caused by the working frequency or speed, and to smooth currents, torque and speed, the fundemental electrical frequency of the machine has to be less than the carrier switching frequency of the voltage source inverter (VSI) by at least twenty times [56].

For example if the rated speed of 20-slot, 18-pole machine is 1200 rpm and the maximum speed is 6000 rpm, then the rated frequency of the machine is 180 Hz ($f_e = p(n/60)$), and the maximum frequency is 900 Hz so that the switching frequency has to be equal or higher than 18 kHz . Nevertheless, 20 slot, 18-pole configuration is suitable for low speed applications up to rated speed since the efficiency of the machine will be so low due to the iron loss caused by working frequency ($\propto f_e$). Based on all the aspects related to fraction slot winding, DL FSCW 10 slot/ 8 pole configuration is selected for design a variable speed five-phase SPM machine.

Chapter 3

Designing an Extended Flux Weakening Capability of a Five-Phase SPM Machine

The presented work in this chapter describes two methods, analytical and 2-D finite element that can be used to calculate the design parameters of the five-phase machine. The primary objective is to achieve the optimal flux-weakening condition in a five-phase SPM machine necessary for attaining a constant-power operation over a wide speed range, and to increase the tolerance to fault by choosing a suitable slot/pole combination and winding type. The star of slots theory is used to determine the winding layout of concentrated, fractional-slot stator windings (FSCWs), while the winding function theory (WFT) is used to calculate the magnetising inductance of the armature winding. A 2-D finite element numerical method has been applied to estimate the parameters of a 1 kW SPM motor from which a prototype has been built.

3.1 Introduction

A fault-tolerant PM machine with flux weakening capability as a part of high performance motor drive system has been one of the attractive research areas due to the importance of producing a reliable drive system needed for a variety of applications. For some safety-critical applications, e.g. electrical actuators in aircraft,

electric/hybrid vehicles, aerospace applications and ship propulsion, tolerance to faults is necessary.

For many applications, in addition to fault tolerance, some machines require an excellent flux-weakening capability for the sake of attaining a wide speed range of constant-power operation above the base speed. The condition for achieving optimum flux weakening above the base speed for three-phase PM synchronous motors was first derived by Schiferl and Lipo [57] and, can be expressed as:

$$I_{ch} = \frac{\lambda_{m-rms}}{L_d} = I_R \quad \text{A rms} \tag{3.1}$$

where I_{ch} is the characteristic current of the machine, λ_{m-rms} is the flux of the magnets (rms value) alone linked by the stator windings, L_d is the d-axis inductance and I_R is the rated armature current.

El-Refaie and Jahns [58] have proposed an analytical method for achieving optimal flux-weakening conditions in a three-phase SPM machine. However, reaching the optimal flux-weakening condition in five-phase SPM machines can be considered more complicated since the design steps, and detailed analytical solutions of five-phase SPM machines equipped with concentrated, fractional-slot stator windings is not well established in the literature.

One of the more significant findings in chapters 6, which will be presented in detail, is that the theoretically calculated, normalised fundamental magnet flux linkage λ_{m1n} under the voltage and current constraints of the VSI determines whether the MF five-phase SPM motor is a finite speed drive or infinite speed drive. The second major finding was that the highest normalised electromagnetic torque in the flux-weakening region for both an infinite speed drive and a finite speed drive is when the motor is controlled as an SF five-phase SPM motor. Taken together, it will be enough to use the same flux-weakening condition of the three-phase PM synchronous motor or the fundamental harmonic plane of the five-phase SPM motor for achieving optimum flux-weakening capability.

The purpose of this chapter is to derive analytically all the parameters of a five-phase SPM machine equipped with FSCWs needed for calculating the characteristic current of the prototype machine. Numerical calculation of the characteristic current is another option which is also investigated in this chapter.

3.2 MMF and Inductances of FSCWs

3.2.1 MMF

The spatial distribution of the armature reaction MMF of PM synchronous machines equipped with FSCWs contains sub-harmonic (harmonic components with order lower than the main harmonic order) components that have sometimes higher amplitude than the synchronous harmonic component. Star of slots method is used to determine the harmonic contents of the MMF. The machine periodicity, t which is given by the greatest common divisor GCD between Q-slot and p-pole pairs, $t = GCD\{Q, p\}$, is used to determine the harmonic content of the winding MMF. The harmonics are only of odd order when Q/t is even, while they are of both even and odd order when Q/t is odd [28].

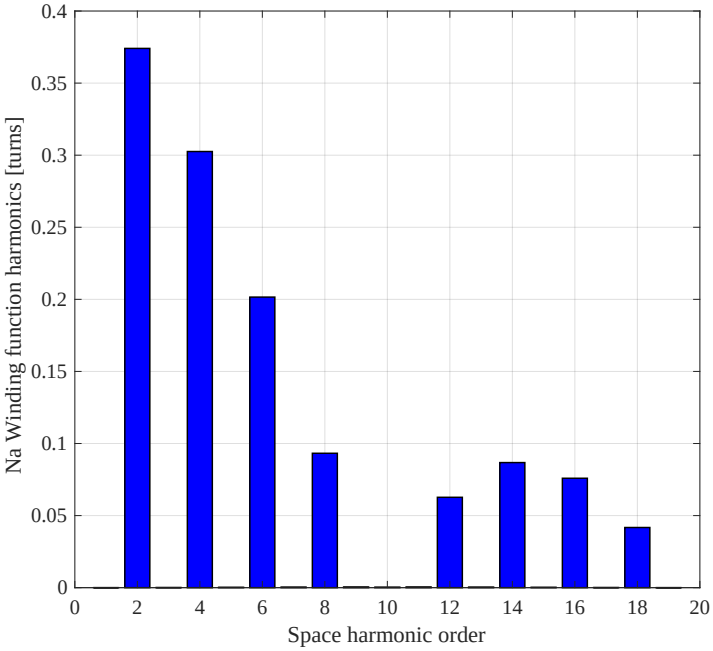

Figure 3.1: Phase winding function harmonic content of 10 slot/ 8 pole DL FSCW SPM machine. N_a : Winding function of phase a.

The prototype five-phase SPM machine has 10 slots and 4 pole pairs which result in $t = 2$ and $Q/t = 5$ is odd. Figure 3.1 shows the harmonic contents of the machine. It can be seen that, with odd Q/t, even harmonics are significant while the odd harmonics have very small amplitudes (can not be seen in the figure). The order of the main harmonic is equal to the number of pole pairs, which is four, for the prototype machine. It is called the main harmonic because it rotates

synchronously with the rotor. In Figure 3.1 the existence of a sub-harmonic which has the frequency order of 2 in the air-gap can be noted. It is worth mentioning that when t is equal to pole pair p the MMF of a fractional-slot winding is free of sub-harmonics. Examining the synchronously rotating resultant MMF wave of the machine shows that the harmonics of a multiple order of five disappear. The spectral content of the resultant rotating MMF of the prototype machine is shown in Figure 3.2 when only the first time and space harmonics are considered (third harmonic is not injected). By comparing the amplitudes of the MMF space-harmonics in Figure 3.1 and Figure 3.2, it is easy to conclude that the rotating MMF space-harmonic amplitude is 5/2 times higher than the magnitude of the phase winding MMF space harmonics. Also, the second sub-harmonic disappears in the rotating MMF.

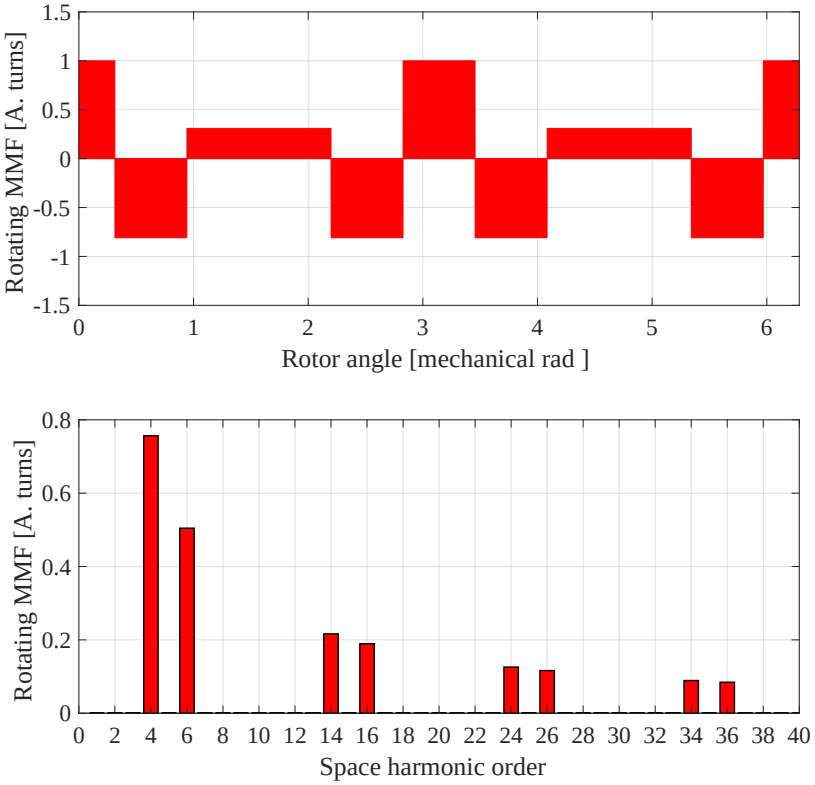

Figure 3.2: Resultant rotating MMF wave of 10-slot 8-pole DL FSCW SPM machine.

3.3 Inductances

To satisfy the optimum flux weakening condition in the fundamental harmonic plane of the machine it is required an acceptable estimation of the machine characteristic current. Since the characteristic current is dependent on the machine parameters, it

is necessary to calculate the machine parameters of the two virtual planes accurately. Besides, accurately estimated machine parameters are necessary to implement different control methods such as the field orientation control method (FOC) and direct torque control method (DTC).

The winding function theory is an important tool for calculating and analysing the magnetising inductance of a non-sinusoidal winding distribution. This method has at least two main advantages. First, it considers exact MMF waveform i.e. all the MMF space harmonics. Second, this technique is computer adapted and on such a manner it is good choice for analysing and comparing different winding layouts for a variety of machine designs. In this method the self inductance of phase n associated with flux crossing the air-gap (magnetising inductance) L_{nn} and mutual inductance L_{nm} between phases n and m are defined for a 2-pole machine ($\theta_e = \theta$) as [59]:

$$L_{nn} = \frac{\mu_{\circ} D_{si}\, l_{eff}}{2g} \int_0^{2\pi} N_n^2(\theta)\, d\theta \quad \text{H} \tag{3.2}$$

$$L_{nm} = \frac{\mu_{\circ} D_{si}\, l_{eff}}{2g} \int_0^{2\pi} N_n(\theta)\, N_m(\theta)\, d\theta \quad \text{H} \tag{3.3}$$

where

- L_{nn} for $n = a, b, c, d$ and e is the stator phase magnetising inductance [H];
- L_{nm} for $n, m = a, b, c, d$ and e is the stator mutual inductance between the phases n and m [H];
- θ rotor angle [mechanical rad];
- l_{eff} effective axial length of the machine [m];
- D_{si} stator inner diameter [m];
- $\mu_{\circ}$ permeability of air [H/m];
- g air-gap thickness [m];

N_n and N_m represent the winding functions of phases n and m respectfully: literally, winding function is MMF per unit current. In further text terms winding function and MMF per unit current will be used interchangeably. The winding function of phase m is defined as:

$$N_m(\theta) = n_m(\theta) - < n_m(\theta) > \tag{3.4}$$

where $n_m(\theta)$ is the turns function of phase m, and its average value $< n_m(\theta) >$ is determined as:

$$< n_m(\theta) >= \frac{1}{2\pi}\int_0^{2\pi} n_m(\theta)\, d\theta \tag{3.5}$$

The winding function method is used to calculate the magnetising and mutual inductances of a prototype vertical DL FSCW 10 slot/ 8 pole, five-phase SPM machine. Figure 3.4 shows the geometrical design and winding layout of the prototype motor, while Table 3.1 shows the summary of the key dimensions. Figure 3.5 shows the turns functions of all phases besides N_a, N_{ab} and the harmonic content of N_a. Plots of the turns function, average and winding function of phase a are illustrated in Figure 3.3. Upon integrating the waveforms in Figure 3.3, the average of the turns function and the self inductance of phase a are obtained in (3.6) and (3.7) by assuming a 2-pole machine.

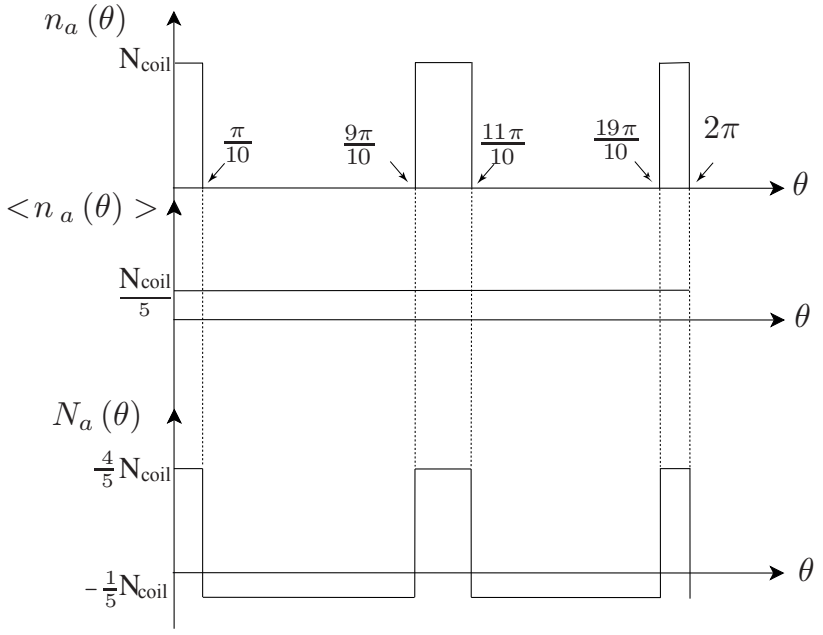

Figure 3.3: Plots of the turns function, average and winding function of phase a.

$$\begin{aligned} < n_a(\theta) > &= \frac{1}{2\pi}\int_0^{2\pi} n_a(\theta)\, d\theta \\ &= \frac{2}{2\pi}\left[\int_0^{\pi/10} N_{coil} \quad d\theta + \int_{9\pi/10}^{\pi} N_{coil} \quad d\theta\right] \\ &= \frac{1}{5}N_{coil} \end{aligned} \tag{3.6}$$

where N_{coil} is the number of turns per coil.

$$\begin{aligned} L_{aa} &= \frac{\mu_\circ \, D_{si} \, l_{eff}}{2g} \int_0^{2\pi} N_a^2(\theta)\, d\theta \\ &= \frac{\mu_\circ \, D_{si} \, l_{eff}}{2g} .2 \left[\begin{array}{l} \int_0^{\pi/10} \left(\frac{4}{5} N_{coil}\right)^2 \, d\theta + \int_{\pi/10}^{9\pi/10} \left(\frac{1}{5} N_{coil}\right)^2 \, d\theta \\ \\ + \int_{9\pi/10}^{\pi} \left(\frac{4}{5} N_{coil}\right)^2 \, d\theta \end{array} \right] \\ &= \frac{\mu_\circ \, D_{si} \, l_{eff}}{2g} \left(\frac{8\pi}{25} N_{coil}^2\right) \quad \text{H} \end{aligned} \tag{3.7}$$

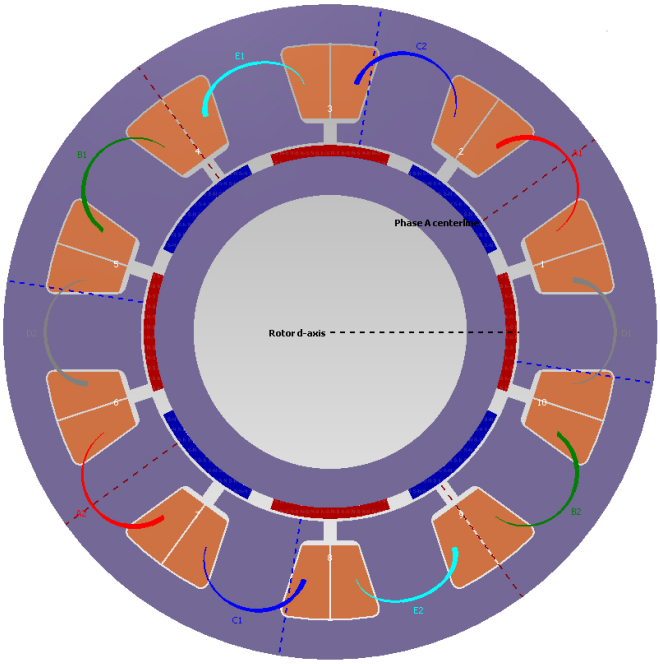

Figure 3.4: Geometrical design and winding layout of the prototype DL FSCW 10 slot/ 8 pole five-phase SPM machine.

Table 3.1: The dimensions summary of the prototype five-phase SPM machine.

Parameter	Value	Parameter	Value
Number of slots	10	Rotor core thickness	7.17 [mm]
Number of poles	8	Rotor inner diameter	50.06 [mm]
Number of phases	5	Rotor outer diameter	64.4 [mm]
Tooth width	13.86 [mm]	Magnet angle	37.46 [deg]
Back iron height	7.17 [mm]	Magnet thickness	2 [mm]
Stator inner diameter	69.4 [mm]	Air-gap thickness	0.5 [mm]
Stator outer diameter	120 [mm]	Tooth width	13.86 [mm]
Slot height	18.13 [mm]	Slot top width	19.334 [mm]
Slot area	212.38 [mm^2]	Slot bottom width	10.142 [mm]
Slot opening width	3.2 [mm]	Slot opening height	3.46 [mm]

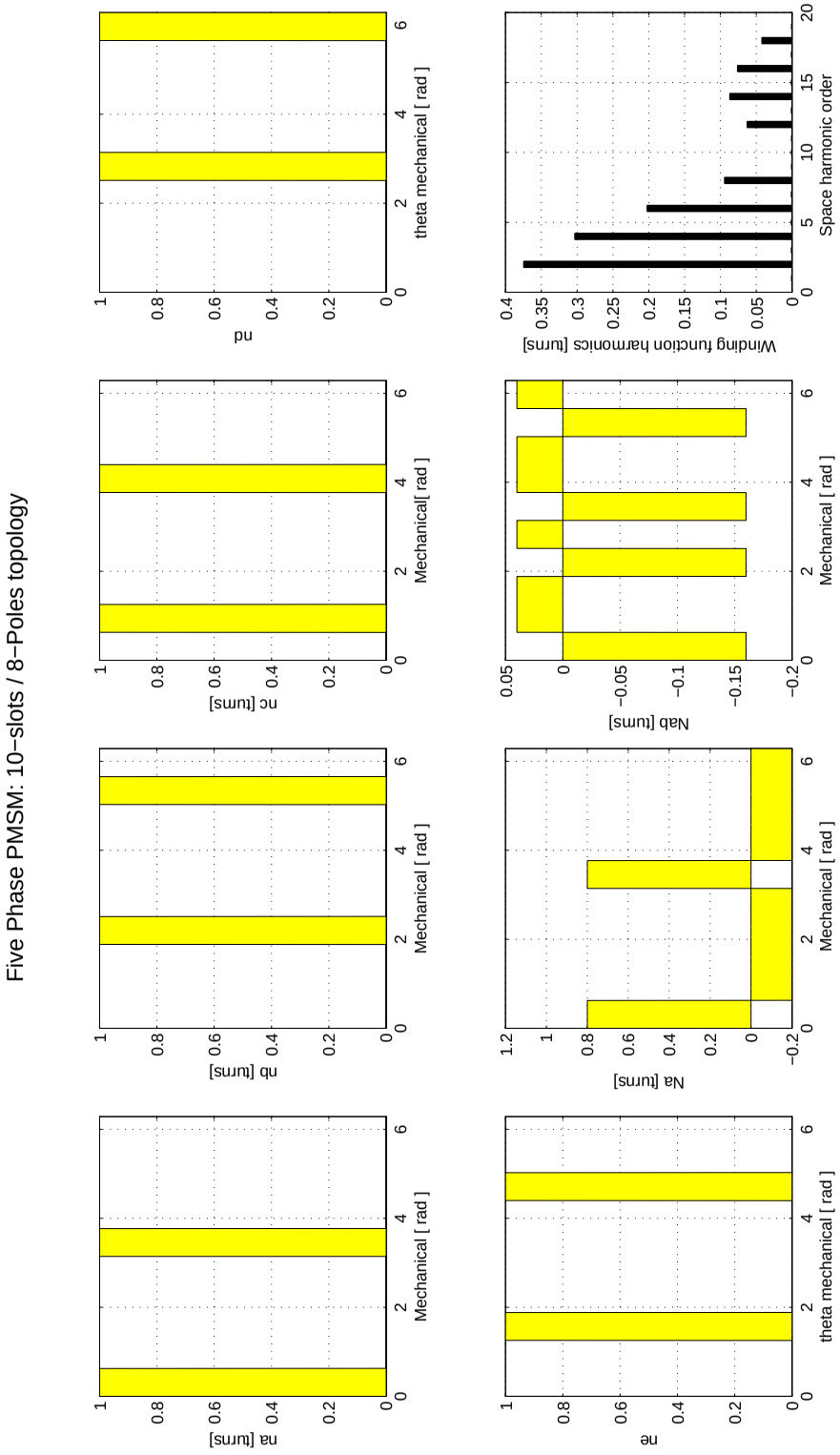

Figure 3.5: Plots of the turns function, average value and the resulting winding function of all five phases and phase a-b combined.

The mutual inductance between phases a and b can be evaluated depending on the winding functions of both windings. The winding functions of phases a, b and their product are shown in Figure 3.6.

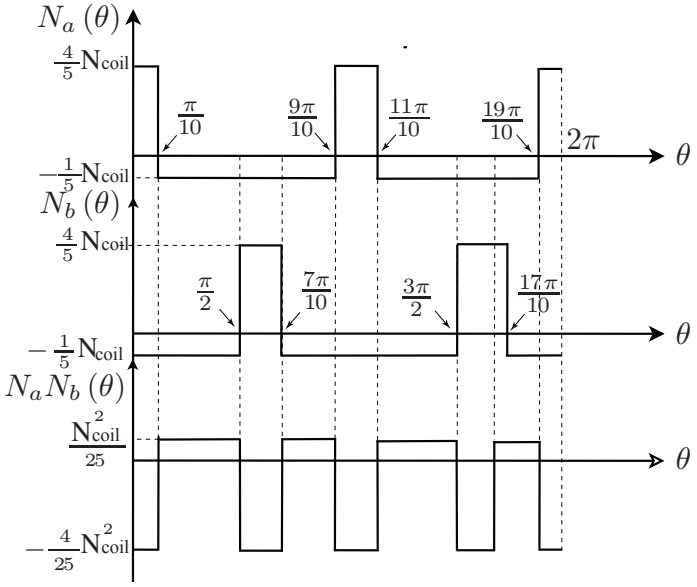

Figure 3.6: Plots of the winding function of phases a, b and the resulting product.

Hence the resulting mutual inductance between phases a and b can be evaluated as:

$$\begin{aligned} L_{ab} &= \frac{\mu_\circ\, D_{si}\, l_{eff}}{2g} \int_0^{2\pi} N_a(\theta)\, N_b(\theta) \quad d\theta \\ &= \frac{\mu_\circ\, D_{si}\, l_{eff}}{2g}.2 \begin{bmatrix} -\int_0^{\pi/10} \frac{4}{25} N^2_{coil} \quad d\theta + \int_{\pi/10}^{\pi/2} \frac{1}{25} N^2_{coil} \quad d\theta \\ -\int_{\pi/2}^{7\pi/10} \frac{4}{25} N^2_{coil} \quad d\theta + \int_{7\pi/10}^{9\pi/10} \frac{1}{25} N^2_{coil} \quad d\theta \\ -\int_{9\pi/10}^{\pi} \frac{4}{25} N^2_{coil} \quad d\theta \end{bmatrix} \\ &= \frac{\mu_\circ\, D_{si}\, l_{eff}}{2g} \left(-\frac{2\pi}{25} N^2_{coil} \right) \\ &= -\frac{1}{4} L_{aa} \quad \text{H} \end{aligned} \tag{3.8}$$

For a P pole machine the result is

$$\begin{aligned} L_{aa} &= \frac{\mu_\circ\, D_{si}\, l_{eff}}{2g} \left(\frac{2}{P} \right) \int_0^{2\pi} N_a^2(\theta_e)\, d\theta_e \\ &= \frac{\mu_\circ\, D_{si}\, l_{eff}}{2g} \left(\frac{2}{P} \right) \left(\frac{8\pi}{25} N^2_{coil} \right) \quad \text{H} \end{aligned} \tag{3.9}$$

$$\begin{aligned} L_{ab} &= \frac{\mu_\circ \, D_{si} \, l_{eff}}{2g} \left(\frac{2}{P}\right) \int_0^{2\pi} N_a\left(\theta_e\right) N_b\left(\theta_e\right) \quad d\theta_e \\ &= \frac{\mu_\circ \, D_{si} \, l_{eff}}{2g} \left(\frac{2}{P}\right) \left(-\frac{2\pi}{25} N_{coil}^2\right) \\ &= -\frac{1}{4} L_{aa} \quad \text{H} \end{aligned} \tag{3.10}$$

To help further analysis it is useful to express the winding function $N(\theta)$ in terms of its Fourier components. Since the winding function is completely defined over the entire stator periphery from 0 to 2π [mechanical rad], it is possible to consider the winding function to be a periodic function of period 2π, i.e., $N(\theta) = N(\theta + 2\pi)$, and it is represented by the Fourier series of the form:

$$N\left(\theta\right) = a_\circ + \sum_{n=1}^{\infty} \left[a_n \cos\left(n\theta\right) + b_n \sin\left(n\theta\right)\right] \tag{3.11}$$

where,

$$a_\circ = \frac{1}{2\pi} \int_{-\pi}^{\pi} N\left(\theta\right) d\theta \tag{3.12}$$

$$a_n = \frac{1}{\pi} \int_{-\pi}^{\pi} N\left(\theta\right) \cos\left(n\theta\right) d\theta \tag{3.13}$$

$$b_n = \frac{1}{\pi} \int_{-\pi}^{\pi} N\left(\theta\right) \sin\left(n\theta\right) d\theta \tag{3.14}$$

To simplify the math, the winding is referred to the magnetic axis of phase a as shown in Figures 3.3 and 3.6. If the winding function shows even symmetry (i.e. f $(\text{-}\theta)$ = f $(\theta\ ))$, b_n is zero for all n. The winding function for even symmetry is given by:

$$N\left(\theta\right) = a_\circ + \sum_{n=1}^{\infty} a_n \cos\left(n\theta\right) \tag{3.15}$$

where,

$$a_\circ = \frac{1}{\pi} \int_{0}^{\pi} N\left(\theta\right) d\theta \tag{3.16}$$

$$a_n = \frac{2}{\pi} \int_{0}^{\pi} N\left(\theta\right) \cos\left(n\theta\right) d\theta \tag{3.17}$$

For most fractional slot windings the coil sides are located such that a positive turn is

situated diametrically opposite the corresponding negative turn [59]. In such cases:

$$\int_0^{2\pi} N(\theta)\, d\theta = 0 \tag{3.18}$$

In other words, $a_\circ = 0$. The winding function of phase a of the proposed machine

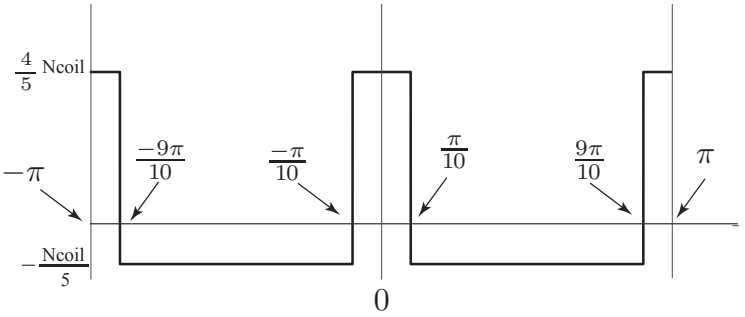

Figure 3.7: Winding function of phase a .

$N_a(\theta)$ is replotted as shown in Figure 3.7. This function can then be described by the Fourier series. It can be noted that since the winding function of Figure 3.7 has the desired even symmetry about $\theta = 0$, that is, $N_a(\theta) = N_a(-\theta)$, the winding series for this function will contain only cosine terms. The Fourier series for this function is:

$$\begin{aligned} N_a(\theta) &= a_2 \cos(2\theta) + a_4 \cos(4\theta) + a_6 \cos(6\theta) + \cdots \\ &= \frac{2N_{coil}}{\pi}\left[K_2\frac{1}{2}\cos(2\theta) + K_4\frac{1}{4}\cos(4\theta) + K_6\frac{1}{6}\cos(6\theta) + \cdots\right] \end{aligned} \tag{3.19}$$

where

$$a_n = \frac{2N_{coil}}{\pi}\sum_{n=2,\ n\ even}^{\infty} K_n\frac{1}{n}\cos(n\theta) \tag{3.20}$$

$$K_n = \sin\left(\frac{n\pi}{10}\right) - \sin\left(\frac{9n\pi}{10}\right) \tag{3.21}$$

The winding function for phase b is

$$N_b(\theta) = \frac{2N_{coil}}{\pi}\left[K_2\frac{1}{2}\cos\left(2\theta - \frac{2\pi}{5}\right) + K_4\frac{1}{4}\cos\left(4\theta - \frac{2\pi}{5}\right) + \cdots\right] \tag{3.22}$$

Due to the winding symmetry, the winding function for all phases can be expressed in matrix form as:

$$\begin{bmatrix} N_a(\theta) \\ N_b(\theta) \\ N_c(\theta) \\ N_d(\theta) \\ N_e(\theta) \end{bmatrix} = \begin{bmatrix} \frac{2N_{coil}}{\pi} \sum_{n=2,\ n\ even}^{\infty} K_n \frac{1}{n} \cos(n\theta) \\ \frac{2N_{coil}}{\pi} \sum_{n=2,\ n\ even}^{\infty} K_n \frac{1}{n} \cos(n\theta - \gamma) \\ \frac{2N_{coil}}{\pi} \sum_{n=2,\ n\ even}^{\infty} K_n \frac{1}{n} \cos(n\theta - 2\gamma) \\ \frac{2N_{coil}}{\pi} \sum_{n=2,\ n\ even}^{\infty} K_n \frac{1}{n} \cos(n\theta - 3\gamma) \\ \frac{2N_{coil}}{\pi} \sum_{n=2,\ n\ even}^{\infty} K_n \frac{1}{n} \cos(n\theta - 4\gamma) \end{bmatrix} \tag{3.23}$$

where $\gamma = 2\pi/5$.

Self inductance of phase a is evaluated as:

$$\begin{aligned} L_{aa} &= \frac{\mu_\circ\, D_{si}\, l_{eff}}{2g} \int_0^{2\pi} N_a^2(\theta)\, d\theta \\ &= \frac{\mu_\circ\, D_{si}\, l_{eff}}{2g} \left(\frac{4N_{coil}^2}{\pi^2}\right) \sum_{n=2,\ n\ even}^{\infty} K_n^2 \frac{1}{n^2} \cos^2(n\theta) \\ &= \frac{\mu_\circ\, D_{si}\, l_{eff}}{2g} \left(\frac{4N_{coil}^2}{\pi}\right) \left[\sum_{n=2,\ n\ even}^{\infty} \left(\frac{K_n}{n}\right)^2\right] \end{aligned} \tag{3.24}$$

The mutual inductance may be expressed as:

$$\begin{aligned} L_{ab} &= \frac{\mu_\circ\, D_{si}\, l_{eff}}{2g} \int_0^{2\pi} N_a(\theta)\, N_b(\theta)\, d\theta \\ &= \frac{\mu_\circ\, D_{si}\, l_{eff}}{2g} \left(\frac{4N_{coil}^2}{\pi^2}\right) \sum_{n=2,\ n\ even}^{\infty} K_n^2 \frac{1}{n^2} \cos(n\theta) \cos(n\theta - \gamma) \\ &= \frac{\mu_\circ\, D_{si}\, l_{eff}}{2g} \left(\frac{4N_{coil}^2}{\pi}\right) \left[\sum_{n=2,\ n\ even}^{\infty} \left(\frac{K_n}{n}\right)^2 \cos(n\gamma)\right] \end{aligned} \tag{3.25}$$

For a P pole machine the result is

$$\begin{aligned} L_{aa} &= \frac{\mu_\circ\, D_{si}\, l_{eff}}{2g} \left(\frac{2}{P}\right) \int_0^{2\pi} N_a^2(\theta_e)\, d\theta_e \\ &= \frac{\mu_\circ\, D_{si}\, l_{eff}}{2g} \left(\frac{4N_{coil}^2}{\pi^2}\right) \left(\frac{2}{P}\right) \sum_{n=2,\ n\ even}^{\infty} K_n^2 \frac{1}{n^2} \cos^2(n\theta_e) \\ &= \frac{\mu_\circ\, D_{si}\, l_{eff}}{2g} \left(\frac{4N_{coil}^2}{\pi}\right) \left(\frac{2}{P}\right) \left[\sum_{n=2,\ n\ even}^{\infty} \left(\frac{K_n}{n}\right)^2\right] \end{aligned} \tag{3.26}$$

$$\begin{aligned} L_{ab} &= \frac{\mu_\circ\, D_{si}\, l_{eff}}{2g} \left(\frac{2}{P}\right) \int_0^{2\pi} N_a(\theta_e)\, N_b(\theta_e)\, d\theta_e \\ &= \frac{\mu_\circ\, D_{si}\, l_{eff}}{2g} \left(\frac{4N_{coil}^2}{\pi^2}\right) \left(\frac{2}{P}\right) \sum_{n=2,\ n\ even}^{\infty} K_n^2 \frac{1}{n^2} \cos(n\theta_e) \cos(n\theta_e - \gamma_e) \\ &= \frac{\mu_\circ\, D_{si}\, l_{eff}}{2g} \left(\frac{4N_{coil}^2}{\pi}\right) \left(\frac{2}{P}\right) \left[\sum_{n=2,\ n\ even}^{\infty} \left(\frac{K_n}{n}\right)^2 \cos(n\gamma_e)\right] \end{aligned} \tag{3.27}$$

where $\theta_e = \frac{P}{2}\theta$ is the displacement of the rotor referred to the magnetic axis of phase a in electrical degrees and $\gamma_e = \frac{P}{2}\gamma$. If few terms of the Fourier expansion of the winding function N_a are added up, the graphical representation would be like the original winding function. Figure 3.8 shows the graphical depiction of the phase a winding function. Due to the winding symmetry the harmonic contents of all phase winding functions are the same.

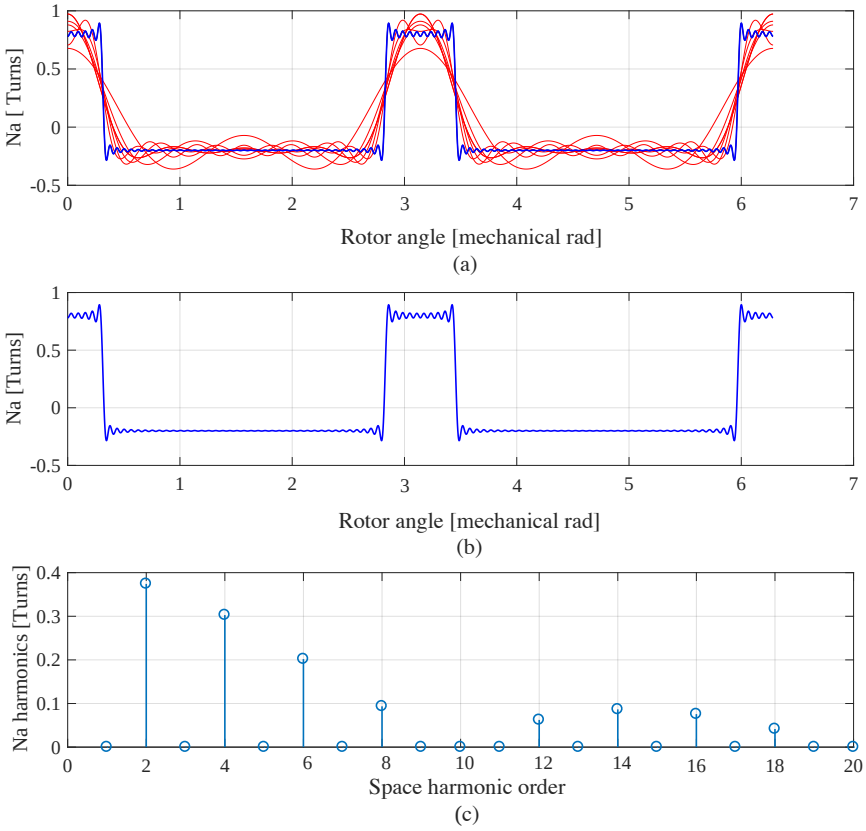

Figure 3.8: Graphical depiction of the phase a winding function for few terms of the Fourier expansion. (a): Adding up 20 terms (red waveforms). (b): Adding up 100 terms. (c): Harmonics content.

3.3.1 Calculation of the Slot Leakage Inductance

The inductance calculation based on the winding function method incorporates both the magnetising inductance and the harmonic leakage inductance, while slot leakage inductance, tooth-tip leakage inductance and end winding leakage inductance are not dealt with and need to be calculated. Although the tooth-tip and end leakage inductances are quite small for an FSCW, the slot leakage component is an essential part of the machine inductance. Classical equations that assume a leakage flux path

parallel to placing the conductors in the slot is usually used in single-layer windings and horizontal double-layer windings [60]. With the purpose of gaining further accurate results, a 2-D Poisson problem associated with the slot region for calculating the slot leakage inductance is the superior choice for the intended vertical double-layer windings [61]. The calculations are based on the assumption of a rectangular slot geometry, which is described by the parameters shown in Figure 3.9. A general expression of the slot leakage inductance for double-layer windings can be stated as [60]:

$$L_{ls} = \frac{2\,\mu_\circ\, l_{eff}\, N_{sr}^2}{p}\,(\lambda_{aa} + \lambda_{ab} - 2\lambda_{ab}) \quad \text{H} \tag{3.28}$$

while the following expressions are used to calculate λ_{aa} and λ_{ab} [61]:

$$\begin{bmatrix}\lambda_{aa}\\ \lambda_{bb}\end{bmatrix} = \begin{bmatrix}\beta_{aa} & \gamma_{aa} & \epsilon_{aa}\\ \beta_{ab} & \gamma_{ab} & \epsilon_{ab}\end{bmatrix} \begin{bmatrix}\frac{h}{3b}\\ \frac{b}{12h}\\ S\end{bmatrix} \tag{3.29}$$

$$S = \frac{h_{s\circ}}{b_{s\circ}} + \frac{8b^2}{b_{s\circ}^2} \sum_{n=2,4,6\ldots}^{\infty} \frac{\sin^2\left(\frac{b_{s\circ}\pi n}{2b}\right)}{(\pi n)^3 \tanh\left(\frac{h\pi n}{b}\right)} \tag{3.30}$$

$$\begin{bmatrix}\beta_{aa} & \gamma_{aa} & \epsilon_{aa}\\ \beta_{ab} & \gamma_{ab} & \epsilon_{ab}\end{bmatrix} = \begin{bmatrix}\frac{1}{q}\left(1 - \frac{mz}{2}\right) & \frac{1}{q} - \beta_{aa} & \beta_{aa}\\ \frac{mz}{4q} & -\beta_{ab} & \beta_{ab}\end{bmatrix} \tag{3.31}$$

$$b = \frac{b_{ss1} + b_{ss2}}{2} \tag{3.32}$$

$$z = \left|\frac{2p}{Q} - 1\right| \tag{3.33}$$

where

- b_{ss1} slot bottom width [m];
- b_{ss2} slot top width [m];
- Q number of slots;
- q number of slots per pole and phase;
- m number of phases;
- N_{sr} number of turns per phase connected in series;

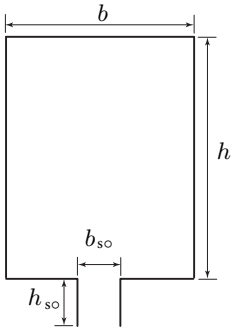

Figure 3.9: Simplified slot geometry.

3.3.2 Inductances in the Rotating Reference Frame

The matrix of the stator armature reaction inductances ($\boldsymbol{L}_s$) of a five-phase PM synchronous machine is given by:

$$\boldsymbol{L}_s = \begin{bmatrix} L_{ls}+L_{aa} & L_{ab} & \cdots & L_{ae} \\ L_{ba} & L_{ls}+L_{bb} & \cdots & L_{be} \\ & & \cdots & \vdots \\ \vdots & \vdots & \cdots & \\ L_{ea} & L_{eb} & \cdots & L_{ls}+L_{ee} \end{bmatrix} \tag{3.34}$$

where:

L_{ls} is the stator leakage inductance [H];

L_{nn} for $n = a, b, c, d$ and e is the stator phase magnetising inductance [H];

L_{nm} for $n, m = a, b, c, d$ and e is the stator mutual inductance between the phases n and m [H];

The magnetising and mutual inductances of the stator phases are calculated by utilising the winding function method:

L_{nn} for $n = a, b, c, d$ and $e = L_m$

L_{nm} for $n, m = a, b, c, d$ and $e = -\frac{1}{4}L_m$

Substituting the calculated values of the magnetising and mutual inductances in (3.34) yields:

$$\mathbf{L}_s = \begin{bmatrix} L_{as} \\ L_{bs} \\ L_{cs} \\ L_{ds} \\ L_{es} \end{bmatrix} = \begin{bmatrix} L_{ls}+L_m & -\frac{L_m}{4} & \cdots & -\frac{L_m}{4} \\ -\frac{L_m}{4} & L_{ls}+L_m & \cdots & -\frac{L_m}{4} \\ & & \cdots & \vdots \\ \vdots & \vdots & \cdots & \\ -\frac{L_m}{4} & -\frac{L_m}{4} & \cdots & L_{ls}+L_m \end{bmatrix} \tag{3.35}$$

The stator inductance matrix in the rotating reference frame (3.36) is obtained by using the Park transformation $\boldsymbol{P}$ [1] (5.25) and its inverse to (3.35).

$$\boldsymbol{P}\boldsymbol{L}_s\boldsymbol{P}^{-1} = \begin{bmatrix} L_{ls}+\frac{5}{4}L_m & & & & \\ & \ddots & & & \\ & & \ddots & & \\ & & & L_{ls}+\frac{5}{4}L_m & \\ & & & & L_{ls} \end{bmatrix} \tag{3.36}$$

Hence, by inspecting the inductance matrix in (3.36), the values of the two plane inductances can be expressed as:

$$\begin{bmatrix} L_{d_1} \\ L_{q_1} \\ L_{d_2} \\ L_{q_2} \\ L_{zs} \end{bmatrix} = \begin{bmatrix} L_{ls}+\frac{5}{4}L_m \\ L_{ls}+\frac{5}{4}L_m \\ L_{ls}+\frac{5}{4}L_m \\ L_{ls}+\frac{5}{4}L_m \\ L_{ls} \end{bmatrix} \quad \text{H} \tag{3.37}$$

This analytical result shows that the inductance of both planes is the same. For surface mounted PM synchronous machines its usual for the d-axis and q-axis components of the same plane to be equal. However, this is not the case for different planes, where their values are affected by the type of the armature winding. Despite the restriction of the determined result of the magnetising inductance to cover only the presented 10-slot, 8-pole combination, the approach can be easily programmed in MATLAB to compute the magnetising inductance for any slot/pole combination by adopting the numerical integration. The author has developed two programs: the first was used to draw the star of slots for any slot/pole combination, and the second accepts the resulting coil distributions of the winding to calculate the magnetising inductance.

3.4 Magnet Flux Linkage Calculation

A magnetic equivalent-circuit method is used to calculate the magnet flux linkage under open-circuit condition where saturation is ignored [62]. The method is fast, robust, and is a good starting point. The main weakness of the equivalent magnetic circuit is the approximation of the spatial distribution of the air-gap flux by as-

[1] Park transformation is covered in detail in chapter five.

suming a sinusoid air-gap spatial distribution. The expression for the fundamental component of the phase magnet flux linkage λ_{m1-rms} can be written as [62–64]:

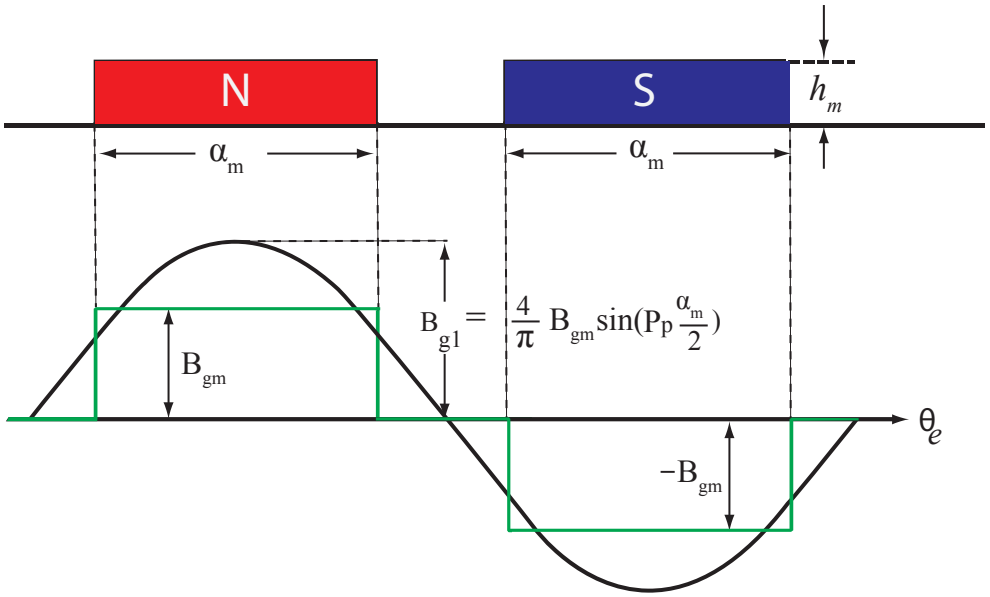

Figure 3.10: Relationship between the air-gap flux density and its fundamental.

$$\begin{aligned} \lambda_{m1-rms} &= \frac{B_{g1}\, D_{si}\, l_{eff}\, N_{sr}\, k_{w1}}{\sqrt{2}\, p} \quad \text{rms Wb} \\ &= \left(\frac{D_{si}\, l_{eff}\ n_c\, k_{w1}}{\sqrt{2}\, p} \right) B_{g1}\ N_c \end{aligned} \tag{3.38}$$

while the magnet flux linkage in the rotating reference frame is equal to

$$\lambda_{m1} = \sqrt{2}\lambda_{m1-rms} \tag{3.39}$$

where k_{w1} is the synchronous component winding factor; B_{g1} is the peak fundamental air-gap magnet flux density and n_c is the number of coils per phase. Although (3.38) does not involve the influence of harmonics, it represents a good approximation to flux linkage and back-emf waveforms that are quite sinusoidal as will be shown in the next chapter. The magnet has an arc of α_m [mechanical radians]. The air-gap flux density will have a constant magnitude of B_{gm} over α_m in the positive half cycle and -B_{gm} over α_m in the negative half cycle as shown in Figure 3.10 for a surface mount magnet rotor. B_{g1} can be calculated as [62].

$$B_{g1} = \frac{4}{\pi} B_{gm} \sin\left(p \frac{\alpha_m}{2}\right) \tag{3.40}$$

By studying the flux path in the machine as shown in Figure 3.11, and assuming a typical flux leakage in the rotor, a reasonable operating point on the demagnetisation characteristics of the magnet may be determined. Figure 3.11 shows that the flux crosses from the north pole of the rotor magnet to the stator through the air-gap and then closes the flux path from the stator to the rotor south pole, via the air-gap. The straight line portion of the magnet demagnetization curve is described by:

$$B_m = \mu_\circ \mu_{rm} H_m + B_r \tag{3.41}$$

whereas in the air-gap

$$B_{gm} = \mu_\circ H_{gm} \tag{3.42}$$

From Ampere's law, assuming that the air-gap is replaced by an equivalent gap,

$$H_m h_m + H_{gm}\, g_e = 0 \tag{3.43}$$

where

H_m is magnetic field intensity in the magnet;

H_{gm} is magnetic field intensity in the air-gap;

The magnet operating flux density is required, and derived by substituting for H_m from (3.43) into (3.41), and then substituting for H_{gm} in terms of B_{gm} from (3.42):

$$B_m = B_r - \mu_{rm} \frac{g_e}{h_m} B_{gm} \tag{3.44}$$

The leakage factor is defined in general as the ratio of air-gap flux ϕ_{gm} to magnet flux ϕ_m:

$$f_{LKG} = \frac{\phi_{gm}}{\phi_m} = \frac{\phi_{gm}}{\phi_{gm} + \phi_L} < 1 \tag{3.45}$$

where ϕ_L is the magnet leakage flux in the rotor

or

$$B_{gm} = \frac{\phi_{gm}}{A_P} = \frac{F_{LKG}\phi_m}{A_P} = \frac{F_{LKG}}{A_P} B_m A_m = F_{LKG} \frac{A_m}{A_P} B_m \tag{3.46}$$

where A_P is the area of one pole measured along the rotor surface and A_m is the

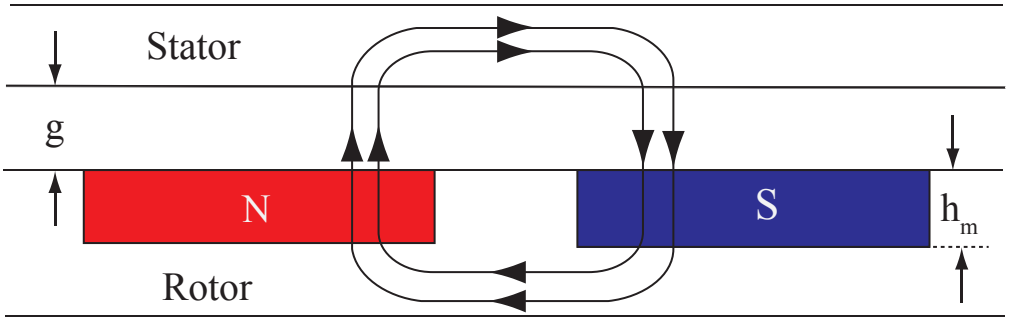

Figure 3.11: Simple layout of a 2-pole PM motor with surface magnets.

magnet area. Eliminating B_m using (3.44), equation (3.46) can now be written as:

$$B_{gm} = \frac{F_{LKG}}{\left(\frac{A_P}{A_m} + F_{LKG}\frac{g_e}{h_m}\mu_{rm}\right)} B_r \tag{3.47}$$

where

B_r is the remanent flux density [T];

h_m is the radial thickness of the magnets [m];

μ_{rm} is the relative permeability of the magnets;

g_e is the effective air-gap length [m];

g_e is calculated as:

$$g_e = k_c g \tag{3.48}$$

where k_c is the Carter's coefficient for correcting the air-gap for stator slotting effect, and is calculated as:

$$k_c = \frac{\tau_s}{\tau_s - \frac{2b_\circ}{\pi}\left\{\tan^{-1}\left(\frac{b_\circ}{2g}\right) - \frac{g}{b_\circ}\ln\left[1 + \left(\frac{b_\circ}{2g}\right)^2\right]\right\}} \tag{3.49}$$

$$\tau_s = \frac{\pi D_{si}}{Q} \tag{3.50}$$

where

τ_s is the slot pitch [m];

D_{si} is the stator inner diameter [m];

$b_\circ$ is the slot opening width [m];

3.5 Resistance Calculation

The phase winding resistance is given by:

$$r_s = \rho \frac{N_{sr}\, l_{av}}{n_p\, A_c} \quad \Omega \tag{3.51}$$

where ρ is the copper resistivity, l_{av} is the average length of a coil turn of a slot winding, A_c is the conductor area, and n_p is the number of parallel paths. r_s is a function of temperature T, primarily because the resistivity of copper is a function of temperature [63].

$$\rho = \rho_{20}\left[1 + \alpha\left(T - 20\right)\right] = 1.72410^{-8}\left[1 + 0.00393\left(T - 20\right)\right] \quad \Omega.\ \mathrm{m} \tag{3.52}$$

where T is in °C. The length of wire is generally impossible to calculate accurately from the geometric dimensions of the motor, mainly because the end-windings do not follow a geometric shape that is mathematically known. For this reason the length l_{av} is often obtained empirically. The average length l_{av} is given approximately as [39]:

$$l_{av} \approx 2l_{st} + 2.4\tau_c + 0.1 \quad \mathrm{m} \tag{3.53}$$

where l_{st} is the length of the stator stack of the machine and τ_c is the average coil span, both expressed in meters. Since the phase windings resistance in (3.51) is proportional to N_{sr}, and by using $N_{sr} = n_c\, N_{coil}$, it is possible to find an expression for r_s which is directly proportional to N_{coil} as follows:

$$\begin{aligned} r_s &= \rho \frac{N_{sr}\, l_{av}}{n_p\, A_c} \quad \Omega \\ &= \left(\rho \frac{n_c\, \left(2l_{st} + 2.4\tau_c + 0.1\right)}{n_p}\right) \frac{N_{coil}}{A_c} \\ &= K_{rs} N_{coil} \end{aligned} \tag{3.54}$$

For $n_p = 1$ and $n_c = 2$, K_{rs} may be expressed as:

$$K_{rs} = \frac{2\rho}{A_c}\left(2l_{st} + 2.4\tau_c + 0.1\right) \tag{3.55}$$

3.6 Calculation of the Number of Turns N_{coil} and the Magnet Remanence B_r

The goal of this section is to calculate the number of turns per coil N_{coil} which satisfies the optimal flux-weakening condition necessary to implement the design of the five-phase SPM machine. The calculated parameters in the last sections, L_{d1} and λ_{m1} can be expressed in effective form as in (3.56) and (3.57), respectively.

$$\begin{aligned} L_{d1} &= L_{ls} + \frac{5}{4}L_m \quad \text{H} \\ &= \frac{2\mu_\circ\, l_{eff}\, N_{sr}^2}{p}\left(\lambda_{aa} + \lambda_{ab} - 2\lambda_{ab}\right) + \frac{5}{4}\frac{\mu_\circ D_{si}\, l_{eff}}{2g}\frac{1}{p}\left(\frac{8\pi}{25}N_{coil}^2\right) \\ &= \left(\frac{2\mu_\circ l_{eff}\ \left(\lambda_{aa} + \lambda_{ab} - 2\lambda_{ab}\right) n_c^2}{p} + \frac{\pi}{5}\frac{\mu_\circ D_{si}\, l_{eff}}{g}\frac{1}{p}\right) N_{coil}^2 \\ &= K_{ld}\, N_{coil}^2 \end{aligned} \tag{3.56}$$

$$\begin{aligned} \lambda_{m1-rms} &= \left(\frac{D_{si}\, l_{eff}\ n_c\, k_{w1}}{\sqrt{2}\, p}\right) B_{g1}\ N_{coil} \\ &= \left\{\left(\frac{D_{si}\, l_{eff}\, n_c\, k_{w1}}{\sqrt{2}p}\right)\left(\frac{F_{LKG}}{\left(\frac{A_P}{A_m} + F_{LKG}\frac{g_e}{h_m}\mu_{rm}\right)}\right)\left(\frac{4}{\pi}\sin\left(p\frac{\alpha_m}{2}\right)\right)\right\} B_r\, N_{coil} \\ &= K_{md} B_r\, N_{coil} \end{aligned} \tag{3.57}$$

where

$$K_{ld} = \left(\frac{2\mu_\circ l_{eff}\ \left(\lambda_{aa} + \lambda_{ab} - 2\lambda_{ab}\right) n_c^2}{p} + \frac{\pi}{5}\frac{\mu_\circ D_{si}\ l_{eff}}{g}\frac{1}{p}\right) \tag{3.58}$$

$$K_{md} = \left\{\left(\frac{D_{si}\, l_{eff}\, n_c\, k_{w1}}{\sqrt{2}p}\right)\left(\frac{F_{LKG}}{\left(\frac{A_P}{A_m} + F_{LKG}\frac{g_e}{h_m}\mu_{rm}\right)}\right)\left(\frac{4}{\pi}\sin\left(p\frac{\alpha_m}{2}\right)\right)\right\} \tag{3.59}$$

leads to the following expression for the characteristic current:

$$I_{ch} = \frac{\lambda_{m1-rms}}{L_{d1}} = \frac{K_{md}\ B_r}{K_{ld}\ N_{coil}} \quad \text{A rms} \tag{3.60}$$

The steady state model for the machine under the assumption of zero reference voltage of the second plane and MTPA control is expressed as:

$$v_{ds1}^{r} = -\omega_e \, L_{s1} \, i_{qs1}^{r} \tag{3.61}$$

$$v_{qs1}^{r} = r_s \, i_{qs1}^{r} + \omega_e \, \lambda_{m1-rms} \tag{3.62}$$

By assuming the rated-fundamental component of the current is equal to the characteristic current and the fundamental phase voltage V_R is equal to the maximum available voltage of V_1, it is possible to solve (3.63) and (3.64) for N_{coil} and B_r:

$$I_R = I_{ch} = \frac{K_{md} \, B_r}{K_{ld} \, N_{coil}} \quad \text{A rms} \tag{3.63}$$

$$\begin{aligned} V_R &= \sqrt{v_{ds1}^{r} + v_{qs1}^{r}} \\ &= \sqrt{\left(r_s I_R + \omega_r \lambda_{m1-rms}\right)^2 + \left(\omega_r L_{s1} I_R\right)^2} \\ &= \sqrt{\left(K_{rs} N_{coil} I_R + \omega_r K_{md} B_r \, N_{coil}\right)^2 + \left(\omega_r K_{ld} \, N_{coil}^2 I_R\right)^2} \quad \text{V rms} \end{aligned} \tag{3.64}$$

where ω_c is the rated angular speed (corner speed) of the machine.

3.7 Finite Element Approach For Optimal Flux Weakening

There is no standard method in the literature for calculating the inductances of the machine, which are necessary for achieving the optimum flux weakening of a five-phase SPM machine by employing a finite element software. The limited capability of the most available design software for the design of a three-phase machine with limited types of commonly used machines make the design of five-phase machines a very complicated task.

3.7.1 Inductance Calculations

MagNet 2D electromagnetic field simulation software is used to calculate the machine inductances in the rotating reference frame. The method is based on the definition of the machine flux linkage equation. In general for five phase PM synchronous

machine the flux linkage equation is defined as [2]:

$$\mathbf{\Lambda}^{s}_{abcde} = \mathbf{L}_s \mathbf{I}^{s}_{abcde} + \mathbf{\Lambda}_m$$

$\mathbf{L}_s$ is the machine winding inductance matrix, $\mathbf{I}^{s}_{abcde}$ is phase current matrix and $\mathbf{\Lambda}_m$ is the magnet flux linkage matrix. The magnet flux linkage is turned off by setting the magnet remanence B_r to zero. The armature flux linkages $\boldsymbol{\lambda}^{r}_{d1q1\,d2q2}$ in the rotating reference frame are determined from the flux linkages of phases a, b, c, d and e as:

$$\boldsymbol{P}\boldsymbol{\Lambda}^{s}_{abcde} = \boldsymbol{P}\boldsymbol{L}_s\boldsymbol{P}^{-1}\boldsymbol{P}\boldsymbol{I}^{s}_{abcde}$$
$$\boldsymbol{\lambda}^{r}_{d1q1\,d2q2} = \boldsymbol{P}\boldsymbol{L}_s\boldsymbol{P}^{-1}\mathbf{i}^{r}_{d1q1\,d2q2}$$

where

$$\boldsymbol{P}\boldsymbol{L}_s\boldsymbol{P}^{-1} = \begin{bmatrix} L_{d1} & & & & \\ & L_{q1} & & & \\ & & L_{d2} & & \\ & & & L_{q2} & \\ & & & & L_{ls} \end{bmatrix}$$

For instance, the phase flux linkage in the MagNet 2D software is calculated for a given current as a sum of the flux linkages of all phase coils. The flux linkage of each coil is equal to the line integral of the magnetic vector potential Az along the contour of the coil. By assuming the calculated flux linkage per phase $\bar{\lambda_a}, \bar{\lambda_b}, \bar{\lambda_c}, \bar{\lambda_d}$ and $\bar{\lambda_e}$ are calculated when $N_{coil} = 1$, the stator flux linkages $\bar{\lambda_{ds1}}, \bar{\lambda_{qs1}}, \bar{\lambda_{ds2}}$ and $\bar{\lambda_{qs2}}$ in the rotor reference frame are obtained by applying the the Park's transformation:

$$\begin{bmatrix} \bar{\lambda_{ds1}} \\ \bar{\lambda_{qs1}} \\ \bar{\lambda_{ds2}} \\ \bar{\lambda_{qs2}} \end{bmatrix} = \boldsymbol{P} \begin{bmatrix} \bar{\lambda_a} \\ \bar{\lambda_b} \\ \bar{\lambda_c} \\ \bar{\lambda_d} \\ \bar{\lambda_e} \end{bmatrix} \tag{3.65}$$

The inductances of the machine L_{d1}, L_{q1}, L_{d2} and L_{q2} can be directly obtained according to only four rotor positions. Four simulations in 2D-MagNet and MATLAB are used to calculate the four inductances. Since the resultant current vector must be aligned with the required rotor axis, the five-phases of the machine should be

[2]Modelling of five-phase PM synchronous machine with a non-sinusoidal shape is covered in detail in chapter five.

supplied with suitable dc currents so that the current space vector has a value only in the required rotor axis. The components of the current space vectors in the rotating reference frame can be expressed as:

$$\begin{bmatrix} i_{ds1} \\ i_{qs1} \\ i_{ds2} \\ i_{qs2} \end{bmatrix} = \boldsymbol{P} \begin{bmatrix} i_a \\ i_b \\ i_c \\ i_d \\ i_e \end{bmatrix} \tag{3.66}$$

The first simulation is used to calculate $\bar{L_{d1}}$. By using MATLAB, we can solve the system of equations (3.66) for i_a, i_b, i_c, i_d and i_e such that $i_{qs1}, i_{ds2}, i_{qs2}$ are equal to zero and i_{ds1} is equal to one. The currents in the stator reference frame are used as an input for calculating the flux linkage of the phases ($\bar{\lambda_a}, \bar{\lambda_b}, \bar{\lambda_c}, \bar{\lambda_d}$ and $\bar{\lambda_e}$). Using (3.65) shows that the flux linkage in the d_1-axis only ($\bar{\lambda_{q1}} = \bar{\lambda_{d2}} = \bar{\lambda_{q2}} = 0$). In general, for different values of i_{ds1}, $\bar{L_{d1}}$ is calculated as:

$$\bar{L_{d1}} = \frac{\bar{\lambda_{d1}}}{i_{ds1}} \tag{3.67}$$

It is worth mentioning that the rotor angle (north pole of one of the rotor magnets)

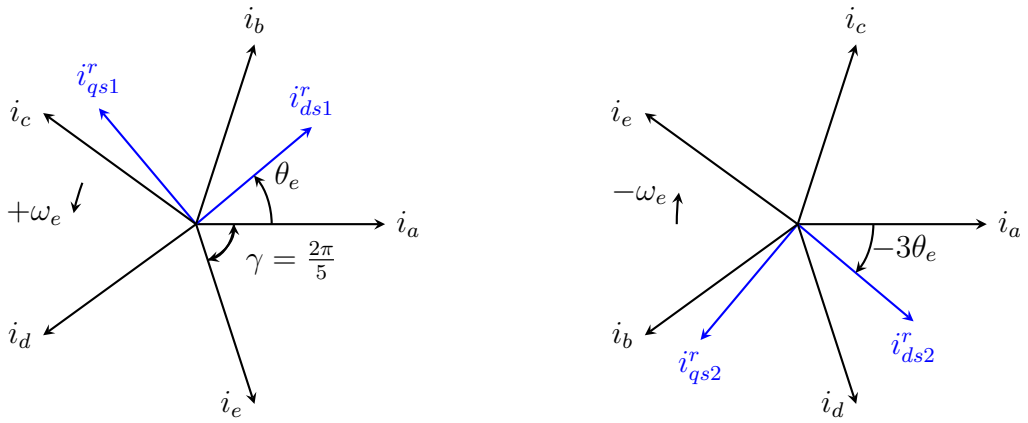

Figure 3.12: References for the rotor reference frame. (a) Fundamental harmonic component with a positive sequence (+). (b) Third harmonic component with a negative sequence (-).

has to be aligned with the magnetic axis of a-phase for getting the θ_e-angle equal to zero as shown in Figure 3.12a. By following the same procedure, the other

inductances are calculated as follows:

$$\bar{L_{q1}} = \frac{\bar{\lambda_{q1}}}{i_{qs1}} \tag{3.68}$$

$$\bar{L_{d2}} = \frac{\bar{\lambda_{d2}}}{i_{ds2}} \tag{3.69}$$

$$\bar{L_{q2}} = \frac{\bar{\lambda_{q2}}}{i_{qs2}} \tag{3.70}$$

The actual values of the inductances in the rotating reference frame are proportional to the number of turns per coil and evaluated as:

$$L_{d1} = \bar{L_{d1}}\ N_{coil}^2 \tag{3.71}$$

$$L_{q1} = \bar{L_{q1}}\ N_{coil}^2 \tag{3.72}$$

$$L_{d2} = \bar{L_{d2}}\ N_{coil}^2 \tag{3.73}$$

$$L_{q2} = \bar{L_{q2}}\ N_{coil}^2 \tag{3.74}$$

3.7.2 Magnet Flux Linkage Calculation

The magnet flux linkages λ_{m1} and λ_{m2} are calculated by analysing the phase magnet flux linked by the armature winding resulting from the magnets in the rotor. The 2D-MagNet software can be used to generate a phase magnet flux waveform by setting the armature currents equal to zero and moving the rotor 2π electrical radians. $\bar{\lambda_{m1}}$ is the amplitude of the first harmonic in the phase magnet flux linkage waveform while $\bar{\lambda_{m2}}$ is the amplitude of the third harmonic in the phase magnet flux linkage waveform. The final values of the magnet flux linkages are calculated as:

$$\lambda_{m1} = \bar{\lambda_{m1}}\ N_{coil} \tag{3.75}$$

$$\lambda_{m2} = \bar{\lambda_{m2}}\ N_{coil} \tag{3.76}$$

3.7.3 Calculating N_{coil} and B_r

The analytical results in (3.56) and (3.57) show that the d_1-axis inductance is proportional to the square of the stator turns per coil ($L_{d1} \propto N_{coil}^2$), while the magnet flux linkage is proportional to the stator turns per coil ($\lambda_{m1} \propto N_{coil}$). These two results can be utilized to calculate the number of turns per coil N_{coil} and remanent flux density B_r which satisfy the optimal flux-weakening condition. L_{d1} and λ_{m1} are calculated with an assumption that there is only one turn per coil. The final values of L_{d1} and λ_{m1} are substituted in (3.63) and (3.64) for calculating N_{coil} and B_r.

Chapter 4

Design of Five-Phase FSCW PM Synchronous Machine

4.1 Design Methodology

This chapter presents a systematic approach for designing a prototype DL FSCW five-phase SPM machine. The initial sizing of the machine can be deduced depending on the required specifications while FEA software should verify the results. Due to the availability of accurate and fast software packages, these design steps are considered as the best choice when compared with completed analytical design methods. It is assumed that the machine is operating in a drive system with variable speed up to five times the specified rated speed. It is worth mentioning that most of the steps of the design process of this methodology can be adopted in designing any machine with fractional or distributed winding configurations. After presenting the design steps, a flowchart is constructed to summarise the initial sizing steps. The initial sizing steps are summarised as follows:

1. Choosing optimum slot/pole combination. In chapter 2 the criteria of choosing optimal slot/pole combination for high inductance fault-tolerant FSCW five-Phase SPM machines have been explained in detail.

2. Determining the outer diameter and active axial length. For many applications, the outer frame is determined due to space constraints. If there is no constraint a sizing method should be used. One of the best sizing methods is the TRV sizing method. In this method the rotor volume $V_{r\circ}$ can be estimated from the

required rated torque $T_\circ$ and a standard value for torque per-unit-volume (TRV):

$$TRV = \frac{T_\circ}{V_{r\circ}} \qquad \mathrm{Nm/m^3} \tag{4.1}$$

The standard values of TRV are given in Table 4.1 for different classes of machines [56].

Table 4.1: Standard values for torque per-unit motor volume (TRV).

Class of machine	TRV $\mathrm{kNm/m^3}$
Small totally- enclosed motors (Ferrite magnets)	7-14
Totally- enclosed motors (Sintered Rare Earth or NdFeB magnets)	14-42
Totally- enclosed motors (Bonded NdFeB magnets)	20
Integral- hp industrial motors	7-30
High performance servomotors	15-50
Aerospace machines	30-75
Large liquid-cooled machines (e.g. turbine-generators)	100-250

3. Determining the rotor to stator diameter ratio ($F_{r/s}$). For a given maximum stator outer diameter $D_{s\circ}$ or calculated rotor outer diameter $D_{r\circ}$, the rotor to stator diameter ratio may be expressed as a function of the rotor pole number as suggested in Table 4.2 [56].

Table 4.2: The rotor to stator diameter ratio as a function of pole number.

P	2	4	6	8	10	12
$F_{r/s}$ [%]	50	53	56	60	65	70

4. Determining the air-gap thickness (g). Despite the critical effect of the air-gap on the machine characteristics, there is no optimum theoretical solution for its thickness [39]. Large air-gap thickness means decreasing the probability of demagnetising the permanent magnets. However, small air-gap reduces the machine efficiency due to the increase of the eddy current losses caused by the created harmonics due to the open or semi-closed slots. The practical range of the air-gap thickness for various motor sizes is presented in [56]. These ranges are summarised in Table 4.3. Furthermore, empirical equations may be used to estimate the air-gap thickness. In the presented work empirical equation is employed, in which the

air-gap thickness is calculated as [39] :

$$g = \begin{Bmatrix} 0.2 + 0.01P_{\circ}^{0.4} & \text{mm} & \text{when } p = 1 \\ 0.18 + 0.006P_{\circ}^{0.4} & \text{mm} & \text{when } p > 1 \end{Bmatrix} \tag{4.2}$$

The rated output power of the machine ($P_{\circ}$) must be given in Watts.

Table 4.3: Practical ranges for the air-gap thickness.

Motor size	Air-gap thickness [mm]
Very small motors	0.127-0.254
Medium motors	0.381-0.508
Large motors	0.635-0.889

5. Determining the magnet to the air-gap thickness ratio ($F_{m/g}$). For a given air-gap thickness, this design parameter decides the thickness of the magnets h_m. Thick magnet reduces the risk of demagnetisation while increasing the cost. Besides, increasing the thickness of the magnets leads to increasing effective air-gap thickness, which in turn, will decrease the rotor volume and subsequently the torque produced by the machine. An estimation of the magnet thickness of approximately 4-10 times the air-gap thickness may be used, which ensures that the permeance coefficient is > 4. Finally, the final design has to be checked by using FEA for demagnetisation effects.

6. Determining the magnet angle divided by the pole pitch ratio (F_{α_m/α_P}). For a given number of poles, F_{α_m/α_P} is used to calculate the magnet arc angle α_m or the angle between successive poles. This ratio can effectively form the shape and value of the cogging torque waveform. The optimum value of the ratio at which the cogging torque is minimum is an attractive subject for researchers due to the significant influence of the cogging torque on machine performance. In FSCWs the optimum value of F_{α_m/α_P} may be calculated as [65]:

$$F_{\alpha_m/\alpha_P} = \frac{x - k_1}{x} + k_2 \qquad , \qquad k_1 = 1, 2, ..., x - 1 \tag{4.3}$$

$$x = \frac{LCM(Q, P)}{P} \tag{4.4}$$

where k_2 is typically 0.01 to 0.03 depending on the air-gap thickness.

7. Determining tooth width (w_{tb}), stator back iron depth (w_{sy}) and rotor core

thickness (w_{ry}). The general steps presented in [66] used in the design of PM synchronous machines are selected to achieve the initial sizing of the prototype machine. If the leakage flux in the rotor is ignored, the total flux leaving the magnet is equal to the flux crossing the air-gap, and it may be calculated as:

$$\phi_{total} = B_{g1} A_g = B_{g1} \left(2\pi R_{r\circ} L_{st}\right) \tag{4.5}$$

where B_{g1} is the fundamental amplitude of the air-gap flux density, L_{st} is the axial stack length, A_g is the air-gap area and $R_{r\circ}$ is the rotor outside radius. The magnitude of the maximum flux in each tooth can be calculated by dividing the total magnet flux by the number of stator teeth (number of slots Q equals the number of teeth). In other words, the tooth flux (ϕ_t) is:

$$\phi_t = \frac{\phi_{total}}{Q} = \frac{B_{g1} \left(2\pi R_{r\circ} L_{st}\right)}{Q} \tag{4.6}$$

The density of the tooth flux B_t is calculated by dividing the tooth flux by the area of the tooth, and is given as:

$$B_t = \frac{\phi_t}{w_{tb} k_{st} L_{st}} \tag{4.7}$$

where w_{tb} is tooth width and k_{st} is the lamination stacking factor. By substitution (4.6) into (4.7) a final expression for the tooth width is deduced as:

$$w_{tb} = \frac{2\pi R_{r\circ} B_{g1}}{Q k_{st} B_t} \tag{4.8}$$

Contrarily, the stator back iron depth w_{sy} and rotor core thickness w_{ry} can be calculated based on the assumption that half of the total flux passes through any one point of the stator back iron and the same for the rotor core. The flux density in the stator back iron B_{sy} and rotor core B_{ry} can be expressed as:

$$B_{sy} = \frac{\phi_{total/2}}{w_{sy} k_{st} L_{st}} \tag{4.9}$$

$$B_{ry} = \frac{\phi_{total/2}}{w_{ry} k_{st} L_{st}} \tag{4.10}$$

where ϕ_{total} in this case is the total flux leaving one magnet. Substitution of (4.5)

into (4.9) and (4.10) leads to expressions for the stator back iron depth and rotor core thickness as:

$$w_{sy} = \frac{\pi R_{r\circ} B_{g1}}{P\, k_{st} B_{sy}} \tag{4.11}$$

$$w_{ry} = \frac{\pi R_{r\circ} B_{g1}}{P\, k_{st} B_{ry}} \tag{4.12}$$

It is worth noting that w_{sy}, w_{ry} and w_{tb} depend on the flux density in each path in addition to the air-gap flux density. For a common machine design, the ferromagnetic material is identical for all iron parts of the machine such that the designer can choose a suitable single value for teeth, stator back iron and rotor core flux densities depending on the magnetic characteristics of the iron such as saturation and losses. However, B_{g1} can be decided depending on past experience or can be obtained from one of the equations (4.8), (4.11) and (4.12) in which all the quantities except B_{g1} are known.

8. Determining the slot cross-section area. A general slot form with all dimensions is depicted in Figure 4.1 [67]. The slot surface area is calculated from initial sizing data, namely (w_{tb}), (w_{sy}), ($D_{r\circ}$) and ($D_{s\circ}$). The slot depth h_{ss} is calculated as:

$$h_{ss} = \frac{1}{2}\left(D_{so} - D_{si} - 2w_{sy}\right) \tag{4.13}$$

where D_{si} is the stator inner diameter, and calculated as:

$$D_{si} = D_{ro} + 2h_m + 2g \tag{4.14}$$

The slot area A_{slot} is calculated as:

$$A_{slot} = \frac{1}{2}\left(b_{ss1} + b_{ss2}\right)\left(h_{ss} - h_{sw}\right) \tag{4.15}$$

where b_{ss1} and b_{ss2} cab be calculated as in (4.16) and (4.17).

$$b_{ss1} = \pi\left(\frac{D_{si} + 2h_{ws}}{Q}\right) - w_{ts} \tag{4.16}$$

$$b_{ss2} = \pi\left(\frac{D_{si} + 2h_{ss}}{Q}\right) - w_{ts} \tag{4.17}$$

9. Determining the number of turns per coil N_{coil}. The first step in finding N_{coil}

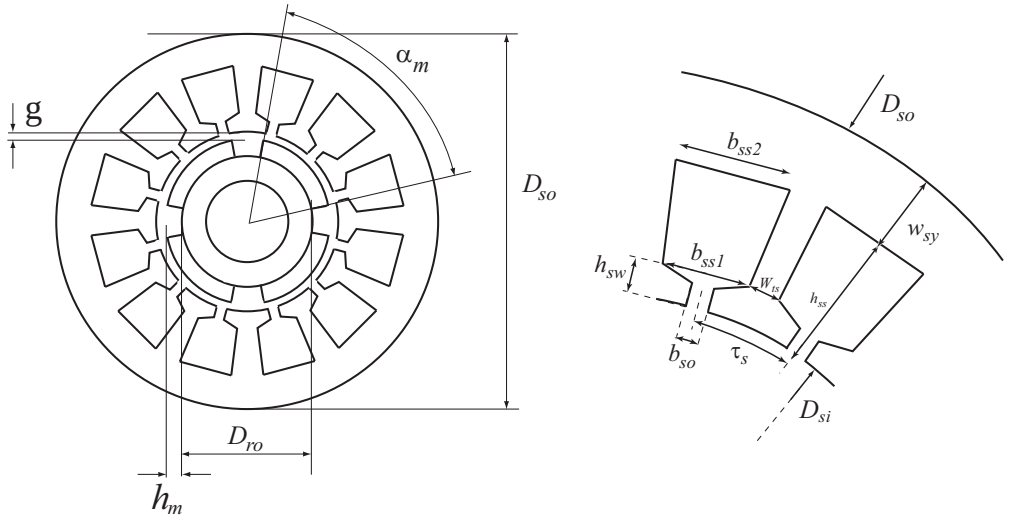

Figure 4.1: Stator slot form and dimensions.

is defining the current density in a slot conductor as:

$$J_c = \frac{I_R}{A_c} \tag{4.18}$$

where I_R is the rated (rms)-phase current of the machine and A_c is the conductor cross section area. Typical values for current densities of different cooling methods are shown in Table 4.4. The conductor cross sectional area is calculated as:

$$A_c = \left\{ \begin{array}{ll} \frac{A_{slot} k_{sf}}{N_{coil}} & \text{for single-layer winding} \\ \frac{1}{2} \frac{A_{slot} k_{sf}}{N_{coil}} & \text{for double-layer winding} \end{array} \right\} \tag{4.19}$$

where k_{sf} is the slot fill factor. Once A_c is set, substitution of (4.19) into (4.18) and simple algebra gives the number of turns per coil as:

$$N_{coil} = \left\{ \begin{array}{ll} \frac{J_c A_{slot} k_{sf}}{I_R} & \text{for single-layer winding} \\ \frac{1}{2} \frac{J_c A_{slot} k_{sf}}{I_R} & \text{for double-layer winding} \end{array} \right\} \tag{4.20}$$

Table 4.4: Typical phase conductor current densities.

Motor enclosure and cooling	A/mm^2
Totally Enclosed (convection)	1.5-5
TEFC Air-over, Fan-cooled	5-10
Totally Enclosed, Liquid cooled	10-30
Hollow Conductor, Liquid Cooled	20-40

During the motor design process, the designer can use the required current density as an indicator for choosing suitable TRV ratio due to the relation between the required torque and the rated current of the machine. Figure 4.2 shows a summary of the initial sizing steps as a flowchart.

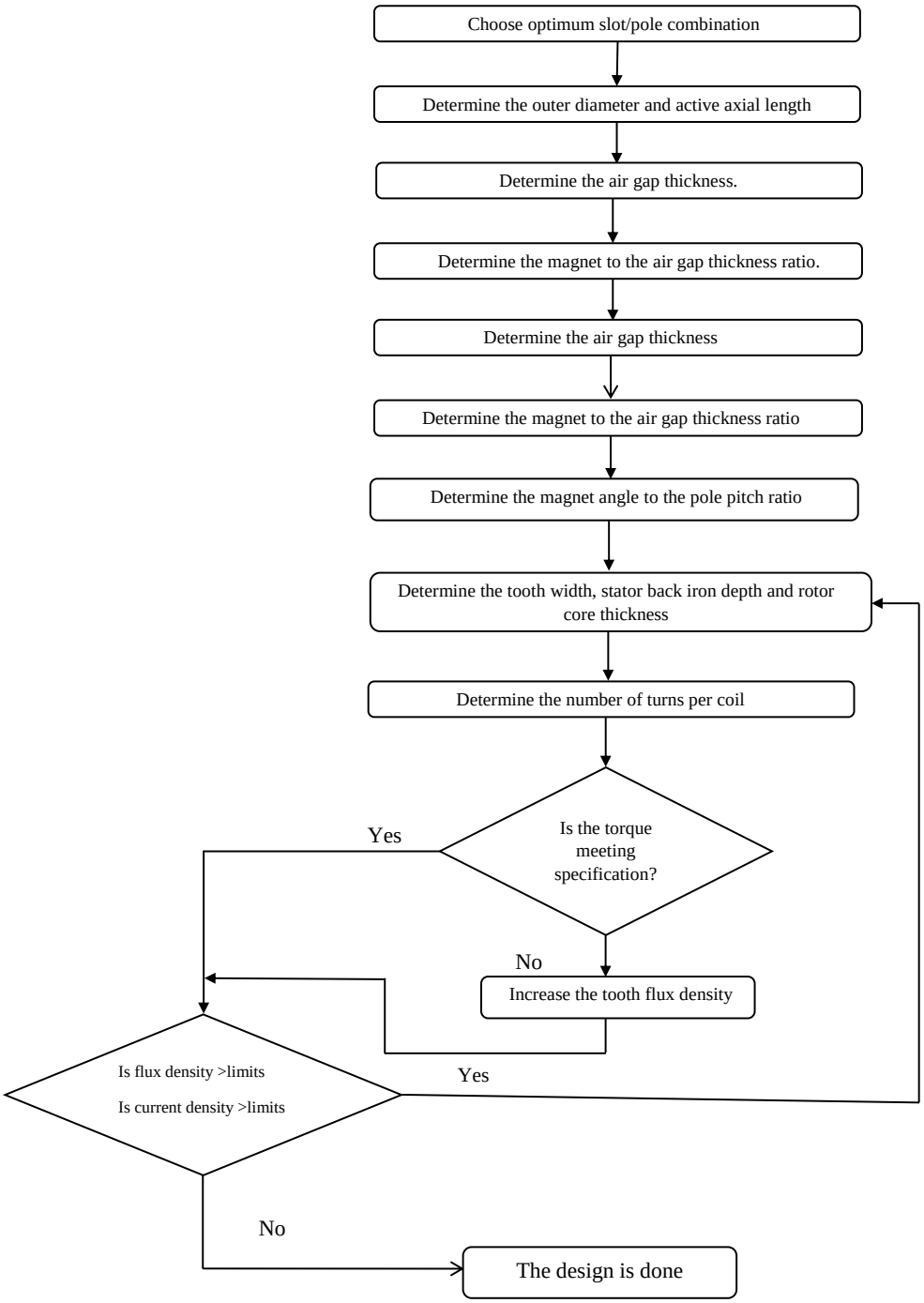

Figure 4.2: Initial sizing flowchart for the designed machine.

4.2 Initial Sizing of the Prototype Machine

The set of the specifications is listed in Table 4.5. The slot/pole combination was selected to be 10/8 according to the presented criteria in chapter 2. The stator outer diameter and the maximum axial length are given as 120mm and 50mm respectively due to the availability of such machine frame in the lab.

The machine is excited by multi-frequency two-level five-phase voltage source inverter fed by a constant dc voltage of 270V. The winding layout was designed by using the star of slots method, and presented in Figure 3.4 in the previous chapter. The rated shaft torque can be calculated as:

$$\begin{aligned} T_\circ &= \frac{P_\circ}{\omega_m} = \frac{P_\circ}{2\pi\left(\frac{n}{60}\right)} \\ &= \frac{1000}{2\pi\left(\frac{2000}{60}\right)} \\ &= 4.77464 \text{ N.m} \end{aligned}$$

while the electrical angular frequency is calculated as:

$$\begin{aligned} \omega_r &= 2\pi f_r = 2\pi\left(p\frac{n}{60}\right) \\ &= 2\pi\left(4 \times \frac{2000}{60}\right) \\ &= 837.758 \text{ rad /sec} \end{aligned}$$

Table 4.5: The design specifications.

Rated power ($P_\circ$)	1 kW
DC voltage (V_{dc})	270 V
Rated speed (n)	2000 rpm
Excitation	fundamental and third harmonics
Number of phases (m)	5
Number of pole pairs (p)	4
Stator outer diameter ($D_{s\circ}$)	120 mm
Axial length (L_{st})	50 mm

so that the rated frequency f_e is equal to 133.333 Hz. The air-gap thickness:

$$\begin{aligned} g &= 0.18 + 0.006P_{\circ}^{0.4} \\ &= 0.18 + 0.006(1500)^{0.4} \\ &= 0.2918 \text{ mm} \end{aligned}$$

Due to the high-speed operation, the calculated value has to be increased by 60% to become 0.4669 mm which can be further approximated to be 0.5 mm [39]. For reducing the cost of the used magnet, a value of 4 could be used for the initial sizing of $F_{m/g}$. By knowing this ratio and the air-gap thickness, the magnet thickness h_m can be calculated as:

$$\begin{aligned} h_m &= F_{m/g} \times g \\ &= 4 \times 0.5 \text{ mm} \\ &= 2 \text{ mm} \end{aligned}$$

Since the prototype machine has four pole pairs, $F_{r/s}$ can be selected as 0.6 so that the rotor outer diameter can be calculated as:

$$\begin{aligned} D_{r\circ} &= F_{r/s} \times D_{s\circ} \\ &= 0.6 \times 120 \text{ mm} \\ &= 72 \text{ mm} \end{aligned}$$

By using (4.3) and (4.4) it is possible to calculate three values for the magnet pole pitch ratio F_{α_m/α_P}. k_1 has been selected to be one depending on the published work in [65], while the value of k_2 is selected to be 0.01. The magnet arc angle can be calculated as:

$$\begin{aligned} \alpha_m &= F_{\alpha_m/\alpha_P} \times \left(\frac{360}{P}\right) \\ &= 0.81 \times \left(\frac{360}{8}\right) \\ &= 36.45^{\circ} \end{aligned}$$

The air-gap flux density is assumed to be 0.85 T while the flux density in the other parts of the machine is fixed and equal to 1.5 T. These assumptions depend on the researcher experience, where a value of 1.5 T in the iron material is high enough for producing the required torque and at the same time below the saturation value of the used iron material. w_{tb}, w_{sy} and w_{sy} are calculated as 12.8177 mm, 8.0111 mm and 8.0111 mm respectively. The stator inner Diameter D_{si} can be calculated as:

$$\begin{aligned} D_{si} &= D_{ro} + 2h_m + 2g \\ &= 72 + 2 \times 2 + 2 \times 0.5 \\ &= 77 \text{ mm} \end{aligned}$$

The slot height can be calculated as:

$$\begin{aligned} h_s &= \frac{1}{2}\left(D_{so} - D_{si} - 2w_{sy}\right) \\ &= \frac{1}{2}\left(120 - 77 - 2 \times 8.0111\right) \\ &= 13.4889 \text{ mm} \end{aligned}$$

The dimension h_{sw} is depicted in the slot shape presented in the Figure 4.1. By choosing the default value in MotorSolve design software for initial sizing to be $h_{sw} = 4.3837$ mm for side-by-side coil placement method b_{ss1} and b_{ss2} are calculated as 14.1269 mm and 19.8479 mm respectively. The slot area A_{slot} is calculated as:

$$\begin{aligned} A_{slot} &= \frac{1}{2}\left(b_{ss1} + b_{ss2}\right)\left(h_s - h_{sw}\right) \\ &= \frac{1}{2}\left(14.1269 + 19.8479\right)\left(13.4889 - 4.3837\right) \\ &= 154.6733 \text{ mm}^2 \end{aligned}$$

The rated current of the machine can be calculated by assuming a reasonable power factor as 0.9. In ten step mode of operation the fundamental component of the output phase-to-neutral voltage has an rms value of;

$$V_R = \frac{\sqrt{2}}{\pi} V_{dc} = 0.45 V_{dc} = 0.45 \times 270 = 121.5 \quad \text{V rms} \qquad \text{TEN STEP} \qquad (4.21)$$

$$I_R = \frac{P_\circ}{5V_R \cos\phi_1} \quad \text{A rms} \qquad \text{TEN STEP}$$
$$= \frac{1000}{5 \times 121.5 \times 0.9}$$
$$= 1.8289 \ \text{A}$$

For SPWM the fundamental component of the output phase-to-neutral voltage has an rms value of:

$$V_R = \frac{\sqrt{2}}{4} V_{dc} = \frac{\sqrt{2}}{4} \times 270 = 95.459 \quad \text{V rms} \qquad \text{SPWM} \tag{4.22}$$

$$I_R = \frac{P_\circ}{5V_R \cos\phi_1} \quad \text{A rms} \qquad \text{SPWM}$$
$$= \frac{1000}{5 \times 95.459 \times 0.9}$$
$$= 2.3279 \ \text{A}$$

At this design stage, the designer has to choose a value for the conductor cross-section area A_c or the current density J_c. The first choice enables the designer to calculate a current density for a given rated current or power, while in the second option the current density has to be decided depending on the necessary application. For this prototype application a fan-cooled, small and enclosed machine application is under design, so 6.5 A/mm^2 is fitting. For double-layer winding half of the slot surface area is used for determining the number of turns per coil:

$$N_{coil} = \frac{1}{2} \frac{J_c A_{slot} k_{sf}}{I_R} \qquad \text{TEN STEP}$$
$$= \frac{1}{2} \frac{6.5 \times 154.6733 \times 0.51}{1.8289}$$
$$\simeq 140 \quad \text{TURNS}$$

$$N_{coil} = \frac{1}{2} \frac{J_c A_{slot} k_{sf}}{I_R} \qquad \text{SPWM}$$
$$= \frac{1}{2} \frac{6.5 \times 154.6733 \times 0.51}{2.3279}$$
$$\simeq 110 \quad \text{TURNS}$$

Those design steps are not optimised for optimum flux weakening. Nevertheless, they can be considered as the starting stage for the next optimising steps.

4.3 Machine Design Optimization

The analytical expressions presented in the previous chapter were developed to predict the motor flux-weakening performance and to calculate necessary parameters. The predicted parameters can be used in the design stage to determine the motor dimensions. The design aims are high efficiency, high torque density, low pulsating torque and wide speed range. A five-phase SPM machine using double-layer fractional slot winding was designed for variable speed drive applications.

Based on the initial design steps, a machine model with all necessary dimensions was used for further optimisation. The magnet arc angle α_m was calculated for minimising the cogging torque. The computed value was further optimised through the finite element numerical software to be 37.46 [mechanical degrees]. The cogging torque is also affected by the slot opening. A large slot opening leads to a higher cogging torque and vice versa. The slot opening was selected to be 3.2mm to fit the practical requirement for the needle-wound coils method. It is worth mentioning that the magnet arc angle substantially controls the shape and harmonic content of the back-emf. In the next chapters, it will be obvious that the third harmonic of the back-emf participates in the developed torque of the machine for speeds below the base or rated speed. However, since the primary purpose is the design of a machine with smooth torque and a wide speed range, the priority of calculating the magnet arc angle is given for reducing the cogging torque.

Besides the design variables there are also a number of parameters with assigned constant values that do not change during the design for optimum flux-weakening. Those parameters are listed in Table 4.6. Machine design for optimum flux-weakening requires calculating the magnet remanence B_r and the number of turns per coil N_{coil} which satisfy the characteristic current and the rated phase voltage of the main virtual plane. The conditions for optimum flux-weakening can be

rewritten in compact form as:

$$I_R = \frac{K_{md}\, B_r}{K_{ld}\, N_{coil}} \quad \text{A rms} \tag{4.23}$$

$$V_R = \sqrt{\left(K_{rs} N_{coil} I_R + \omega_r K_{md} B_r\, N_{coil}\right)^2 + \left(\omega_r K_{ld}\, N_{coil}^2 I_R\right)^2} \quad \text{V rms} \tag{4.24}$$

Table 4.6: Parameters with assigned constant values.

Parameters	Value
Stator outer diameter	120 [mm]
Slot opening width	3.2 [mm]
Slot opening height	3.46 [mm]
Axial length	50 [mm]
Magnet arc angle	37.46 [mec degrees]
Air-gap thickness	0.5 [mm]

In this design methodology, its assumed that the rated voltage of the machine is equal to the maximum available voltage of the voltage source inverter. For single-frequency drive, five-phase SPM machine, the maximum phase voltage, $V_{s\max}$, is decided by the dc link voltage, V_{dc} of the PWM inverter and the PWM method. If the carrier-based pulse width modulation method (SPWM) is used, the obtained $V_{s\max}$ in the linear control range is $V_{dc}/2$. If the inverter is controlled in the ten-step mode of operation, $V_{s\max}$, can be increased up to $2V_{dc}/\pi$.

The next step in the optimising process of the machine design for optimum flux weakening is checking the values of the flux density in the rotor, stator tooth and back iron and making sure they are below the maximum value for the iron material. Checking the value of the current density is an important step to make sure it is also below the standard limit for the given application. It is important to make the required adjustments to the tooth thickness and back iron thickness to limit the flux density and current density to practical and acceptable values.The magnet thickness could also be varied to optimise the design based on cost, then check that the machine is producing the required power at the rated speed. In most cases the calculated values of N_{coil} and B_r are impractical. In this case, their values should be approximated to the nearest available value and then readjust the machine dimensions to fit the required power and speed.

4.4 Results for Optimal Flux-Weakening Design

A double-layer FSCW five-phase SPM synchronous machine was designed for a fault tolerant variable speed drive application. The requirements suggest a constant torque region for speeds up to 2000 rpm and a constant power region for speeds up to five times the rated speed of the machine. The set of the dimensions, specifications and the calculated parameters are listed in Table 4.7. The machine was designed and analysed initially using the standard sizing procedure presented in the previous sections with the help of two software packages from Infolytica; MotorSolve and 2D-MagNet.

Table 4.7: Summary of the dimensions, specifications and the numerically calculated parameters of the designed SPM machine.

Parameter	Value	Parameter	Value
Number of slots	10	Rotor core thickness	7.17 [mm]
Number of poles	8	Rotor inner diameter	50.06 [mm]
Number of phases	5	Rotor outer diameter	64.4 [mm]
Series turns per coil	123	Magnet angle	37.46 [mec deg]
Back iron height	7.17 [mm]	Magnet thickness	2 [mm]
Stator inner diameter	69.4 [mm]	Slot fill factor	51.17 [%]
Stator outer diameter	120 [mm]	Winding resistance	2.603 [Ω]
Slot height	18.13 [mm]	Efficiency	89.5 [%]
Air-gap thikness	0.5 [mm]	Rated current	2.43 [A]
Slot area	212.38 [mm^2]	Total loss	0.0926 [kW]
Slot opening width	3.2 [mm]	Rotor speed	2000 [rpm]
Slot top width	19.334 [mm]	Rated torque	3.77 [Nm]
Slot bottom width	10.142 [mm]	Remanent flux density	0.72 [T]
Slot opening height	3.46 [mm]	Relative permeability of the magnets	1.3022
Tooth width	13.86 [mm]		

The slot opening was selected to be 3.2mm due to practical constraints. The flux pattern at rated load is shown in Figure 4.3. It is clear from the flux patterns that the flux density in the rotor core, stator teeth and back iron is uniformly distributed and approximately equals to 1.5 T at rated load conditions, which is below the maximum limit of the used M19 steel material. The waveform of the air-gap flux density is shown in Figures 4.4 .

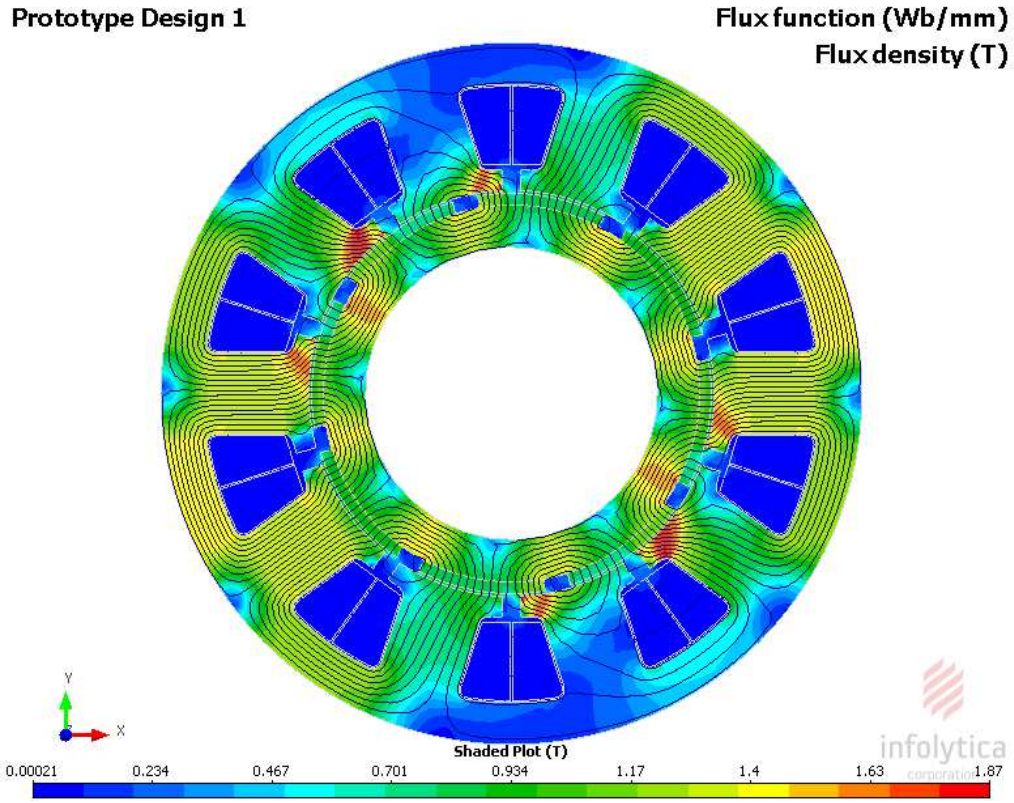

Figure 4.3: Flux-line pattern of the designed machine at the rated load.

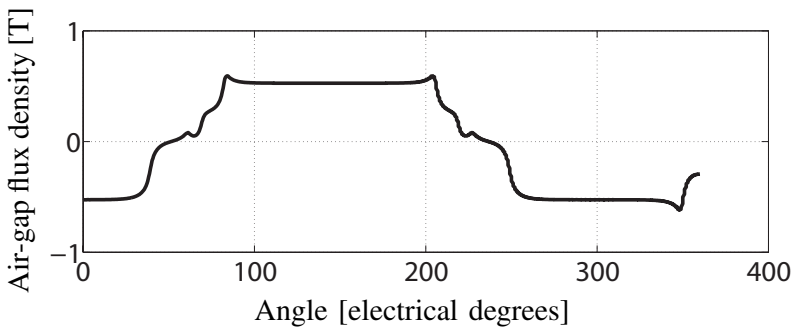

Figure 4.4: Airgap flux density of DL 10 slot/ 8 pole five-phase SPM machine.

4.4.1 Resistance

The stator resistance was determined to be $r_s = 3.037\ \Omega$ by measuring the voltage across one of the phase windings while excited by the rated value of dc current. Ideally, the resistance has to be the same for all phases, but realistically, a minimal error is expected. The problem was solved by repeating the measuring process for all five phase windings and taking the average. Table 4.8 shows the measured and calculated per phase resistance of the prototype five-phase machine.

Table 4.8: The measured and calculated per phase resistance of the prototype five-phase machine at 25 °C.

Resistance calculation	
Lab measurement	Analytical calculation
3.037 [Ω]	2.603 [Ω]

4.4.2 Inductances

Techniques for lab measurement of the different components of the machine inductance in PM synchronous machines can be arranged into two general categories: the standstill tests [68–71], and the rotational tests [72,73]. The latter category requires a drive system for running the machine under different loading conditions, whereas the standstill tests can be performed without the need for a drive system. The self- and mutual inductances of the lab prototype five-phase machine are measured by using the single-phase excitation at standstill with a blocked rotor test.

The main reason for choosing this technique is that the air-gap permeance, and consequently the winding inductance of the SPM machine does not vary with rotor position, because the air-gap permeance is approximately equal to magnet permeance, such that few measurements at specific rotor positions are enough to measure the machine inductances in the linear operation conditions. Cross-coupling and non-linearity are out of the scope of this thesis and this will be part of the future work. In this technique, one phase of the stator is supplied with a constant AC current, while the four other phases are open circuited. The five-phase voltages are then measured at different locked rotor positions. The self- and mutual inductances can

be derived as a function of the rotor position θ_e, as follows:

$$L_a(\theta_e) = \frac{\sqrt{(V_a/I_a)^2 - r_s^2}}{2\pi f} \tag{4.25}$$

$$M_{ax}(\theta_e) = \frac{V_x}{2\pi f I_a} \tag{4.26}$$

where V_a is the line-to-neutral rms voltage of phase a and V_x is the line-to-neutral rms voltage of phases b, c, d and e respectively. I_a is the rms current in phase a, and f is the supply frequency. Assuming the machine to be symmetric, the complete 5×5 stator inductance matrix for any particular rotor position can be constructed from this data. For example, the stator inductance at the rotor position of $\theta_e = 0°$ is given in the matrix below:

$$\begin{bmatrix} 0.023091603 & -0.003551995 & -0.006844593 & -0.006843384 & -0.003824159 \\ -0.003824159 & 0.023091603 & -0.003551995 & -0.006844593 & -0.006843384 \\ -0.006843384 & -0.003824159 & 0.023091603 & -0.003551995- & 0.006844593 \\ -0.006844593 & -0.006843384 & -0.003824159 & 0.023091603 & -0.003551995 \\ -0.003551995 & -0.006844593 & -0.006843384 & -0.003824159 & 0.023091603 \end{bmatrix}$$

Here, the d_1-q_1 plane inductances and d_2-q_2 plane inductances can be indirectly calculated from the obtained self- and mutual inductances. By application of Park's transformation, the stator measured inductance matrix is computed in dq coordinates as:

$$[\mathbf{L_{d1q1d2q2}}] = \boldsymbol{P}\boldsymbol{L}_s\boldsymbol{P}^{-1} = \begin{bmatrix} 0.031886 & & & & \\ & 0.031886 & & & \\ & & 0.024829 & & \\ & & & 0.024829 & \\ & & & & 0.002027 \end{bmatrix}$$

From this matrix, the dq inductance components can be identified and are stated in Table 4.9. Practical measurements show that the mutual inductance between the AC supplied coil (phase a) and the closest coils (phases c and d) are higher than the inductance of the other coils (phases b and e). This result fully aligns with the classical machine theory as explained in equation (5.16).

The lab measurements, numerical simulation and analytical calculations show that $L_{d1} = L_{q1}$ and $L_{d2} = L_{q2}$. The analytical calculations show that those dq components of both planes are exactly equal. Analytical calculations of the $d_1 - q_1$

match very well with the experimentally obtained data and numerical simulation. However, the analytical calculations of the second plane inductances give very different values from the measured and numerically obtained values. The harmonics present in the MMF as a result of the FSCW layout are responsible for the deviation of the second plane inductances. The winding function method considers the exact per phase MMF. In other words, the calculation of the mutual inductance between any two phases assumes all MMF harmonics of an excited phase winding are linking the other phase windings, while the practical results indicate different outcomes where the closest phase windings to the AC excited phase have a higher mutual inductance due to a higher number of linking flux lines.

Table 4.9: Lab prototype five-phase machine stator inductance components, analytical calculation and numerical simulation in *dq* coordinates.

	Inductance calculation [H]		
	Lab measurement	Numerical simulation	Analytical calculation
L_{d1}	0.0319	0.0315	0.03175
L_{q1}	0.0319	0.0315	0.03175
L_{d2}	0.0248	0.0239	0.03175
L_{q2}	0.0248	0.0239	0.03175

4.5 Back-emf and Magnet Flux Linkage

Figure 4.5 shows the lab measured back-emf waveform of the prototype five-phase machine while figure 4.6 shows its harmonic content. As will be presented in the next chapters the torque producing component of the main virtual machine is the fundamental component of the back-emf waveform, while the torque producing component of the secondary virtual machine is the third harmonic of the back-emf waveform. In spite of the magnet arc angle is optimised for minimising the cogging torque and the magnet thickness is optimised for decreasing the magnet cost, the 3rd harmonic represents 8.455% of the fundamental harmonic which may be used as an additional torque-producing component for speeds below the rated speed. The increase in torque ratio ($\%T_{e-increase}$) as a result of controlling the second plane parameters

was calculated as follows:

$$\begin{aligned}\%T_{e-increase} &= \frac{(T_{e1}+T_{e2})-T_{e1}}{T_{e1}} \times 100 \\ &= \frac{T_{e2}}{T_{e1}} \times 100 \\ &= 3\frac{i_{q2}}{i_{q1}}\frac{\lambda_{m2}}{\lambda_{m1}} \times 100 \\ &= 9\frac{\lambda_{m2}^2}{\lambda_{m1}^2} \times 100\end{aligned}$$

where the i_{q2}/i_{q_1} ratio is calculated for speeds up to the rated speed of the machine in (6.27) as:

$$\frac{i_{q2}}{i_{q1}} = \frac{3\lambda_{m2}}{\lambda_{m1}}$$

For $\lambda_{m1} = 0.10882$ Wb and $\lambda_{m2} = 0.00306$ Wb, $\%T_{e-increase} = 0.7117$.

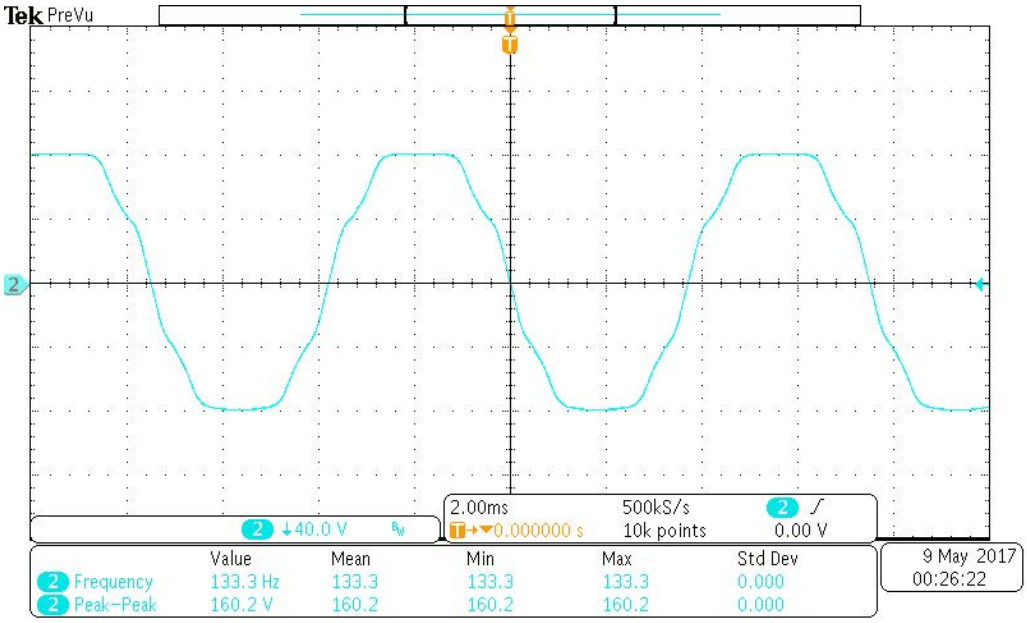

Figure 4.5: The back-emf waveform of the lab prototype five-phase machine.

The 9$^{\text{th}}$ harmonic represents only 3.279% of the fundamental harmonic. If the prototype machine is controlled as a single frequency drive system for a sinusoidal current, the torque ripple is almost the same as the torque produced by pure sinusoidal back-emf synchronous machines. The 7$^{\text{th}}$ harmonic of the back-emf, which is only 3.702% of the fundamental, represents 43.78% of the 3$^{\text{rd}}$ harmonic. Consequently, the back-emf of the secondary machine is composed of 3$^{\text{rd}}$ and 7$^{\text{th}}$ harmonics.

Table 4.10 presents the list of the lab measurement, analytical calculation and

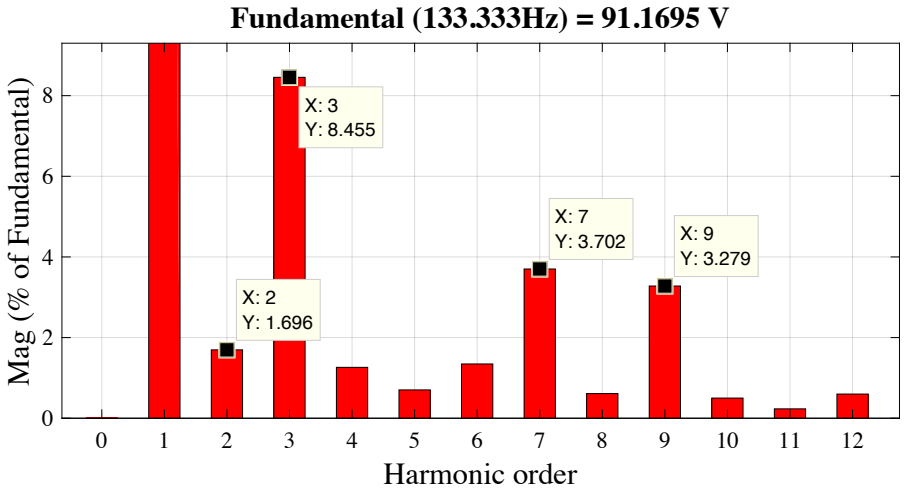

Figure 4.6: The harmonic content of the lab prototype five-phase machine.

numerical simulation of the back-emf and magnet flux linkage for the lab prototype five-phase machine. The numerical simulation is performed by using the 2D-Static MagNet software. The percentage error of the numerical simulation to the lab measurement is about 0.5%, while the percentage error of the numerical simulation to the lab measurement is about 0.6%. The numerical simulation waveform of the back-emf is shown in Figure 4.7. This figure shows the back-emf concerning the fundamental harmonic. The waveform represents a reasonable approximation of the sinusoidal fundamental harmonic.

Table 4.10: Prototype five-phase machine stator back-emf and magnet flux linkage: lab measurement, analytical calculation and numerical simulation.

Parameter	Lab measurement	Numerical simulation	Analytical calculation
λ_{m1}	0.10882 [Wb]	0.1082 [Wb]	0.108175 [Wb]
λ_{m2}	0.0031 [Wb]	0.003 [Wb]	—
E_{b1-max}	91.1695 [V]	90.707 [V]	90.616 [V]
E_{b2-max}	7.7084 [V]	7.6522 [V]	—

4.6 Cogging Torque

The cogging torque is minimised by an extensive study with the purpose of selecting the angle between successive poles or the magnet angle (α_m). The cogging torque of one period for different magnet angles is shown in Figure 4.8. The peak-to-peak cogging torque amplitude is approximately 1.39% of the machine average rated

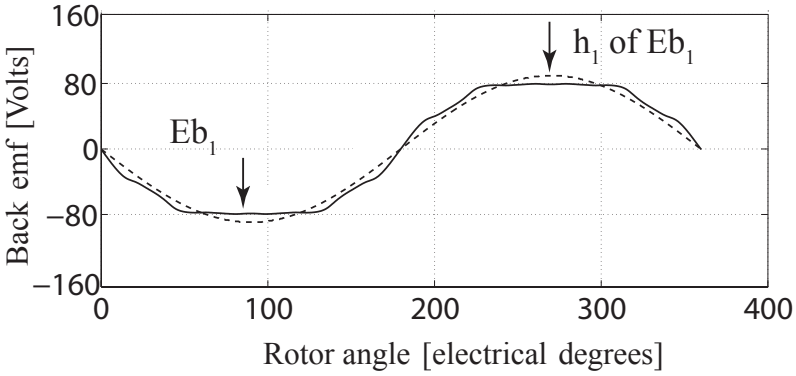

Figure 4.7: The numerical simulation waveform of the back-emf of the lab prototype machine.

torque which can be considered an acceptable result.

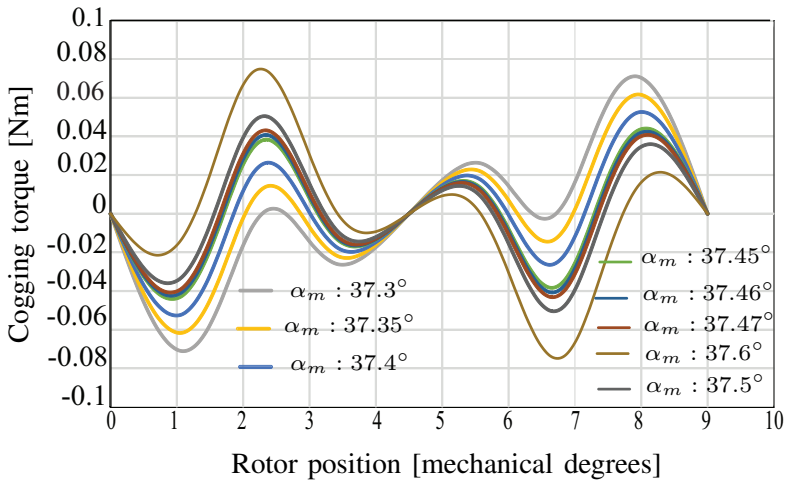

Figure 4.8: Cogging torque of DL 10 slot/ 8 pole five-phase SPM. Optimum magnet angle is 37.46°.

4.7 Characteristic Current

The characteristic current of the machine was calculated during the design stage by using the analytical method which is described in the previous chapter. The numerical simulation was used to calculate the magnet leakage flux, to validate the analytically computed values of the inductances, and the magnet flux linkage of the prototype machine. The magnet leakage flux was calculated for the initially sized machine to be 8% of the magnet linkage flux to be used in the analytical model of the computed magnet linkage flux. The numerically calculated value, the analytically calculated value of the characteristic current, and the rated current of the prototype

machine are listed in Table 4.11.

Table 4.11: The numerically calculated value, the analytically calculated value of the characteristic current, and the rated current of the prototype machine. All variables are rms quantities.

Parameter	Lab measurement	Numerical simulation	Analytical calculation
I_{ch}	2.412 [A]	2.430 [A]	2.409 [A]
I_R	2.365 [A]		

Figure 4.9 shows the torque-speed characteristic of the prototype machine based on both the numerical simulation and the analytically calculated parameters. The numerically estimated value of I_{ch} is 1.0274 times the rated current of the machine, the analytically derived value of I_{ch} is 1.0186 times the rated current of the machine while the lab measured value of I_{ch} is 1.0198 times the rated current of the machine. Those results show that the prototype machine substantially satisfies the condition for optimum flux-weakening operation, enabling a wide constant-power speed range for speeds higher than the rated or base speed.

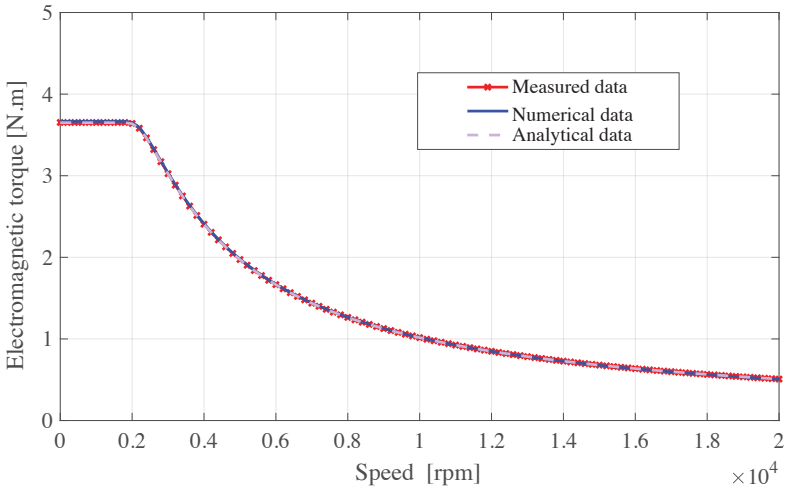

Figure 4.9: The torque-speed characteristic of the designed machine.

Chapter 5

Modelling and Control of the MF Five-Phase PM Synchronous Motor Based Drive

5.1 Modelling of the Two- Level Five-Phase Voltage Source Inverter

The power circuit topology of a two-level five-phase voltage source inverter is shown in Figure 5.1, where the inverter is feeding a five-phase PM synchronous motor. This topology was first proposed by [74]. it is assumed that constant ripple-free dc voltage is provided at the inverter input and all the power semiconductor switches are assumed to be ideal. Each leg consists of two switches connected in series and is controlled by pulses obtained by the comparison between the reference command and the triangular carrier waveform. It is important to note that the two switches in the same leg are never conducting simultaneously since in such shoot-through case a high short-circuit current passes through the leg and leads to damage of the inverter module. However, practical inverters will need a dead-time based on the power switch data sheets to avoid the shoot-through problem.

Considering the states of the two switches in the same inverter leg are complementary, then the number of possible switching states for this topology is equal to 2^n, where n is the number of inverter legs/phases. For a five-phase VSI, if it

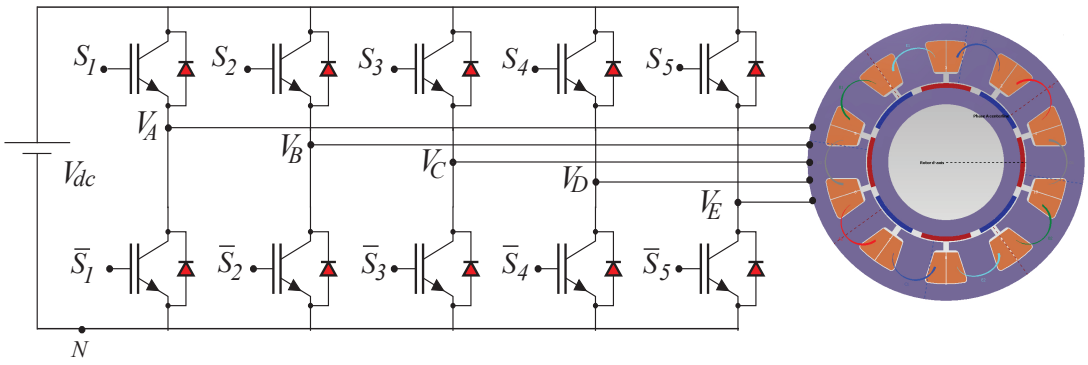

Figure 5.1: Five-leg VSI supplying a five-phase PM synchronous motor.

is operated in Sinusoidal Pulse Width Modulation (SPWM) mode, there will be 32 switching states (2^5). The relation between the phase-to-neutral voltage (v_i) where $i \in \{a, b, c, d, e\}$ and the pole voltages V_K where $K \in \{A, B, C, D, E\}$ can be expressed as:

$$\begin{aligned} V_A(t) &= v_a(t) + v_{nN}(t) \\ V_B(t) &= v_b(t) + v_{nN}(t) \\ V_C(t) &= v_c(t) + v_{nN}(t) \\ V_D(t) &= v_d(t) + v_{nN}(t) \\ V_E(t) &= v_e(t) + v_{nN}(t) \end{aligned} \tag{5.1}$$

where $v_{nN}(t)$ is the voltage difference between the star point n of the load and the negative rail of the dc bus N. By adding each term of the equation (5.1), and putting the sum of phase-to-neutral voltage equal to zero (assuming a balanced five-phase voltage), we obtain:

$$v_{nN}(t) = \left(\frac{1}{5}\right)(V_A(t) + V_B(t) + V_C(t) + V_D(t) + V_E(t)) \tag{5.2}$$

Substituting equation (5.2) back into equation (5.1), the following expressions for the phase-to-neutral voltage are obtained

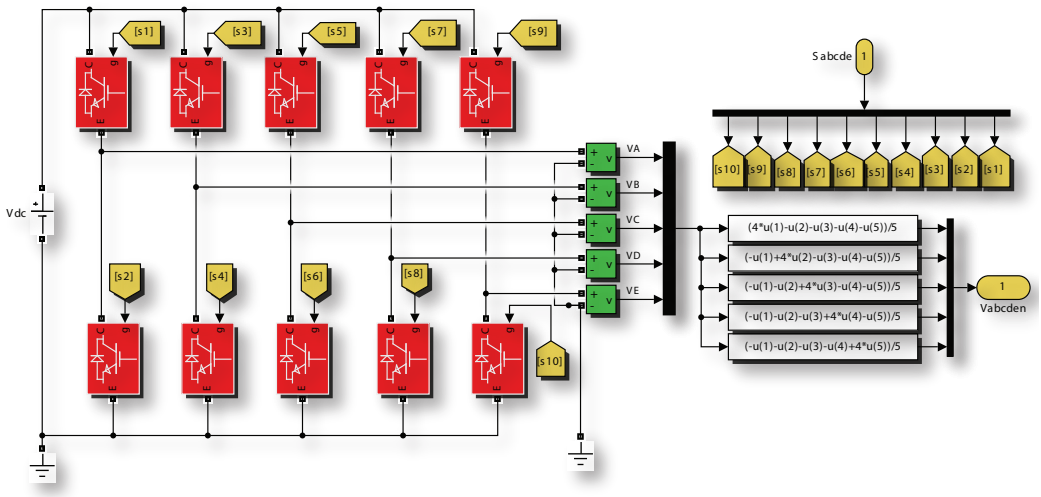

Figure 5.2: Power converter

$$
\begin{aligned}
v_a(t) &= (4/5)\,V_A(t) - (1/5)\,(V_B(t) + V_C(t) + V_D(t) + V_E(t)) \\
v_b(t) &= (4/5)\,V_B(t) - (1/5)\,(V_A(t) + V_C(t) + V_D(t) + V_E(t)) \\
v_c(t) &= (4/5)\,V_C(t) - (1/5)\,(V_B(t) + V_A(t) + V_D(t) + V_E(t)) \\
v_d(t) &= (4/5)\,V_D(t) - (1/5)\,(V_B(t) + V_C(t) + V_A(t) + V_E(t)) \\
v_e(t) &= (4/5)\,V_E(t) - (1/5)\,(V_B(t) + V_C(t) + V_D(t) + V_A(t))
\end{aligned}
\tag{5.3}
$$

The relationship between pole voltage and switching signals is given as:

$$V_k = S_s V_{dc}; \qquad k \in \{A, B, C, D, E\} \tag{5.4}$$

where $S_s = 1$ when the upper power switch is 'ON' and $S_s = 0$ when the lower switch is 'ON'. Substituting equation (5.4) back into equation (5.3), gives a values for the phase-to-neutral voltages v_j, $(j \in \{a, b, c, d, e\})$ for each state of the 32 switching states. Figure 5.2 shows the SIMULINK/MATLAB model of the two-level five-phase voltage source inverter that includes the expressions for the phase-to-neutral voltage. Phase-to-neutral voltages for the 32 switching states are listed in Table B.1.

5.1.1 Phase Voltage Space Vectors of the Five-Phase VSI

The phase to neutral voltage space vectors of n-phase system (n is an odd number), can be entirely described by using $(n-1)/2$ two-dimensional (2-D) planes plus zero-

space component which are obtained with the use of a decoupling transformation applied to an n-phase VSI. Particularly the five-phase inverter can be represented by two space vectors plus a zero-space component. In other words, space vectors of phase voltages in the two orthogonal planes $\alpha1-\beta1$ and $\alpha2-\beta2$ can be defined in the stationary reference frame by substituting the phase voltages of the 32 switching states into the Clarke transformation [75]. Space vectors for the $\alpha1-\beta1$ plane are expressed in equations (5.5) and (5.6), while space vectors for $\alpha2-\beta2$ plane are expressed in equations (5.7) and (5.8). The third plane is single-dimensional (zero-sequence) and is assumed to be zero as a result of the star connection of the motor. The phase voltage space vectors in $\alpha1-\beta1$ and $\alpha2-\beta2$ planes are listed in Table B.2 for all 32 switching states. The five-phase VSI space vectors in the $\alpha1-\beta1$ plane and $\alpha2-\beta2$ plane are shown in Figure 5.3.

It can be seen from Figure 5.3 that for each plane there will be 32 space vectors, two of them are zero space vectors and the rest forming three concentric groups based on their magnitudes. The nonzero space vectors can be categorized into three groups (each consists of ten space vectors) based on their magnitudes: small, medium and large. The amplitudes of the small, medium and large space vectors are equal to $0.2472V_{dc}, 0.4V_{dc}, 0.6472V_{dc}$, respectively [76]. Further, it is observed from Figure 5.3 [76]:

- The large space vectors of the $\alpha1-\beta1$ plane form the small space vectors in the $\alpha2-\beta2$ plane.
- The small space vectors of the $\alpha1-\beta1$ plane form the large space vectors in the $\alpha2-\beta2$ plane.
- The middle space vectors of the $\alpha1-\beta1$ plane form the same space vectors in the $\alpha2-\beta2$ plane.
- The phase sequence a, b, c, d, e of the $\alpha1-\beta1$ plane corresponds to a, c, e, b, d sequence of the $\alpha2-\beta2$ plane, which are the 3^{rd} harmonics of the phase voltages.

each plane can be broken into ten sectors each spanning $\pi/5$.

$$\underline{v}_{\alpha1\beta1\cdots k} = v_{\alpha1\cdots k} + jv_{\beta1\cdots k} \qquad k \in \{1, 2, \cdots, 32\} \tag{5.5}$$

$$\begin{bmatrix} v_{\alpha1\beta1\ldots1} \\ v_{\alpha1\beta1\ldots2} \\ \vdots \\ v_{\alpha1\beta1\ldots32} \end{bmatrix} = \frac{2}{5}\begin{bmatrix} 1 & \cos\gamma & \cos 2\gamma & \cos 2\gamma & \cos\gamma \\ 0 & \sin\gamma & \sin 2\gamma & -\sin 2\gamma & -\sin\gamma \end{bmatrix} \begin{bmatrix} v_{a1} & v_{a2} & \cdots & v_{a32} \\ v_{b1} & v_{b2} & \cdots & v_{b32} \\ v_{c1} & v_{c2} & \cdots & v_{c32} \\ v_{d1} & v_{d2} & \cdots & v_{d32} \\ v_{e1} & v_{e2} & \cdots & v_{e32} \end{bmatrix} \tag{5.6}$$

$$\underline{v}_{\alpha2\beta2\cdots k} = v_{\alpha2\cdots k} + jv_{\beta2\cdots k} \qquad k \in \{1, 2, \cdots, 32\} \tag{5.7}$$

$$\begin{bmatrix} v_{\alpha2\beta2\ldots1} \\ v_{\alpha2\beta2\ldots2} \\ \vdots \\ v_{\alpha2\beta2\ldots32} \end{bmatrix} = \frac{2}{5}\begin{bmatrix} 1 & \cos 2\gamma & \cos 4\gamma & \cos 4\gamma & \cos 2\gamma \\ 0 & \sin 2\gamma & \sin 4\gamma & -\sin 4\gamma & -\sin 2\gamma \end{bmatrix} \begin{bmatrix} v_{a1} & v_{a2} & \cdots & v_{a32} \\ v_{b1} & v_{b2} & \cdots & v_{b32} \\ v_{c1} & v_{c2} & \cdots & v_{c32} \\ v_{d1} & v_{d2} & \cdots & v_{d32} \\ v_{e1} & v_{e2} & \cdots & v_{e32} \end{bmatrix} \tag{5.8}$$

Harmonic mapping into different planes can be accomplished with the use of space vector decomposition [76]. Families of odd harmonics are mapped according to the rules listed in Table 5.1 [76, 78, 79]. When a five-phase VSI supplies a five-phase machine with a concentrated stator winding the first plane is used to control the 1^{st} harmonic of the phase voltage while the second plane is used to control of the 3^{rd} harmonic of the phase voltage. Table 5.1 shows that output voltage harmonics of the order $(1, 9, 11, \cdots)$ map into the $\alpha_1 - \beta_1$ plane while harmonics of the order $(3, 7, 13, \cdots)$ belong to the $\alpha_2 - \beta_2$ plane.

Table 5.1: Distribution of the harmonic families for Y-connected, five-phase machine.

$\alpha_1 - \beta_1$	$\alpha_2 - \beta_2$
$1, 9, 11, \cdots,\ 5h \pm 1$	$3, 7, 13, \cdots,\ 5h \pm 2$

The second harmonic component in the $\alpha_1 - \beta_1$ plane is the 9^{th}, of which the emf component of the fractional slot winding machine is likely to be low with a high frequency (ten times the fundamental frequency) leading to almost a sinusoidal emf [78]. Concerning the $\alpha_2 - \beta_2$ plane, the main harmonic component is the 3^{rd} while the second harmonic is the 7^{th}. If the emf amplitude of the third harmonic is high enough, it is possible to generate an additional constant torque. However, the 7^{th} harmonic component of the phase currents may interact with the emf 7^{th} harmonic component and cause torque ripple [78, 79]. Consequently, the emf of the secondary machine can not be considered as sinusoidal because it is composed of 3^{rd} and 7^{th} harmonics.

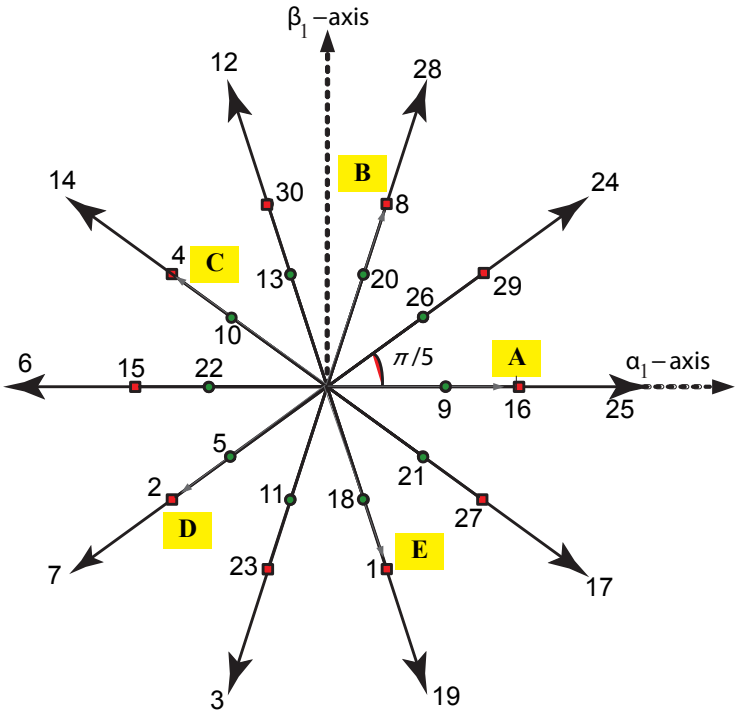

(a) $\alpha_1 - \beta_1$ plane.

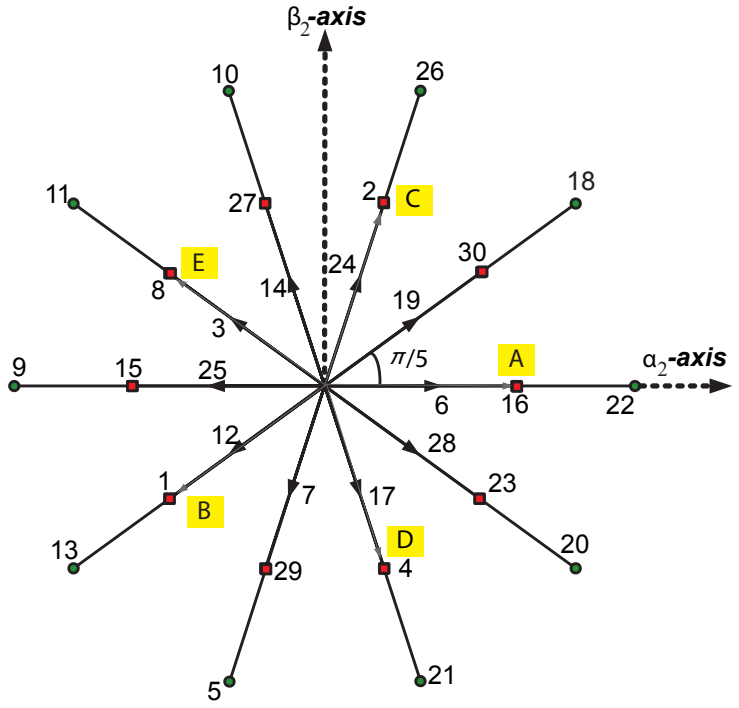

(b) $\alpha_2 - \beta_2$ plane.

Figure 5.3: Five-phase VSI phase voltage space vectors in the: a. $\alpha_1 - \beta_1$ plane, and b. $\alpha_2 - \beta_2$ plane [77].

5.2 Modelling of the MF Five-Phase PM Synchronous Motor

In this section power-variant model for modelling five-phase electrical machine in a compact and general form is proposed. In particular, the section deals with the modelling of five-phase permanent magnet synchronous machines with a non-sinusoidal shape of the rotor flux. The mathematical model of the motor in terms of physical variables (natural phase variables) is considered first. A space vector representation of the two orthogonal planes of the machine is applied. The resulting equations are with time-varying coefficients. For this reason, a rotational transformation is applied. The dynamic model of the motor is obtained using a two-phase fictitious equivalent to a five-phase machine approach and in the rotor frame reference.

5.2.1 Phase Domain Model of the MF Five-Phase PM Synchronous Motor

A five-phase symmetrical concentrated winding permanent magnet synchronous machine, such that the spatial displacement between any two mmfs produced by any two consecutive phases is ($\gamma = 2\pi/5$), is under consideration. The following assumptions were made:

- The air-gap is uniform.
- The B-H curve of the iron core is linear and so the main flux saturation can be neglected.
- Iron core losses are neglected.
- The winding resistance and inductance are constant.

The phase voltage equations of a five-phase machine can be written in matrix form as [75] [80],

$$\mathbf{V}^s_{abcde} = \mathbf{R}_s \mathbf{I}^s_{abcde} + \frac{d\mathbf{\Lambda}^s_{abcde}}{dt} \tag{5.9}$$

$$\mathbf{\Lambda}^s_{abcde} = \mathbf{L}_s \mathbf{I}^s_{abcde} + \mathbf{\Lambda}_m \tag{5.10}$$

The following definitions of the phase voltage matrix $\mathbf{V}^s_{abcde}$, current matrix $\mathbf{I}^s_{abcde}$, resistance matrix $\mathbf{R}_s$, and flux linkage matrix $\mathbf{\Lambda}^s_{abcde}$ are applied to equations (5.9)

and (5.10).

$$\mathbf{V}^s_{abcde} = \begin{bmatrix} v_{as} & v_{bs} & v_{cs} & v_{ds} & v_{es} \end{bmatrix}^T \tag{5.11}$$

$$\mathbf{I}^s_{abcde} = \begin{bmatrix} i_{as} & i_{bs} & i_{cs} & i_{ds} & i_{es} \end{bmatrix}^T \tag{5.12}$$

$$\mathbf{\Lambda}^s_{abcde} = \begin{bmatrix} \lambda_{as} & \lambda_{bs} & \lambda_{cs} & \lambda_{ds} & \lambda_{es} \end{bmatrix}^T \tag{5.13}$$

$$\mathbf{R}_s = \mathrm{diag}\begin{pmatrix} r_s & r_s & r_s & r_s & r_s \end{pmatrix} \tag{5.14}$$

The flux linkage of the stator winding matrix $\mathbf{\Lambda}^s_{abcde}$ is related to the stator currents by the stator inductance matrix $\mathbf{L}_s$. The matrix of the stator inductances is given as:

$$\mathbf{L}_s = \begin{bmatrix} L_{as} \\ L_{bs} \\ L_{cs} \\ L_{ds} \\ L_{es} \end{bmatrix} = \begin{bmatrix} L_{ls}+L_{aa} & L_{ab} & L_{ac} & L_{ad} & L_{ae} \\ L_{ba} & L_{ls}+L_{bb} & L_{bc} & L_{bd} & L_{be} \\ L_{ca} & L_{cb} & L_{ls}+L_{cc} & L_{cd} & L_{ce} \\ L_{da} & L_{db} & L_{dc} & L_{ls}+L_{dd} & L_{de} \\ L_{ea} & L_{eb} & L_{ec} & L_{ed} & L_{ls}+L_{ee} \end{bmatrix} \tag{5.15}$$

Due to the symmetry of the machine configuration under study, the inductance matrix can be written with ($\gamma = 2\pi/5$):

$$\mathbf{L}_s = \begin{bmatrix} L_{ls}+L_m & L_m\cos(\gamma) & L_m\cos(2\gamma) & L_m\cos(3\gamma) & L_m\cos(4\gamma) \\ L_m\cos(4\gamma) & L_{ls}+L_m & L_m\cos(\gamma) & L_m\cos(2\gamma) & L_m\cos(3\gamma) \\ L_m\cos(3\gamma) & L_m\cos(4\gamma) & L_{ls}+L_m & L_m\cos(\gamma) & L_m\cos(2\gamma) \\ L_m\cos(2\gamma) & L_m\cos(3\gamma) & L_m\cos(4\gamma) & L_{ls}+L_m & L_m\cos(\gamma) \\ L_m\cos(\gamma) & L_m\cos(2\gamma) & L_m\cos(3\gamma) & L_m\cos(4\gamma) & L_{ls}+L_m \end{bmatrix} \tag{5.16}$$

$$L_{aa} = L_{bb} = L_{cc} = L_{dd} = L_{ee} = L_m \tag{5.17}$$

where L_{kk} ($kk \in \{aa, bb, cc, dd, ee\}$) is the magnetising inductance per phase and L_{ls} is the slot leakage inductance per phase. This symmetry is termed as "circulant" [75]: the second row of the inductance matrix is written by placing the last element in row 1 at the start of row 2 and shifting all other elements to the right. Similarly, row 3 can be formed from row 2, etc., until the the 5^{th} row is reached. $\mathbf{\Lambda}_m$ is the flux linkage matrix due to the permanent magnets and is expressed as:

$$\mathbf{\Lambda}_m = \begin{bmatrix} \lambda_{ma} & \lambda_{mb} & \lambda_{mc} & \lambda_{md} & \lambda_{me} \end{bmatrix}^T \tag{5.18}$$

As the fundamental and third harmonic components of the permanent magnet flux linkage are the torque producing components of the main and secondary fictitious

machines, they will be used in developing the machine model. λ_{m1} and λ_{m2} in (5.19) are the amplitudes of the fundamental and the third harmonic flux linkage components established by the permanent magnets on the rotor as viewed from the stator windings.

$$\boldsymbol{\Lambda}_m = \begin{bmatrix} \lambda_{ma} \\ \lambda_{mb} \\ \lambda_{mc} \\ \lambda_{md} \\ \lambda_{me} \end{bmatrix} = \lambda_{m1} \begin{bmatrix} \sin(\theta_r) \\ \sin\left(\theta_r - \frac{2\pi}{5}\right) \\ \sin\left(\theta_r - \frac{4\pi}{5}\right) \\ \sin\left(\theta_r + \frac{4\pi}{5}\right) \\ \sin\left(\theta_r + \frac{2\pi}{5}\right) \end{bmatrix} + \lambda_{m2} \begin{bmatrix} \sin(3\theta_r) \\ \sin 3\left(\theta_r - \frac{2\pi}{5}\right) \\ \sin 3\left(\theta_r - \frac{4\pi}{5}\right) \\ \sin 3\left(\theta_r + \frac{4\pi}{5}\right) \\ \sin 3\left(\theta_r + \frac{2\pi}{5}\right) \end{bmatrix} \tag{5.19}$$

5.2.2 Machine Model in the Stator Reference Frame

The stator reference frame of the physical machine variables x (voltage, currents and flux linkage) is achieved by applying Clarke's transformation $\boldsymbol{K}_s$ defined in [75]:

$$\boldsymbol{K}_s = \frac{2}{5} \begin{bmatrix} 1 & \cos\gamma & \cos 2\gamma & \cos 2\gamma & \cos\gamma \\ 0 & \sin\gamma & \sin 2\gamma & -\sin 2\gamma & -\sin\gamma \\ 1 & \cos 2\gamma & \cos 4\gamma & \cos 4\gamma & \cos 2\gamma \\ 0 & \sin 2\gamma & \sin 4\gamma & -\sin 4\gamma & -\sin 2\gamma \\ \frac{1}{2} & \frac{1}{2} & \frac{1}{2} & \frac{1}{2} & \frac{1}{2} \end{bmatrix} \tag{5.20}$$

$$\begin{bmatrix} x_{\alpha 1} \\ x_{\beta 1} \\ x_{\alpha 2} \\ x_{\beta 2} \\ x_{zs} \end{bmatrix} = \boldsymbol{K}_s \begin{bmatrix} x_a \\ x_b \\ x_c \\ x_d \\ x_e \end{bmatrix} \tag{5.21}$$

where $\gamma = 2\pi/5$. This is so-called real decoupling transformation in power-variant form (Clarke's transformation), which in essence decomposes a 5-dimensional vector space into two 2D and mutually decoupled planes (no magnetic coupling between the planes) based on the generalisation of Concordia's transformation [80]. Transformation of the phase variables results in two pairs of torque producing orthogonal space vectors $(x_{\alpha 1} + jx_{\beta 1}, x_{\alpha 2} + jx_{\beta 2})$ and one single-dimensional variable (zero-sequence component). Since the motor is balanced and star-connected with an isolated neutral point, the zero-sequence space component is zero. By resolving every space vector into a real and imaginary part, two components of the corresponding 2-D plane can be recognised as shown in Figure 5.4. Applying Clarke's transformation

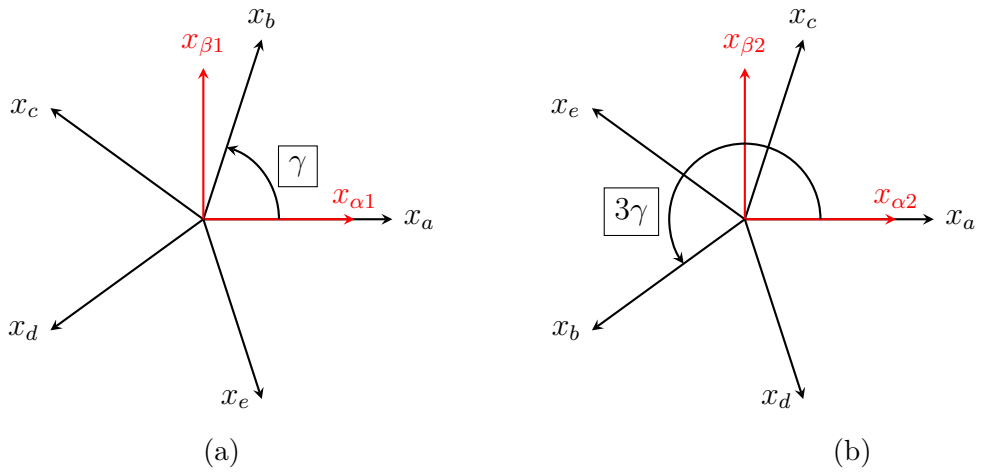

Figure 5.4: Two 2D and mutually decoupled planes of a five-phase motor. (a) $\alpha_1-\beta_1$ plane. (b) $\alpha_2-\beta_2$ plane.

(5.21) to the stator voltage equations (5.9), (5.10) leads to:

$$\begin{aligned}
\boldsymbol{K}_s\mathbf{V}^s_{abcdes} &= \mathbf{R}_s\boldsymbol{K}_s\mathbf{I}^s_{abcdes} + \boldsymbol{K}_s\frac{d\boldsymbol{\Lambda}^s_{abcdes}}{dt} \\
\mathbf{V}^s_{\alpha 1\beta 1\,\alpha 2\beta 2\,zs} &= \mathbf{R}_s\mathbf{I}^s_{\alpha 1\beta 1\,\alpha 2\beta 2\,zs} + \boldsymbol{K}_s\frac{d}{dt}\left(\mathbf{L}_s\mathbf{I}^s_{abcde} + \boldsymbol{\Lambda}_m\right) \\
\mathbf{V}^s_{\alpha 1\beta 1\,\alpha 2\beta 2\,zs} &= \mathbf{R}_s\mathbf{I}^s_{\alpha 1\beta 1\,\alpha 2\beta 2\,zs} + \boldsymbol{K}_s\frac{d}{dt}\left(\mathbf{L}_s\boldsymbol{K}_s^{-1}\mathbf{I}^s_{\alpha 1\beta 1\,\alpha 2\beta 2\,zs} + \boldsymbol{\Lambda}_m\right) \\
&= \mathbf{R}_s\mathbf{I}^s_{\alpha 1\beta 1\,\alpha 2\beta 2\,zs} + \mathbf{L}^s_{\alpha 1\beta 1\,\alpha 2\beta 2\,zs}\frac{d}{dt}\left(\mathbf{I}^s_{\alpha 1\beta 1\,\alpha 2\beta 2\,zs}\right) + \frac{d}{dt}\left(\boldsymbol{\Lambda}_{m\cdots\alpha 1\beta 1\,\alpha 2\beta 2\,zs}\right)
\end{aligned}$$

where

$$\mathbf{L}^s_{\alpha 1\beta 1\,\alpha 2\beta 2\,zs} = \boldsymbol{K}_s\mathbf{L}_s\boldsymbol{K}_s^{-1} \tag{5.22}$$

5.3 Machine Model in the Rotor Reference Frame

The $\alpha_1-\beta_1$ and $\alpha_2-\beta_2$ planes components of the stator current space vectors in the stationary reference frame can be transformed to d_1-q_1 and d_2-q_2 by using the rotational matrix as defined by [81]:

$$\mathbf{R} = \begin{bmatrix}
\cos(\theta_e) & \sin(\theta_e) & 0 & 0 & 0 \\
-\sin(\theta_e) & \cos(\theta_e) & 0 & 0 & 0 \\
0 & 0 & \cos(-3\theta_e) & \sin(-3\theta_e) & 0 \\
0 & 0 & \sin(-3\theta_e) & -\cos(-3\theta_e) & 0 \\
0 & 0 & 0 & 0 & 1
\end{bmatrix} \tag{5.23}$$

The electrical rotor position θ_e is zero when the axis of a magnet's north pole is aligned with the axis of phase a. Figure 5.5 shows the references for the rotor

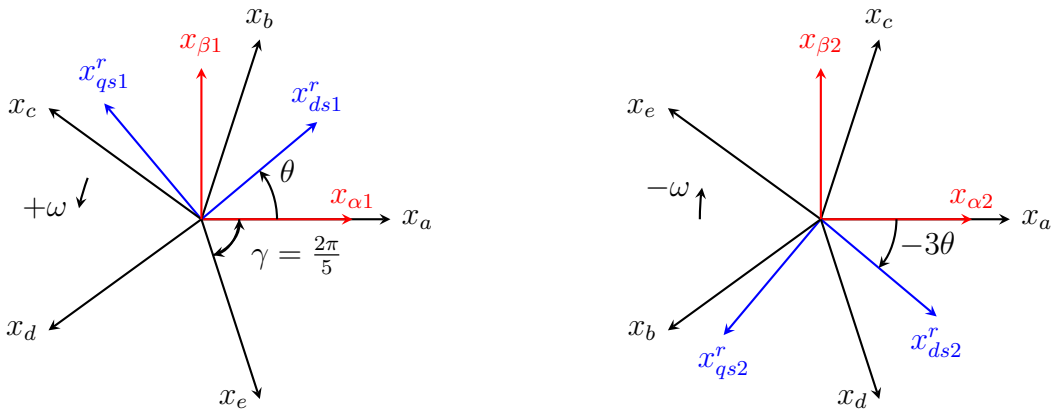

Figure 5.5: References for the rotor reference frame. (a) Fundamental harmonic component with a positive sequence (+). (b) Third harmonic component with a negative sequence (-).

reference frame. However, it is possible to transform the physical variables (voltage, current and flux linkage) directly to the rotor frame reference by using the Park transformation which is defined as $\boldsymbol{P}$:

$$\begin{bmatrix} x^r_{ds1} \\ x^r_{qs1} \\ x^r_{ds2} \\ x^r_{qs2} \end{bmatrix} = \boldsymbol{P} \begin{bmatrix} x_a \\ x_b \\ x_c \\ x_d \\ x_e \end{bmatrix} \tag{5.24}$$

where

$$\boldsymbol{P} = \boldsymbol{R}\,\boldsymbol{K}_s \tag{5.25}$$

5.3.1 Voltage Transformation

In the rotor reference frame, the inductance parameters become constant, independent of position. Because the field orientation control in a motor drive system employs space vectors, the dq model of the machine leads to the ready adaptation of position or speed for different control strategies for speed and torque such as variable speed control and direct torque control. By applying the Park transformation

matrix to the stator voltage equations, the following can be obtained:

$$\begin{aligned}
\boldsymbol{P}\mathbf{V}^{s}_{abcdes} &= \mathbf{R}_s \boldsymbol{P}\mathbf{I}^{s}_{abcdes} + \boldsymbol{P}\frac{d\boldsymbol{\Lambda}^{s}_{abcdes}}{dt} \\
\mathbf{v}^{r}_{d1q1\,d2q2\,zs} &= \mathbf{R}_s \mathbf{i}^{s}_{d1q1\,d2q2\,zs} + \boldsymbol{P}\frac{d}{dt}\left(\boldsymbol{P}^{-1}\boldsymbol{\lambda}^{r}_{d1q1\,d2q2\,zs}\right) \\
\mathbf{v}^{r}_{d1q1\,d2q2\,zs} &= \mathbf{R}_s \mathbf{i}^{s}_{d1q1\,d2q2\,zs} \cdots \\
&\quad + \boldsymbol{P}\boldsymbol{P}^{-1}\frac{d}{dt}\left(\boldsymbol{\lambda}^{r}_{d1q1\,d2q2\,zs}\right) + \boldsymbol{P}\frac{d}{dt}\left(\boldsymbol{P}^{-1}\right)\lambda_{d1q1\,d2q2\,zs}
\end{aligned}$$

but

$$\boldsymbol{P}\boldsymbol{P}^{-1} = \boldsymbol{I}$$

and

$$\boldsymbol{P}\frac{d}{dt}\left(\boldsymbol{P}^{-1}\right) = \omega_e \begin{bmatrix} 0 & -1 & 0 & 0 & 0 \\ 1 & 0 & 0 & 0 & 0 \\ 0 & 0 & 0 & -3 & 0 \\ 0 & 0 & 3 & 0 & 0 \\ 0 & 0 & 0 & 0 & 0 \end{bmatrix} = \omega_e \boldsymbol{m}$$

The stator voltage equation can be expressed as:

$$\boldsymbol{v}^{r}_{d1q1\,d2q2} = \boldsymbol{r}_s \boldsymbol{i}^{r}_{d1q1\,d2q2} + \frac{d}{dt}\left(\boldsymbol{\lambda}_{d1q1\,d2q2}\right) + \omega_e \boldsymbol{m}\boldsymbol{\lambda}_{d1q1\,d2q2} \tag{5.26}$$

the stator phase voltages in the rotor frame reference are:

$$v^{r}_{ds1} = r_s\, i^{r}_{ds1} + \frac{d\lambda_{ds1}}{dt} - \omega_e\, \lambda_{qs1} \tag{5.27}$$

$$v^{r}_{qs1} = r_s\, i^{r}_{qs1} + \frac{d\lambda_{qs1}}{dt} + \omega_e\, \lambda_{ds1} \tag{5.28}$$

$$v^{r}_{ds2} = r_s\, i^{r}_{ds2} + \frac{d\lambda_{ds2}}{dt} - 3\,\omega_e\, \lambda_{qs2} \tag{5.29}$$

$$v^{r}_{qs2} = r_s\, i^{r}_{qs2} + \frac{d\lambda_{qs2}}{dt} + 3\,\omega_e\, \lambda_{ds2} \tag{5.30}$$

5.3.2 Flux Transformation

The stator flux equations in the rotor frame reference are obtained by applying Park's transformation (5.25) matrix to (5.10) as follows:

$$\begin{aligned} \boldsymbol{P}\boldsymbol{\Lambda}^{s}_{abcde} &= \boldsymbol{P}\boldsymbol{L}_s\boldsymbol{P}^{-1}\boldsymbol{P}\boldsymbol{I}^{s}_{abcde} + \boldsymbol{P}\boldsymbol{\Lambda}_m \\ \boldsymbol{\lambda}^{r}_{d1q1\,d2q2} &= \boldsymbol{P}\boldsymbol{L}_s\boldsymbol{P}^{-1}\mathbf{i}^{r}_{d1q1\,d2q2} + \boldsymbol{\lambda}^{r}_{d1q1\,d2q2} \end{aligned} \tag{5.31}$$

where

$$\boldsymbol{P}\boldsymbol{L}_s\boldsymbol{P}^{-1} = \begin{bmatrix} L_{d1} & & & & \\ & L_{q1} & & & \\ & & L_{d2} & & \\ & & & L_{q2} & \\ & & & & L_{ls} \end{bmatrix} \tag{5.32}$$

$$\boldsymbol{\lambda}^{r}_{d1q1\,d2q2} = \boldsymbol{P}\boldsymbol{\Lambda}_m = \begin{bmatrix} \lambda_{m1} \\ 0 \\ \lambda_{m2} \\ 0 \\ 0 \end{bmatrix} \tag{5.33}$$

The stator flux equations in the rotor frame reference are as follows:

$$\lambda^{r}_{ds1} = L_{d1}\, i^{r}_{ds1} + \lambda_{m1} \tag{5.34}$$

$$\lambda^{r}_{qs1} = L_{q1}\, i^{r}_{qs1} \tag{5.35}$$

$$\lambda^{r}_{ds2} = L_{d2}\, i^{r}_{ds2} + \lambda_{m2} \tag{5.36}$$

$$\lambda^{r}_{qs2} = L_{q2}\, i^{r}_{qs2} \tag{5.37}$$

Substituting the relationships in (5.34), (5.35), (5.36) and (5.37) into (5.27), (5.28), (5.29) and (5.30) the most common form of the machine voltage equations in the rotor reference frame can be obtained as

$$v^{r}_{ds1} = r_s\, i^{r}_{ds1} + L_{d1}\,\frac{d\, i^{r}_{ds1}}{dt} - \omega_e\, L_{q1}\, i^{r}_{qs1} \tag{5.38}$$

$$v^{r}_{qs1} = r_s\, i^{r}_{qs1} + L_{q1}\,\frac{d\, i^{r}_{qs1}}{dt} + \omega_e\, L_{d1}\, i^{r}_{ds1} + \omega_e\, \lambda_{m1} \tag{5.39}$$

$$v^{r}_{ds2} = r_s\, i^{r}_{ds2} + L_{d2}\frac{d\, i^{r}_{ds2}}{dt} - 3\,\omega_e\, L_{q2}\, i^{r}_{qs2} \tag{5.40}$$

$$v^{r}_{qs2} = r_s\, i^{r}_{qs2} + L_{q2}\,\frac{d\, i^{r}_{qs2}}{dt} + 3\,\omega_e\, L_{d2}\, i^{r}_{ds2} + 3\,\omega_e\, \lambda_{m2} \tag{5.41}$$

5.3.3 Electromagnetic Torque Transformation

The electromagnetic torque equation can be derived by applying the co-energy method. When there is no saliency on the rotor, the electromagnetic torque is expressed as [27]:

$$T_e = \frac{\partial \mathbf{W_{co}}}{\partial \theta_m} \tag{5.42}$$

Co-energy is defined as follows:

$$\mathbf{W}_{co} = \frac{1}{2} \left[\mathbf{I}^s_{abcde}\right]^T \mathbf{L}_s \mathbf{I}^s_{abcde} + \left[\mathbf{I}^s_{abcde}\right]^T \mathbf{\Lambda}_m \tag{5.43}$$

Taking the partial derivative with respect to θ_e ($\theta_e = \frac{P}{2}\theta_m$) and considering that there is no saliency on the rotor yields:

$$\begin{aligned} T_e &= \frac{P}{2} \left[\mathbf{I}^s_{abcde}\right]^T \frac{\partial \mathbf{\Lambda}_m}{\partial \theta_e} \\ &= \frac{P}{2} \left[\boldsymbol{P}^{-1} \mathbf{i}^r_{d1q1\,d2q2}\right]^T \frac{\partial \mathbf{\Lambda}_m}{\partial \theta_e} \\ &= \frac{5}{2}\frac{P}{2} \left[\mathbf{i}^r_{d1q1\,d2q2}\right]^T \boldsymbol{P} \frac{\partial \mathbf{\Lambda}_m}{\partial \theta_e} \\ &= \frac{5}{2}\frac{P}{2} \left(\lambda_{m1}\, i^r_{qs1} + 3\lambda_{m2}\, i^r_{qs2}\right) \end{aligned} \tag{5.44}$$

where P is the number of poles and $\boldsymbol{P}^{-1}$ is related to $[\boldsymbol{P}]^T$ by:

$$\boldsymbol{P}^{-1} = \frac{5}{2} \left[\boldsymbol{P}\right]^T \tag{5.45}$$

If the rotor structure is salient with different L_{dx} and L_{qx}, $x \in \{1, 2\}$, the electromagnetic torque equation changes to:

$$T_e = \frac{5}{2}\frac{P}{2} \begin{bmatrix} (L_{d1} - L_{q1})\, i^r_{ds1}\, i^r_{qs1} + (L_{d2} - L_{q2})\, i^r_{ds2}\, i^r_{qs2} \\ +\lambda_{m1}\, i^r_{qs1} + 3\lambda_{m2}\, i^r_{qs2} \end{bmatrix} \tag{5.46}$$

5.3.4 Mechanical System

The modelling of the motor electrical speed begins at the equation of the electromagnetic torque generated by the machine (5.47). Equation (5.47) generally represents the electromagnetic torque generated in the two types of five-phase PM synchronous motor: interior PM synchronous motor and surface mounted PM synchronous mo-

tor. Surface mounted PM synchronous motor can be considered as a special case in which L_{d1} equals L_{q1} and L_{d2} equals L_{q2} . Hence, the reluctance torque of the electromagnetic torque equals zero.

In order for the motor to operate at a given speed, the electromagnetic torque needs to overcome all torque components in the opposite direction, which include load torque, friction torque, and the torque that results from the combined rotor and load moment of inertia. The torque equation is expressed by:

$$T_e = J\frac{d\omega_m}{dt} + T_l + B\,\omega_m \tag{5.47}$$

where J is the moment of inertia of the load and machine rotor combined in [kg m^2]. ω_m is rotor mechanical speed in [rad s^{-1}]. T_l is the load torque in [N m]. B is the friction coefficient of the load and the machine in [N m rad s^{-1}]. Rearranging equation (5.47) gives the mechanical speed:

$$\omega_m = \frac{1}{J}\left[\int (T_e - T_l - B\omega_m)\,dt\right] \tag{5.48}$$

5.4 Field Orientation Control of the Drive System

The PWM and the digital control delay cause the digital implementation to deviate from the continuous-time domain model. The robustness of the system is degraded if a controller designed in the continuous-time domain is simply converted to the discrete-time domain. A discrete-time domain model of the machines is proposed. Based on this model, a discrete-time domain current regulator design methodology is proposed.

5.4.1 The Control Structure of the Five-Phase PM Synchronous Motor Drive System

The implementation of the vector-controlled PM synchronous motor is presented in this section. The machine model, Clarke's transformation and Park's transformation play important role in deriving the speed and current controllers.

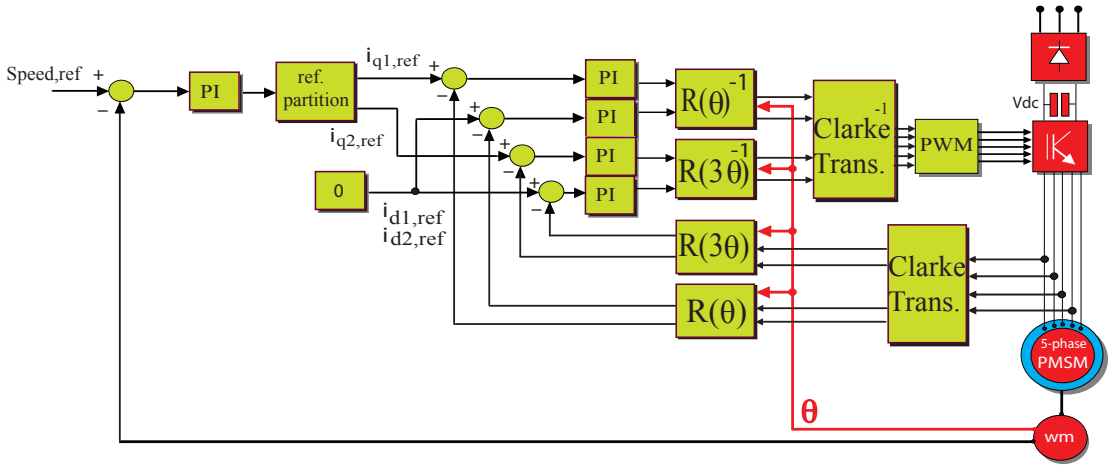

Figure 5.6: Field orientation control diagram of the five-phase PM synchronous motor.

5.4.2 Current Controller

The structure of the five-phase PM synchronous motor field orientation control is shown in Figure 5.6. The current regulator consists of four PI controllers, each one acting on an axis of current, as shown in Figure 5.7. The outputs of the current regulators result in a rotor reference frame voltage command which is converted to a phase voltage command in the stationary reference frame. The conversion is accomplished using the measured or estimated rotor angle, θ_e. The starting point is rearranging equations (5.38), (5.39), (5.40) and (5.41) to be

$$\frac{d\,i^r_{ds1}(t)}{dt} = \frac{1}{L_{d1}}\left(v^r_{ds1}(t) - r_s i^r_{ds1}(t) + \omega_e \lambda_{q1}\right) = \frac{1}{L_{d1}} v^{\bar{r}}_{ds1} \tag{5.49}$$

$$\frac{d\,i^r_{qs1}(t)}{dt} = \frac{1}{L_{q1}}\left(v^r_{qs1}(t) - r_s i^r_{qs1}(t) - \omega_e \lambda_{d1}\right) = \frac{1}{L_{q1}} v^{\bar{r}}_{qs1} \tag{5.50}$$

$$\frac{d\,i^r_{ds2}(t)}{dt} = \frac{1}{L_{d2}}\left(v^r_{ds2}(t) - r_s i^r_{ds2}(t) + 3\omega_e \lambda_{q2}\right) = \frac{1}{L_{d2}} v^{\bar{r}}_{ds2} \tag{5.51}$$

$$\frac{d\,i^r_{qs2}(t)}{dt} = \frac{1}{L_{q2}}\left(v^r_{qs2}(t) - r_s i^r_{qs2}(t) - 3\omega_e \lambda_{d2}\right) = \frac{1}{L_{q2}} v^{\bar{r}}_{qs2} \tag{5.52}$$

The nonlinear cross-coupling terms in d_1q_1 and d_2q_2 planes defined by (5.49), (5.50), (5.51) and (5.52) through $\omega_e\lambda_{q1}$, $\omega_e\lambda_{d1}$, $3\omega_e\lambda_{q2}$, $3\omega_e\lambda_{d2}$ respectively, can be eliminated by using a technique called input-and-output linearisation and also decoupling using feed-forward manipulation [82]. Using the auxiliary variables $v^{\bar{r}}_{ds1}$, $v^{\bar{r}}_{qs1}$, $v^{\bar{r}}_{ds2}$ and $v^{\bar{r}}_{qs2}$, and then applying the Laplace transform and rearranging the expression for the

functions, we obtain the first order transfer functions for the electrical part of the machine dynamics as:

$$\frac{I^r_{ds1}(s)}{V^{\bar{r}}_{ds1}(s)} = \frac{1}{r_s + L_{d1}} \tag{5.53}$$

$$\frac{I^r_{qs1}(s)}{V^{\bar{r}}_{qs1}(s)} = \frac{1}{r_s + L_{q1}} \tag{5.54}$$

$$\frac{I^r_{ds2}(s)}{V^{\bar{r}}_{ds2}(s)} = \frac{1}{r_s + L_{d2}} \tag{5.55}$$

$$\frac{I^r_{qs2}(s)}{V^{\bar{r}}_{qs2}(s)} = \frac{1}{r_s + L_{q2}} \tag{5.56}$$

Note that with a simple R-L model of the motor in the rotor reference frame, there is no cross-coupling between the d_1-axis and q_1-axis and between d_2-axis and q_2-axis. The machine model can now be combined with the current regulator models and nonlinear feedforward compensation into one block diagram so that the initial tuning of the regulator can be obtained as shown in Figure 5.7. The discrete model of

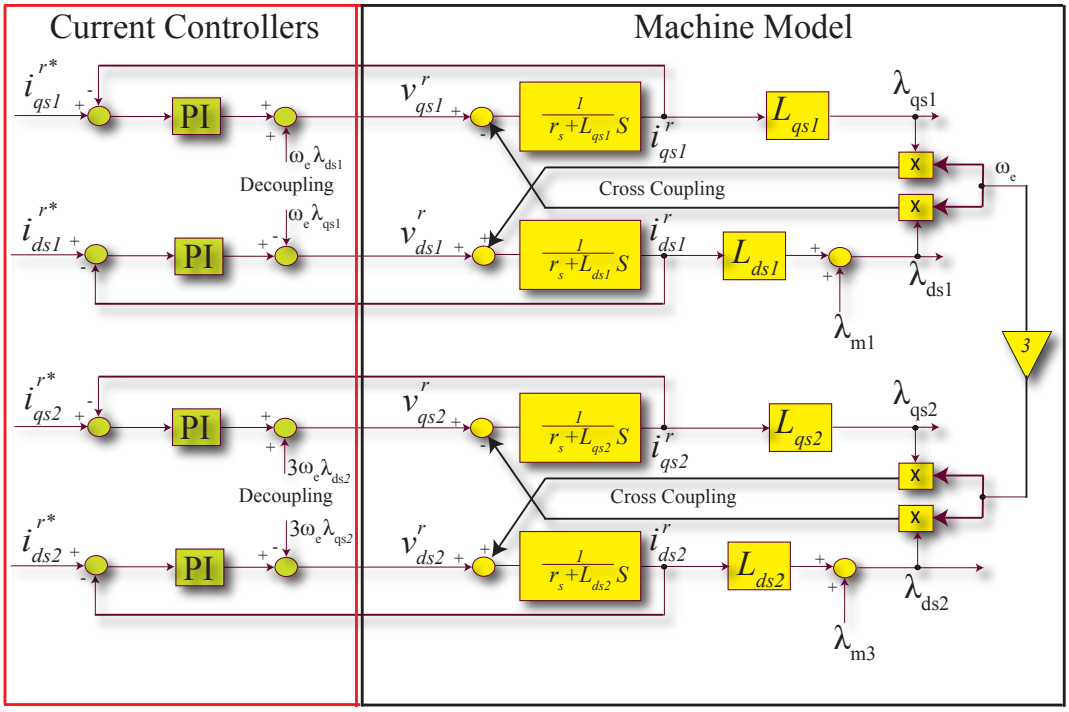

Figure 5.7: Electrical part of the machine dynamics and current controllers.

the electrical dynamic model of the machine is shown in Figure 5.8. The discrete-time domain transfer function of the PI controllers can be derived by using the backward difference approximation of Laplace transform. The backward difference

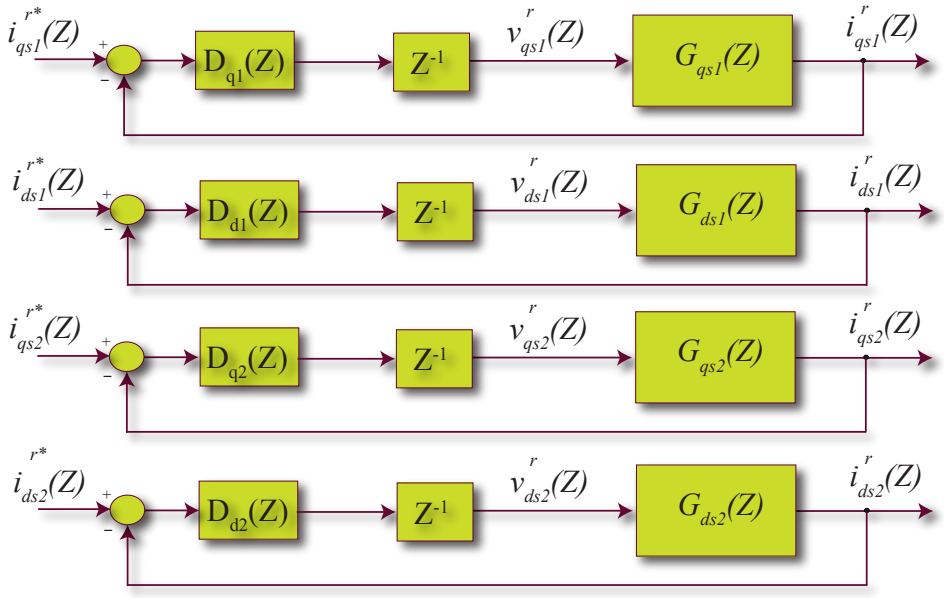

Figure 5.8: The discrete models for designing the $D_x(z)$ controllers for $i^r_{ds1}, i^r_{qs1}, i^r_{ds2}$ and i^r_{qs2}.

approximation of the Laplace transform is [83]:

$$\frac{1}{s} = \frac{Tz}{z-1} \tag{5.57}$$

T is the sampling time of the digital system. Figure 5.9 shows the model of the suggested discrete-time domain PI controller $D_x(z)$. Based on the backward difference approximation of the Laplace transform, $D_x(z)$ is obtained as:

$$\begin{aligned} D_x(z) &= k_{px} + k_{ix} Z\left\{\frac{1}{s}\right\} \\ &k_{px} + k_{ix}\left(\frac{z}{z-1}\right) \\ &= k_{px} + \frac{k_{ix}}{1-z^{-1}} \\ &= \frac{(k_{px}+k_{ix})\left(z - \frac{k_{px}}{k_{px}+k_{ix}}\right)}{z-1} \end{aligned} \tag{5.58}$$

where, k_{px} and k_{ix} are proportional and integral gain respectively, and $x \in \{d_1, q_1, d_2, q_2\}$. The discrete-time domain transfer function for the electrical part of the machine dynamics $G_x(z)$ ($x \in \{d_1, q_1, d_2, q_2\}$) is derived by introducing a zero order hold [82]:

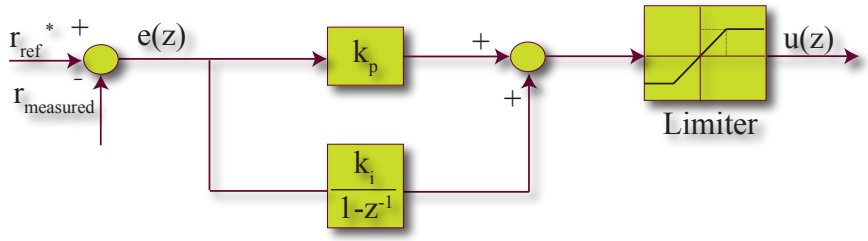

Figure 5.9: Backward difference approximation discrete PI controller.

$$\begin{aligned} G_x(z) &= Z\left\{\left(\frac{1-e^{Ts}}{s}\right)G_x(s)\right\} \\ &= \left(1-e^{-Ts}\right)Z\left\{\frac{G_x(s)}{s}\right\} \\ &= \left(1-z^{-1}\right)Z\left\{\frac{1}{s\left(r_s+sL_x\right)}\right\} \\ &= \frac{\left(1-z^{-1}\right)z\left(1-e^{\frac{-T}{\tau_x}}\right)}{r_s\left(z-1\right)\left(z-e^{\frac{-T}{\tau_x}}\right)} \\ &= \frac{\left(1-e^{\frac{-T}{\tau_x}}\right)}{r_s\left(z-e^{\frac{-T}{\tau_x}}\right)} \\ &= \frac{a_x}{z-b_x} \end{aligned} \tag{5.59}$$

where,

$$G_x(s) = \frac{1}{r_s+sL_x} \tag{5.60}$$

$$\tau_x = \frac{L_x}{r_s}, \quad a_x = \frac{\left(1-e^{\frac{-T}{\tau_x}}\right)}{r_s}, \quad b_x = e^{\frac{-T}{\tau_x}}$$

By assuming one sampling time delay z^{-1} for data conversion and computation as shown in Figure 5.8, the unity gain, negative feedback transfer function of the two planes in the rotating reference frame ($x \in \{d_1, q_1, d_2, q_2\}$) can be expressed as:

$$\frac{i^r_{xs}(z)}{i^{r*}_{xs}(z)} = \frac{D_x(z)G_x(z)z^{-1}}{1+D_x(z)G_x(z)z^{-1}} \tag{5.61}$$

The forward transfer function of the system is

$$\begin{aligned}\frac{i_{xs}^{r}(z)}{i_{xs}^{r*}(z)-i_{xs}^{r}(z)} &= D_x(z)G_x(z)z^{-1} \\ &= \frac{(k_{px}+k_{ix})\left(z-\frac{k_{px}}{k_{px}+k_{ix}}\right)}{z-1}\frac{a_x}{z-b_x}z^{-1} \\ &= \frac{a_x\,(k_{px}+k_{ix})\left(z-\frac{k_{px}}{k_{px}+k_{ix}}\right)}{z\,(z-1)\,(z-b_x)} \\ &= k_s H_x\,(z)\end{aligned} \tag{5.62}$$

where

$$k_s = a_x\,(k_{px}+k_{ix}) \tag{5.63}$$

$$H_x\,(z) = \frac{\left(z-\frac{k_{px}}{k_{px}+k_{ix}}\right)}{z\,(z-1)\,(z-b_x)} \tag{5.64}$$

The pole-zero cancellation approach proposed in [84] is used to obtain the gain of the system (k_x) . In this approach, the complex system pole is cancelled by placing a zero at the same location by:

$$b_x = \frac{k_{px}}{k_{px}+k_{ix}} \tag{5.65}$$

Table 5.2: Practical measurements of the machine parameters.

Machine parameters	Values
r_s	3.037 [Ω]
J	0.001128 [kg/m^2]
B	0.0002178 [Nm s/rad]
L_{d1}	31.9 [mH]
L_{q1}	31.9 [mH]
L_{d2}	24.8 [mH]
L_{q2}	24.8 [mH]
λ_{m1}	108.82 [mWb]
λ_{m2}	3.1 [mWb]
P	8

Suitable software such as MATLAB/SIMULINK can be utilized for plotting the discrete root locus based on the listed parameters of the machine in Table 5.2. Since the machine under consideration is a surface mounted PM synchronous motor, the

d-axis inductance approximately equals the q-axis inductance in each plane. As a result, only one discrete root locus is enough to calculate the parameters of the PI controller for each plane. For a given system gain k_s and machine parameters, the proportional and integral gains for each PI controller are obtained as:

$$k_{px} = \frac{k_s}{a_x} b_x \tag{5.66}$$

$$k_{ix} = \frac{k_s}{a_x} (1 - b_x) \tag{5.67}$$

The root locus and the selected closed-loop poles for the rotor i^r_{ds1} and i^r_{qs1} axes

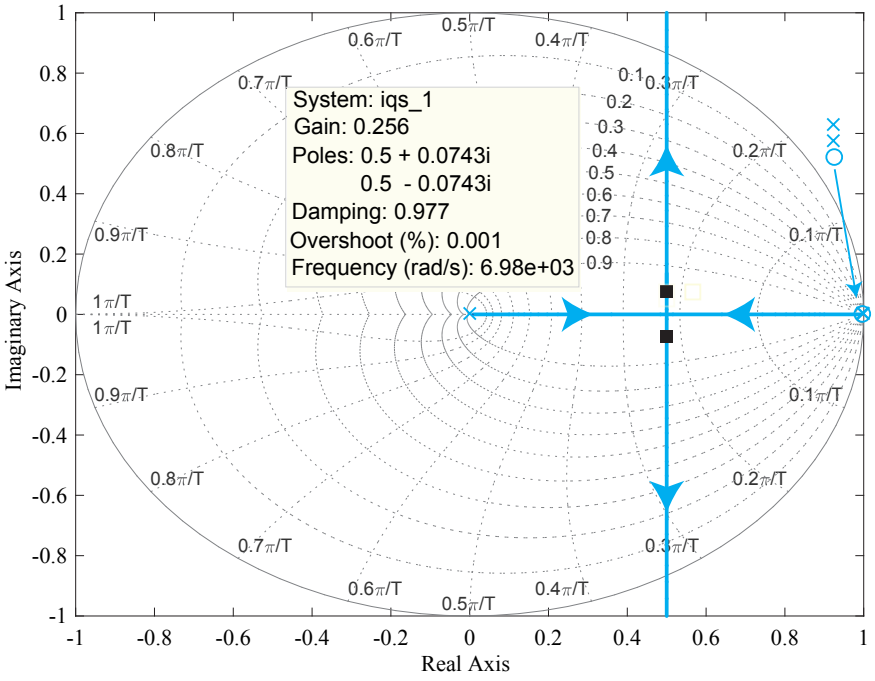

Figure 5.10: The discrete root locus of the negative feedback loop of the rotor i^r_{ds1} and i^r_{qs1} axes currents.

currents are shows in Figure 5.10, while the root locus and the selected closed-loop poles for the rotor i^r_{ds2} and i^r_{qs2} axes currents are shown in Figure 5.11. The natural frequency (ω_n) of the rotor i^r_{ds1} and i^r_{qs1} axes currents is 6980 rad/sec, which gives the bandwidth of the current controller as 1111 Hz, which is about 0.11 times the sampling frequency of the system (10 kHz). Nevertheless, ω_n of the rotor i^r_{ds2} and i^r_{qs2} axes currents is 7040 rad/sec, which gives the bandwidth of the current controller as 1121 Hz, which is about 0.1121 times the sampling frequency of the system. The resulting proportional and integral gains of the machine electrical dynamics parts

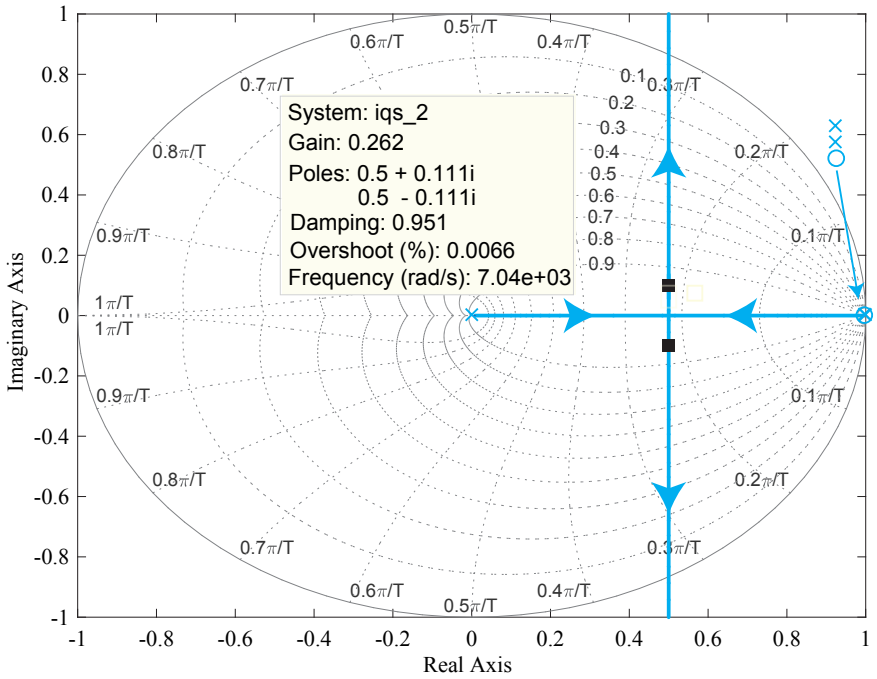

Figure 5.11: The discrete root locus of the negative feedback loop of the rotor i^r_{ds2} and i^r_{qs2} axes currents.

are listed in Table 5.3.

5.4.3 Speed Controller

The speed control of the five-phase PM synchronous motor requires studying and analysis of a cascade feedback control structure, in which the inner-loops are designed to control i^r_{qs1} and i^r_{qs2} currents, while the outer-loop is utilised to control the speed. Since the bandwidth of the inner-loops is designed to be much higher than the outer-loop bandwidth, the dynamics of the inner-loops is neglected by assuming it as a unity gain. The starting point for designing the outer-loop control system is by rearranging equation (5.47) to be:

$$\frac{\mathrm{d}\,\omega_m(t)}{\mathrm{d}t} = \frac{1}{J}\left(T_e(t) - B\,\omega_m(t) - T_l\right) \tag{5.68}$$

but

$$\omega_m = \frac{2}{P}\,\omega_e \tag{5.69}$$

Table 5.3: Proportional and integral gains of the machine electrical dynamics controllers.

paramters	values
k_{pd1}	88.1879
k_{id1}	0.7774
k_{pq1}	88.1879
k_{iq1}	0.7774
k_{pd2}	85.8008
k_{id2}	0.7956
k_{pq2}	85.8008
k_{iq2}	0.7956
$k_{p\omega}$	0.1770
$k_{i\omega}$	3.4176×10^{-6}

hence

$$\begin{aligned} \frac{\mathrm{d}\ \omega_e(t)}{\mathrm{d}t} &= \frac{(P/2)}{J}\left(T_e(t) - \frac{B}{(P/2)}\omega_e(t) - T_l\right) \\ \frac{\mathrm{d}\ \omega_e(t)}{\mathrm{d}t} + \frac{B}{J}\,\omega_e &= \frac{(P/2)}{J}\left(T_e\left(t\right) - T_l\right) \\ s\,\Omega_e + \frac{B}{J}\,\Omega_e\left(s\right) &= \frac{(P/2)}{J}\left(T_e\left(s\right) - T_l\right) \\ \frac{\Omega_e\left(s\right)}{T_e\left(s\right) - T_l} &= \frac{(P/2)}{Js + B} \end{aligned} \tag{5.70}$$

The load torque is regarded as a disturbance. The outer-loop controller should contain an integrator to entirely reject the disturbance caused by the load torque. The structure of the speed control system is shown in Figure 5.12. By using the same steps which are used in deriving the current controllers, the discrete PI speed controller $D_\omega(z)$ is derived in equation (5.71).

$$\begin{aligned} D_\omega\left(z\right) &= k_{p\omega} + \frac{k_{i\omega}}{1 - z^{-1}} \\ &= \frac{\left(k_{p\omega} + k_{i\omega}\right)\left(z - \frac{k_{p\omega}}{k_{p\omega}+k_{i\omega}}\right)}{z - 1} \end{aligned} \tag{5.71}$$

where, $k_{p\omega}$ and $k_{i\omega}$ are proportional and integral gains of the speed controller respectively. The discrete transfer function of the machine's mechanical dynamics part is

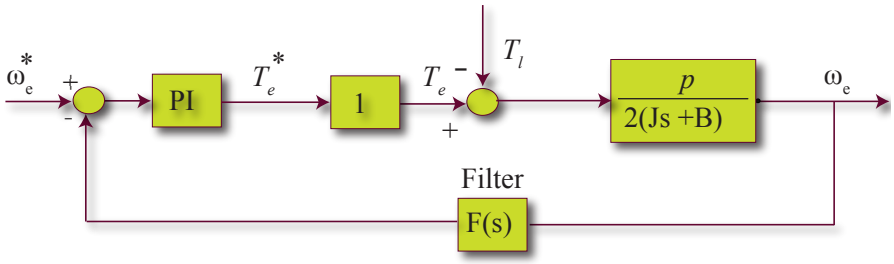

(a) Analogue feedback control system.

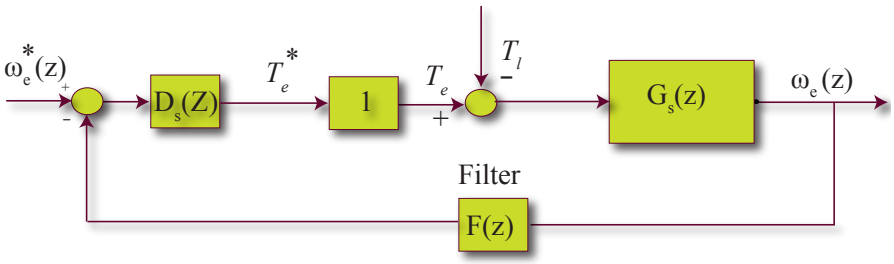

(b) Discrete feedback control system.

Figure 5.12: Feedback control system for the speed controller design.

derived as:

$$\begin{aligned} G_\omega(z) &= Z\left\{\left(\frac{1-e^{Ts}}{s}\right)G_\omega(s)\right\} \\ &= \left(1-e^{-Ts}\right)Z\left\{\frac{G_\omega(s)}{s}\right\} \\ &= \left(1-z^{-1}\right)Z\left\{\frac{p_p}{s\left(Js+B\right)}\right\} \\ &= \frac{p\left(1-z^{-1}\right)z\left(1-e^{\frac{-T}{\tau_\omega}}\right)}{B\left(z-1\right)\left(z-e^{\frac{-T}{\tau_\omega}}\right)} \\ &= \frac{p_p\left(1-e^{\frac{-T}{\tau_\omega}}\right)}{B\left(z-e^{\frac{-T}{\tau_\omega}}\right)} \\ &= \frac{a_\omega}{z-b_\omega} \end{aligned} \tag{5.72}$$

where

$$G_\omega(s) = \frac{p_p}{(Js+B)} \tag{5.73}$$

$$\tau_\omega = \frac{J}{B}, \quad a_\omega = \frac{p_p\left(1 - e^{\frac{-T}{\tau_\omega}}\right)}{B}, \quad b_\omega = e^{\frac{-T}{\tau_\omega}} \tag{5.74}$$

First order low-pass filter $F(s)$ with a cut-off frequency f_c is used to filter speed measurements:

$$F(s) = \frac{\omega_c}{s + \omega_c} \tag{5.75}$$

$$\omega_c = 2\pi f_c \tag{5.76}$$

Using the bilinear transform [82] which is stated in equation (5.77), gives the discrete form of the speed filter $F(z)$ as expressed in equation (5.78):

$$s = \frac{2(z-1)}{T(z+1)} \tag{5.77}$$

$$F(z) = \frac{c_\omega(z+1)}{z - d_\omega} \tag{5.78}$$

where

$$c_\omega = \frac{T\omega_c}{2 + T\omega_c} \tag{5.79}$$

$$d_\omega = \frac{2 - T\omega_c}{2 + T\omega_c} \tag{5.80}$$

The forward transfer function of the speed feedback system is

$$\begin{aligned} \frac{\omega_e(z)}{\omega_e^*(z) - \omega_e(z)} &= D_\omega(Z) + G_\omega(z)F(z) \\ &= \frac{a_\omega c_\omega(k_{p\omega} + k_{i\omega})\left(z - \frac{k_{p\omega}}{k_{p\omega}+k_{i\omega}}\right)(z+1)}{(z-1)(z-b_\omega)(z-d_\omega)} \\ &= k_\omega H_\omega(z) \end{aligned} \tag{5.81}$$

where

$$k_\omega = a_\omega c_\omega(k_{p\omega} + k_{i\omega}) \tag{5.82}$$

$$H_\omega = \frac{\left(z - \frac{k_{p\omega}}{k_{p\omega}+k_{i\omega}}\right)(z+1)}{(z-1)(z-b_\omega)(z-d_\omega)} \tag{5.83}$$

The pole-zero cancellation approach is also used to obtain the gain of the system (k_ω). The system slow pole is cancelled by placing a zero at the same location by:

$$b_\omega = \frac{k_{p\omega}}{k_{p\omega} + k_{i\omega}} \tag{5.84}$$

The discrete root locus is used to design the transient response of the speed feedback system based on the listed parameters of the machine in Table 5.2. For a given system gain k_ω and machine parameters, the proportional and integral gains for the speed PI controller are obtained as:

$$k_{p\omega} = \frac{k_\omega}{a_\omega c_\omega} b_\omega \tag{5.85}$$

$$k_{i\omega} = \frac{k_\omega}{a_\omega c_\omega} (1 - b_\omega) \tag{5.86}$$

The discrete root locus and the selected closed-loop poles for the speed controller are shown in Figure 5.13. The natural frequency (ω_n) of the outer speed loop is 888 rad/sec giving the bandwidth of the speed controller to be 141 Hz, which is about 0.014 times the sampling frequency of the system (10 kHz). Nevertheless, the ratio of the bandwidth of the current controllers of i^r_{qs1} and i^r_{qs2} to the bandwidth of the speed controller is about 7.86 and 7.93 respectively. Hence the dynamics of the inner-loops control of the q_1-axis current and q_2-axis current are ensured to be much faster than the dynamics of the mechanical system. The resulting proportional and integral gains of the machine electrical dynamics parts are listed in Table 5.3.

5.4.4 Symmetric Sampling SPWM

The practical implementation of the motor drive system is entirely covered in the next chapter. However, for accurate modelling and simulation of the implemented drive system, it is necessary to build the exact model of the SPWM in the SIMULINK/-MATLAB software. The modelling of the SPWM requires sampling the reference phase voltage for comparison with the SPWM carrier signals to generate the SPWM duty cycles. The symmetric sampling method is utilized. The sampling frequency of the digitised sample reference is equal to the carrier SPWM frequency, and it is assumed that it is executed at the instant of the positive peak of the SPWM carrier

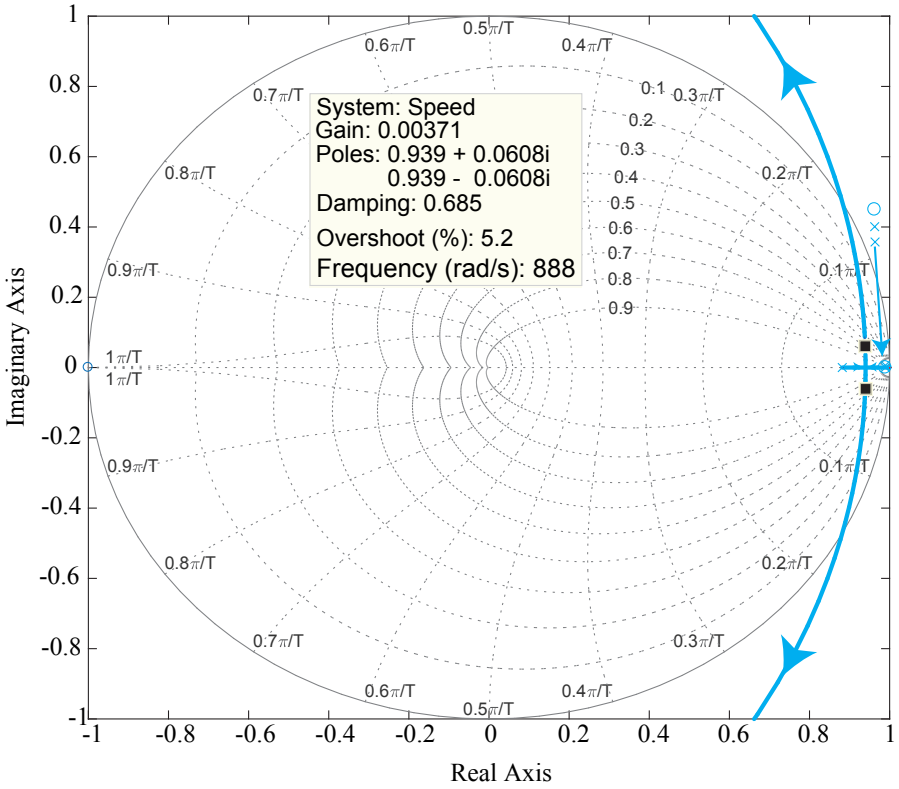

Figure 5.13: The discrete root locus and the selected closed-loop poles for the speed controller.

signal.

The resulting gate pulse from the comparison of the digitised sample reference signal with the carrier SPWM signal is symmetric about the negative peak of the carrier SPWM signal as shown in Figure 5.14. Figure 5.15 presents the SIMULINK model of the symmetric sampling SPWM, while Figure 5.16 shows the result of the comparison of the digitised sample reference signal with the carrier SPWM signal. In PWM converters, the feedback currents contain the sideband harmonics of the switching frequency, which lead to current ripple. Synchronous sampling can be sufficient enough to avoid low-pass filtering before sampling [85].

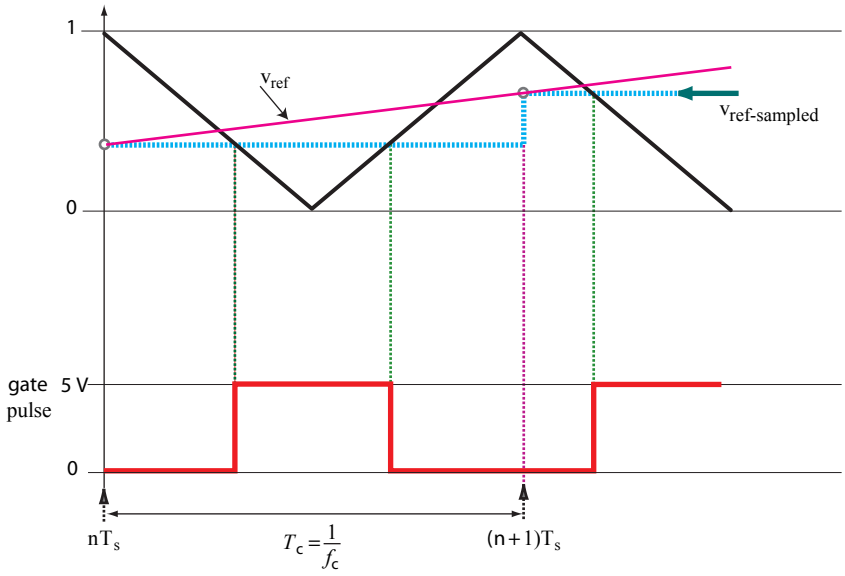

Figure 5.14: Symmetric sampling SPWM at carrier frequency.

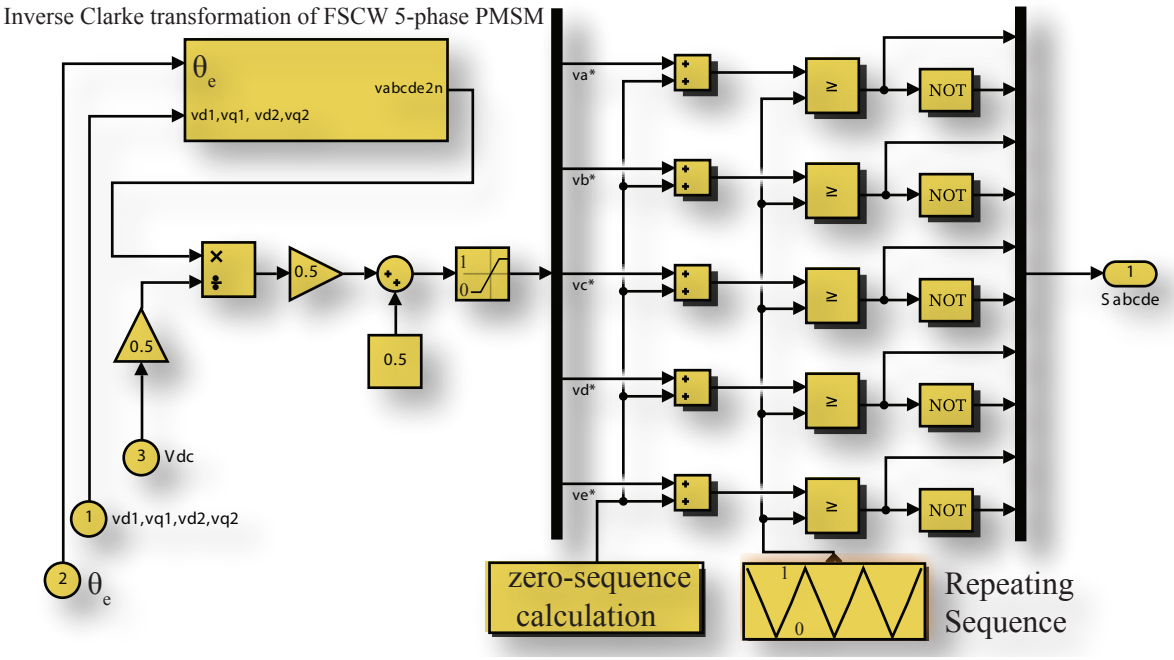

Figure 5.15: SIMULINK Model of the symmetric sampling SPWM.

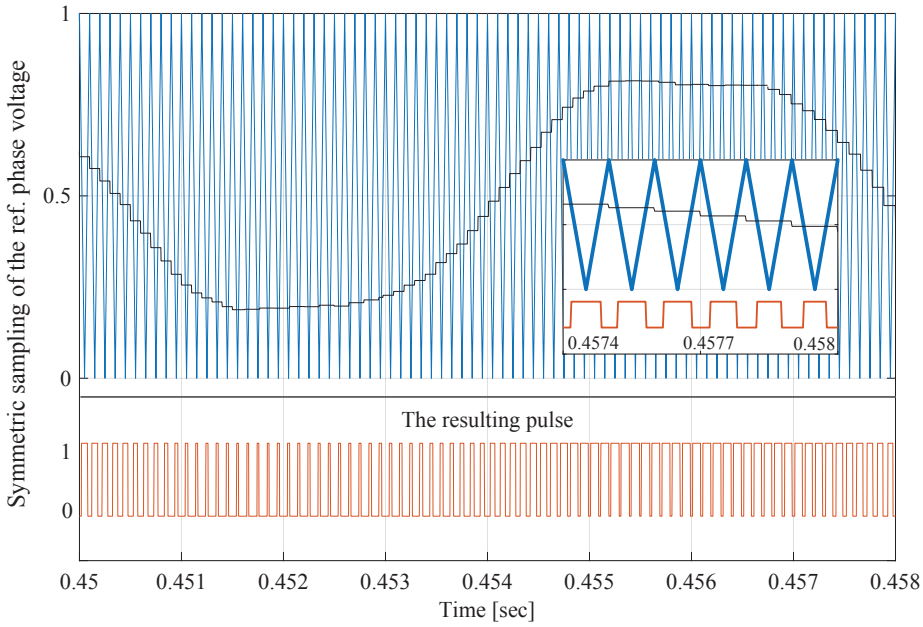

Figure 5.16: Comparison of the digitised sample reference signal with the carrier PWM signal.

5.5 The Dynamic Performance of the Drive System

5.5.1 Simulation

Using the measured parameters of the drive system and the controller design parameters listed in Table 5.2 and Table 5.3 respectively, the entire drive system described in Figure 5.6 was simulated. Both the switching frequency and sampling frequency of the drive system were set to 10 kHz. There are two sampling intervals used in the simulation. One is the sampling interval for the control system (0.0001 sec), and the other is the sampling interval for the IGBT semiconductors (2×10^{-6} sec). Three speeds within the operating range of the drive system in the constant torque region, 500 rpm, 1000 rpm and 2000 rpm, were tested. The load torque T_l was chosen to be zero.

In general, the response was fast, and there was very little overshoot. Figure 5.17 shows the speed response to a step change command in motor speed from standstill to 500 rpm, and from 500 rpm to 2000 rpm, then step down to 1000 rpm. Figure 5.18 shows the speed response through the use of an acceleration and deceleration

ramp. The speed reference rate of change follows the acceleration and deceleration ramp that was defined to avoid sudden reference changes that could cause armature over-current and destabilise the system.

Figures 5.19 through 5.23 show the results at 2000 rpm. Figure 5.19 shows the electromagnetic torque response of the machine for a step load torque of 2 N.m. at t =0.3 sec. There is an overshoot as the electromagnetic torque reaches the load torque. The overshoot of the total electromagnetic torque of the two planes reaches almost 23 % of the commanded value and takes about 20 msec to reach the commanded value, which can be considered acceptable. Figure 5.20 shows the response of the i_{qs1} current while Figure 5.21 shows the response of the i_{qs2} current. Both responses are similar to the electromagnetic torque response of each plane. This result coincides with the torque production of the SPM machine in which the electromagnetic torque is proportional to the q_1-axis and q_2-axis currents only as the magnet flux linkage is constant in the rotating reference frame $\left(T_e = \frac{5}{2}\frac{p}{2}\left[\lambda_{m1}\, i^r_{qs1} + 3\lambda_{m2}\, i^r_{qs2}\right]\right)$. Figure 5.22 shows α_1-axis, β_1-axis, α_2-axis, and β_2-axis currents while Figure 5.23 shows i_a, i_b, i_c, i_d and i_e phase currents.

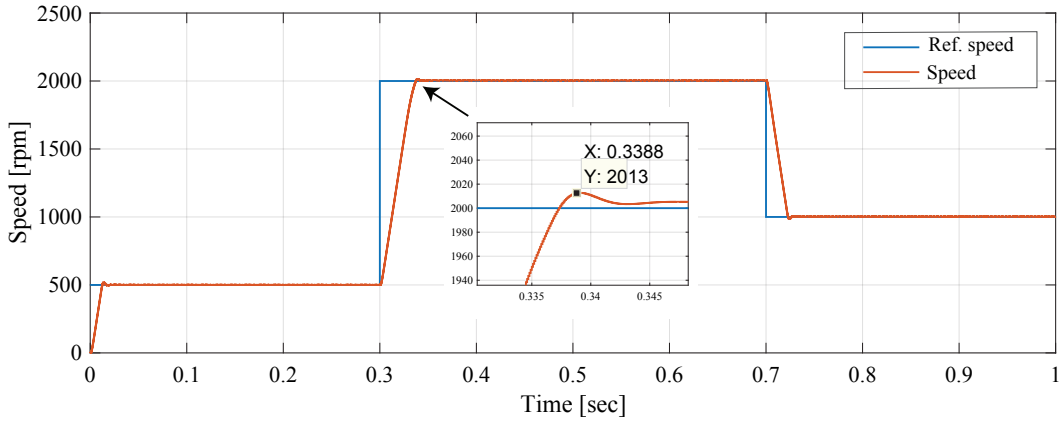

Figure 5.17: Motor speed response for a step change in the speed set-point speed at $t = 0, 0.3$ and 0.7 sec.

5.5.2 Dynamic Test of the Prototype Motor

The field-oriented drive system including the five-phase SPM motor is implemented in the laboratory. Speed information is calculated by direct measurement of the rotor position available through the incremental encoder with a resolution of 500

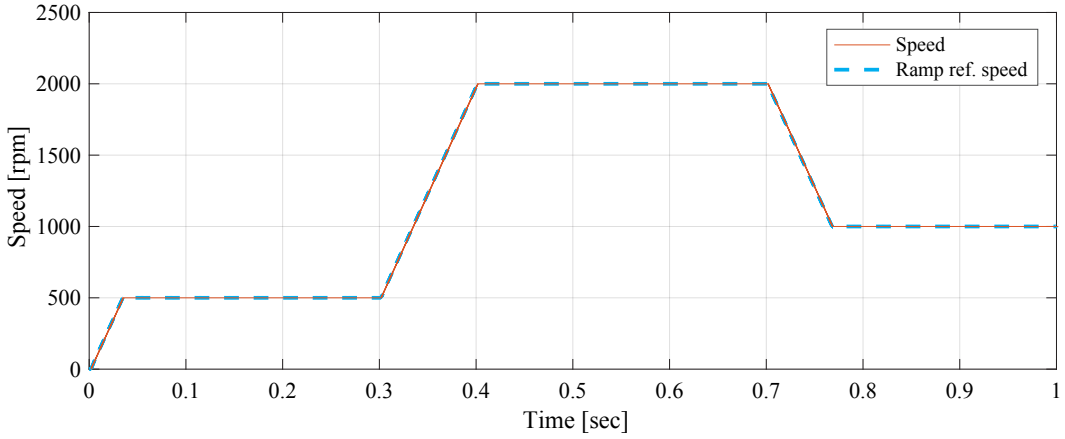

Figure 5.18: Motor speed response for a step change and acceleration/deceleration ramp in the speed set-point at $t = 0, 0.3$ and 0.7 sec.

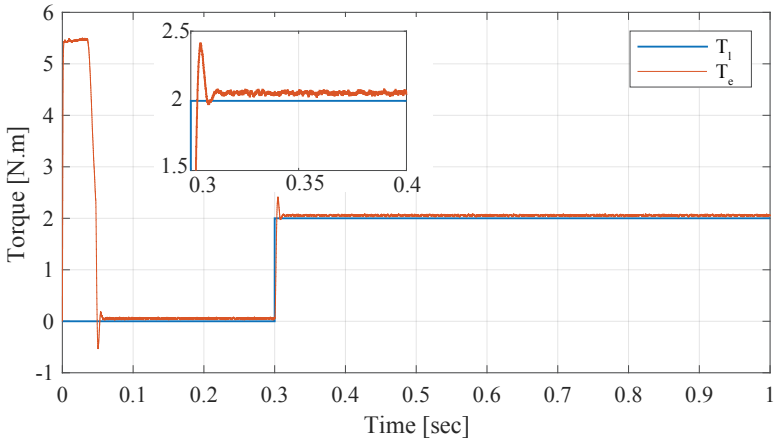

Figure 5.19: The response of the electromagnetic torque at the rated speed (2000 rpm) for a step change in the load torque of 2 N.m. at t =0.3 sec.

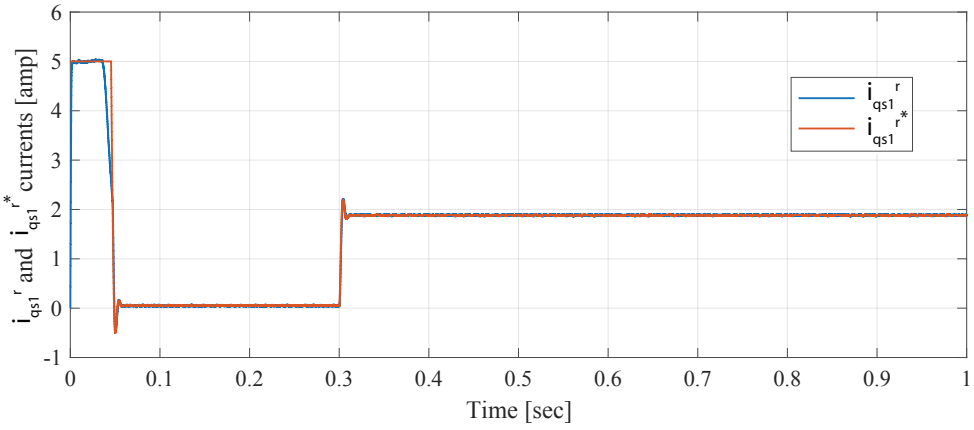

Figure 5.20: The response of the q_1-axis current at the rated speed (2000 rpm) for a step change in the load torque of 2 N.m. at t =0.3 sec.

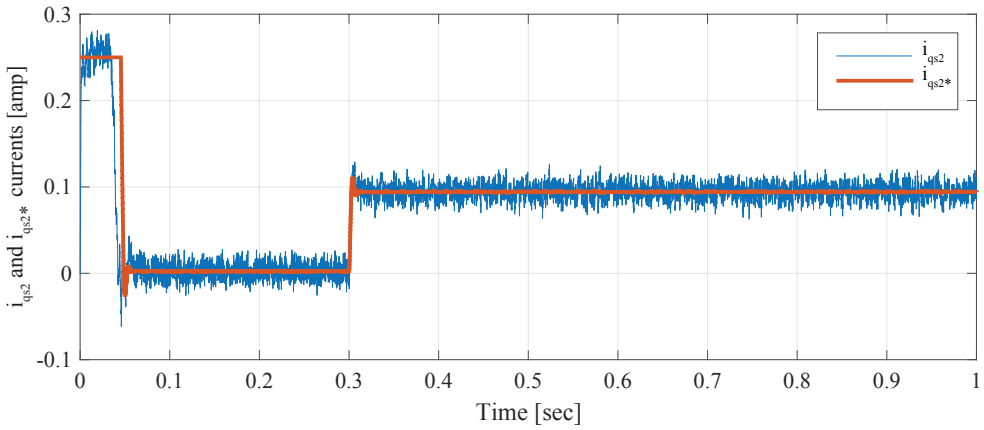

Figure 5.21: The response of the q_2-axis current at the rated speed (2000 rpm) for a step change in load torque of 2 N.m. at t =0.3 sec.

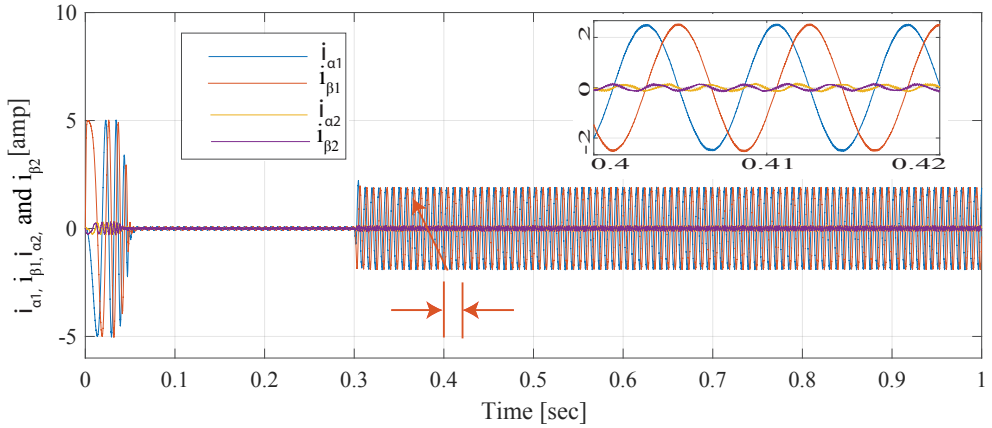

Figure 5.22: The response of the α_1-axis, β_1-axis, α_2-axis, and β_2-axis currents at the rated speed (2000 rpm) for a step change in load torque of 2 N.m. at t =0.3 sec.

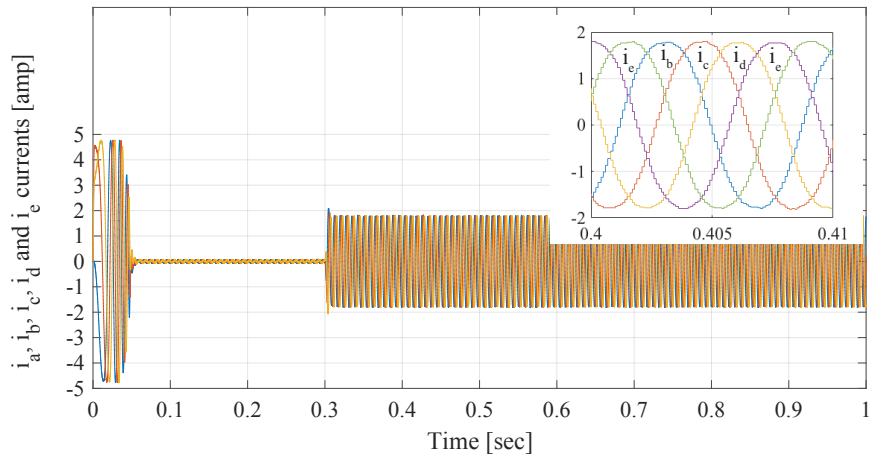

Figure 5.23: The response of the i_a, i_b, i_c, i_d and i_e phase currents at the rated speed of 2000 rpm for a step load torque of 2 N.m. at t =0.3 sec.

pulses per revolution (PPR). The laboratory tests show the performance of the drive at 50% of the rated speed. The speed response is shown in Figure 5.24. The overshoot in the measured speed is about 7% while the designed value is 5.2 %. This small deviation of the overshoot in the speed measurement is expected, because the various delay times in the control system were estimated.

Figures 5.25, 5.26, 5.27 and 5.28 show the current response of q_1-axis, d_1-axis, q_2-axis and d_2-axis respectively. The high noise in the system is caused by the quantisation error of the incremental encoder which depends on the number of encoder pulses per revolution (500 PPR) and the observation time window (0.1 msec). Figure 5.30 shows the response of i_a, i_b, i_c, i_d and i_e phase currents. Although the contribution of the third harmonic current is insignificant, ($i_{qs2} = 0.08\ i_{qs1}$), its impact on the shape of the current waveforms is obvious. Figure 5.31 the motor phase currents when the third harmonic is not injected. The currents are almost sinusoidal while the motor was running very smoothly.

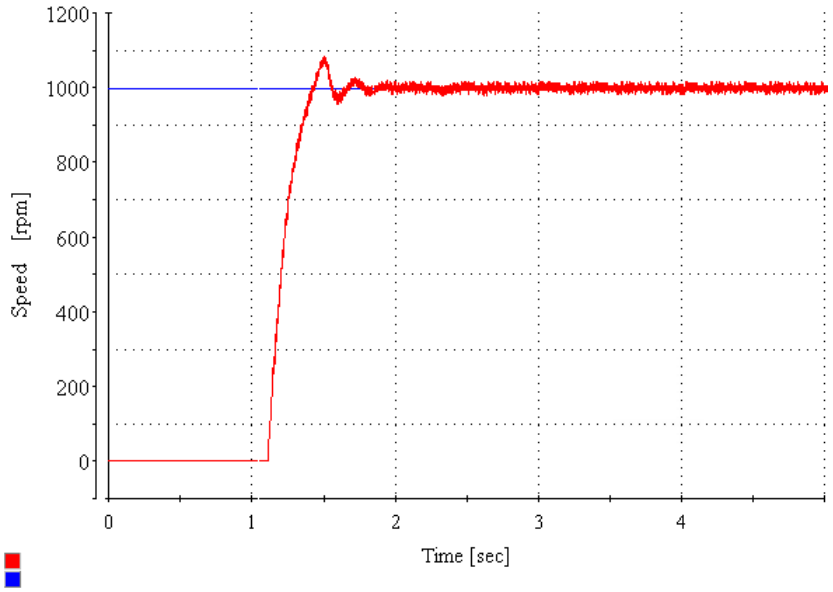

Figure 5.24: The speed response of the prototype motor for a step change in the speed set-point speed at $t = 1.15$ sec.

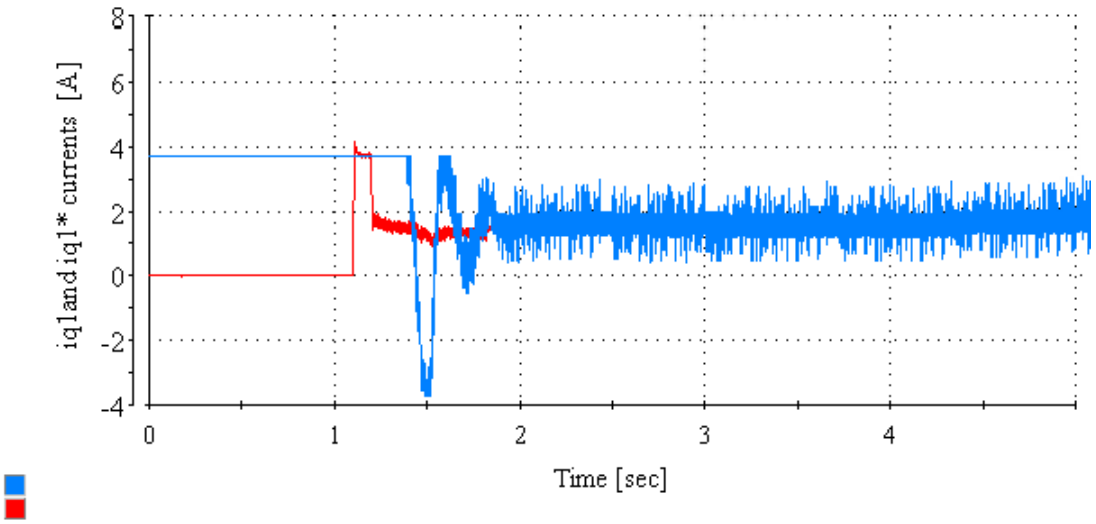

Figure 5.25: The q_1-axis current response of the prototype motor.

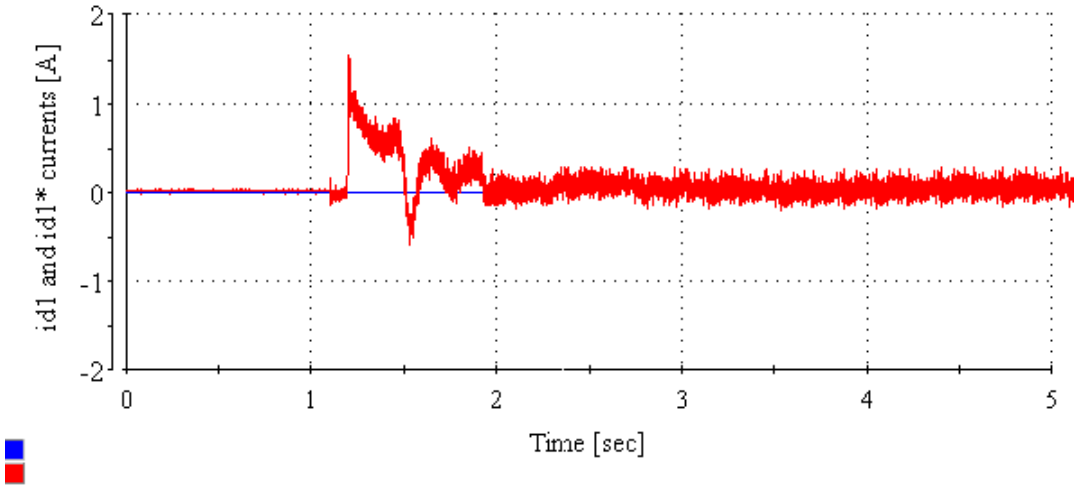

Figure 5.26: The d_1-axis current response of the prototype motor.

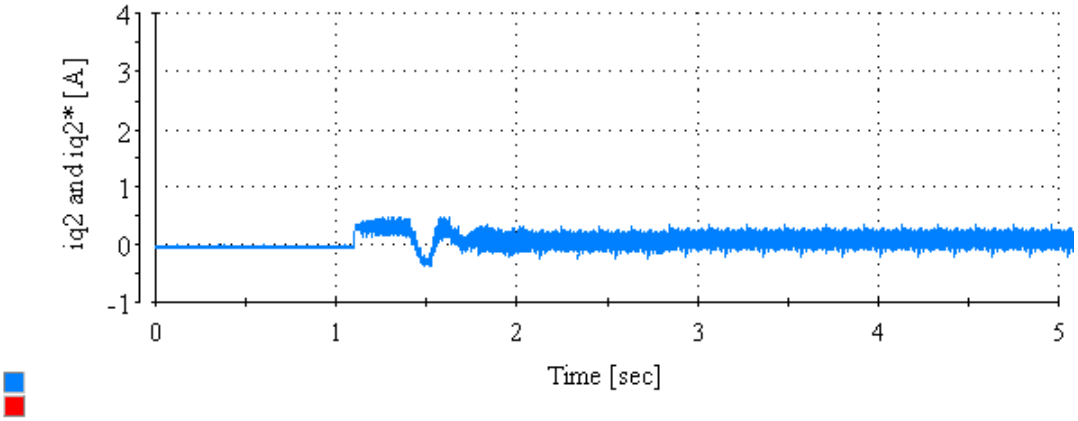

Figure 5.27: The q_2-axis current response of the prototype motor.

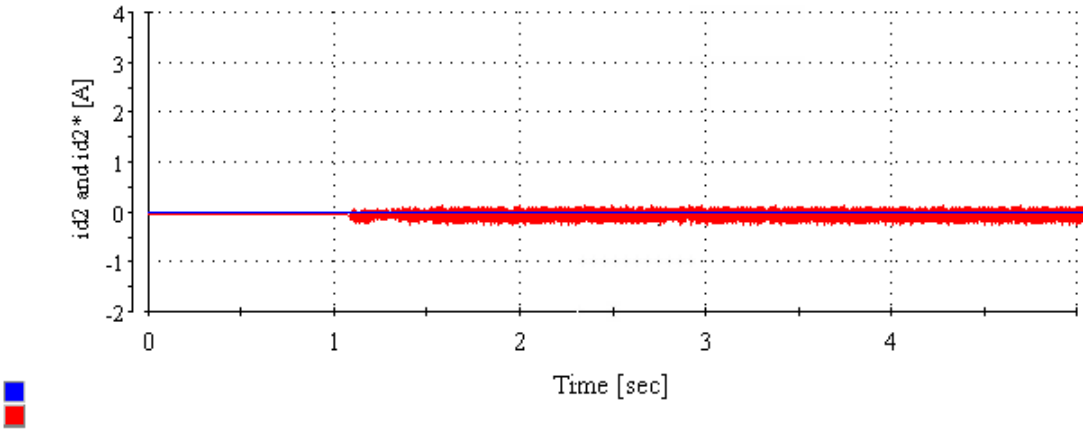

Figure 5.28: The d_2-axis current response of the prototype motor.

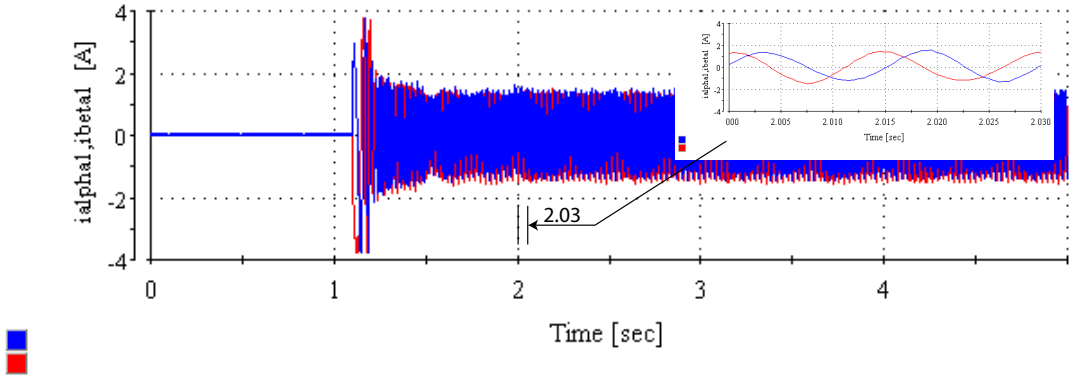

Figure 5.29: The α_1-axis and β_1-axis currents response of the prototype motor.

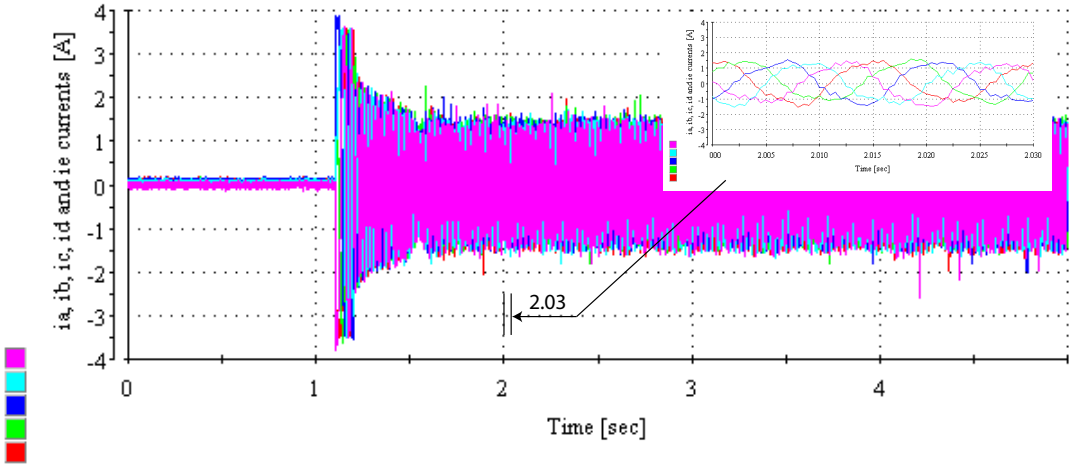

Figure 5.30: The response of the i_a, i_b, i_c, i_d and i_e phase currents of the prototype motor.

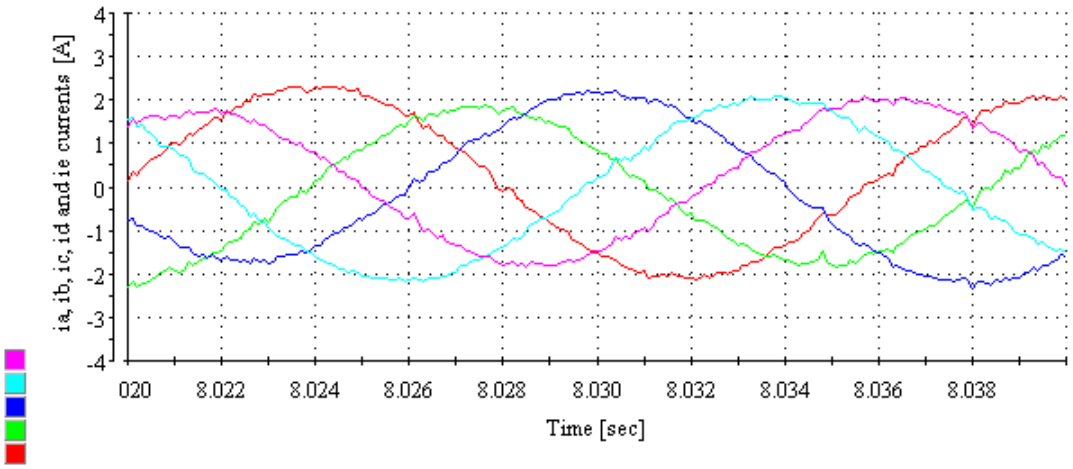

Figure 5.31: Steady state phase currents of the prototype motor when the third harmonic is not injected.

Chapter 6

Flux Weakening Theoretical Limitation for Five-Phase SPM Drive

This chapter aims to explore the effect of varying the motor drive parameters on the optimum flux-weakening performance of the Multi-Frequency (MF) five-phase surface mount permanent magnet synchronous motor drive (MF five-phase SPM). A lossless, steady-state per-unit, DQ model is presented. The flux-weakening performance of the Single Frequency (SF) five-phase surface mount permanent magnet synchronous motor (SF five-phase SPM) is considered first because it represents a simplified case of the MF five-phase SPM drive and gives an insight into the operation of the MF five-phase SPM motor drive. Only the fundamental and the third harmonics are assumed to be in the spectrum of the back electromotive force (EMF) and are considered as the torque producing terms in the first plane and the second plane, respectively. A new DQ normalisation for an MF five-phase SPM drive, based on the rated quantities of the first DQ plane, is developed to be used in the optimisation process necessary for studying the effect of varying the motor parameters on the flux weakening performance. The non-linear optimisation problem that aims to maximise the electromagnetic torque of the MF five-phase SPM machine under the voltage and current constraints, for operation in the linear modulation region, is formulated.

6.1 Introduction

The five-phase surface mounted permanent magnet brushless AC motor (SPM) can be classified based on the torque producing harmonics of the back-emf as a Single Frequency SPM motor (SF-SPM) and a multi-frequency SPM motor (MF-SPM). The SF-SPM has distributed windings (near sinusoidal mmf distribution), while the MF-SPM has concentrated windings. Both machine types are equipped with a non-salient iron rotor with magnets. These magnets can either be glued in position or held in place by an enclosing can or binding. Ideally, the SF-SPM has a pure sinusoidal back-emf such that the electromagnetic torque is produced through the interaction of the armature current and the fundamental harmonic of the back-emf. To control such a machine, it is necessary to set the current references of the second plane equal to zero and use the rotating transformation in the first plane only. Examining the model of the MF five-phase PM synchronous motor with $i^r_{ds2} = i^r_{qs2} = \lambda_{m2} = 0$ leads to the machine model, exactly, the same as the well-known model of the three-phase PM synchronous motor. However, the MF five-phase SPM behaves as a two DQ-circuit machine in which the fundamental harmonic of the back-emf is the main harmonic of the first plane, while the third harmonic of the back-emf is the main harmonic of the second plane.

In the classical variable speed drive system, the three-phase PM synchronous motor runs in two modes of operations: constant torque below the base speed and constant power above the base speed, as shown in Figure 6.1. The base speed is defined as the maximum speed at which rated torque can be developed with rated current flowing without exceeding the maximum terminal voltage available from the inverter.

Developing flux-weakening control techniques for three phase PM synchronous machines has been one of the central areas of research for many decades [86–93]. In [57] a lossless per-phase DQ model is described to determine the effects of varying the machine parameters on the power capability of three-phase salient pole permanent magnet motors in variable speed drives. The analysis is based on the normalisation of the drive parameters with the inverter kVA. The normalisation model of the DQ equations of the three-phase PM synchronous motor to per unit rated speed was utilised in [90, 94] to examine the field-weakening performance of the finite speed

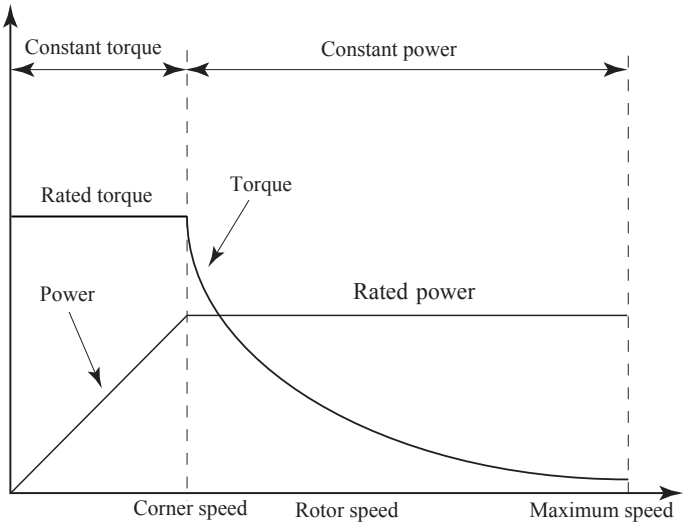

Figure 6.1: Mode of operations of PM synchronous motors.

drive SPM. In [91] the authors provide an in-depth analysis of the field-weakening performance of the the theoretically infinite speed SPM drive by using the unity speed, per-phase DQ model. The authors have classified the drive as either finite or infinite drive based on the calculated torque versus speed characteristic.

Moreover, three-phase PM synchronous motors are designed to meet a given requirement of power, torque and speed such that the back-emf at rated speed allows rated current to be drawn to develop the required rated torque. Thus once the machine reaches rated speed, it is impossible to further increase the speed of the motor unless weakening the flux or field of the magnets, as the back-emf, which is speed dependent, will prevent any further increase of stator current, and hence a reduction of output torque condition. Above base speed maintaining constant power requires satisfying the optimal flux weakening condition, which can be defined as the equality of the rated current and the characteristic current of a machine, while the characteristic current is the ratio of the magnet flux linkage to the d-axis inductance.

Design and control of a multi-phase SPM machine, particularly, an MF five-phase SPM machine for a wide speed range requires studying and analysing the effect of varying each independent variable on the performance of the motor drive system. Based on a literature review up to 2018, no analytical derivation exists for the torque-speed characteristic of the MF-SPM motor drive. The reasons are detailed as follows:

1. For a three-phase SPM motor drive there are four parameters; magnet flux (λ_m), synchronous inductance (L_s), maximum available voltage and current per phase (V_{max} and I_{max}). Using a per-unit model assuming unity base speed, such that the rated voltage and current of the machine is equal to the maximum voltage and current of the inverter leads to only one independent variable. However, The MF five-phase SPM motor drive has six parameters; fundamental magnet flux λ_{m1}, third harmonic magnet flux λ_{m2}, first plane inductance L_{s1}, second plane inductance L_{s2}, inverter voltage constraint and inverter current constraint. The per-unit, DQ model based on the first plane can reduce the number of independent parameters to three, but the problem is still difficult to solve analytically.

2. The operation of the MF-SPM machine as a part of a variable speed drive in the linear modulation region requires the modulation indices of all planes to satisfy specific relations, as addressed in detail in [95]. These relations force the reference voltages of the two planes to obey two non-linear constraints, which is difficult to adopt in an analytical solution.

In contrast to three-phase machines, multi-phase permanent magnet synchronous machines are regarded as a new area for research, particularly in the flux-weakening mode of operation. Because there is no analytical solution due to the high number of the independent parameters and the non-linear constraints, an optimisation problem is necessary to be adopted [96–98]. The first attempt to analyse the maximum torque and power of a five-phase SPM in a wide speed range is presented in [98] and [99]. The authors introduced a per phase natural variable model to find the torque versus speed and power versus speed characteristics for unity magnet flux linkage. Although the model is considered as the first serious attempt to analyse the performance of the MF five-phase SPM machine, it is based on a particular case, as it does not examine the effect of different normalised values of the magnet flux linkage nor the performance characteristics of the infinite speed drive system.

In recent years two questions have been raised regarding the control and design of MF multi-phase SPM machines. Firstly, how to control a MF multi-phase SPM machine in the flux-weakening region such that the machine is capable of producing the maximum electromagnetic torque for the whole speed range? For speeds below the rated or base speed the demagnetising currents (i^r_{ds1} and i^r_{ds2}) in both planes are

equal to zero to ensure that the MF multi-phase SPM machine is operating under the maximum torque per ampere (MTPA) or torque angle control strategy. But for higher speeds, there is no such study or general analysis to cover a broad spectrum of the available machine parameters. Secondly, how to design a MF multi-phase SPM machine to be capable of producing an acceptable electromagnetic torque for a wide speed range? For a three-phase SPM machine it is well known that the condition for optimal flux-weakening occurs when the machine characteristic current equals the rated current [100]. The characteristic current of a three-phase surface PM machine, is defined as:

$$I_{ch} = \frac{\lambda_m}{L_d} \qquad \text{[Amps]} \tag{6.1}$$

where λ_m is the rms magnet flux linkage and L_d is the d-axis inductance. However, regarding MF-SPM machines there is ambiguity about the condition of optimal flux weakening condition due to the new parameters of the second plane and the constraints of the voltage source inverter.

The main purpose of this chapter is to develop an understanding of the behaviour of the MF five-phase SPM currents, torque, and power under the condition of maximum torque per ampere for the whole speed range. Therefore, this study makes a major contribution to research on the control and design of MF five-phase SPM machines by demonstrating the effect of varying the machine parameters on the flux-weakening mode of operation. Also, this study can be extended in the future to include interior permanent magnet synchronous machines.

6.2 Voltage and Current Constraints of MF-SPM

To understand the limits of the high-speed operation in MF-SPM machines, it is useful to commence the discussion by considering the impact of the voltage and current constraints. For a single-frequency drive five-phase SPM machine, the maximum phase voltage, $V_{s\max}$, is set by the dc link voltage, V_{dc} of a PWM inverter and the PWM method. If the carrier-based pulse width modulation method (SPWM) is used, $V_{s\max}$ obtained in the linear control range is $V_{dc}/2$. If the inverter is controlled in the ten-step mode of operation, $V_{s\max}$, can be increased up to $2V_{dc}/\pi$. However, in this mode of operation, current ripple and torque ripple are much larger than

those in SPWM mode of operation.

It is worth mentioning that the current ripple and torque ripple of a five-phase permeant magnet synchronous machine operated in the ten-step mode of operation are lower than the same ripple generated in a three-phase permanent magnet synchronous machine operated in the six-step mode of operation. This is because increasing the number of phases leads to an increase in the frequency of the torque ripple, with a corresponding decrease of the ripple magnitude at the same time [101]. The maximum phase current of a PM synchronous machine, $I_{s\max}$, is usually set by the thermal limit of the inverter or the PM synchronous machine itself. If the constraint is set by the limitations of the PM synchronous machine, then the limiting condition of the current is set by the heat dissipation from the iron and copper losses.

However, for a MF five-phase SPM the determination of the maximum voltage for each plane is not easy to decide since the line voltages are, in general, unrelated and of arbitrary frequencies, magnitudes, and phase shifts [95]. Authors in [95] have determined the linear operation region for a MF five-phase, two-level voltage source inverter (VSI) by assuming the voltages in both planes reach the peak value at the same instant, which represents the worse case. Equation (6.3) gives the constraints that have to be satisfied if PWM operation is to remain in the linear modulation region. These two equations define an area when plotted in a coordinate system with modulation indices M_1 and M_2 as axes, The modulation index M_i is defined as:

$$M_i = \frac{V_b}{0.5V_{dc}} \tag{6.2}$$

where V_b is the phase voltage fundamental peak value and V_{dc} is the dc-bus voltage. Graphical illustration of (6.3) is shown in Figure 6.2. Any operating point (i.e., any combination of the two modulation indices) within the shaded area is available in the linear modulation region. Fortunately, this assumption is completely valid for a surface mounted SPM machine if the rotating transformation is chosen such that the back-emf of both planes are in the same direction. Figure 6.2 shows that:

1. When M_2 is zero the machine operates as a SF-SPM machine ($d_1 - q_1$ plane) with a modulation index range (0-1.0515).

2. When M_1 is zero the machine operates as a SF-SPM machine ($d_2 - q_2$ plane)

with a modulation index range (0-1.0515).

3. When M_1 and M_2 are non-zero, the dc voltage utilisation will be the summation of the two modulation indexes based on their operating point in the shaded area.

4. The maximum dc voltage utilisation occurs when both modulations indices are equal ($M_1 = M_2 = 0.6498$) which is equivalent to 1.2996.

$$\left.\begin{array}{l} \frac{M_1}{A} + \frac{M_2}{B} \leq 1 \\ \frac{M_1}{B} + \frac{M_2}{A} \leq 1 \end{array}\right\} \text{where} \begin{cases} A = \frac{1}{\cos\left(\frac{3\pi}{10}\right)} = 1.7013 \\ B = \frac{1}{\left(\frac{\pi}{10}\right)} = 1.0515 \end{cases} \tag{6.3}$$

Based on (6.3) the authors in [102] have determined the reference voltage vector limit of the MF five-phase PM synchronous motor fed by a two-level five-phase voltage source inverter (VSI) as:

$$\left.\begin{array}{l} \frac{\sqrt{v_{qs1}^{r2}+v_{ds1}^{r2}}}{A} + \frac{\sqrt{v_{qs2}^{r2}+v_{ds2}^{r2}}}{B} \leq \frac{V_{dc}}{2} \\ \frac{\sqrt{v_{qs1}^{r2}+v_{ds1}^{r2}}}{B} + \frac{\sqrt{v_{qs2}^{r2}+v_{ds2}^{r2}}}{A} \leq \frac{V_{dc}}{2} \end{array}\right\} \text{where} \begin{cases} A = \frac{1}{\cos\left(\frac{3\pi}{10}\right)} = 1.7013 \\ B = \frac{1}{\left(\frac{\pi}{10}\right)} = 1.0515 \end{cases} \tag{6.4}$$

$$\left.\begin{array}{l} \frac{V_{1s}}{A} + \frac{V_{2s}}{B} \leq \frac{V_{dc}}{2} \\ \frac{V_{1s}}{B} + \frac{V_{2s}}{A} \leq \frac{V_{dc}}{2} \end{array}\right\} \text{where} \begin{cases} V_{1s} = \sqrt{v_{qs1}^{r2} + v_{ds1}^{r2}} \\ V_{2s} = \sqrt{v_{qs2}^{r2} + v_{ds2}^{r2}} \end{cases} \tag{6.5}$$

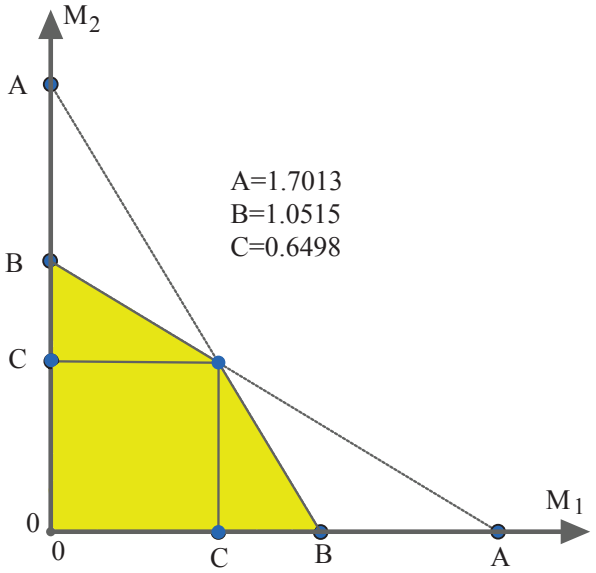

Figure 6.2: linear modulation region.

6.3 Machine Model and Hypothesis

In arriving at a mathematical model of the star-connected MF five-phase SPM machine the following simplifying assumptions were made:

- The rotor saliency is neglected. This is a standard assumption for surface mounted PM machines, and suggests $L_{d1} = L_{q1} = L_{s1}$ and $L_{d2} = L_{q2} = L_{s2}$.
- The B-H curve of the iron core is linear, and so the main flux saturation can be neglected. This standard assumption implies that the inductances L_{s1} and L_{s2} are constant and there is no mutual inductance between the $d-q$ axes of the same plane or between the axes of different planes [103]. Also, authors in [98,99,104] revealed that the machine under the above assumption, behaves as two two-phase virtual machines that are magnetically independent but electrically and mechanically coupled. The virtual machine in which the torque producing harmonic is the fundamental is called the Main Machine (MM), whereas the virtual machine in which the torque producing harmonic is the third harmonic is called the Secondary Machine (SM).
- The machine model is a lossless model such that the input power is equal to the output power, and iron core losses and winding resistance are neglected.
- The space harmonics are the fundamental and the third harmonics only.
- The back-emf harmonics are assumed to be the fundamental and the third harmonics only.
- The fundamental harmonic of the back-emf is the main harmonic of the $d_1 - q_1$ plane.
- The third harmonic of the back-emf is the main harmonic of the $d_2 - q_2$ plane.
- The d-axis of the main virtual machine and the d-axis of the secondary virtual machine are always superimposed and in the same direction. For a star-connected MF five-phase SPM machine the d-axes of the two virtual machines are always superimposed because of the mechanical coupling between the two virtual machines [98, 99]. The d-axes of the two virtual machines are not necessarily in the same direction. In the following sections, it is assumed that the correct choice of the rotating transformation ensures that the back-emf of the two planes are in the same direction.

Equation (6.6) represents the model of the MF five-phase SPM drive under the above assumptions [102] . Here $v^r_{ds1}, v^r_{qs1}, i^r_{ds1}$ and i^r_{qs1} are the d_1- and q_1-axis components of the main virtual machine voltage and current respectively, while $v^r_{ds2}, v^r_{qs2}, i^r_{ds2}$ and i^r_{qs2} are the d_2- and q_2-axis components of the secondary virtual machine voltage and current respectively.

$$\left\{\begin{array}{l} v^r_{ds1} = -\omega_e\, L_{s1}\, i^r_{qs1} \\ v^r_{qs1} = \omega_e\, L_{s1}\, i^r_{ds1} + \omega_e\, \lambda_{m1} \\ v^r_{ds2} = -3\,\omega_e\, L_{s2}\, i^r_{qs2} \\ v^r_{qs2} = 3\,\omega_e\, L_{s2}\, i^r_{ds2} + 3\,\omega_e\, \lambda_{m2} \\ T_e = \dfrac{5}{2}\dfrac{P}{2}\left[\lambda_{m1}\, i^r_{qs1} + 3\lambda_{m2}\, i^r_{qs2}\right] \end{array}\right\} \tag{6.6}$$

where

$$\left\{\begin{array}{l} \dfrac{V_{1s}}{A} + \dfrac{V_{2s}}{B} \leq \dfrac{V_{dc}}{2} \\ \dfrac{V_{1s}}{B} + \dfrac{V_{2s}}{A} \leq \dfrac{V_{dc}}{2} \\ I^2_{1s} + I^2_{2s} \leq I^2 \\ I_{1s} = \sqrt{i^{r2}_{qs1} + i^{r2}_{ds1}} \\ I_{2s} = \sqrt{i^{r2}_{qs2} + i^{r2}_{ds2}} \end{array}\right\}$$

The phasor diagram of the MF five-phase SPM motor is shown in Figure 6.3. Figure 6.3a represents the phasor diagram of the main virtual machine, while Figure 6.3b represents the phasor diagram of the secondary virtual machine. In both virtual machines the magnet flux λ_{m1} and λ_{m2} lie along the positive d_1- and d_2-axis and hence the back-emf phasors E_{b1} and E_{b2} are in the same direction, and along the positive q_1- and q_2-axes. The current-angles γ_1 and γ_2 are the angles by which the currents I_{1s} and I_{2s} lead the back-emf phasors E_{b1} and E_{b2}, respectively. The input power factor angles ϕ_1 and ϕ_2 are the angles between the terminal voltages of the two virtual machines V_{1s} and V_{2s} and the phase currents I_{1s} and I_{2s} respectively.

6.4 Per Unit Model

The lossless model of the MF five-phase SPM machine drive (6.6) has six parameters: $L_{s1}, L_{s2}, \lambda_{m1}, \lambda_{m2}, V_{dc}$ and I. Although the analysis in this chapter is accomplished

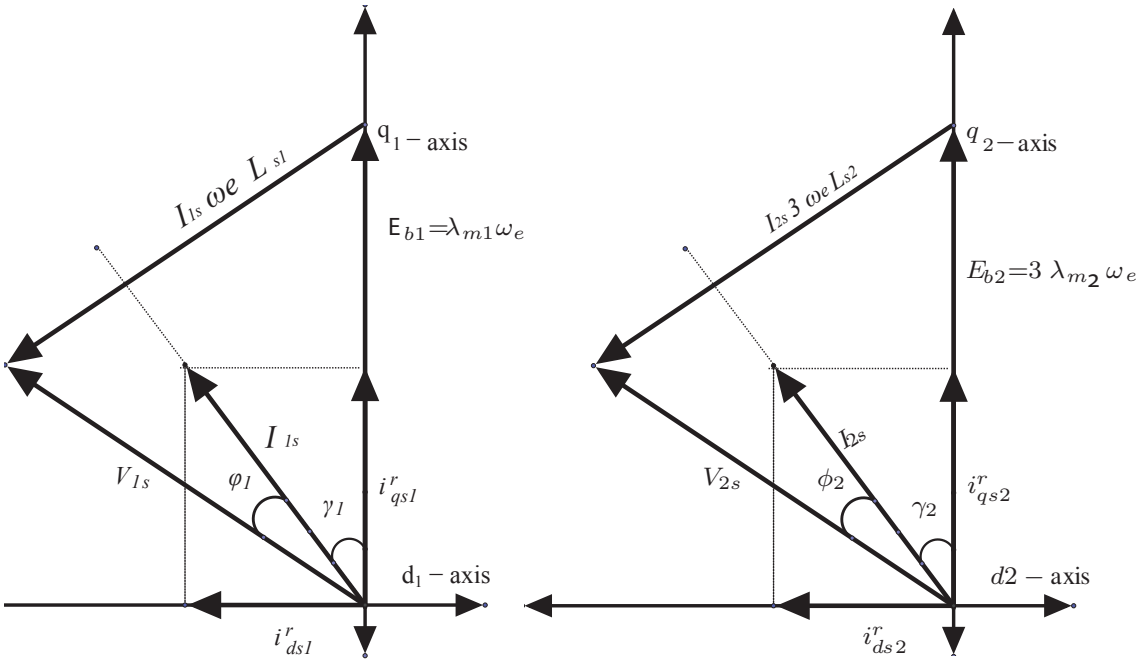

(a) Phasor diagram of the d_1-q_1 plane. (b) Phasor diagram of the d_2-q_2 plane.

Figure 6.3: Phasor diagram of the MF five-phase permanent magnet synchronous motor.

by using a fast optimisation algorithm, reducing the number of the drive parameters makes the analysis of the machine performance in the flux-weakening region simpler. The classical normalisation technique which is presented for three-phase SPM in [57] is adopted for a MF-five phase SPM machine. For the three-phase SPM machine by choosing the base phase voltage V_b and base phase current I_b to be equal to the rated values of the inverter, reduces the number of the independent parameters to only two, that is L_s and λ_m. However, choosing the same base quantities for the main virtual machine of the MF five-phase SPM machine reduces the number of independent parameters to only four, which are $L_{s1}, \lambda_{m1}, L_{s2}$ and λ_{m2}.

Based on the definition of the base speed, the rated voltage can be defined as the available voltage per phase at which the maximum speed can be reached at the rated torque with a rated current flowing. Since the design of a machine, in general, is based on the required torque, power and speed for a given slot/pole combination, choosing a single-frequency phase voltage as a rated voltage to supply the main virtual machine is a natural choice [99].

In the *abcde* natural variables, let the rms value of the rated phase voltage V_b^{ϕ} and the rms value of the rated phase current I_b^{ϕ} of the *main virtual machine* form

the base quantities. The base power is defined assuming unity power factor as:

$$P_b = 5V_b^{\phi} I_b^{\phi} \tag{6.7}$$

Selecting the base quantities in the $d_1 - q_1$ plane denoted by V_b and I_b to be equal to the peak value of the phase voltage and current in *abcde* natural variables results in:

$$P_b = 5V_b^{\phi} I_b^{\phi} = 5\frac{V_b}{\sqrt{2}}\frac{I_b}{\sqrt{2}} = \frac{5}{2}V_b I_b \tag{6.8}$$

The base torque is given as:

$$T_b = \frac{P}{2}\frac{P_b}{\omega_b} = \frac{P}{2}\frac{5}{2}\frac{V_b I_b}{\omega_b} \tag{6.9}$$

where P is the machine pole number. From (6.9) the normalised electromagnetic torque of the $d_1 - q_1$ plane is obtained as:

$$T_{1n} = \frac{T_1}{T_b} = \frac{\lambda_{m1} i_{qs1}^r}{\frac{V_b I_b}{\omega_b}} = \frac{i_{qs1}^r}{I_b}\frac{\lambda_{m1}}{\frac{V_b}{\omega_b}} = I_{q1n}\lambda_{m1n} \tag{6.10}$$

where the base flux linkage is defined based on the normalised electromagnetic torque equation of the $d_1 - q_1$ plane as:

$$\lambda_b = \frac{V_b}{\omega_b} = \frac{Z_b I_b}{\omega_b} = L_b I_b \tag{6.11}$$

The normalised parameters and variables are defined as:

$$\left.\begin{array}{cccc} R_{sn} = \frac{r_s}{Z_b}, & L_{s1n} = \frac{L_{s1}}{L_b}, & L_{s2n} = \frac{L_{s2}}{L_b}, & \omega_n = \frac{\omega_e}{\omega_b} \\ I_{q1n} = \frac{i_{qs1}^r}{I_b}, & I_{d1n} = \frac{i_{ds1}^r}{I_b}, & V_{q1n} = \frac{v_{qs1}^r}{V_b}, & V_{d1n} = \frac{v_{ds1}^r}{V_b}, \\ I_{q2n} = \frac{i_{qs2}^r}{I_b}, & I_{d2n} = \frac{i_{ds2}^r}{I_b}, & V_{q2n} = \frac{v_{qs2}^r}{V_b}, & V_{d2n} = \frac{v_{ds2}^r}{V_b}, \end{array}\right\} \tag{6.12}$$

From (6.3) and Figure 6.2 it can be seen that the maximum modulation index for each plane or virtual machine (MM and SM) is obtained when:

$$\left.\begin{array}{l} M_{1-max} = B \\ M_{2-max} = B \end{array}\right\} \tag{6.13}$$

Substituting (6.4) into (6.3) shows that the maximum available voltage per plane V_{1s-max} and V_{2s-max} can be expressed as:

$$\left.\begin{aligned} V_{1s-max} &= B\tfrac{V_{dc}}{2} \\ V_{2s-max} &= B\tfrac{V_{dc}}{2} \end{aligned}\right\} \tag{6.14}$$

By choosing the maximum available voltage and the maximum available current per plane to be equal to the base voltage and current of the machine ($V_b = B\frac{V_{dc}}{2}$ and $I_b = I$) reduces the number of parameters to only four, which are $L_{s1}, \lambda_{m1}, L_{s2}$ and λ_{m2}. Using (6.8), (6.9), (6.11) and (6.12), (6.6) can be written in per-unit form as:

$$\left.\begin{aligned} V_{d1n} &= -\omega_n\, L_{s1n}\, I_{q1n} \\ V_{q1n} &= \omega_n\, L_{s1n}\, I_{d1n} + \omega_n\, \lambda_{m1n} \\ V_{d2n} &= -3\,\omega_n\, L_{s2n}\, I_{q2n} \\ V_{q2n} &= 3\,\omega_n\, L_{s2n}\, I_{d2n} + 3\,\omega_n\, \lambda_{m2n} \\ T_n &= \lambda_{m1n}\, I_{q1n} + 3\lambda_{m2n}\, I_{q2n} \end{aligned}\right\} \text{where} \quad \left\{\begin{aligned} &\frac{V_{1n}}{A} + \frac{V_{2n}}{B} \le \frac{1}{B} \\ &\frac{V_{1n}}{B} + \frac{V_{2n}}{A} \le \frac{1}{B} \\ &I_{1n}^2 + I_{2n}^2 \le 1 \\ &V_{1n}^2 = V_{q1n}^2 + V_{d1n}^2 \\ &V_{2n}^2 = V_{q2n}^2 + V_{d2n}^2 \\ &I_{1n}^2 = I_{q1n}^2 + I_{d1n}^2 \\ &I_{2n}^2 = I_{q2n}^2 + I_{d2n}^2 \end{aligned}\right\} \tag{6.15}$$

The parameters can be reduced to three by choosing the base speed ω_b to be equal to the rated speed. This makes the per-unit rated speed equal to unity. Choosing $M_1 = B$ ($V_{1s} = B\frac{V_{dc}}{2}$ and $I_{1s} = I$) as an operating point in the shaded area in Figure 6.2, the machine produces the rated torque at the rated speed for the maximum available voltage for a plane. From Figure 6.3 the maximum torque is obtained when the current angles γ_1 and γ_2 are equal to zero ($i^r_{ds1} = i^r_{ds2} = 0$). By applying this operating point to the voltage equation in (6.15) and solving $V_{1n} = 1$ at $\omega_n = 1$ and $I_{q1n} = 1$ when $V_{2n} = I_{2n} = 0$, It can be shown that the two per-unit parameters L_{s1n} and λ_{m1n} are dependent:

$$L_{s1n} = \sqrt{1 - \lambda_{m1n}^2} \tag{6.16}$$

Using (6.16), (6.15) can be written in terms of λ_{m1n} as:

$$\left\{\begin{array}{l} V_{d1n} = -\omega_n \sqrt{1-\lambda_{m1n}^2}\, I_{q1n} \\ V_{q1n} = \omega_n \sqrt{1-\lambda_{m1n}^2}\, I_{d1n} + \omega_n\, \lambda_{m1n} \\ V_{d2n} = -3\,\omega_n\, L_{s2n}\, I_{q2n} \\ V_{q2n} = 3\,\omega_n\, L_{s2n}\, I_{d2n} + 3\,\omega_n\, \lambda_{m2n} \\ T_n = \lambda_{m1n}\, I_{q1n} + 3\lambda_{m2n}\, I_{q2n} \end{array}\right\} \text{where} \quad \left\{\begin{array}{l} \dfrac{V_{1n}}{A} + \dfrac{V_{2n}}{B} \le \dfrac{1}{B} \\ \dfrac{V_{1n}}{B} + \dfrac{V_{2n}}{A} \le \dfrac{1}{B} \\ I_{1n}^2 + I_{2n}^2 \le 1 \\ V_{1n}^2 = V_{q1n}^2 + V_{d1n}^2 \\ V_{2n}^2 = V_{q2n}^2 + V_{d2n}^2 \\ I_{1n}^2 = I_{q1n}^2 + I_{d1n}^2 \\ I_{2n}^2 = I_{q2n}^2 + I_{d2n}^2 \end{array}\right\} \tag{6.17}$$

The $d_1 - q_1$ and $d_2 - q_2$ current components can be expressed in terms of the current angles γ_1, γ_2 and currents I_{1s}, I_{2s} utilising the phasor diagram in Figure 6.3 as:

$$\left\{\begin{array}{l} I_{q1n} = I_{1n} \cos\gamma_1 \\ I_{d1n} = -I_{1n} \sin\gamma_1 \\ I_{q2n} = I_{2n} \cos\gamma_2 \\ I_{d2n} = -I_{2n} \sin\gamma_2 \end{array}\right\} \tag{6.18}$$

Using (6.18), (6.17) can be written as:

$$\left\{\begin{array}{l} V_{d1n} = -\omega_n \sqrt{1-\lambda_{m1n}^2}\, I_{1n} \cos\gamma_1 \\ V_{q1n} = -\omega_n \sqrt{1-\lambda_{m1n}^2}\, I_{1n} \sin\gamma_1 + \omega_n\, \lambda_{m1n} \\ V_{d2n} = -3\,\omega_n\, L_{s2n}\, I_{2n} \cos\gamma_2 \\ V_{q2n} = -3\,\omega_n\, L_{s2n}\, I_{2n} \sin\gamma_2 + 3\,\omega_n\, \lambda_{m2n} \\ T_n = \lambda_{m1n}\, I_{1n} \cos\gamma_1 + 3\lambda_{m2n}\, I_{2n} \cos\gamma_2 \end{array}\right\} \text{where} \left\{\begin{array}{l} \dfrac{V_{1n}}{A} + \dfrac{V_{2n}}{B} \le \dfrac{1}{B} \\ \dfrac{V_{1n}}{B} + \dfrac{V_{2n}}{A} \le \dfrac{1}{B} \\ I_{1n}^2 + I_{2n}^2 \le 1 \\ V_{1n}^2 = V_{q1n}^2 + V_{d1n}^2 \\ V_{2n}^2 = V_{q2n}^2 + V_{d2n}^2 \\ I_{1n}^2 = I_{q1n}^2 + I_{d1n}^2 \\ I_{2n}^2 = I_{q2n}^2 + I_{d2n}^2 \end{array}\right\} \tag{6.19}$$

Equation (6.19) shows that the per-unit flux-weakening characteristics of the MF-five phase SPM can be analysed by utilizing three parameters only λ_{m1n}, L_{s1n} and λ_{m2n}. To simplify the analysis it is possible to define the following two parameters:

- E_{b21} as the ratio of the normalised back-emf of SM to the normalised back-emf

of the MM as:

$$E_{b21} = \frac{E_{b2n}}{E_{b1n}} = \frac{3\lambda_{m2n}\omega_n}{\lambda_{m1n}\omega_n} = \frac{3\lambda_{m2n}}{\lambda_{m1n}} = \frac{3\lambda_{m2}}{\lambda_{m1}} \tag{6.20}$$

- L_{21} as the ratio of the normalised inductance of the SM to the normalised inductance of the MM:

$$L_{21} = \frac{L_{s2n}}{L_{s1n}} = \frac{L_{s2}}{L_{s1}} \tag{6.21}$$

For a given λ_{m1n}, E_{b21} and L_{21} the remaining machine parameters are determined as follows:

$$L_{s2n} = L_{21}L_{s1n} = L_{21}\sqrt{1-\lambda_{m1n}^2}$$

$$\lambda_{m2n} = \frac{1}{3}E_{b21}\lambda_{m1n}$$

A numerical optimisation method is applied to solve the torque optimisation problem under the non-linear constraints of the inverter. The optimisation variables are the current components and current angles of both virtual machines. The optimisation variables are stated as:

$$\mathbf{X} = \begin{bmatrix} X(1) \\ X(2) \\ X(3) \\ X(4) \end{bmatrix} = \begin{bmatrix} I_{1n} \\ \gamma_1 \\ I_{2n} \\ \gamma_2 \end{bmatrix} \tag{6.22}$$

The lower and upper limits of the optimisation variables are expressed as:

$$\begin{bmatrix} 0 \\ -\pi \\ 0 \\ -\pi \end{bmatrix} \leq \mathbf{X} \leq \begin{bmatrix} 1 \\ \pi \\ 1 \\ \pi \end{bmatrix} \tag{6.23}$$

The objective of the optimisation problem was to maximise the electromagnetic torque. The effective function was formulated by using a MATLAB built-in function called "fmincon" as expressed in (6.24) and (6.25).

$$[\mathbf{X}, \text{cost}] = \text{fmincon}\left(-\lambda_{m1n}\, X(1)\cos X(2) - 3\lambda_{m2n}\, X(3)\cos X(4)\right) \tag{6.24}$$

$$T_{n,max}(\mathbf{X}) = -\text{cost} \tag{6.25}$$

The inverter non-linear constraints are:

$$\begin{aligned} \frac{V_{1n(\mathbf{X})}}{A} + \frac{V_{2n(\mathbf{X})}}{B} &\leq \frac{1}{B} \\ \frac{V_{1n(\mathbf{X})}}{B} + \frac{V_{2n(\mathbf{X})}}{A} &\leq \frac{1}{B} \\ X^2(1) + X^2(3) &\leq 1 \end{aligned} \tag{6.26}$$

6.5 Results

6.5.1 Characteristics of the SF Five-Phase SPM Machine

Figure 6.4 shows the performance characteristics of the SF five-phase SPM machine. In this machine type, there is no third harmonic, and the torque production is from the fundamental only. The machine characteristics are entirely determined using the MM magnet flux linkage parameter only (λ_{m1n}). It can be recognized that the machine under the inverter current and voltage constraints acts as an infinite speed drive for $\lambda_{m1n} \leq 0.71$, and a finite speed drive for higher values. Those results confirm that the SF five-phase SPM operates exactly as the classical three-phase SPM machine in which the optimum flux-weakening occurs when $\lambda_{m1n} = 0.71$ [91]. Although those results can be determined analytically, the primary purpose of showing the results is to validate the optimisation code and to confirm the condition for optimum flux-weakening.

6.5.2 Drive System Characteristics for Different Back-emf Ratios

Figures 6.5a, 6.6a and 6.7a show three examples of the torque versus speed characteristics of MF five-phase SPM machines. The calculations are for different values of the back-emf ratio (E_{b21}) under the optimum flux-weakening condition of the main virtual machine and different inductance ratio: $L_{21} = 1$, $L_{21} = 0.5$ and $L_{21} = 1.5$ respectively. The results show that for all values of E_{b21} the drive shows infinite speed characteristics. The highest torque in the flux-weakening region is when $E_{b21} = 0$. For speeds lower than the base speed, the normalised electromagnetic torque is proportional to the back-emf ratio, E_{b21}, while the speed range for constant maximum torque is inversely proportional to E_{b21}.

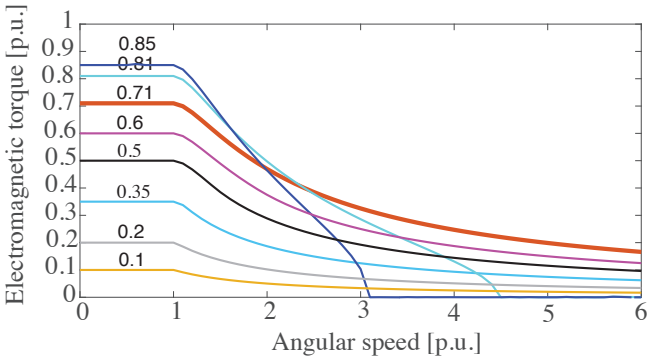

(a) Electromagnetic torque characteristic.

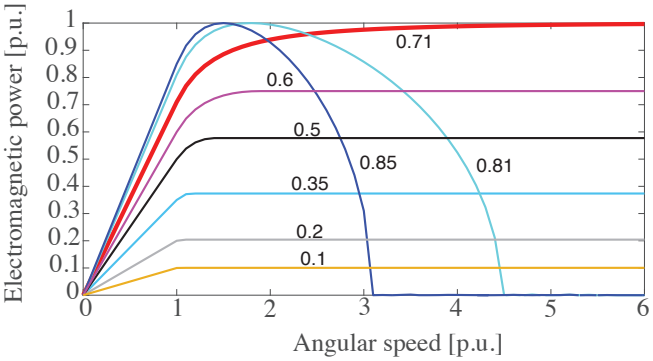

(b) Power characteristic.

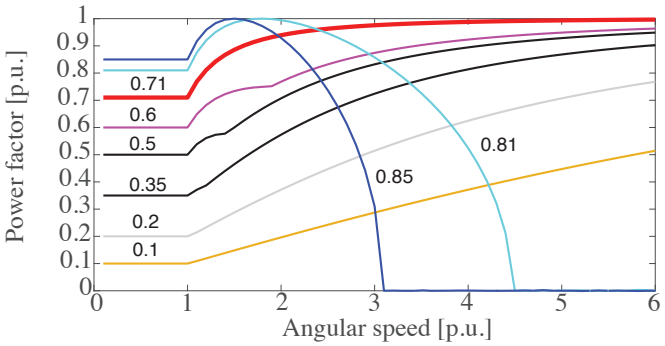

(c) Power factor characteristic.

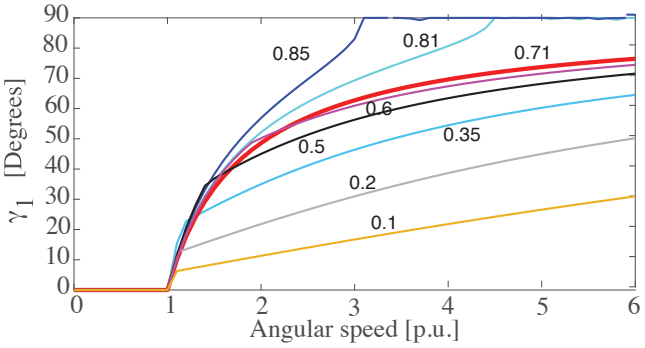

(d) Torque angle characteristic.

Figure 6.4: Characteristics of the SF five-phase SPM machine based drive with λ_{m1n} as a parameter.

Figures 6.5b, 6.6b and 6.7b show the variation of the machine variables for a particular case in Figures 6.5a, 6.6a and 6.7a respectvely, in which $E_{b21} = 0.25$. For speeds below the base speed, I_{d1n} and $I_{d2n} = 0$. This indicates that the current angles γ_1 and γ_2 are equal to zero, and the machine satisfies the maximum torque per current angle control strategy (MTPA). The prediction of the current sharing between I_{q1n} and I_{q2n} requires the back-emf and the current vectors to be co-linear [105]. In other words, MTPA assumes:

$$\frac{I_{q2n}}{I_{q1n}} = E_{b21} \tag{6.27}$$

Using (6.27) and assuming the machine to operate at rated maximum torque at rated speed gives the predicted values of the currents in the two planes under MTPA as:

$$\left.\begin{aligned} I_{q1n_{\max}} &= \frac{1}{\sqrt{1+E_{b21}^2}} \\ I_{q2n_{\max}} &= \frac{E_{b21}}{\sqrt{1+E_{b21}^2}} \end{aligned}\right\} \tag{6.28}$$

In the flux-weakening region, the electromagnetic torque is proportional to I_{q1n} only ($I_{q2n} = 0$). The flux-weakening components are I_{d1n} and I_{d2n}. It can be seen that I_{d1} increases negatively with speed while I_{d2n} is constant and equal to $-\lambda_{m2n}/L_{s2n}$.

Figure 6.5c, 6.6c and 6.7c show the torque versus speed characteristics of another examples MF five-phase SPM machines. The calculations are for different values of the back-emf ratio (E_{b21}), a particular value of magnet flux linkage ($\lambda_{m1n} = 0.85$) and different inductance ratio: $L_{21} = 1$, $L_{21} = 0.5$ and $L_{21} = 1.5$ respectively. The results show that for all values of E_{b21} the drive shows finite speed characteristics. The highest torque in the flux-weakening region is when $E_{b21} = 0$. For speeds lower than the base speed, the normalised electromagnetic torque is proportional to the E_{b21}, while the speed range for constant maximum torque is inversely proportional to E_{b21}.

Figure 6.5d, 6.6d and 6.7d show the variation of the machine variables for a particular case in Figures 6.5c, 6.6c and 6.7c respectively, in which $E_{b21} = 0.25$. For speeds below the base speed, I_{d1n} and $I_{d2n} = 0$. This indicates that the current angles γ_1 and γ_2 are equal to zero, and the machine satisfies the maximum torque per current angle control strategy (MTPA). In the flux-weakening region, the elec-

tromagnetic torque is proportional to I_{q1n} only ($I_{q2n} = 0$). The flux-weakening components are I_{d1n} and I_{d2n}. It can be seen that I_{d1} increases negatively with speed while I_{d2n} is constant and equal to $-\lambda_{m2n}/L_{s2n}$

6.5.3 Drive System Characteristics for Different Inductance Ratios

Figure 6.8a shows the torque versus speed characteristics of another example for an MF five-phase SPM machine. The calculations are for different values of the inductance ratio ratio (L_{21}), a particular value of magnet flux linkage ($\lambda_{m1n} = 0.71$) and back-emf ratio ($E_{b21} = 0.5$). The results show that for all values of L_{21} the drive shows an infinite speed characteristics. Although there is no big difference in the torque-speed characteristics for the whole speed range, it can be seen that the highest torque in the flux-weakening region is when $L_{21} = 1.5$. For speeds lower than the base speed, the highest normalised electromagnetic torque is the same for all inductance ratios, while the speed range for constant maximum torque is proportional to L_{21}.

Figure 6.8b shows the torque versus speed characteristics of another example for an MF five-phase SPM machine. The calculations are for different values of the inductance ratio (L_{21}), a particular value of magnet flux linkage ($\lambda_{m1n} = 0.85$) and back-emf ratio ($E_{b21} = 0.5$). The results show that for all values of L_{21} the drive shows a finite speed characteristics. There is a large difference in the torque-speed characteristics for the whole speed range, it can be seen that the highest torque in the flux-weakening region is when $L_{21} = 1.5$. For speeds lower than the base speed, the highest normalised electromagnetic torque is the same for all inductance ratios, while the speed range for constant maximum torque is proportional to L_{21}.

6.6 Discussion

The fundamental magnet flux linkage determines whether the MF five-phase SPM machine is a finite speed drive or an infinite speed drive. The back-emf ratio increases the normalised electromagnetic torque for speeds below the base speed, while it decreases the normalised electromagnetic torque for speeds higher than the base

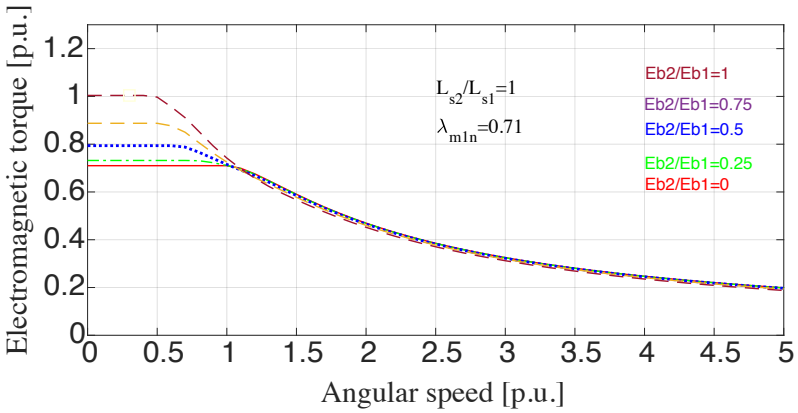

(a) Calculated characteristics of an MF five-phase SPM machine based infinite drive.

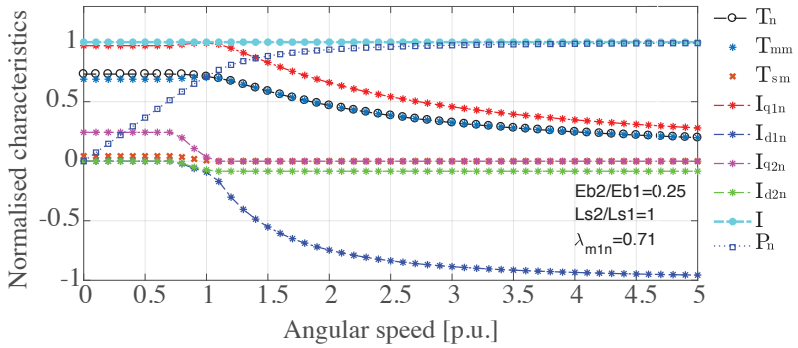

(b) Variation of an MF five-phase SPM machine based infinite drive variables.

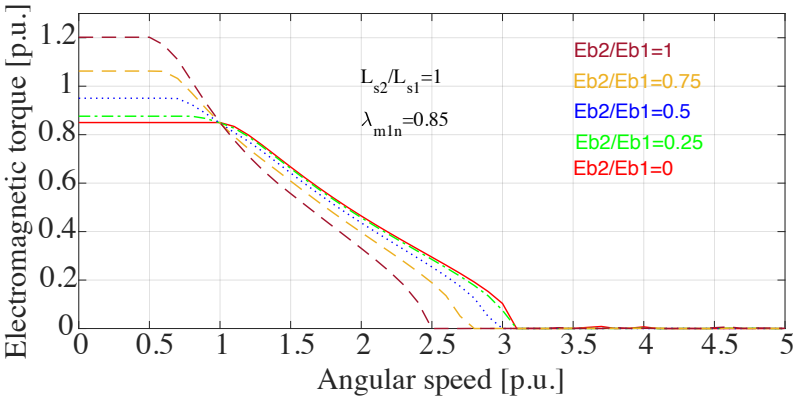

(c) Calculated characteristics of an MF five-phase SPM machine based finite drive.

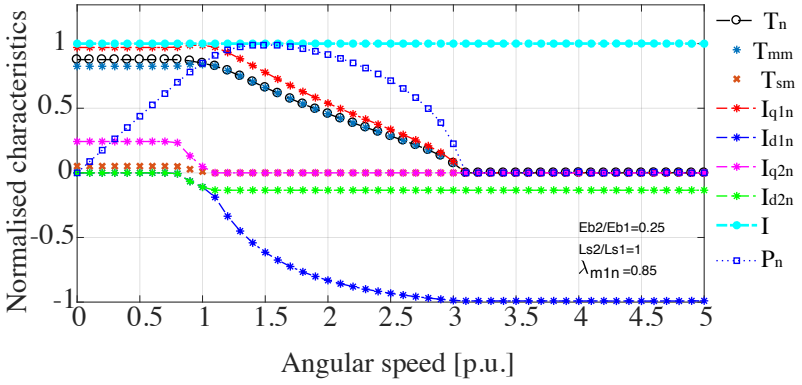

(d) Variation of an MF five-phase SPM machine based finite drive variables.

Figure 6.5: Calculated characteristics of an MF five-phase SPM machine based drive for unity inductance ratio ($L_{21} = 1$).

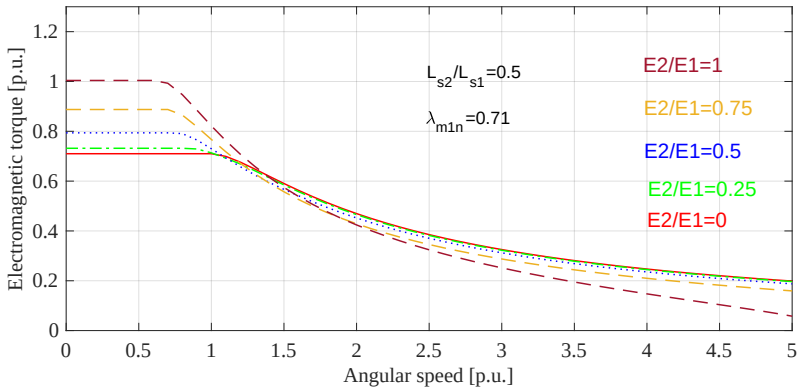

(a) Calculated characteristics of an MF five-phase SPM machine based infinite drive.

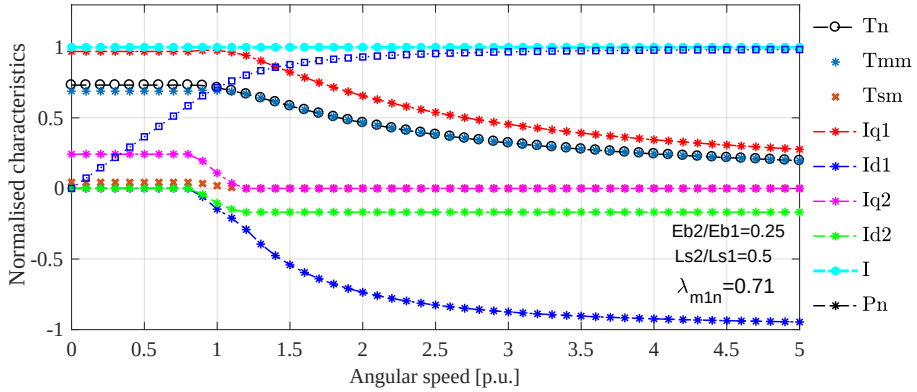

(b) Variation of an MF five-phase SPM machine based infinite drive variables.

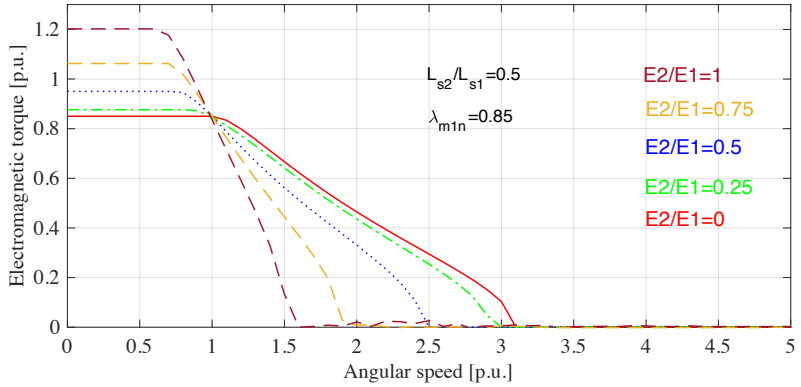

(c) Calculated characteristics of an MF five-phase SPM machine based finite drive.

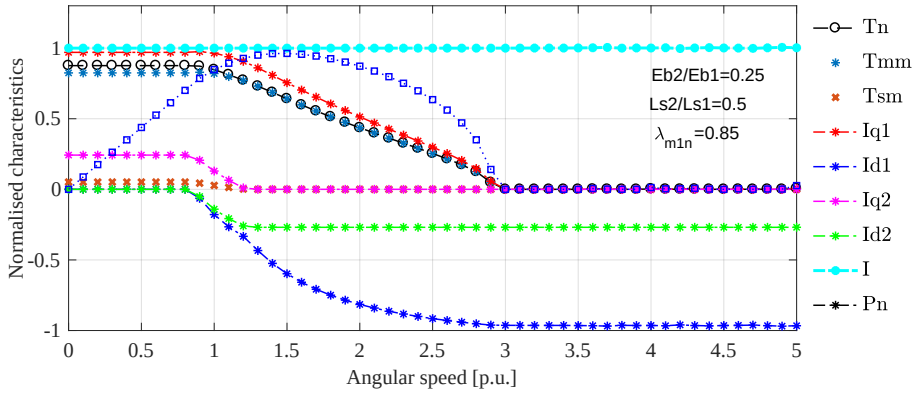

(d) Variation of an MF five-phase SPM machine based finite drive variables.

Figure 6.6: Calculated characteristics of an MF five-phase SPM machine based drive for inductance ratio $L_{21} = 0.5$.

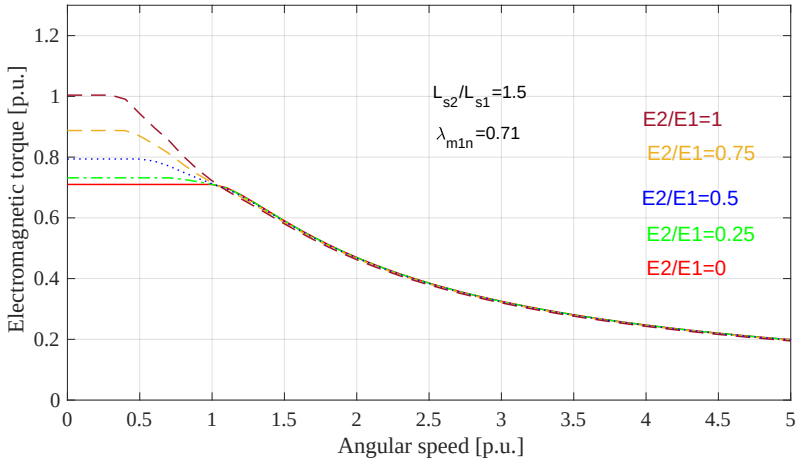

(a) Calculated characteristics of an MF five-phase SPM machine based infinite drive.

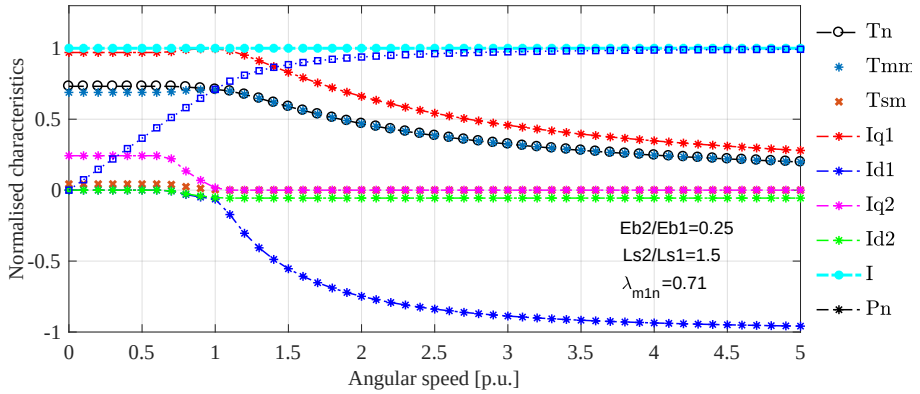

(b) Variation of an MF five-phase SPM machine based infinite drive variables.

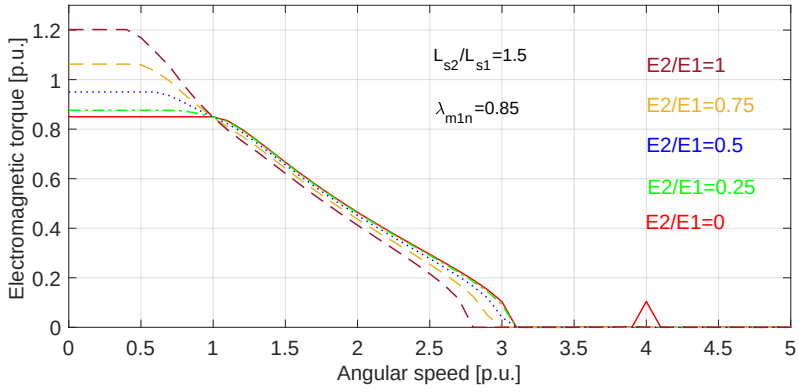

(c) Calculated characteristics of an MF five-phase SPM machine based finite drive.

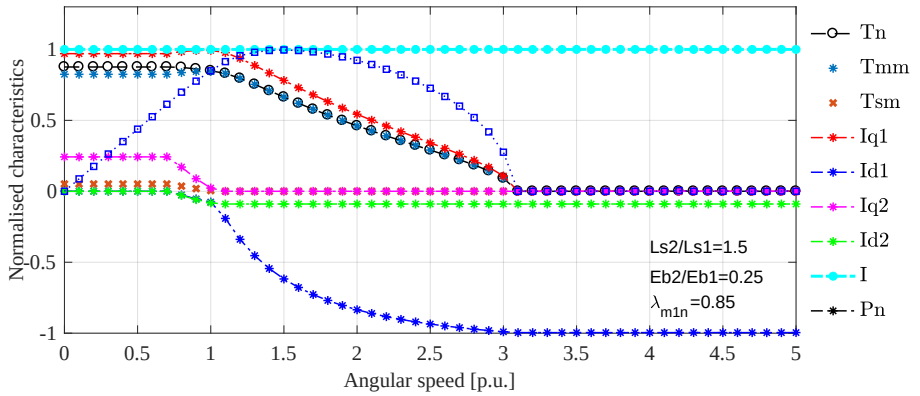

(d) Variation of an MF five-phase SPM machine based finite drive variables.

Figure 6.7: Calculated characteristics of an MF five-phase SPM machine based drive for inductance ratio $L_{21} = 1.5$.

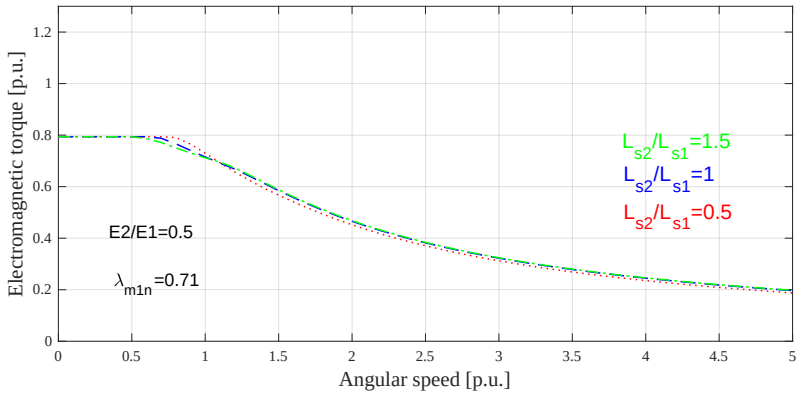

(a) Calculated characteristics of an MF five-phase SPM machine based infinite drive.

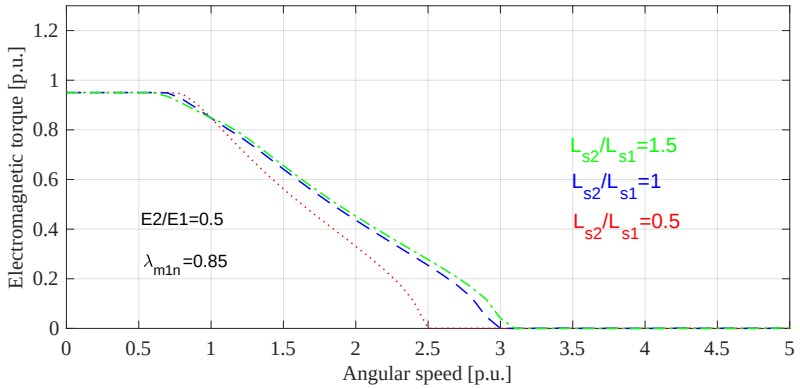

(b) Variation of an MF five-phase SPM machine based finite drive variables.

Figure 6.8: Calculated characteristics of an MF five-phase SPM machine based drive for $\lambda_{m1n} = 0.71$ and 0.85, $E_{b21} = 0.5$ and different inductance ratios.

speed. The highest normalised electromagnetic torque in the flux-weakening region for both an infinite speed drive and a finite speed drive is when the machine is controlled as a SF five-phase SPM. Maximising the electromagnetic torque for the whole speed range requires:

- The use of the MTPA control strategy for both planes or virtual machines for speeds below the rated speed.
- The use of the classical control methods for the main virtual machine, while setting the reference currents of the secondary virtual machine equal to zero for speeds higher than the rated or base speed.

Chapter 7

Flux Weakening Control for Five-Phase SPM Permanent Magnet Synchronous Machines

7.1 Introduction

Permanent magnet synchronous machines as part of a field oriented-variable speed drive system feature typical torque-speed characteristics at low to rated speeds. However, as rotor speed increases the back-emf rises, which results in loss of current regulation and decreased torque. To obtain adequate motor performance under various load conditions, numerous studies about control strategies were reported in the literature. The maximum torque per ampere (MTPA) is widely used in industrial applications due to developing a high torque, efficient utilisation of the dc bus voltage, and minimisation of copper losses. For the high-speed operation of PM synchronous motor drives with a limited inverter voltage, it is necessary to adopt a flux-weakening technique by which an acceptable torque-speed range is produced by reducing the air-gap flux density. This chapter aims to investigate the performance of the designed prototype five-phase SPM motor in the flux-weakening region using the feed-forward flux-weakening technique under the MTPA condition for a given dc bus voltage and current constraints. In the discussion of the MTPA control strategy of the star-connected MF five-phase SPM machine the following simplifying assumptions were made:

- A constant parameter steady-state model of the five-phase SPM synchronous machines can be used.
- The variation in inductances due to saturation and cross-saturation effects is neglected.
- The stator resistance and PM flux are also assumed to remain constant in the entire operating range.
- The motor is supplied via an inverter having limited current and voltage rating.

7.2 MTPA and Flux-Weakening Circle Diagram

Based on the results of the previous chapter the condition of MTPA for multi-frequency five-phase SPM motors is satisfied when the machine is controlled as a multi-frequency machine for speeds below the base speed and as a single frequency machine for higher speeds. For speeds below the base speed, the MTPA control strategy is realised by setting the demagnetising current components i_{ds1} and i_{ds2} to be equal zero. In the constant power region, the MTPA control strategy is realised by forcing the reference currents i_{ds2} and i_{qs2} to be equal zero, where the dc bus voltage would be utilised by the main virtual machine only such that the classical control theory of three-phase synchronous machines can be equally applied to multi-frequency five-phase SPM motors.

For non-salient PM synchronous motors with $L_{d1} = L_{q1} = L_{s1}$ and $L_{d2} = L_{q2} = L_{s2}$, equation (7.1) represents a drive system for speeds up to the rated speed. For higher speeds, the machine is controlled by utilising the parameters of the first plane only. Equation (7.2) represents the drive system for speeds above the base speed.

$$\left\{\begin{array}{l} v^r_{ds1} = r_s\, i^r_{ds1} - \omega_e\, L_{s1}\, i^r_{qs1} \\ v^r_{qs1} = r_s\, i^r_{qs1} + \omega_e\, L_{s1}\, i^r_{ds1} + \omega_e\, \lambda_{m1} \\ v^r_{ds2} = r_s\, i^r_{ds2} - 3\,\omega_e\, L_{s2}\, i^r_{qs2} \\ v^r_{qs2} = r_s\, i^r_{qs2} + 3\,\omega_e\, L_{s2}\, i^r_{ds2} + 3\,\omega_e\, \lambda_{m2} \\ T_e = \dfrac{5}{2}\dfrac{P}{2}\left[\lambda_{m1}\, i^r_{qs1} + 3\lambda_{m2}\, i^r_{qs2}\right] \end{array}\right\} \quad \text{where} \quad \left\{\begin{array}{l} \dfrac{V_{1s}}{A} + \dfrac{V_{2s}}{B} \le V_{\text{smax}} \\ \dfrac{V_{1s}}{B} + \dfrac{V_{2s}}{A} \le V_{\text{smax}} \\ I^2_{1s} + I^2_{2s} \le I^2_{\text{smax}} \\ I_{1s} = \sqrt{i^{r2}_{qs1} + i^{r2}_{ds1}} \\ I_{2s} = \sqrt{i^{r2}_{qs2} + i^{r2}_{ds2}} \end{array}\right\} \tag{7.1}$$

$$\left\{\begin{array}{l} v_{ds1}^r = r_s\, i_{ds1}^r - \omega_e\, L_{s1}\, i_{qs1}^r \\ v_{qs1}^r = r_s\, i_{qs1}^r + \omega_e\, L_{s1}\, i_{ds1}^r + \omega_e\, \lambda_{m1} \\ T_e = \dfrac{5}{2}\dfrac{P}{2}\left[\lambda_{m1}\, i_{qs1}^r\right] \end{array}\right\} \text{ where } \left\{\begin{array}{l} I_{1s} = \sqrt{i_{qs1}^{r2} + i_{ds1}^{r2}} \leq I_{s\max} \\ V_{1s} = \sqrt{V_{qs1}^{r2} + V_{ds1}^{r2}} \leq V_{s\max} \end{array}\right\} \tag{7.2}$$

In (7.1) and (7.2) $V_{s\max}$ is the maximum available amplitude of the phase voltage at the inverter output when the machine is controlled as a SF machine, while $I_{s\max}$ is the maximum allowable phase current. $V_{s\max}$ is set by the PWM method, and $I_{s\max}$ is decided by other factors, e.g., thermal dissipation, cooling methods and the available output current of the inverter.

Since the drive system is usually implemented with closed-loop current control, it is convenient to define an operating region regarding its location in the rotor reference frame by using the circle diagram. The circle diagram is a well-known graphical technique to determine the optimal field-weakening control strategy for classical three-phase brushless synchronous AC motor drives [57, 88, 94, 106–108]. Let the maximum amplitude of the fundamental phase voltage be equal to $V_{s\max}$, and the maximum amplitude of the fundamental phase current be $I_{s\max}$ then, the area which satisfies the current limit of (7.2) is the interior of the red circle in Figure 7.1 whose centre is at the origin [91]. The current limit is mathematically represented as:

$$i_{qs1}^{r2} + i_{ds1}^{r2} \leq I_{s\max}^2 \tag{7.3}$$

Any operating point which lies on or within this circle will not exceed the current rating of the inverter. The area which satisfies the voltage limit of (7.2) is the interior of the dotted green circle in Figure 7.1. The voltage-limit circle is obtained by applying the voltage constraint $V_{qs1}^{r2} + V_{ds1}^{r2} \leq V_{s\max}^2$ to the machine model in (7.2) which yields [109]:

$$\left(i_{ds1}^r + \frac{\omega_e^2 L_{s1}\lambda_{m1}}{r_s^2 + \omega_e^2 L_{s1}^2}\right)^2 + \left(i_{qs1}^r + \frac{\omega_e r_s \lambda_{m1}}{r_s^2 + \omega_e^2 L_{s1}^2}\right)^2 \leqslant \frac{V_{s\max}}{r_s^2 + \omega_e^2 L_{s1}^2} \tag{7.4}$$

and its center in the $d_1 - q_1$ plane is $\left(-\frac{\omega_e r_s \lambda_{m1}}{r_s^2+\omega_e^2 L_{s1}^2}, -\frac{\omega_e^2 L_{s1}\lambda_{m1}}{r_s^2+\omega_e^2 L_{s1}^2}\right)$. If the speed of the machine is high enough and the stator resistance voltage drop is small, then the voltage drop by the stator resistance can be neglected. Hence, (7.4) can be approximated

as (7.5):

$$\left(i_{ds1}^{r}+\frac{\lambda_{m1}}{L_{s1}}\right)^{2}+i_{qs1}^{r2}\leqslant\frac{V_{\mathrm{smax}}}{\omega_{e}^{2}L_{s1}^{2}} \tag{7.5}$$

and the area which satisfies (7.5) is that of the solid green circle in Figure 7.1 whose radius is directly proportional to V_{smax} and inversely proportional to speed, and its center is $\left(-\frac{\lambda_{m1}}{L_{s1}},0\right)$ [92,110,111]. The voltage limit circle encloses all the operating

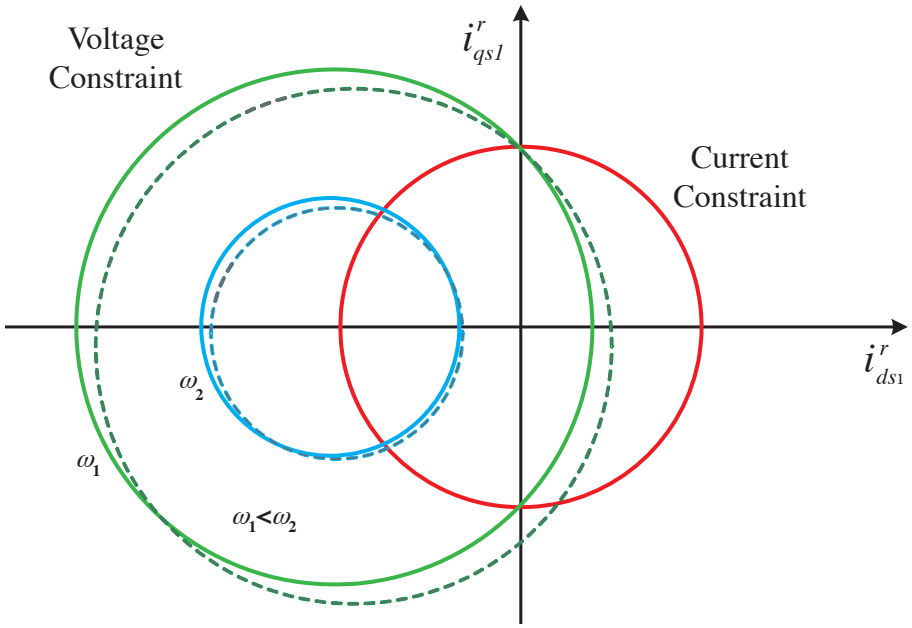

Figure 7.1: Voltage and current constraints of surface-mounted permanent magnet synchronous machine depicted in d_1-q_1 plane [109].

points where the terminal voltage does not exceed the maximum voltage when the machine operates as a main virtual machine only. All i_{qs1}-i_{ds1} current pairs that exist on or within the intersection of voltage circle and current circle are the allowable points of operation at any speed.

7.3 Operating Region Under Current and Voltage Constraints

The torque-speed characteristics and maximum reachable speed in the constant power region of an MF five-phase SPM machine drive system are determined by the relative location of the centre of the circle of the voltage constraint to the circle of the current constraint. The centre is set by the ratio of the fundemental magnet

flux linkage to the d_1-axis inductance $\left(-\frac{\lambda_{m1}}{L_{s1}}, 0\right)$. An SPM synchronous machine drive can be classified as a finite-speed drive and an infinite speed drive depending on whether the centre of the circle of the voltage constraint is inside the circle of the current constraint or outside of that circle [91].

7.3.1 Finite-Speed Drive System

In this drive system, the centre of the circle of the voltage constraint of the main virtual machine lies outside of the current constraint circle. In other words, the characteristic current of the main virtual machine is higher than the rated current of the machine. Figure 7.2 shows the trajectory of the MM current for both operating regions: low speed region (up to the rated speed) and constant power region (above the rated speed).

The machine operates under the MTPA control strategy of both virtual machines up to the rated speed (ω_{1f}), where the current, I_{1s}, moves along the q_1-axis of the MM and I_{2s} moves along the q_2-axis of the SM. The line "OA" represents the current trajectory along the q_1- axis. For speeds above ω_{1f} the current moves on the boundary of the current constraint circle, which is the curve "AB" where the inverter voltage is utilised by the MM only. Above a certain speed, ω_{3f}, there is no more common area for both circles, and the machine cannot be operated above that speed even if there is no mechanical reason to limit the speed.

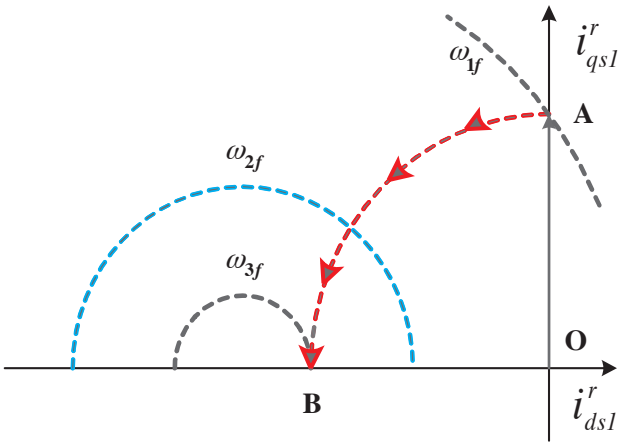

Figure 7.2: Voltage constraint, current constraint and current trajectory in a finite-speed SPM drive depicted in $d_1 - q_1$ plane.

7.3.2 Infinite-Speed Drive System

In this drive system, the centre of the voltage constraint of the main virtual machine lies inside or on the boundary of its current constraint circle; the maximum speed is limited only by the mechanical reasons such as centrifugal forces and / or the stress in the bearing. Figure 7.3 shows the current trajectory of the main virtual machine for the infinite speed-drive system.

The machine operates under MTPA control strategy for both virtual machines up to the rated speed (ω_{1i}), where the current, I_{1s}, moves along the q_1-axis of the MM and I_{2s} moves along q_2-axis of the SM. The line "OA" represents the current trajectory along the q_1-axis. Above ω_{1i} the current moves along the boundary of the current constraint circle, which is the curve "AB", like the case of the finite-speed drive system. However, above ω_{2i} the current moves not on the boundary of the current constraint circle, but on the line parallel to q_1-axis, which is the line "BC". In this mode of operation, the speed is not limited by electrical constraints, and theoretically, the machine is capable of operating at unlimited speed if there are no mechanical limitations.

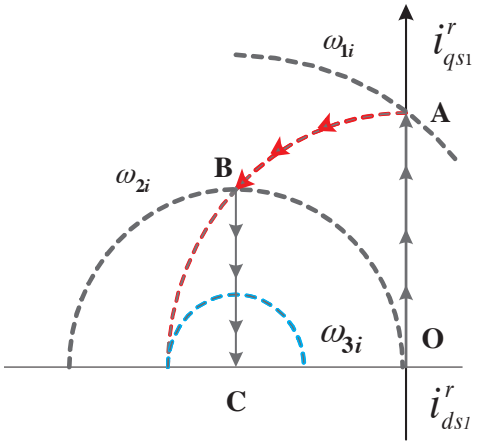

Figure 7.3: Voltage constraint, current constraint and current trajectory in an infinite-speed SPM machine drive in which $I_{\text{smax}} > \frac{\lambda_{m1}}{L_{s1}}$ depicted in $d_1 - q_1$ plane.

Figure 7.4 shows a special case of an infinite-speed drive system in which the characteristic current of the main virtual machine is equal to the rated current ($I_{\text{smax}} = \frac{\lambda_{m1}}{L_{s1}}$). For speeds higher than the rated speed ω_{1i}, the current moves along the boundary of the current constraint circle, which is the curve "AC", like the case of the finite-speed drive but for unlimited speed.

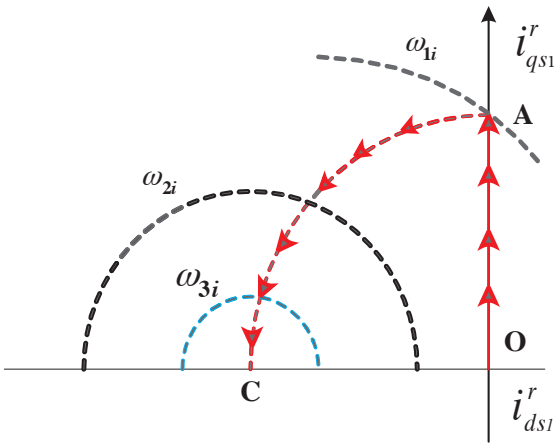

Figure 7.4: Voltage constraint, current constraint and current trajectory of the MM in infinite-speed SPM machine drive in which $I_{s\max} = \frac{\lambda_{m1}}{L_{s1}}$ depicted in $d_1 - q_1$ plane.

7.4 Rated speed, Maximum Speed and i^{r*}_{ds1} Current

Since the performance of the MF five-phase SPM machine in the constant power region is controlled by the parameters of the MM only, its enough to use the MM $d_1 - q_1$ equations in arriving at an expression for the amount of the d_1-axis current which must be injected to effectively reduce the back-emf of the machine. Let the rated phase voltage and the rated phase current of the main virtual machine form the rated quantities of the MF five-phase SPM machine. To analytically predict the performance of the drive system at different speeds in the steady state, from (5.38) and (5.39) the commanded q_1- and d_1- axis voltages corresponding to the demanded q_1-and d_1-axis currents are given by:

$$v^{r*}_{ds1} = r_s\, i^{r*}_{ds1} - \omega_e\, L_{s1}\, i^{r*}_{qs1} \tag{7.6}$$

$$v^{r*}_{qs1} = r_s\, i^{r*}_{qs1} + \omega_e\, L_{s1}\, i^{r*}_{ds1} + \omega_e\, \lambda_{m1} \tag{7.7}$$

The phase to neutral voltage which must be supplied by the inverter stated in terms of the q_1-and d_1-axis voltages is

$$V_{1s} = \sqrt{v^{r*}_{ds1} + v^{r*}_{qs1}} \tag{7.8}$$

Substituting (7.6) and (7.7) into (7.8) assuming MTPA ($i^r_{ds1} = 0$) and solving for ω_e yields the following expression:

$$\omega_e \mid_{\underset{MTPA}{=}} \frac{-r_s i^{r*}_{qs1}\lambda_{m1}}{\lambda^2_{m1} + L^2_{s1} i^{r*}_{qs1}} + \frac{\sqrt{r^2_s\lambda^2_{m1} i^{r2}_{qs1} + \left[V^2_{1s} - r^2_s i^{r*2}_{qs1}\right]\left[\lambda^2_{m1} + L^2_{s1} i^{r*2}_{qs1}\right]}}{\lambda^2_{m1} + L^2_{s1} i^{r2}_{qs1}} \tag{7.9}$$

An expression for the base or rated speed is found by substituting V_{smax} instead of V_{1s} and I_{smax} instead of i^{r*}_{qs1} and solving for ω_e, which yields

$$\omega_{base} = \frac{-r_s I_{\mathrm{smax}}\lambda_{m1}}{\lambda^2_{m1} + L^2_{s1} I_{\mathrm{smax}}} + \frac{\sqrt{r^2_s\lambda^2_{m1} I^2_{\mathrm{smax}} + \left[V^2_{\mathrm{smax}} - r^2_s I^2_{\mathrm{smax}}\right]\left[\lambda^2_{m1} + L^2_{s1} I^2_{\mathrm{smax}}\right]}}{\lambda^2_{m1} + L^2_{s1} I^2_{\mathrm{smax}}} \tag{7.10}$$

If the stator winding resistance is small enough to be neglected, a more straightforward expression for the base speed is obtained:

$$\omega_{base} \mid_{\underset{r_s=0}{=}} \frac{V_{\mathrm{smax}}}{\sqrt{\lambda^2_{m1} + \left(L_{s1} I_{\mathrm{smax}}\right)^2}} \tag{7.11}$$

In the finite-speed drive system, the maximum speed is the speed at which the electromagnetic torque is zero or when the armature current is entirely utilised to demagnetise the magnet ($i_{qs1=0}$). In the circle diagram, the maximum speed represents the last common point or area between the current constraint circle and the voltage constraint circle. The maximum speed can be derived by substituting (7.6) and (7.7) into (7.8) and solving for ω_e to produce the following expression:

$$\omega_e \mid_{\underset{finite-speed}{=}} \left\{ \begin{array}{c} \frac{-r_s i^{r*}_{qs1}\lambda_{m1}}{\left(L_{s1} i^{r*}_{ds1} + \lambda_{m1}\right)^2 + L^2_{s1} i^{r*}_{qs1}} + \\ \frac{\sqrt{r^2_s\lambda^2_{m1} i^{r*2}_{qs1} + \left[V^2_{\mathrm{smax}} - r^2_s\left(i^{r*2}_{qs1} + i^{r*2}_{ds1}\right)\right]\left[\left(L_{s1} i^{r*}_{ds1} + \lambda_{m1}\right)^2 + L^2_{s1} i^{r*2}_{qs1}\right]}}{\left(L_{s1} i^{r*}_{ds1} + \lambda_{m1}\right)^2 + L^2_{s1} i^{r*2}_{qs1}} \end{array} \right\} \tag{7.12}$$

Now assuming ($i^{r*}_{qs1} = 0$) in (7.12) yields the following exact expression for the maximum speed.

$$\omega_{e-max} \mid_{\underset{finite-speed}{=}} \frac{\sqrt{\left(V^2_{\mathrm{smax}} - r^2_s i^{r*2}_{ds1}\right)\left(L_{s1} i^{r*}_{ds1} + \lambda_{m1}\right)^2}}{\left(L_{s1} i^{r*}_{ds1} + \lambda_{m1}\right)^2} \tag{7.13}$$

After neglecting the stator resistance voltage drop, and substituting ($I_{\text{smax}} = i^{r*}_{ds1}$), the maximum speed in the finite-speed drive system can be stated as:

$$\omega_{e-max} \mid_{\substack{r_s=0 \\ finite-speed}} = \frac{V_{\text{smax}}}{\lambda_{m1} - L_{s1} I_{\text{smax}}} \tag{7.14}$$

An expression for the demanded d_1-axis current is calculated by solving (7.12) for i^{r*}_{ds1}, which yields [93]:

$$i^{r*}_{ds1} = \frac{-\lambda_{m1} L_{s1} \omega_e^2 + \sqrt{\left(r_s^2 + w_e^2 L_{s1}^2\right) V_{smax}^2 - \left(r_s \lambda_{m1} \omega_e + \left(r_s^2 + w_e^2 L_{s1}^2\right) i^{r*}_{qs1}\right)^2}}{r_s^2 + w_e^2 L_{s1}^2} \tag{7.15}$$

If the effect of the stator resistance is neglected, $r_s = 0$ in equations (7.6) and (7.7), and if the equality sign is used in the voltage constraint, the maximum attainable torque and the corresponding reference i^{r*}_{ds1} are obtained as presented in [92, 112]:

$$T_{e\text{max}} = \frac{5}{2}\frac{P}{2}\lambda_{m1}\sqrt{\frac{V_{\text{smax}}^2}{\left(\omega_e L_{s1}\right)^2} - \frac{1}{4}\frac{\lambda_{m1}}{L_{s1}}\left[1 + \frac{V_{\text{smax}}^2}{\left(\omega_e \lambda_{m1}\right)^2} - \frac{\left(L_{s1} I_{\text{smax}}\right)^2}{\lambda_{m1}^2}\right]} \tag{7.16}$$

$$i^*_{ds1} = \frac{1}{2}\frac{L_{s1}}{\lambda_{m1}}\left[\left(\frac{V_{\text{smax}}}{\omega_e \lambda_{m1}}\right)^2 - \left(\frac{\lambda_{m1}}{L_{s1}}\right)^2 + I_{\text{smax}}^2\right] \tag{7.17}$$

7.5 Flux Weakening Control with Feed-Forward Compensation

To weaken the flux, the feed-forward compensation technique can be implemented based on the steady-state voltage equations of the main virtual machine. The method can be easily applied with the rated machine parameters, and it is simple because no gains have to be set for the flux weakening control. From the previous section, the analytically calculated d_1-axis current demand is used to develop a flux-weakening feed-forward controller to simulate the prototype machine in the flux weakening region. The feed-forward controller is schematically captured as shown in Appendix C .

The analytically calculated d_1-axis current demand, i^*_{ds1}, in (7.17) along with the maximum current limit determine the maximum i_{qs1} current, $i_{qs1-max}$, in the

flux weakening region, $i_{qs1-max} = \sqrt{I_{smax}^2 - i_{ds1}^{*2}}$. This q_1-axis current with the calculated d_1-axis current determine the maximum electromagnetic torque allowed within maximum voltage and current constraints. The q_1-axis reference current, i_{qs1}^* is equal to the q_1- axis current generated by the speed error if it is less than the calculated maximum i_{qs1} current; otherwise it equals the calculated maximum i_{qs1} current. In other words, the following logic statements are applied to find the q_1-axis current reference i_{qs1}^*.

$$\begin{aligned} i_{qs1-\text{speed error}} > i_{qs1-max} \quad &\text{then} \quad i_{qs1}^* = i_{qs1-max} \\ i_{qs1-\text{speed error}} < i_{qs1-max} \quad &\text{then} \quad i_{qs1}^* = i_{qs1-\text{speed error}} \end{aligned}$$

The flux weakening controller is initiated when the rotor speed is higher than the rated speed.

Simulation

Using the measured parameters of the drive system and the controller design parameters listed in Table 5.2 and Table 5.3 respectively, the entire drive system including the feed-forward compensation was simulated for speeds higher than the rated speed (2000 rpm). As a matter of fact, an accurate flux-weakening simulator requires a good machine, dynamic model. Two speeds within the operating range of the drive system, 2000 rpm and 4000 rpm, were tested. The load torque T_l was chosen to be 1.1 Nm. In general, the response was fast, and there was very little overshoot. Figure 7.5 shows the speed response to a step change demand in motor speed from standstill to 2000 rpm, and from 2000 rpm to 4000 rpm for a step load torque of 1.1 [N.m].

The simulation results in Figures 7.6, 7.7, 7.8 and 7.9 verify that the feed-forward scheme is fully operational and that it provides the expected operation over the desired speed range. When the flux weakening is initiated as soon as the speed set-point is higher than the rated speed, negative i_{ds1} is injected. We can see that i_{qs1} jumped to the current limit as a response to the step change in the speed set-point. Then i_{qs1} started to decrease because the total current is subject to the current limit from equation (7.3). Apparently, if the machine operates at its rated operating point (rated torque and rated speed), then i_{qs1} current will decrease while the i_{ds1} increases

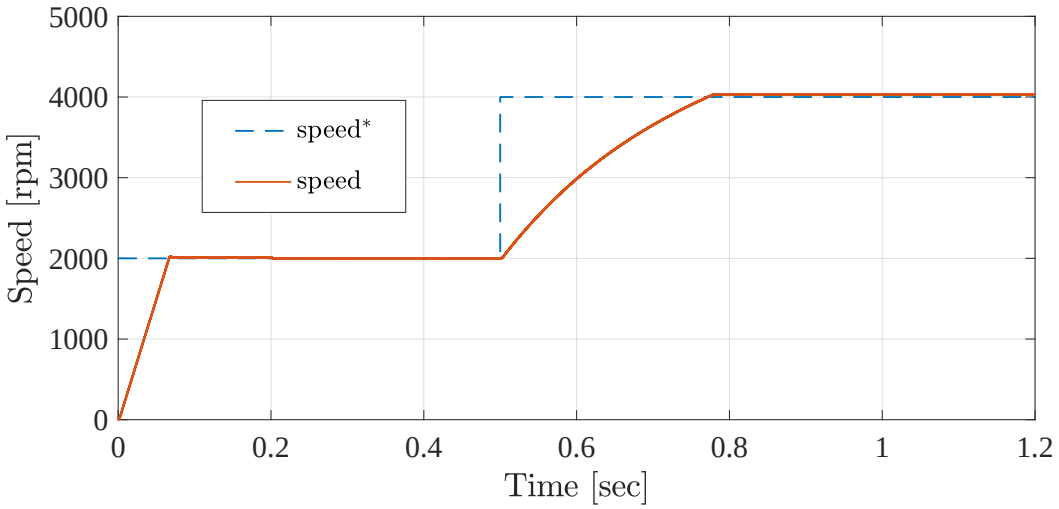

Figure 7.5: Motor speed response for commanded speeds 2000 rpm at t =0 sec and 4000 rpm at t =0.5 sec for a step load torque of 1.1 N.m at t =0.2 sec.

negatively.

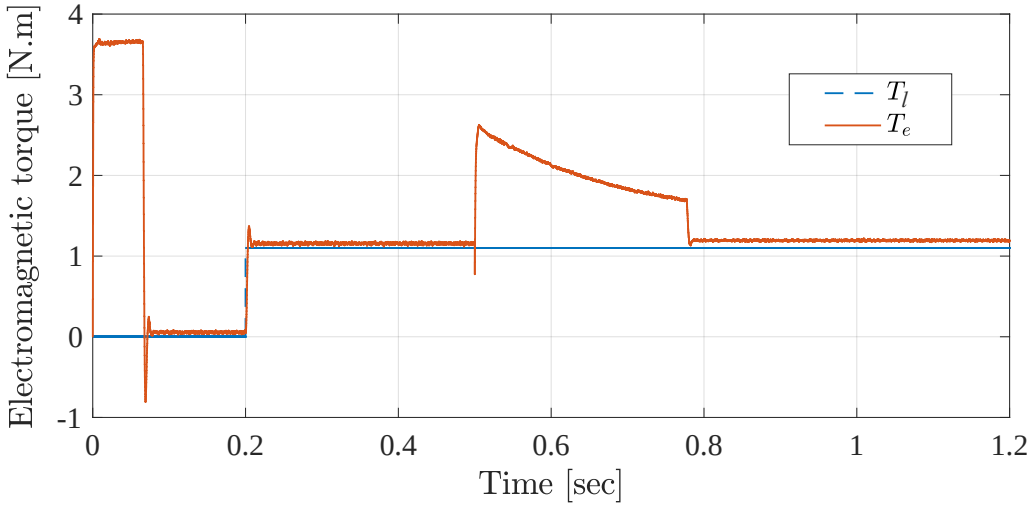

Figure 7.6: The response of the electromagnetic torque for speed demands of 2000 rpm at t =0 sec, 4000 rpm at t =0.5 sec and a step load torque of 1.1 N.m at t = 0.2 sec.

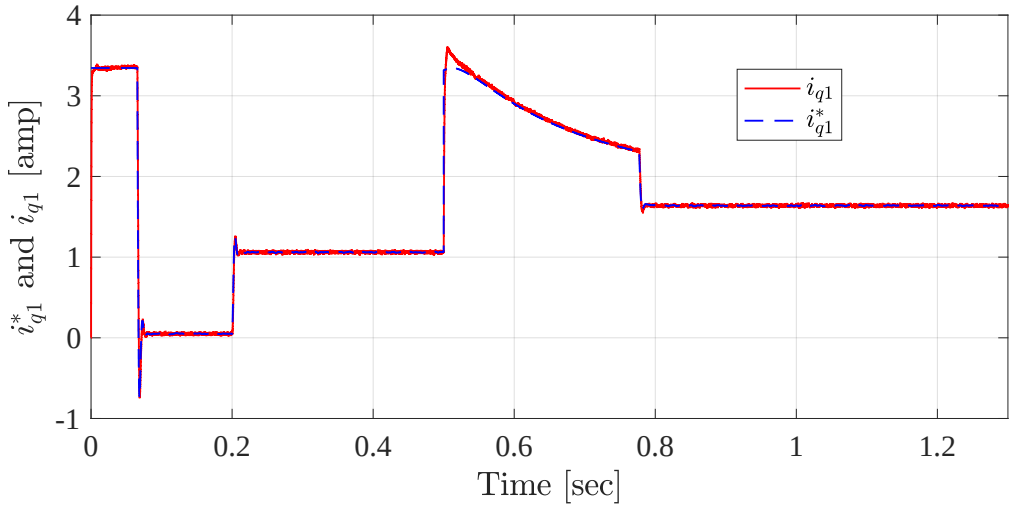

Figure 7.7: The response of the q_1-axis current for speed demands of 2000 rpm at t =0 sec, 4000 rpm at t =0.5 sec and a step load torque of 1.1 N.m at t = 0.2 sec.

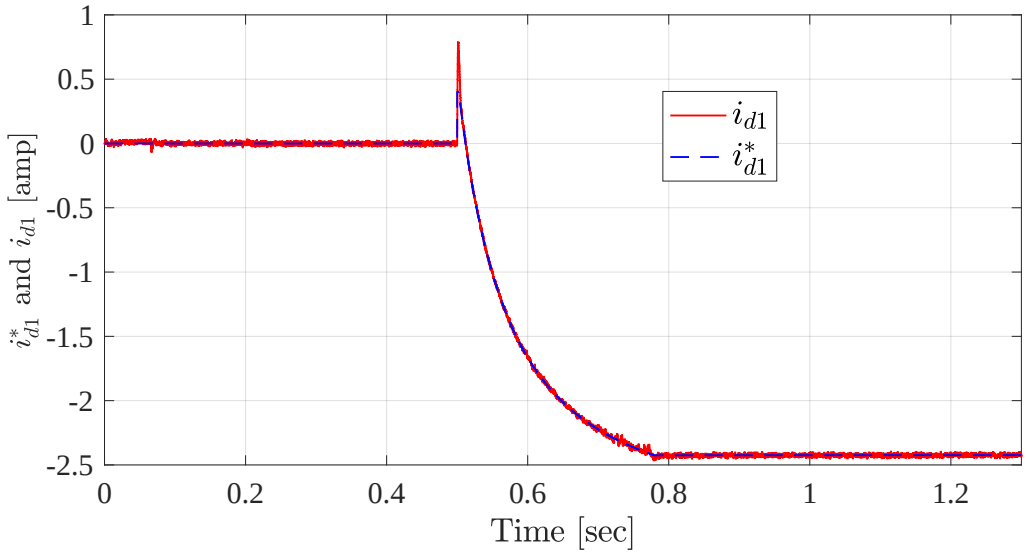

Figure 7.8: The response of the d_1-axis current for speed demands of 2000 rpm at t =0 sec, 4000 rpm at t =0.5 sec and a step load torque of 1.1 N.m at t = 0.2 sec.

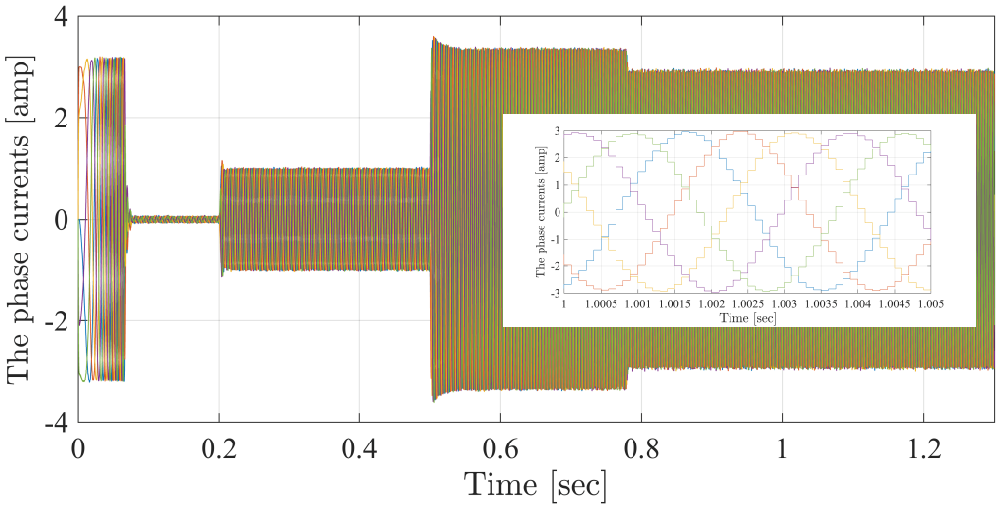

Figure 7.9: The response of the phase currents for speed demands of 2000 rpm at t =0 sec, 4000 rpm at t =0.5 sec and a step load torque of 1.1 N.m at t = 0.2 sec.

Chapter 8

Conclusions and Future Work

In this thesis, the aim was to analyse, design, control, implement and experimentally evaluate five-phase SPM machine drive system with extended high-speed operation by using high inductance non-overlapping concentrated windings. Key conclusions achieved in the thesis are summarised in Section 8.1. The significant contributions resulting from this research program are summarised in Section 1.3.

8.1 Conclusions and Contributions

Based on the literature survey, presented in chapter 2, FSCWs five-phase PM machines are candidate for fault-tolerance applications. However, for some applications, tolerance to faults is essential but not the only requirement. Some applications require, besides a fault-tolerance capability, an adequate wide speed range capacity, and thus, the machine needs to be an integral part of a reliable variable speed drive system. One of the the essential requirements for a fault-tolerant machine is high phase self-inductance to limit the short circuit current and a low mutual inductance between phases to physically separate the phase windings. Simultaneously, for SPM machines, FSCWs are utilised to increase the machine inductance for the same magnet flux linkage for meeting the critical design condition for optimum flux weakening.

Based on a review for choosing the best possible combinations, it has been shown that the choice of slot/pole combination is equally important for meeting the optimum flux weakening condition and the maximum fault tolerance capability. Single-

layer windings offer better physical isolation than double-layer FSCWs, but rotor losses due to high space harmonic content must be addressed. Since the double-layer windings exhibit significant phase to phase coupling through mutual slot leakage inductance, it is feasible to produce double-layer FSCWs with low mutual coupling between phases by selecting a combination for which $2p \approx Q$.

Two design methods, analytical and 2-D finite element, presented in chapter 3, were needed for calculating the design parameters of the FSCW five-phase PM synchronous machine. The primary objective was to achieve the optimal flux-weakening condition necessary for attaining a constant-power operation over a wide speed range.

A detailed, accurate analytical method which included the effect of the winding resistance has been presented for analysing five-phase SPM machines using FSCWs, recognising that the standard calculations based on a horizontal double-layer winding are not accurate for such machines. The laboratory tests show that the back-emf waveform represents a reasonable approximation of the sinusoidal fundamental harmonic. This result confirms that for $q = 0.25$ (q is the number of slots per pole and phase), a simple magnetic equivalent-circuit method for calculating the magnet flux linkage under open-circuit conditions is sufficient, and can be used if a standard correction factor for the rotor leakage flux is estimated.

In chapter 4, 1kW 10 slot / 8 pole FSCW five-phase SPM has been designed. The numerical and analytical simulations show that the design satisfies the optimum flux-weakening condition with approximately sinusoidal back-emf waveforms and low cogging torque.

In chapter 5, the mathematical model for a MF five-phase PM synchronous motor has been derived. It has been shown that application of decoupling and rotational transformations results in a simplified mathematical model due to the absence of position dependent inductances in the derived model. Moreover, a discrete drive model suitable for real-time implementation has been developed. The Z domain root locus method is used to design the current and speed controllers for the digital system.

To validate the controllers' design and the performance of the drive system, various simulation and experimental results were collected under different operating

conditions. A simple analysis was primarily given through the evaluation of the time-domain waveforms of the motor variables like phase currents, voltages and electromagnetic torque. The results showed a good agreement between the theoretical results obtained from the computational simulations and the experimental outcomes, collected from the practical experiments.

In chapter 6 the effect of varying the motor drive parameters on the optimum flux-weakening performance of the MF five-phase SPM motor has been investigated. A new DQ normalisation for an MF five-phase SPM drive was developed and used in the optimisation process. The non-linear optimisation problem that aimed to maximise the electromagnetic torque of the MF five-phase SPM machine under the voltage and current constraints, for operation in the linear modulation region, was formulated. The study covered a feasible range of the back-emf ratio (Eb_{21}) under the optimum flux-weakening condition of the main virtual machine and inductance ratios of $L_{21} = 0.5, 1$ and 1.5. It has been shown that the fundamental magnet flux linkage determines whether the MF five-phase SPM machine is a finite speed drive or infinite speed drive. The back-emf ratio increases the normalised electromagnetic torque for speeds below the base speed, but decreases the normalised electromagnetic torque for speeds higher than the base speed. The highest normalised electromagnetic torque in the flux-weakening region for both an infinite speed drive and a finite speed drive is when the machine is controlled as an SF five-phase SPM.

The performance of the designed prototype five-phase SPM motor in the flux-weakening region using the feed-forward flux-weakening technique under the MTPA condition for a given dc bus voltage and current constraints has been investigated in chapter 7. The simulation results verified that the feed-forward scheme is fully operational and that it provides the expected operation over the desired speed range.

8.2 Future Work

1. Studying the effect of varying the motor drive parameters on the optimum flux-weakening performance of a MF five-phase interior PM synchronous motor for achieving the necessary conditions for optimal flux weakening.
2. Using the developed design tools for optimising the machine design such that

the third harmonic represents an essential part of the total electromagnetic torque whilst keeping the cogging torque under acceptable limits.

3. Using segmented stator structures as an additional optimisation technique.
4. Testing the designed machine under different control strategies, for example, implementing appropriate control software to maintain operation under fault conditions, where one or even two phases are non-functional.

REFERENCES

REFERENCES

[1] W. Hassan, P. Lefley, and M. Kansara, "Optimum flux-weakening characteristics for five-phase surface mount permanent magnet synchronous machines," in *2018 International Symposium on Electrical Machines (SME)*, June 2018, pp. 1–5.

[2] N. Bianchi, *Theory and Design of Fractional-slot PM Machines: IEEE IAS Tutorial Corse (sic) Notes*. Cleup, 2007.

[3] T. M. Jahns, "Improved reliability in solid-state ac drives by means of multiple independent phase drive units," *IEEE Transactions on Industry Applications*, no. 3, pp. 321–331, 1980.

[4] L. Parsa, H. Toliyat *et al.*, "Fault-tolerant five-phase permanent magnet motor drives," in *Industry Applications Conference, 2004. 39th IAS Annual Meeting. Conference Record of the 2004 IEEE*, vol. 2. IEEE, 2004, pp. 1048–1054.

[5] A. El-Refaie, "Fault-tolerant permanent magnet machines: a review," *IET Electric Power Applications*, vol. 5, no. 1, pp. 59–74, 2011.

[6] B. Mecrow, A. Jack, J. Haylock, and J. Coles, "Fault-tolerant permanent magnet machine drives," *IEE Proceedings-Electric Power Applications*, vol. 143, no. 6, pp. 437–442, 1996.

[7] A. M. El-Refaie, "Fractional-slot concentrated-windings synchronous permanent magnet machines: Opportunities and challenges," *IEEE Transactions on Industrial Electronics*, vol. 57, no. 1, pp. 107–121, 2010.

[8] W. Ouyang and T. A. Lipo, "Modular permanent magnet machine with fault tolerant capability," in *Applied Power Electronics Conference and Exposition, 2009. APEC 2009. Twenty-Fourth Annual IEEE*. IEEE, 2009, pp. 930–937.

[9] A. Mitcham, G. Antonopoulos, and J. Cullen, "Favourable slot and pole number combinations for fault-tolerant pm machines," *IEE Proceedings-Electric Power Applications*, vol. 151, no. 5, pp. 520–525, 2004.

[10] N. Bianchi, S. Bolognani, and M. D. Pre, "Impact of stator winding of a five-phase permanent-magnet motor on postfault operations," *IEEE Transactions on Industrial Electronics*, vol. 55, no. 5, pp. 1978–1987, 2008.

[11] N. Bianchi, S. Bolognani, and M. Dai Pré, "Strategies for the fault-tolerant current control of a five-phase permanent-magnet motor," *IEEE Transactions on Industry Applications*, vol. 43, no. 4, pp. 960–970, 2007.

[12] L. Parsa, H. A. Toliyat, and A. Goodarzi, "Five-phase interior permanent-magnet motors with low torque pulsation," *IEEE Transactions on Industry Applications*, vol. 43, no. 1, pp. 40–46, 2007.

[13] J. He, G. Liang, and S. Wang, "The design of a switched reluctance motor drive system," in *Informatics in Control, Automation and Robotics, 2009. CAR'09. International Asia Conference on.* IEEE, 2009, pp. 445–449.

[14] I. P. Brown, D. M. Ionel, and D. G. Dorrell, "Influence of parallel paths on current-regulated sine-wave interior-permanent-magnet machines with rotor eccentricity," *IEEE Transactions on Industry Applications*, vol. 48, no. 2, pp. 642–652, 2012.

[15] R. P. Deodhar, S. Andersson, I. Boldea, and T. J. Miller, "The flux-reversal machine: A new brushless doubly-salient permanent-magnet machine," *IEEE Transactions on Industry Applications*, vol. 33, no. 4, pp. 925–934, 1997.

[16] Y. Liao, F. Liang, and T. A. Lipo, "A novel permanent magnet motor with doubly salient structure," *IEEE Transactions on Industry Applications*, vol. 31, no. 5, pp. 1069–1078, 1995.

[17] Z. Zhu and J. Chen, "Advanced flux-switching permanent magnet brushless machines," *IEEE Transactions on Magnetics*, vol. 46, no. 6, pp. 1447–1453, 2010.

[18] J. Chen and Z. Zhu, "Winding configurations and optimal stator and rotor pole combination of flux-switching pm brushless ac machines," *IEEE Transactions on Energy Conversion*, vol. 25, no. 2, pp. 293–302, 2010.

[19] W. Hua, M. Cheng, H. Jia, and X. Fu, "Comparative study of flux-switching and doubly-salient pm machines particularly on torque capability," in *Industry Applications Society Annual Meeting, 2008. IAS'08. IEEE.* IEEE, 2008, pp. 1–8.

[20] D. M. Ionel, R. J. Heideman, and R. P. Bartos, "Spoke permanent magnet rotors for electrical machines and methods of manufacturing same," Dec. 12 2006, US Patent 7,148,598.

[21] K.-C. Kim and J. Lee, "The dynamic analysis of a spoke-type permanent magnet generator with large overhang," *IEEE Transactions on Magnetics*, vol. 41, no. 10, pp. 3805–3807, 2005.

[22] D. G. Dorrell, M.-F. Hsieh, and A. M. Knight, "Alternative rotor designs for high performance brushless permanent magnet machines for hybrid electric vehicles," *IEEE Transactions on Magnetics*, vol. 48, no. 2, pp. 835–838, 2012.

[23] H.-W. Kim, K.-T. Kim, B.-W. Kim, J. Hur, and Y.-S. Jo, "Design of new spoke type brushless dc motor for neodymium permanent magnet free," in *Vehicle Power and Propulsion Conference (VPPC), 2012 IEEE*. IEEE, 2012, pp. 133–137.

[24] S.-I. Kim, J. Cho, S. Park, T. Park, and S. Lim, "Characteristics comparison of a conventional and modified spoke-type ferrite magnet motor for traction drives of low-speed electric vehicles," *IEEE Transactions on Industry Applications*, vol. 49, no. 6, pp. 2516–2523, 2013.

[25] N. Bianchi, M. Pré, G. Grezzani, and S. Bolognani, "Design considerations on fractional-slot fault-tolerant synchronous motors," in *Electric Machines and Drives, 2005 IEEE International Conference on*. IEEE, 2005, pp. 902–909.

[26] A. G. Jack, B. C. Mecrow, J. Haylock *et al.*, "A comparative study of permanent magnet and switched reluctance motors for high-performance fault-tolerant applications," *IEEE Transactions on Industry Applications*, vol. 32, no. 4, pp. 889–895, 1996.

[27] L. Parsa, H. Toliyat *et al.*, "Five-phase permanent-magnet motor drives," *IEEE Transactions on Industry Applications*, vol. 41, no. 1, pp. 30–37, 2005.

[28] N. Bianchi, S. Bolognani, M. D. Pré, and G. Grezzani, "Design considerations for fractional-slot winding configurations of synchronous machines," *IEEE Transactions on Industry Applications*, vol. 42, no. 4, pp. 997–1006, 2006.

[29] C. Bianchini, E. Fornasiero, T. N. Matzen, N. Bianchi, and A. Bellini, "Fault detection of a five-phase permanent-magnet machine," in *Industrial Electronics, 2008. IECON 2008. 34th Annual Conference of IEEE*. IEEE, 2008, pp. 1200–1205.

[30] N. Bianchi, S. Bolognani, M. Dai Pre, and E. Fornasiero, "Post-fault operations of five-phase motor using a full-bridge inverter," in *Power Electronics Specialists Conference, 2008. PESC 2008. IEEE*. IEEE, 2008, pp. 2528–2534.

[31] S. Dwari and L. Parsa, "An optimal control technique for multiphase pm machines under open-circuit faults," *IEEE Transactions on Industrial Electronics*, vol. 55, no. 5, pp. 1988–1995, 2008.

[32] S. Dwari and L. Parsa, "Disturbance free operation of permanent magnet motor drives under short circuit faults using center-split winding," in *Industry Applications Conference, 2007. 42nd IAS Annual Meeting. Conference Record of the 2007 IEEE.* IEEE, 2007, pp. 1329–1334.

[33] S. Dwari and L. Parsa, "Optimum fault-tolerant control of multi-phase permanent magnet machines for open-circuit and short-circuit faults," in *Applied Power Electronics Conference, APEC 2007-Twenty Second Annual IEEE.* IEEE, 2007, pp. 1417–1422.

[34] W. Ouyang and T. Lipo, "Multiphase modular permanent magnet drive system design and realization," in *Electric Machines & Drives Conference, 2007. IEMDC'07. IEEE International*, vol. 1. IEEE, 2007, pp. 787–792.

[35] B. Vaseghi, N. Takorabet, J. P. Caron, B. Nahid-Mobarakeh, F. Meibody-Tabar, and G. Humbert, "Study of different architectures of fault-tolerant actuator using a two-channel pm motor," *IEEE Transactions on Industry Applications*, vol. 47, no. 1, pp. 47–54, 2011.

[36] C. J. Ifedi, B. C. Mecrow, S. T. Brockway, G. S. Boast, G. J. Atkinson, and D. Kostic-Perovic, "Fault-tolerant in-wheel motor topologies for high-performance electric vehicles," *IEEE Transactions on Industry Applications*, vol. 49, no. 3, pp. 1249–1257, 2013.

[37] M. Barcaro, N. Bianchi, and F. Magnussen, "Analysis and tests of a dual three-phase 12-slot 10-pole permanent magnet motor," in *Energy Conversion Congress and Exposition, 2009. ECCE 2009. IEEE.* IEEE, 2009, pp. 3587–3594.

[38] J. Chai, J. Wang, K. Atallah, and D. Howe, "Performance comparison and winding fault detection of duplex 2-phase and 3-phase fault-tolerant permanent magnet brushless machines," in *Industry Applications Conference, 2007. 42nd IAS Annual Meeting. Conference Record of the 2007 IEEE.* IEEE, 2007, pp. 566–572.

[39] J. Pyrhonen, T. Jokinen, and V. Hrabovcova, *Design of rotating electrical machines.* John Wiley & Sons, 2013.

[40] N. Bianchi and M. Dai Prè, "Use of the star of slots in designing fractional-slot single-layer synchronous motors," *IEE Proceedings-Electric Power Applications*, vol. 153, no. 3, pp. 459–466, 2006.

[41] A. M. EL-Refaie, Z. Zhu, T. M. Jahns, and D. Howe, "Winding inductances of fractional slot surface-mounted permanent magnet brushless machines," in *Industry Applications Society Annual Meeting, 2008. IAS'08. IEEE*. IEEE, 2008, pp. 1–8.

[42] A. M. El-Refaie, M. R. Shah, R. Qu, and J. M. Kern, "Effect of number of phases on losses in conducting sleeves of high speed surface pm machine rotors," in *Industry Applications Conference, 2007. 42nd IAS Annual Meeting. Conference Record of the 2007 IEEE*. IEEE, 2007, pp. 1522–1529.

[43] D. Ishak, Z. Zhu, and D. Howe, "Comparison of pm brushless motors, having either all teeth or alternate teeth wound," *IEEE Transactions on Energy Conversion*, vol. 21, no. 1, pp. 95–103, 2006.

[44] D. Ishak, Z. Zhu, and D. Howe, "Comparative study of permanent magnet brushless motors with all teeth and alternative teeth windings," in *Power Electronics, Machines and Drives, 2004.(PEMD 2004). Second International Conference on (Conf. Publ. No. 498)*, vol. 2. IET, 2004, pp. 834–839.

[45] D. Ishak, Z. Zhu, and D. Howe, "Permanent magnet brushless machines with unequal tooth widths and similar slot and pole numbers," in *Industry Applications Conference, 2004. 39th IAS Annual Meeting. Conference Record of the 2004 IEEE*, vol. 2. IEEE, 2004, pp. 1055–1061.

[46] A. M. El-Refaie and T. M. Jahns, "Impact of winding layer number and magnet type on synchronous surface pm machines designed for wide constant-power speed range operation," in *Industry Applications Conference, 2006. 41st IAS Annual Meeting. Conference Record of the 2006 IEEE*, vol. 3. IEEE, 2006, pp. 1486–1493.

[47] E. Fornasiero, L. Alberti, N. Bianchi, and S. Bolognani, "Considerations on selecting fractional—slot windings," in *Energy Conversion Congress and Exposition (ECCE), 2010 IEEE*. IEEE, 2010, pp. 1376–1383.

[48] Y. Asano, Y. Honda, H. Murakami, Y. Takeda, and S. Morimoto, "Novel noise improvement technique for a pmsm with concentrated winding," in *Power Conversion Conference, 2002. PCC-Osaka 2002. Proceedings of the*, vol. 2. IEEE, 2002, pp. 460–465.

[49] T. A. Lipo, *Vector control and dynamics of AC drives*. Oxford University Press, 1996.

[50] M. Liwschitz, "Distribution factors and pitch factors of the harmonics of a fractional-slot winding," *Transactions of the American Institute of Electrical Engineers*, vol. 62, no. 10, pp. 664–666, 1943.

[51] F. Magnussen and C. Sadarangani, "Winding factors and joule losses of permanent magnet machines with concentrated windings," in *Electric Machines and Drives Conference, 2003. IEMDC'03. IEEE International*, vol. 1. IEEE, 2003, pp. 333–339.

[52] B. Aslan, E. Semail, J. Korecki, and J. Legranger, "Slot/pole combinations choice for concentrated multiphase machines dedicated to mild-hybrid applications," in *IECON 2011-37th Annual Conference on IEEE Industrial Electronics Society*. IEEE, 2011, pp. 3698–3703.

[53] N. Bianchi and E. Fornasiero, "Impact of mmf space harmonic on rotor losses in fractional-slot permanent-magnet machines," *IEEE Transactions on Energy Conversion*, vol. 24, no. 2, pp. 323–328, 2009.

[54] N. Bianchi, S. Bolognani, and E. Fornasiero, "An overview of rotor losses determination in three-phase fractional-slot pm machines," *IEEE Transactions on Industry Applications*, vol. 46, no. 6, pp. 2338–2345, 2010.

[55] Z. Zhu, Z. Xia, L. Wu, and G. Jewell, "Influence of slot and pole number combination on radial force and vibration modes in fractional slot pm brushless machines having single-and double-layer windings," in *Energy Conversion Congress and Exposition, 2009. ECCE 2009. IEEE*. IEEE, 2009, pp. 3443–3450.

[56] J. R. Hendershot and T. J. E. Miller, *Design of brushless permanent-magnet motors*. Magna Physics Pub., 1994.

[57] R. Schiferl and T. Lipo, "Power capability of salient pole permanent magnet synchronous motors in variable speed drive applications," *IEEE Transactions on Industry Applications*, vol. 26, no. 1, pp. 115–123, 1990.

[58] A. M. El-Refaie and T. M. Jahns, "Optimal flux weakening in surface pm machines using fractional-slot concentrated windings," *IEEE Transactions on Industry Applications*, vol. 41, no. 3, pp. 790–800, 2005.

[59] T. A. Lipo, *Analysis of synchronous machines*. CRC Press, 2012.

[60] T. A. Lipo, *Introduction to AC machine design*. Wisconsin Power Electronics Research Center, University of Wisconsin, 2004.

[61] B. Prieto, M. Martinez-Iturralde, L. Fontan, and I. Elosegui, "Analytical calculation of the slot leakage inductance in fractional-slot concentrated-winding machines," *IEEE Transactions on Industrial Electronics*, vol. 62, no. 5, pp. 2742–2752, 2015.

[62] R. Krishnan, *Permanent magnet synchronous and brushless DC motor drives*. CRC press, 2009.

[63] T. Miller, *SPEED's Electric Machines*. Glasgow, U.K.: SPEED Lab., Univ. Glasgow, 2006.

[64] T. A. Lipo, *Introduction to AC machine design*. John Wiley & Sons, 2017.

[65] Z. Zhu and D. Howe, "Influence of design parameters on cogging torque in permanent magnet machines," *IEEE Transactions on Energy Conversion*, vol. 15, no. 4, pp. 407–412, 2000.

[66] D. C. Hanselman, *Brushless permanent magnet motor design*. Magna Physics Publishing, 2006.

[67] F. Libert, "Design, optimization and comparison of permanent magnet motors for a low-speed direct-driven mixer," *Partial fulfillment of the requirements for the degree of Technical Licentiate. Royal Institute of Technology Department of Electrical Engineering Electrical Machines and Power Electronics, Stockholm*, 2004.

[68] "IEEE standard procedures for obtaining synchronous machine parameters by standstill frequency response testing," *IEEE Std 115A-1987*, 1987.

[69] T. Sun, S.-O. Kwon, J.-P. Hong, and G.-H. Lee, "Inductance measurement of interior permanent magnet synchronous motor in stationary reference frame," in *Industry Applications Society Annual Meeting, 2009. IAS 2009. IEEE*. IEEE, 2009, pp. 1–7.

[70] Y. Gao, R. Qu, and Y. Liu, "An improved ac standstill method for inductance measurement of interior permanent magnet synchronous motors," in *Electrical Machines and Systems (ICEMS), 2013 International Conference on*. IEEE, 2013, pp. 927–931.

[71] K. Lu, M. Vetuschi, P. O. Rasmussen, and A. E. Ritchie, "Determination of high-frequency d-and q-axis inductances for surface-mounted permanent-magnet synchronous machines," *IEEE Transactions on Instrumentation and Measurement*, vol. 59, no. 9, pp. 2376–2382, 2010.

[72] C. Choi, W. Lee, S.-O. Kwon, and J.-P. Hong, "Experimental estimation of inductance for interior permanent magnet synchronous machine considering temperature distribution," *IEEE Transactions on Magnetics*, vol. 49, no. 6, pp. 2990–2996, 2013.

[73] J.-Y. Lee, S.-H. Lee, G.-H. Lee, J.-P. Hong, and J. Hur, "Determination of parameters considering magnetic nonlinearity in an interior permanent magnet synchronous motor," *IEEE Transactions on Magnetics*, vol. 42, no. 4, pp. 1303–1306, 2006.

[74] E. Ward and H. Härer, "Preliminary investigation of an invertor-fed 5-phase induction motor," in *Proceedings of the Institution of Electrical Engineers*, vol. 116, no. 6. IEE, 1969, pp. 980–984.

[75] D. C. White and H. H. Woodson, *Electromechanical energy conversion.* Wiley, 1959.

[76] A. Iqbal and E. Levi, "Space vector modulation schemes for a five-phase voltage source inverter," in *Power Electronics and Applications, 2005 European Conference on.* IEEE, 2005, pp. 1–12.

[77] H. Abu-Rub, A. Iqbal, and J. Guzinski, *High performance control of AC drives with MATLAB/Simulink models.* John Wiley & Sons, 2012.

[78] E. Semail, X. Kestelyn, and A. Bouscayrol, "Right harmonic spectrum for the back-electromotive force of an n-phase synchronous motor," in *Industry Applications Conference, 2004. 39th IAS Annual Meeting. Conference Record of the 2004 IEEE*, vol. 1. IEEE, 2004.

[79] E. Semail, X. Kestelyn, and A. Bouscayrol, "Sensitivity of a 5-phase brushless dc machine to the 7th harmonic of the back-electromotive force," in *2004 IEEE 35th Annual Power Electronics Specialists Conference*, vol. 6, 2004, pp. 4564–4570.

[80] X. Kestelyn, E. Semail, and J. Hautier, "Vectorial multi-machine modeling for a five-phase machine," in *International Conference on Electrical Machines (ICEM'02)*, 2002.

[81] N. K. Nguyen, F. Meinguet, E. Semail, and X. Kestelyn, "Fault-tolerant operation of an open-end winding five-phase pmsm drive with short-circuit inverter fault," *IEEE Transactions on Industrial Electronics*, vol. 63, no. 1, pp. 595–605, 2016.

[82] L. Wang, S. Chai, D. Yoo, L. Gan, and K. Ng, *PID and predictive control of electrical drives and power converters using MATLAB/Simulink.* John Wiley & Sons, 2015.

[83] I. Grout, *Digital systems design with FPGAs and CPLDs.* Newnes, 2011.

[84] K.-K. Huh and R. D. Lorenz, "Discrete-time domain modeling and design for ac machine current regulation," in *Industry Applications Conference, 2007. 42nd IAS Annual Meeting. Conference Record of the 2007 IEEE.* IEEE, 2007, pp. 2066–2073.

[85] S. N. Vukosavić, L. S. Perić, and E. Levi, "Ac current controller with error-free feedback acquisition system," *IEEE Transactions on Energy Conversion*, vol. 31, no. 1, pp. 381–391, 2016.

[86] G. Schaefer, "Field weakening of brushless permanent magnet servomotors with rectangular current," in *European Conference on Power Electronics and Applications (EPE)*, vol. 3. IEE, 1991, pp. 429–434.

[87] R. C. Becerra and M. Ehsani, "High-speed torque control of brushless permanent magnet motors," *IEEE Transactions on Industrial Electronics*, vol. 35, no. 3, pp. 402–406, 1988.

[88] T. M. Jahns, "Flux-weakening regime operation of an interior permanent-magnet synchronous motor drive," *IEEE Transactions on Industry Applications*, no. 4, pp. 681–689, 1987.

[89] A. Kumamoto and Y. Hirane, "A semi-closed loop torque control of a buried permanent magnet motor based on a new flux weakening approach," in *Industry Applications Society Annual Meeting, 1989., Conference Record of the 1989 IEEE.* IEEE, 1989, pp. 656–661.

[90] A. K. Adnanes and T. M. Undeland, "Optimum torque performance in pmsm drives above rated speed," in *Industry Applications Society Annual Meeting, 1991., Conference Record of the 1991 IEEE.* IEEE, 1991, pp. 169–175.

[91] W. Soong and T. Miller, "Theoretical limitations to the field-weakening performance of the five classes of brushless synchronous ac motor drive," in *Electrical Machines and Drives, 1993. Sixth International Conference on.* IET, 1993, pp. 127–132.

[92] J.-H. Song, J.-M. Kim, and S.-K. Sul, "A new robust spmsm control to parameter variations in flux weakening region," in *Industrial Electronics, Control, and Instrumentation, 1996., Proceedings of the 1996 IEEE IECON 22nd International Conference on*, vol. 2. IEEE, 1996, pp. 1193–1198.

[93] S. Sudhoff, K. Corzine, and H. Hegner, "A flux-weakening strategy for current-regulated surface-mounted permanent-magnet machine drives," *IEEE Transactions on Energy Conversion*, vol. 10, no. 3, pp. 431–437, 1995.

[94] A. K. Adnanes, "Torque analysis of permanent magnet synchronous motors," in *Power Electronics Specialists Conference, 1991. PESC'91 Record., 22nd Annual IEEE.* IEEE, 1991, pp. 695–701.

[95] E. Levi, D. Dujic, M. Jones, and G. Grandi, "Analytical determination of dc-bus utilization limits in multiphase vsi supplied ac drives," *IEEE Transactions on Energy Conversion*, vol. 23, no. 2, pp. 433–443, 2008.

[96] L. Lu, B. Aslan, L. Kobylanski, P. Sandulescu, F. Meinguet, X. Kestelyn, and E. Semail, "Computation of optimal current references for flux-weakening of multi-phase synchronous machines," in *IECON 2012-38th Annual Conference on IEEE Industrial Electronics Society.* IEEE, 2012, pp. 3610–3615.

[97] J. Gong, B. Aslan, F. Gillon, and E. Semail, "High-speed functionality optimization of five-phase pm machine using third harmonic current," *COMPEL: The International Journal for Computation and Mathematics in Electrical and Electronic Engineering*, vol. 33, no. 3, pp. 879–893, 2014.

[98] F. Scuiller and E. Semail, "Inductances and back-emf harmonics influence on the torque/speed characteristic of five-phase spm machine," in *Vehicle Power and Propulsion Conference (VPPC), 2014 IEEE.* IEEE, 2014, pp. 1–6.

[99] F. Scuiller, H. Zahr, and E. Semail, "Maximum reachable torque, power and speed for five-phase spm machine with low armature reaction," *IEEE Transactions on Energy Conversion*, vol. 31, no. 3, pp. 959–969, 2016.

[100] W. L. Soong and T. Miller, "Field-weakening performance of brushless synchronous ac motor drives," *IEE Proceedings-Electric Power Applications*, vol. 141, no. 6, pp. 331–340, 1994.

[101] J. Apsley, S. Williamson, A. Smith, and M. Barnes, "Induction motor performance as a function of phase number," *IEE Proceedings-Electric Power Applications*, vol. 153, no. 6, pp. 898–904, 2006.

[102] S. Xuelei, W. Xuhui, and C. Wei, "Research on field-weakening control of multiphase permanent magnet synchronous motor," in *Electrical Machines and Systems (ICEMS), 2011 International Conference on.* IEEE, 2011, pp. 1–5.

[103] C. E. Nino, A. R. Tariq, S. Jurkovic, and E. G. Strangas, "Optimal speed control of an interior permanent magnet synchronous motor including cross saturation," in *Electric Machines and Drives Conference, 2009. IEMDC'09. IEEE International.* IEEE, 2009, pp. 292–298.

[104] E. Semail, A. Bouscayrol, and J.-P. Hautier, "Vectorial formalism for analysis and design of polyphase synchronous machines," *The European Physical Journal-Applied Physics*, vol. 22, no. 3, pp. 207–220, 2003.

[105] H. Zahr, M. Trabelsi, E. Semail, and N. K. Nguyen, "Five-phase bi-harmonic pmsm control under voltage and currents limits," in *Industrial Electronics Society, IECON 2017-43rd Annual Conference of the IEEE*. IEEE, 2017, pp. 7995–8000.

[106] T. Miller, *Permanent Magnet and Reluctance Motor Drives*. Oxford, UK: Oxford Science Publications, 1989.

[107] T. M. Jahns, G. B. Kliman, and T. W. Neumann, "Interior permanent-magnet synchronous motors for adjustable-speed drives," *IEEE Transactions on Industry Applications*, no. 4, pp. 738–747, 1986.

[108] S. Morimoto, Y. Takeda, T. Hirasa, and K. Taniguchi, "Expansion of operating limits for permanent magnet motor by current vector control considering inverter capacity," *IEEE Transactions on Industry Applications*, vol. 26, no. 5, pp. 866–871, 1990.

[109] S.-K. Sul, *Control of electric machine drive systems*. John Wiley & Sons, 2011, vol. 88.

[110] B. K. Bose, *Power electronics and variable frequency drives-technology and application*. IEEE Press, 1997.

[111] D. S. Maric, S. Hiti, C. C. Stancu, J. M. Nagashima, and D. B. Rutledge, "Robust flux weakening scheme for surface-mounted permanent-magnet synchronous drives employing an adaptive lattice-structure filter," in *Applied Power Electronics Conference and Exposition, 1999. APEC'99. Fourteenth Annual*, vol. 1. IEEE, 1999, pp. 271–276.

[112] D. Maric, S. Hiti, C. Stancu, and J. Nagashima, "Two improved flux weakening schemes for surface mounted permanent magnet synchronous machine drives employing space vector modulation," in *Industrial Electronics Society, 1998. IECON'98. Proceedings of the 24th Annual Conference of the IEEE*, vol. 1. IEEE, 1998, pp. 508–512.

APPENDICES

Appendix A

Machine Fabrication and Test Bench Description

A.1 Machine Fabrication

This section provides information about the fabrication of the prototype motor. Figure A.1 shows the stator core, rotor core, covers and bearings of the prototype motor. The concentrated stator windings and their short non-overlapping end turns are also shown in Figure A.1. Figure A.2 shows the stator core, which is made of insulated steel laminations. The thickness of the laminations and the type of steel are chosen to minimise the eddy current and hysteresis losses. Figure A.3 shows the frame of the prototype motor while figure A.4 show a close up view of rotor.

A.2 Test Bench Description

This section presents the test bench which has been entirely built by the author. The test bench is designed to implement the field orientation control of the prototype five-phase SPM motor. A general view of the test bench is shown in Figure A.5. The main parts are:

1. The moving part of the test bench consists of the prototype motor and a dc generator which are connected via couplings that include a torque meter and an incremental encoder.
2. Two electrical sources have been used; a low voltage dc source which is con-

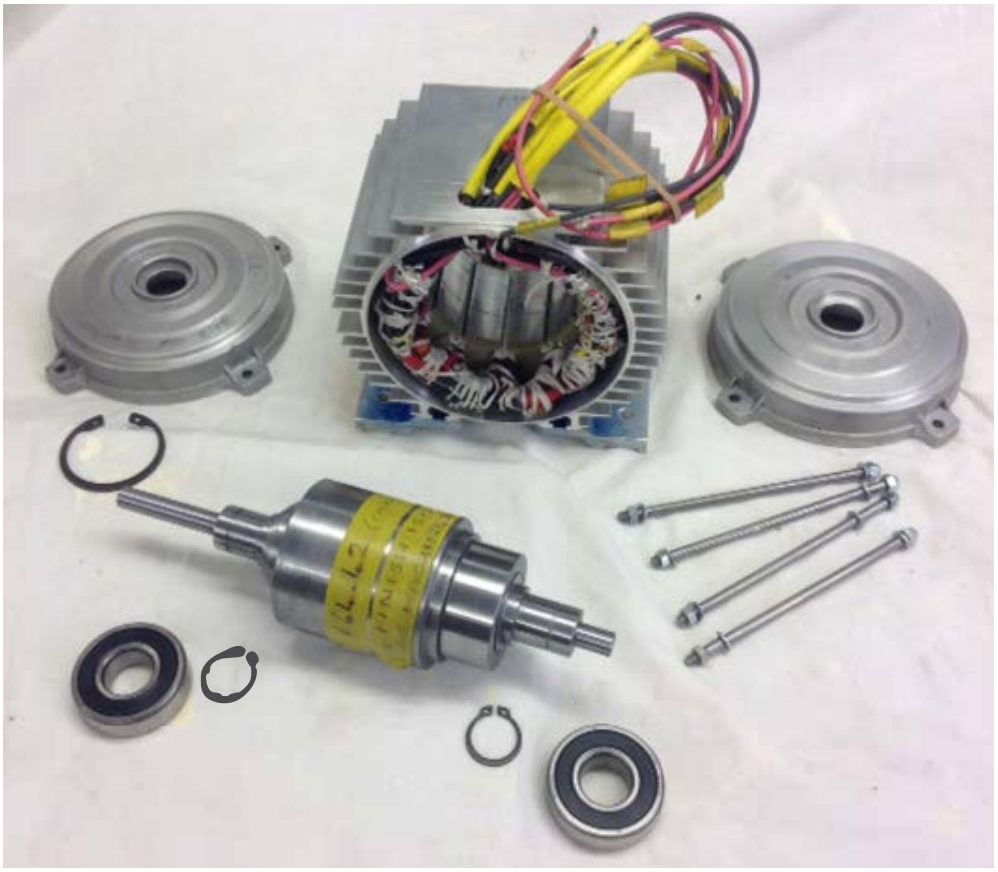

Figure A.1: Stator, rotor, covers and bearings of the prototype motor.

Figure A.2: Prototype machine stator core.

Figure A.3: The frame of the prototype motor.

Figure A.4: The cylindrical shaped rotor, including bearings.

nected directly to the dc-link and a fixed 230 V.

3. Two-level five-phase IGBT VSI, single phase diode-bridge rectifier and dc link capacitors.
4. DC-link voltage sensor and the current sensors.
5. The control system, which includes the dSPACE DS1103 Workstation, the host computer and the signal interface between the dSPACE controller and the power converter.

A.2.1 The dSPACE DS1103 Workstation

The hardware of dSPACE DS1103 Workstation consists mainly of two parts; the DS1103 control board and the CLP1103 Connector Panel which serves as an interface between the DS1103 control board and all external hardware. Figure A.6 shows the CLP1103 Connector Panel. The CLP1103 Connector Panel contains connectors for twenty (20) Analog-to-Digital inputs, eight (8) Digital-to-Analog outputs, and several other connectors that can be used for Digital I/O, Slave/DSP I/O, Incremental Encoder Interfacing, CAN interfacing, and Serial Interfacing. High resolution 6 A/D channels are used for the acquisition of the currents, dc link voltage and torque measurements. The current measurements are synchronised with the PWM clock. The PWM block "DS1103SL DSP PWM3" is linked to an interruption "DS1103 SLAVE PWMINT". The interruption is generated every positive peak of the triangular waveform of the PWM block. One channel analogue incremental encoder interface is used for measuring the rotor position and speed.

The dSPACE DS1103 control system is capable of generating 10 PWM signals. Six of them are programmable in one block to control a 3-phase motor (three signals for the upper switches and three inverted signals for the lower switches) with programmable dead-time. Four single PWM outputs with no dead-time were used for different control applications. The dSPACE DS1103 control system is not designed to control a five-phase motor. To solve the problem the author has modified the interface of the dSPACE system by using five isolated PWM signals with zero dead time as an input for the newly designed circuit board which is able of inserting a suitable dead-time, an opto-isolation and generating the inverted five signals.

The other part of the dSPACE workstation is the host PC. The host PC is used

to manage and monitor the system variables such as speed set-point in real time through the real-time interface software. The real-time interface software is called the Control Desk which is linked to MATLAB/SIMULINK. Figure A.7 shows the test instrumentation panel which is developed by using the Control Desk software.

Figure A.5: General view of the test bench.

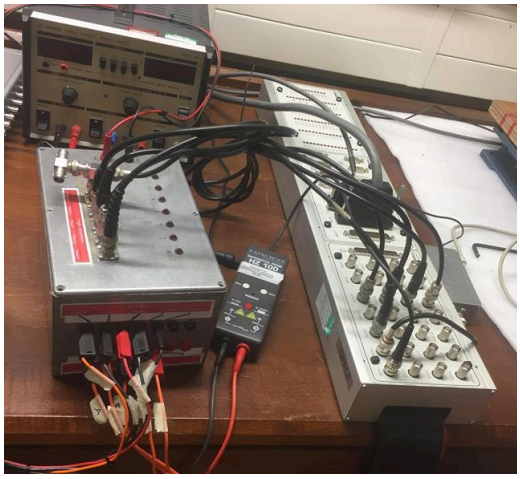

Figure A.6: The CLP1103 Connector Panel.

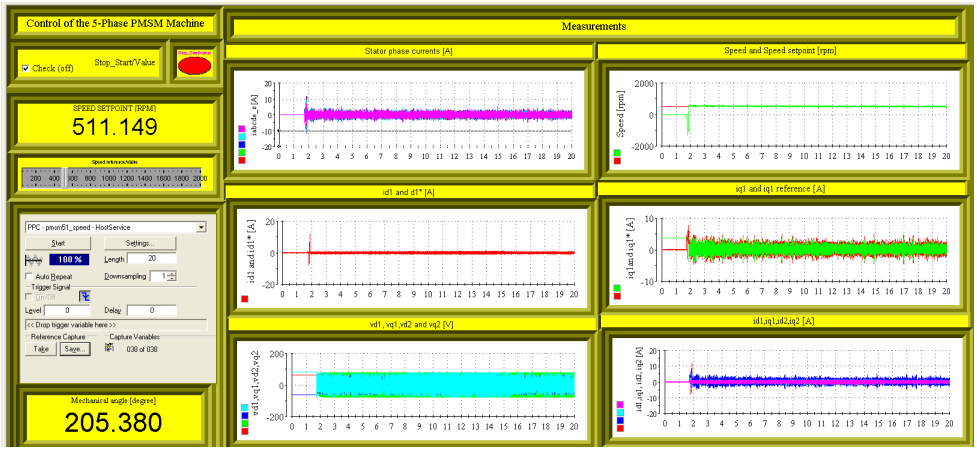

Figure A.7: The test instrumentation panel of the host PC.

Appendix B

Voltage Source Inverter

Figure B.1: Prototype five phase two-level VSI.

Table B.1: Phase-to-neutral voltages of a star connected load supplied from a five-phase VSI.

Mode	Switches ON	v_a	v_b	v_c	v_d	v_e
1	$S_1, S_2, \bar{S}_3, \bar{S}_4, S_5$	$2/5V_{dc}$	$2/5V_{dc}$	$-3/5V_{dc}$	$-3/5V_{dc}$	$2/5V_{dc}$
2	$S_1, S_2, \bar{S}_3, \bar{S}_4, \bar{S}_5$	$3/5V_{dc}$	$3/5V_{dc}$	$-2/5V_{dc}$	$-2/5V_{dc}$	$-2/5V_{dc}$
3	$S_1, S_2, S_3, \bar{S}_4, \bar{S}_5$	$2/5V_{dc}$	$2/5V_{dc}$	$2/5V_{dc}$	$-3/5V_{dc}$	$-3/5V_{dc}$
4	$\bar{S}_1, S_2, S_3, \bar{S}_4, \bar{S}_5$	$-2/5V_{dc}$	$3/5V_{dc}$	$3/5V_{dc}$	$-2/5V_{dc}$	$-2/5V_{dc}$
5	$\bar{S}_1, S_2, S_3, S_4, \bar{S}_5$	$-3/5V_{dc}$	$2/5V_{dc}$	$2/5V_{dc}$	$2/5V_{dc}$	$-3/5V_{dc}$
6	$\bar{S}_1, \bar{S}_2, S_3, S_4, \bar{S}_5$	$-2/5V_{dc}$	$-2/5V_{dc}$	$3/5V_{dc}$	$3/5V_{dc}$	$-2/5V_{dc}$
7	$\bar{S}_1, \bar{S}_2, S_3, S_4, S_5$	$-3/5V_{dc}$	$-3/5V_{dc}$	$2/5V_{dc}$	$2/5V_{dc}$	$2/5V_{dc}$
8	$\bar{S}_1, \bar{S}_2, \bar{S}_3, S_4, S_5$	$-2/5V_{dc}$	$-2/5V_{dc}$	$-2/5V_{dc}$	$3/5V_{dc}$	$3/5V_{dc}$
9	$S_1, \bar{S}_2, \bar{S}_3, S_4, S_5$	$2/5V_{dc}$	$-3/5V_{dc}$	$-3/5V_{dc}$	$2/5V_{dc}$	$2/5V_{dc}$
10	$S_1, \bar{S}_2, \bar{S}_3, \bar{S}_4, S_5$	$3/5V_{dc}$	$-2/5V_{dc}$	$-2/5V_{dc}$	$-2/5V_{dc}$	$3/5V_{dc}$
11	$S_1, \bar{S}_4, \bar{S}_2, \bar{S}_3, \bar{S}_5$	$4/5V_{dc}$	$-1/5V_{dc}$	$-1/5V_{dc}$	$-1/5V_{dc}$	$-1/5V_{dc}$
12	$S_1, \bar{S}_4, S_2, S_3, S_5$	$1/5V_{dc}$	$1/5V_{dc}$	$1/5V_{dc}$	$-4/5V_{dc}$	$1/5V_{dc}$
13	$\bar{S}_4, S_2, \bar{S}_5, \bar{S}_1, \bar{S}_3$	$-1/5V_{dc}$	$4/5V_{dc}$	$-1/5V_{dc}$	$-1/5V_{dc}$	$-1/5V_{dc}$
14	$S_1, S_2, \bar{S}_5, S_3, S_4$	$1/5V_{dc}$	$1/5V_{dc}$	$1/5V_{dc}$	$1/5V_{dc}$	$-4/5V_{dc}$
15	$\bar{S}_4, \bar{S}_5, S_3, \bar{S}_1, \bar{S}_2$	$-1/5V_{dc}$	$-1/5V_{dc}$	$4/5V_{dc}$	$-1/5V_{dc}$	$-1/5V_{dc}$
16	$S_2, S_3, \bar{S}_1, S_4, S_5$	$-4/5V_{dc}$	$1/5V_{dc}$	$1/5V_{dc}$	$1/5V_{dc}$	$1/5V_{dc}$
17	$\bar{S}_5, \bar{S}_1, S_4, \bar{S}_2, \bar{S}_3$	$-1/5V_{dc}$	$-1/5V_{dc}$	$-1/5V_{dc}$	$4/5V_{dc}$	$-1/5V_{dc}$
18	$S_1, S_3, S_4, \bar{S}_2, S_5$	$1/5V_{dc}$	$-4/5V_{dc}$	$1/5V_{dc}$	$1/5V_{dc}$	$1/5V_{dc}$
19	$\bar{S}_4, \bar{S}_1, \bar{S}_2, S_5, \bar{S}_3$	$-1/5V_{dc}$	$-1/5V_{dc}$	$-1/5V_{dc}$	$-1/5V_{dc}$	$4/5V_{dc}$
20	$S_1, S_2, S_4, S_5, \bar{S}_3$	$1/5V_{dc}$	$1/5V_{dc}$	$-4/5V_{dc}$	$1/5V_{dc}$	$1/5V_{dc}$
21	$\bar{S}_4, S_2, \bar{S}_1, S_5, \bar{S}_3$	$-2/5V_{dc}$	$3/5V_{dc}$	$-2/5V_{dc}$	$-2/5V_{dc}$	$3/5V_{dc}$
22	$S_1, S_2, \bar{S}_3, S_4, \bar{S}_5$	$2/5V_{dc}$	$2/5V_{dc}$	$-3/5V_{dc}$	$2/5V_{dc}$	$-3/5V_{dc}$
23	$S_1, \bar{S}_2, S_3, \bar{S}_4, \bar{S}_5$	$3/5V_{dc}$	$-2/5V_{dc}$	$3/5V_{dc}$	$-2/5V_{dc}$	$-2/5V_{dc}$
24	$\bar{S}_1, S_2, S_3, \bar{S}_4, S_5$	$-3/5V_{dc}$	$2/5V_{dc}$	$2/5V_{dc}$	$-3/5V_{dc}$	$2/5V_{dc}$
25	$\bar{S}_1, S_2, \bar{S}_3, S_4, \bar{S}_5$	$-2/5V_{dc}$	$3/5V_{dc}$	$-2/5V_{dc}$	$3/5V_{dc}$	$-2/5V_{dc}$
26	$S_1, \bar{S}_2, S_3, S_4, \bar{S}_5$	$3/5V_{dc}$	$-2/5V_{dc}$	$3/5V_{dc}$	$3/5V_{dc}$	$-2/5V_{dc}$
27	$\bar{S}_1, \bar{S}_2, S_3, \bar{S}_4, S_5$	$-2/5V_{dc}$	$-2/5V_{dc}$	$3/5V_{dc}$	$-2/5V_{dc}$	$3/5V_{dc}$
28	$\bar{S}_1, S_2, \bar{S}_3, S_4, S_5$	$-3/5V_{dc}$	$2/5V_{dc}$	$-3/5V_{dc}$	$2/5V_{dc}$	$2/5V_{dc}$
29	$S_1, \bar{S}_2, \bar{S}_3, S_4, \bar{S}_5$	$3/5V_{dc}$	$-2/5V_{dc}$	$-2/5V_{dc}$	$3/5V_{dc}$	$-2/5V_{dc}$
30	$S_1, \bar{S}_2, S_3, \bar{S}_4, S_5$	$2/5V_{dc}$	$-3/5V_{dc}$	$2/5V_{dc}$	$-3/5V_{dc}$	$2/5V_{dc}$
31	S_1, S_2, S_3, S_4, S_5	V_{dc}	V_{dc}	V_{dc}	V_{dc}	V_{dc}
32	$\bar{S}_1, \bar{S}_2, \bar{S}_3, \bar{S}_4, \bar{S}_5$	V_{dc}	V_{dc}	V_{dc}	V_{dc}	V_{dc}

Table B.2: Space vector table of the phase voltages for a five-phase VSI.

S. No.	Switching States	States Space vectors in $\alpha_1 - \beta_1$ plane	Space vectors in $\alpha_2 - \beta_2$ plane
0	00000	0	0
1	00001	$2/5\ V_{dc}2\exp(j8\pi/5)$	$2/5\ V_{dc}2\exp(j6\pi/5)$
2	00010	$2/5\ V_{dc}2\exp(j6\pi/5)$	$2/5\ V_{dc}2\exp(j2\pi/5)$
3	00011	$2/5\ V_{dc}2\cos(\pi/5)\exp(j7\pi/5)$	$2/5\ V_{dc}4\cos(2\pi/5)\exp(j4\pi/5)$
4	00100	$2/5\ V_{dc}2\exp(j4\pi/5)$	$2/5\ V_{dc}2\exp(j8\pi/5)$
5	00101	$2/5\ V_{dc}4\cos(2\pi/5)\exp(j6\pi/5)$	$2/5\ V_{dc}2\cos(\pi/5)\exp(j7\pi/5)$
6	00110	$2/5\ V_{dc}2\cos(\pi/5)\exp(j\pi/5)$	$2/5\ V_{dc}4\cos(2\pi/5)\exp(0)$
7	00111	$2/5\ V_{dc}2\cos(\pi/5)\exp(j6\pi/5)$	$2/5\ V_{dc}4\cos(2\pi/5)\exp(j7\pi/5)$
8	01000	$2/5\ V_{dc}2\exp(j2\pi/5)$	$2/5\ V_{dc}2\exp(j4\pi/5)$
9	01001	$2/5\ V_{dc}4\cos(2\pi/5)\exp(0)$	$2/5\ V_{dc}2\cos(\pi/5)\exp(j\pi/5)$
10	01010	$2/5\ V_{dc}4\cos(2\pi/5)\exp(j4\pi/5)$	$2/5\ V_{dc}2\cos(\pi/5)\exp(j3\pi/5)$
11	01011	$2/5\ V_{dc}4\cos(2\pi/5)\exp(j7\pi/5)$	$2/5\ V_{dc}2\cos(\pi/5)\exp(j4\pi/5)$
12	01100	$2/5\ V_{dc}2\cos(\pi/5)\exp(j3\pi/5)$	$2/5\ V_{dc}4\cos(2\pi/5)\exp(j6\pi/5)$
13	01101	$2/5\ V_{dc}4\cos(2\pi/5)\exp(j3\pi/5)$	$2/5\ V_{dc}2\cos(\pi/5)\exp(j6\pi/5)$
14	01110	$2/5\ V_{dc}2\cos(\pi/5)\exp(j4\pi/5)$	$2/5\ V_{dc}4\cos(2\pi/5)\exp(j3\pi/5)$
15	01111	$2/5\ V_{dc}2\exp(j\pi)$	$2/5\ V_{dc}2\exp(j\pi)$
16	10000	$2/5\ V_{dc}2\exp(j0)$	$2/5\ V_{dc}2\exp(j0)$
17	10001	$2/5\ V_{dc}2\cos(\pi/5)\exp(j9\pi/5)$	$2/5\ V_{dc}4\cos(2\pi/5)\exp(j8\pi/5)$
18	10010	$2/5\ V_{dc}4\cos(2\pi/5)\exp(j8\pi/5)$	$2/5\ V_{dc}2\cos(\pi/5)\exp(j\pi/5)$
19	10011	$2/5\ V_{dc}2\cos(\pi/5)\exp(j7\pi/5)$	$2/5\ V_{dc}4\cos(2\pi/5)\exp(j\pi/5)$
20	10100	$2/5\ V_{dc}4\cos(2\pi/5)\exp(j2\pi/5)$	$2/5\ V_{dc}2\cos(\pi/5)\exp(j9\pi/5)$
21	10101	$2/5\ V_{dc}4\cos(2\pi/5)\exp(j9\pi/5)$	$2/5\ V_{dc}2\cos(\pi/5)\exp(j7\pi/5)$
22	10110	$2/5\ V_{dc}2\cos(2\pi/5)\exp(j\pi)$	$2/5\ V_{dc}2\cos(\pi/5)\exp(j0)$
23	10111	$2/5\ V_{dc}2\exp(j7\pi/5)$	$2/5\ V_{dc}2\exp(j9\pi/5)$
24	11000	$2/5\ V_{dc}2\cos(\pi/5)\exp(j\pi/5)$	$2/5\ V_{dc}4\cos(2\pi/5)\exp(j2\pi/5)$
25	11001	$2/5\ V_{dc}2\cos(\pi/5)\exp(j0)$	$2/5\ V_{dc}4\cos(2\pi/5)\exp(j\pi/5)$
26	11010	$2/5\ V_{dc}4\cos(2\pi/5)\exp(j\pi/5)$	$2/5\ V_{dc}2\cos(\pi/5)\exp(j2\pi/5)$
27	11011	$2/5\ V_{dc}2\exp(j9\pi/5)$	$2/5\ V_{dc}2\exp(j3\pi/5)$
28	11100	$2/5\ V_{dc}2\cos(\pi/5)\exp(j2\pi/5)$	$2/5\ V_{dc}4\cos(2\pi/5)\exp(j9\pi/5)$
29	11101	$2/5\ V_{dc}2\exp(j\pi/5)$	$2/5\ V_{dc}2\exp(j7\pi/5)$
30	11110	$2/5\ V_{dc}2\exp(j3\pi/5)$	$2/5\ V_{dc}2\exp(j\pi/5)$
31	11111	0	0

Appendix C

Flux Weakening Control

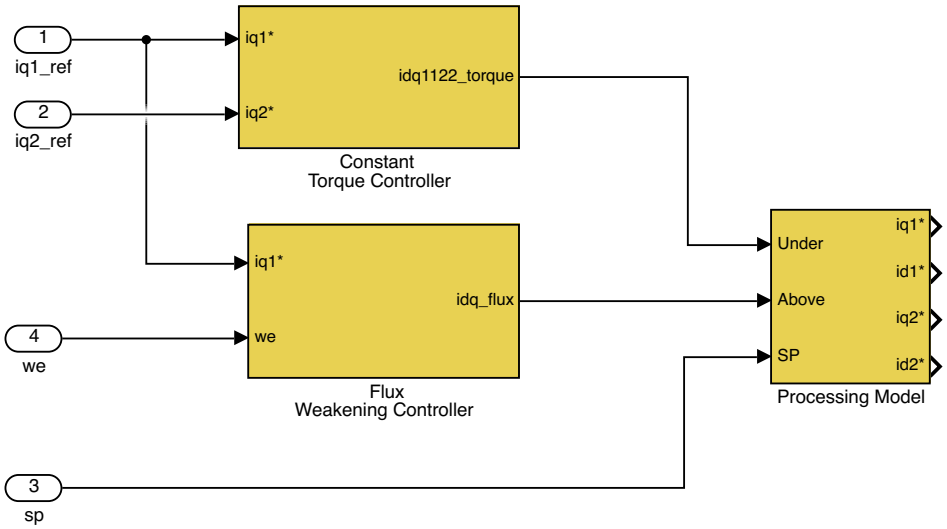

Figure C.1: The currents demand control.

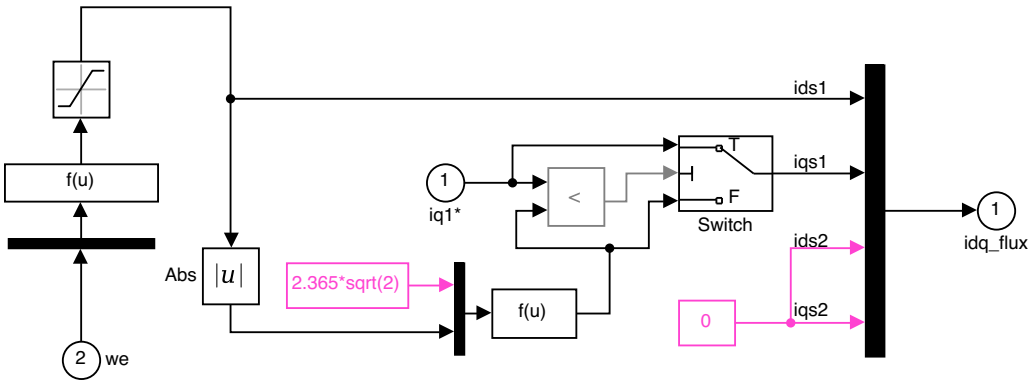

Figure C.2: Flux-Weakening control Block.

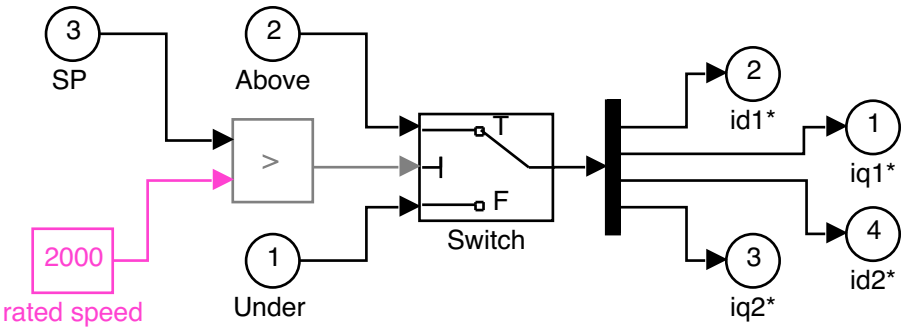

Figure C.3: Constant torque control block.

Appendix D

The Star of Slots

The following code is used to plot the star of slots which is necessary for determining the layout of the winding.

```
%                    STAR OF SLOTS
%                  MATLAB CODE copyright
%                  BY WALEED J HASSAN
clc
clear all
 Q=input('The number of slot =');
 p=input('The number of poles =');
 F=input('The number of phases =');
 alph_s=360/Q;
alpha_se=(p/2)*alph_s;
for x=1:1:Q-1 ;
          angle(x)=alpha_se*x;
          m=1;
            if angle(x) <= 360 ;
               y(x)=angle(x);
            elseif angle(x) >360
    while m<40;
            y(x)=angle(x)-360*m;
            if y(x)<0
                 y(x)=angle(x)-360*(m-1);
                 break
            else
                 m=m+1;
            end
     end
end
    fprintf('%s,%i,%s,%i,\r\n','The angle of the spoke '.....
    , x+1,'=', y(x));
end
x=1:1:Q-1 ;
a=[0 y(x)] ;
theta=a*(pi/180);
r = 7;
u = r * cos(theta);
v = r * sin(theta);
x=zeros(1,Q);
y=x;
quiver(x,y,u,v,'k','LineWidth',1);
set(gca, 'XLim', [-10 10], 'YLim', [-10 10],'LineWidth',0.5);
for  i = 1:length(a)
   r =7;
   u = r * cos(theta);
   v = r * sin(theta);
   m= num2str(i);
  text(u(i),v(i),m)
end
hold on
  ang=0.174:0.01:pi/F;
 ang1=pi+0.174:0.01:pi+pi/F;
  r1=8;
xp=r1*cos(ang);
yp=r1*sin(ang);
plot(xp,yp);
hold on
xp1=r1*cos(ang1);
yp1=r1*sin(ang1);
plot(xp1,yp1);
```